



Trapping and nondemolition measurement of cold atoms in a high-finesse ring cavity

Simon Bernon

► To cite this version:

Simon Bernon. Trapping and nondemolition measurement of cold atoms in a high-finesse ring cavity. Atomic Physics [physics.atom-ph]. Ecole Polytechnique X, 2011. English. NNT : . tel-00624195v2

HAL Id: tel-00624195

<https://pastel.hal.science/tel-00624195v2>

Submitted on 19 Sep 2011

HAL is a multi-disciplinary open access archive for the deposit and dissemination of scientific research documents, whether they are published or not. The documents may come from teaching and research institutions in France or abroad, or from public or private research centers.

L'archive ouverte pluridisciplinaire **HAL**, est destinée au dépôt et à la diffusion de documents scientifiques de niveau recherche, publiés ou non, émanant des établissements d'enseignement et de recherche français ou étrangers, des laboratoires publics ou privés.

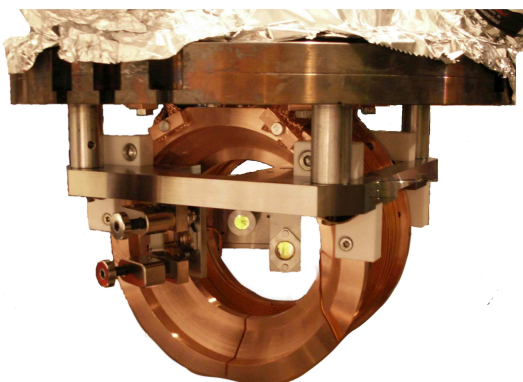
**Laboratoire Charles Fabry
Institut d'Optique Graduate School**

**THESE DE DOCTORAT DE
L'ECOLE POLYTECHNIQUE**

Sujet de la thèse:

**Piégeage et mesure non-destructive d'atomes froids
dans une cavité en anneau de haute finesse**

Trapping and nondemolition measurement of cold
atoms in a high-finesse ring cavity



Simon BERNON

soutenue le 15 avril 2011 devant la commission d'examen composée de:

M. Michel Brune	Rapporteur
M. Vincent Boyer	Rapporteur
M. Morgan Mitchell	Examineur
M. Alain Aspect	Examineur
M. Jean-François Roch	Président
M. Philippe Bouyer	Directeur de thèse
M. Arnaud Landragin	Membre invité
M. Mark Kasevich	Membre invité

Palaiseau, September 9, 2011

Remerciements

Je tiens tout d'abord à remercier très chaleureusement Vincent BOYER et Michel BRUNE d'avoir accepté de rapporter ce manuscrit. C'est un manuscrit assez long qui contient à la fois des parties théoriques et expérimentales et qui leur a très certainement demandé plusieurs heures de travail. La précision de leurs commentaires m'a montré l'attention particulière qu'ils ont portée à la relecture de ce manuscrit. Je les remercie pour toutes leurs remarques et toutes les discussions qu'ils ont initiées et qui ont grandement enrichi ce manuscrit. Je remercie également les autres membres du jury : Morgan MITCHELL, Alain ASPECT, Philippe BOUYER, Arnaud LANDRAGIN et Mark KASEVICH pour leurs multiples questions. Celles-ci m'ont donné la possibilité de mettre en valeur les résultats obtenus durant ces trois années de doctorat. Parmi les membres de mon jury, je remercie particulièrement Jean François ROCH pour l'avoir présidé.

Les recherches que j'ai menées dans le groupe d'Optique Atomique à l'Institut d'Optique ont été financées par une bourse AMX de l'école doctorale de l'école polytechnique. Pour m'avoir ainsi soutenu à la fois financièrement mais également pour leur soutien administratif durant le déroulement de ce doctorat, je tiens à remercier toute l'équipe de l'école doctorale et particulièrement Audrey, Alexandra et Christine avec qui j'ai été en contact régulièrement.

A l'institut, j'ai été tout d'abord accueilli par son premier directeur de la recherche Pierre CHAVEL dont j'ai apprécié le contact et qui m'a impressionné par ses qualités d'organisation et par la rigueur avec laquelle il a dirigé le pôle recherche. Je remercie également son successeur Christian CHARDONNET pour avoir soutenu notre projet de recherche.

Si je suis arrivé à l'Institut, c'est bel et bien grâce aux cours de physique quantique de l'école polytechnique de Jean DALIBARD, d'Alain ASPECT et de Philippe GRANGIER. Tous les trois ont su nous enseigner la physique quantique comme s'il s'agissait d'une histoire passionnante toujours à écrire. Mais je crois que c'est vraiment Alain qui a suscité en moi l'intérêt que je porte aujourd'hui pour l'optique. Son cours sur les lasers m'a enseigné de toujours chercher à comprendre la physique qui se cache derrière les techniques que nous utilisons au quotidien dans les laboratoires. Pendant mes années de thèse, Alain, qui dirige le groupe d'optique atomique s'est toujours montré très avide de nous transmettre ses connaissances, ce dont je lui suis très reconnaissant.

Philippe BOUYER a dirigé les recherches que je présente dans ce manuscrit. C'est un directeur de recherche qui fourmille de nouvelles idées et de nouveaux projets. Je le remercie beaucoup de m'avoir fait confiance sur ce projet. Il a toujours su mettre en oeuvre les moyens financiers et humains nécessaires à la réussite du projet, ce qui est à mes yeux une très grande qualité de directeur. J'ai été très content de travailler avec lui et j'ai beaucoup apprécié l'enthousiasme qu'il a envers la physique expérimentale. Grâce à lui j'ai également pu passer 6 mois à Stanford dans le groupe de Mark KASEVICH. Cela a été une expérience mémorable dont il a clairement été à l'initiative. Philippe, je te souhaite beaucoup de réussite dans la fonction de directeur du LP2N, ton dernier projet en date. Si Philippe était mon seul directeur sur le

papier, j'estime néanmoins qu'Arnaud LANDRAGIN peut également en revendiquer une part. Je le remercie pour son enthousiasme envers la physique expérimentale et ses problèmes techniques. Tout ce que je connais des intégrateurs en série, c'est à Arnaud que je le dois, mais cela n'est qu'un exemple parmi tant d'autres. C'est le plus grand bavard que je connaisse, souvent avisé, en particulier quand il s'agit de science, parfois saugrenu, pour cela il faut l'entendre parler de la nocivité du sport, mais toujours amical. Merci Arnaud d'avoir partagé avec moi tes nombreux avis sur tout ;)

Si c'est l'école doctorale de Polytechnique qui m'a donné ma bourse de doctorat, c'est vraiment l'IFRAF qui a été à l'initiative du projet BIARO. Je tiens ici à en remercier particulièrement sa directrice Michèle LEDUC qui s'est toujours beaucoup intéressée aux avancées de notre expérience.

Venons en maintenant aux travailleurs des premières heures de l'expérience et des dernières heures de la soirée. Merci tout d'abord à Thierry avec qui j'ai été très heureux de faire mes premiers pas en physique atomique lors de mon stage de Master. Andréa, Thomas et Ralf ont été tous les trois de très bons camarades sur cette expérience. Je remercie Andréa d'avoir accepté le challenge d'une expérience en construction, ce qui est toujours un pari risqué pour un post-doctorat. Ces connaissances en électronique nous ont vraiment dépatouillé de nos problèmes d'asservissement de la cavité. Je le remercie pour la rigueur qu'il nous a apportée et que je me fait, aujourd'hui, fort d'appliquer à mon tour. J'ai également été très heureux de travailler avec Thomas. Il a été un très bon compagnon des discussions de la dernière heure. Nos nombreuses discussions nous ont vraiment permis à tous les deux d'avancer dans la compréhension du sujet. Je le remercie sincèrement pour tout ce qu'il m'a apporté et j'espère que le futur nous donnera à nouveau la possibilité de travailler ensemble... enfin si tu arrives à te réveiller plus tôt... Comme Thomas, Ralf a toujours été très enthousiaste à discuter la physique de l'expérience. Je le remercie de nous avoir apporté son oeil nouveau et la fraîcheur de sa jeunesse et de sa bonne humeur.

Si chez BIARO, nous avons toujours aimé travailler nos électroniques d'asservissement par nous même, aucune n'auraient probablement fonctionné sans Frédéric. Personnellement, je le remercie pour tout ce qu'il m'a appris en électronique et pour tous les boîtiers qu'il nous a confectionné et qui eux fonctionnaient à tous les coups ;) Un grand merci également à André sans qui nos expériences n'aurait jamais trouvé la cadence. Je remercie également les mécaniciens de l'institut, André GUILBAUD et Patrick ROTH, qui ont toujours répondu à nos demandes dans des délais exceptionnels. On avait toujours besoin des pièces pour hier et eux, les faisaient pour avant-hier et ce, avec le sourire...

Je remercie tous les membres permanents du groupe d'Optique Atomique, Isabelle, Vincent, Karen, Thomas, Denis, Nathalie et Chris. Sur cette expérience, qui n'avait pas de membre permanent quotidiennement présent, ils se sont toujours montrés très disponibles et nous ont beaucoup aidé à avancer. Merci également aux mousquetaires, David, Karim, Jeff, Thomas pour être simplement devenus des amis. Et parmi les mousquetaires se cache toujours une fille... incarnée cette fois en la personne de Juliette. Je remercie également Sébastien pour sa bonne humeur et son humour sans équivalent... Je te souhaite beaucoup de réussite dans ton nouveau projet. Mais quoiqu'il arrive n'oublie pas comment couper une pomme en deux à la main, ça peut toujours servir. Merci aussi à tous les doctorants de la première heure avec qui nous avons pu partager les joies et les peines des expériences : Jean Philippe, Valentina, JC, Martin, Alain et Julien. Un grand merci également à la nouvelle génération Thomas, Ralf, Thibaut, Baptiste, Marie, Antoine, Josselin, Fréd, Kilian et Lynn. Là où les anciens avaient déjà leur histoire, ils ont su réinsuffler de la nouveauté et je leur souhaite à tous beaucoup de réussite

dans leur projets respectifs. Je remercie également nos astronautes en herbe Rémi, Vincent, Guillaume et Patrick toujours de bonne humeur et de gravité nulle... Je vous souhaite beaucoup de bonheur pour vos voies respectives.

Les expériences d'atomes froids sont souvent aujourd'hui des montages mécaniques de la complexité d'une cathédrale. Si la notre ne l'ai pas "trop" devenue, c'est essentiellement grâce à David HOLLEVILLE de l'Observatoire de Paris qui m'a beaucoup aidé sur toute la conception mécanique. Un grand merci David pour avoir repris tous mes plans. Ce n'est pas le plus drôle d'une conception mais tu me l'as toujours fait avec le sourire. Je te remercie aussi pour tout ce que tu m'as appris sur les techniques de vide et de design du vide. A l'observatoire, je souhaite également remercier les mécaniciens Jean-Pierre AOUSTIN, Laurent PELAY, Jean-Jacques BOUSQUET pour nous avoir littéralement réalisé toute la mécanique de la cavité au dixième. Merci également à Annie GERARD et à Florence CORNU qui ont fait "le vide" dans notre expérience. Etuver les bobines n'a pas été une mince affaire et leur expérience a clairement rendu la chose possible. Merci également à Bertrand VENON qui a été un parfait acolyte pour le montage des bobines ultra-vide. Je suis vraiment très content que pour toi, l'aventure puisse se poursuivre à l'Obs. Tant que je suis à L'Observatoire, je souhaiterai en remercier leurs électroniciens Laurent VOLODIMER et Michel LOURS dont l'aide sur les problèmes micro-onde nous aura été précieuse.

Je remercie également les différents services de l'institut. Tous les services administratifs qui font tourner la boutique. Je remercie également les membres du service technique, Jacky ROBIN, Eric VIGNE, Mehdi BEN HARIZ et Jean-Luc CADORE qui gèrent tous les problèmes du bâtiment. Merci à tout le pôle enseignement, aux administratifs qui se cassent la tête sur les emplois du temps et à tous les enseignants avec qui j'ai eu le loisir de travailler : Nicolas SCHLOSSER, François BALEMBOIS, Jean Michel JONATHAN, Martin ROBERT DE ST VINCENT, Gâelle LUCAS-LECLIN. Je remercie particulièrement Nicolas DUBREUIL, à la fois pour avoir travaillé avec lui mais également pour avoir été mon tuteur et pour avoir partagé avec moi sa vision de l'enseignement. Merci à Lionel JACUBOWIEZ et Vincent JOSSE de m'avoir épaulé pour l'encadrement des TP. Merci également à Thierry AVIGNON, non seulement pour son aide technique lors des TP mais aussi pour tout le matériel qu'il nous a prêté... pour un expérimentateur, chez lui, c'est la caverne d'Ali Baba.

Je remercie également Mark KASEVICH chez qui j'ai pu travailler les six derniers mois de ma thèse. J'ai énormément appris à son contact et j'ai été vraiment très impressionné par ses qualités et sa culture de physicien. J'espère que l'avenir me donnera à nouveau l'occasion de collaborer avec lui.

J'aimerai également remercier mes parents. A la fois ma mère pour les encouragements qu'elle m'a toujours apportés et pour le soutien qu'elle m'a montré à la veille de toutes mes reprises scolaires, mais également mon père qui m'a vraiment donné le goût du travail bien fait et qui m'a toujours poussé à me dépasser. Il a toujours mis beaucoup d'effort dans tout ce qu'il faisait et il est pour moi un modèle de conviction et de foi en l'avenir...

Enfin, je tiens à remercier mon épouse Nadège. Tu es et tu resteras mon plus grand appui. Ce n'est qu'avec toi que ma vie prend tout son sens. Les recherches que j'ai menées pendant ces trois années te doivent beaucoup. A la fois pour ton soutien au quotidien lorsque mon morale vaquait au rythme de l'expérience, mais également pour ton enthousiasme à nous lancer toujours dans de nouvelles aventures et de beaux défis. Si j'ai pu autant m'investir dans ces recherches c'est aussi parce que tu as été capable de parfois me les sortir de la tête. Pour tout ton amour, MERCI.

à mon épouse, Nadège,

Contents

Remerciements	i
Introduction	1
1 Introduction to non-classical interferometry	5
1.1 Atom interferometric measurement	6
1.1.1 The concept	6
1.1.2 State of the Art	7
1.2 The international context of non-classical state preparation.	9
1.2.1 Measurement induced spin squeezing in a Mach Zehnder interferometer	10
1.2.2 Measurement/Cavity induced spin squeezing at MIT	11
1.2.3 Measurement induced spin squeezing in Stanford	13
1.3 The initial orientation of the experiment	14
1.3.1 New sources for new types of gravimeter	14
1.3.2 Pushing forward the quantum	15
2 Experimental set-up	17
2.1 Optical bench	17
2.1.1 Extended cavity diode lasers	17
2.1.2 Laser frequency	19
2.1.3 Scheme of the optical bench	21
2.1.4 Laser locks	23
2.2 Apparatus for cold atom trapping	29
2.2.1 Cooling and trapping of atoms	29
2.2.2 Two dimensional Magneto-Optical Trap	31
2.2.3 Ultra High vacuum set up	35
2.3 Imaging system	39
2.4 Summary	43
3 The high finesse cavity	45
3.1 The considered geometries	46
3.1.1 Different possible geometries... but a common description	46
3.1.2 Triangle and star geometry	47
3.2 The Butterfly geometry	52
3.2.1 The a priori cavity properties	52
3.2.2 The gaussian mode : TEM ₀₀	55
3.2.3 Cavity alignment	61
3.2.4 Transverse mode study, an indication of the anisotropy	64
3.2.5 Measurement of the optical profile	65

3.2.6	Cavity parameters at 1560 nm.	74
3.2.7	Losses of the cavity	75
3.3	Locking of the 1560 nm laser to the cavity	78
3.3.1	The cavity: a low pass frequency filter	78
3.3.2	Pound Drever Hall Method	79
3.3.3	Locking a Koheras fiber laser to the cavity	82
3.3.4	Opto-mechanical injection of the cavity	83
3.4	Summary	83
4	Atomic samples trapped in a high finesse cavity	87
4.1	Introduction to Bose Einstein condensation	87
4.1.1	Saturation of the excited states	88
4.1.2	Effect of the interactions	89
4.2	Trapping atoms in a crossed optical cavity	90
4.2.1	Trapping cold atoms	92
4.2.2	Perspectives	99
4.3	Summary	101
5	Atomic squeezing induced by Quantum Non-Demolition measurement: theory	103
5.1	Introduction to the Bloch sphere	104
5.1.1	Coherent manipulation of a single two level system	104
5.1.2	The rotation operators and the Bloch sphere	106
5.1.3	Extension to the many body system	108
5.1.4	Shot noise in atomic interferometry	111
5.2	Quantum Non-Demolition measurement	114
5.2.1	Global measurement	114
5.2.2	Element of theory	114
5.2.3	Optical phase detection	119
5.3	Quantum trajectories in a wavefunction analysis of the squeezing process . . .	121
5.3.1	Background formalism	121
5.3.2	The Mach-Zehnder interferometer	122
5.3.3	Long term behavior	128
5.3.4	The Mach-Zehnder including losses and in an optical cavity	130
5.3.5	The heterodyne measurement	134
5.3.6	Comparison between the Mach-Zehnder interferometer and the heterodyne measurement	143
5.3.7	Comment on the photon by photon versus single pulse measurement . .	143
5.3.8	Perspectives	145
5.4	Summary	149
6	Non-demolition measurement: experiment	151
6.1	Heterodyne detection and detector performance	152
6.1.1	General Argumentation	152
6.1.2	Considered case	154
6.1.3	A low sensitivity to common mode noise	156
6.1.4	Optical set-up	158
6.1.5	The optical detector	159

6.1.6	Atomic phase and spontaneous emission	161
6.2	Non demolition measurement of the atomic sample	164
6.2.1	Dispersive spectroscopic measurement	164
6.2.2	Probe induced destructivity	164
6.2.3	Non-demolition measurement of Rabi oscillations.	166
6.2.4	Interferometric phase in a spin-echo sequence	171
6.2.5	First study of the atomic noise	173
6.3	Perspectives: High SNR cavity measurement	177
6.4	Summary	179
7	Raman laser	181
7.1	Experimental set-up	181
7.1.1	Vacuum chamber integrated cavity	182
7.1.2	The linear cavity	182
7.1.3	The laser system	183
7.2	Raman laser	185
7.2.1	Principle	185
7.2.2	Laser characteristics	186
7.3	Summary	190
	Conclusion	193
A	Rubidium D_2 transition	197
B	Phase and frequency modulation	199
C	Interlude on alignment locks	203
D	Complete expression of the polarizability	205
D.1	Dipole elements	205
D.2	Dipolar electric interaction: complete expression of the polarizability	206
E	Theory calculation	209
E.1	The Gaussian approximation of the Mach Zehnder interferometer	209
E.2	Losses	210
E.3	Frequency splitter	210
F	CQED and classical definitions	213
G	Mechanical design	215
	Bibliography	227

List of Figures

1.1	<i>Analogy between optical and atomic interferometer</i>	7
1.2	<i>Detection sensitivity of an atomic clock limited to the shot noise.</i>	9
1.3	<i>Schematic of the Mach Zehnder interferometer used in the group of Eugen Polzik</i>	10
1.4	<i>Atomic projection reduction in a two color probing</i>	11
1.5	<i>Probing the population difference by a measurement of the transmission of a cavity.</i>	12
1.6	<i>Shearing effect of a coherent state</i>	13
1.7	<i>Heterodyne Non demolition measurement apparatus developed at Stanford.</i>	14
1.8	<i>A bouncing gravimeter sequence</i>	15
1.9	<i>The four mirror cavity geometry.</i>	16
2.1	<i>Scheme of the extended cavity diode.</i>	18
2.2	<i>Beatnote of two extended cavity diodes.</i>	19
2.3	<i>Atomic transition and lasers frequencies.</i>	20
2.4	<i>Scheme of the optical bench.</i>	22
2.5	<i>Saturated absorption</i>	23
2.6	<i>Scheme of the beatnote lock.</i>	25
2.7	<i>Scheme of the frequency and phase lock of the Raman beams</i>	27
2.8	<i>Phase lock beatnote</i>	28
2.9	<i>Microwave frequency chain</i>	29
2.10	<i>Cooling and Trapping mechanism</i>	31
2.11	<i>Two dimensional magneto-optical trap</i>	33
2.12	<i>Loading of the 3D MOT.</i>	34
2.13	<i>Overview of the complete vacuum system</i>	36
2.14	<i>The copper support of the coils</i>	38
2.15	<i>UHV coils support</i>	38
2.16	<i>Life time of the 3D MOT.</i>	39
2.17	<i>Mechanical design of the cavity</i>	40
2.18	<i>Imaging system.</i>	41
2.19	<i>Modulation Transfer Function of the telescope.</i>	42
3.1	<i>Geometry considered for the cavity</i>	47
3.2	<i>Notation for the electric field in the cavity.</i>	48
3.3	<i>Reflectivity of the cavities in p polarisation</i>	49
3.4	<i>The crossed cavity configuration</i>	53
3.5	<i>UHV mirror mount mechanics.</i>	54
3.6	<i>Gaussian beam profile and definitions</i>	57
3.7	<i>ABCD formalism</i>	58
3.8	<i>Ray traces</i>	59
3.9	<i>Profile of the beam along the optical axis for 1560 nm radiation.</i>	60

3.10	<i>Alignment and injection of the cavity</i>	61
3.11	<i>Translation and rotation of a mirror</i>	63
3.12	<i>Trajectory of the mode compared to the theoretical optical axis. The curve are obtained for $\theta_0 = 100 \mu\text{rad}$ and $T_0 = 0 \mu\text{m}$.</i>	63
3.13	<i>Trajectory of the mode compared to the theoretical optical axis. The curves are obtained for $\theta_0 = 100 \mu\text{rad}$ and $T_0 = 100 \mu\text{m}$.</i>	64
3.14	<i>Transverse mode frequency position</i>	65
3.15	<i>Transverse mode splitting</i>	66
3.16	<i>Divergence of the beam measured on a diagonal output.</i>	67
3.17	<i>Differential light shift structure.</i>	69
3.18	<i>Tomographic images of the fundamental</i>	70
3.19	<i>Tomographic profile of the fundamental</i>	71
3.20	<i>Phase mask transformation.</i>	72
3.21	<i>Tomographic absorption images of the TEM_{01}</i>	72
3.22	<i>Tomographic absorption images of the TEM_{02}.</i>	73
3.23	<i>Tomographic profiles of the first modes.</i>	73
3.24	<i>Linewidth of the cavity at 1560 nm</i>	75
3.25	<i>Reversed light in the cavity as a function of the forward intensity</i>	76
3.26	<i>Effect of the losses on the cavity response.</i>	78
3.27	<i>The cavity as a low pass frequency filter</i>	80
3.28	<i>PDH like error signal with an amplitude modulator.</i>	81
3.29	<i>Locking scheme and noise of the laser</i>	83
3.30	<i>Cavity injection opto-mechanics.</i>	84
4.1	<i>Atoms loaded in the dipole trap.</i>	93
4.2	<i>Scheme realized to load the dipole trap.</i>	94
4.3	<i>Acoustic resonance of the cavity.</i>	96
4.4	<i>Free evaporation in the trap.</i>	96
4.5	<i>Trapping frequencies measurement by parametric excitations.</i>	97
4.6	<i>Trapping frequencies measurement by time of flight expansion.</i>	98
4.7	<i>Trapping in the transverse modes.</i>	100
4.8	<i>1529 nm compensation of the light shift.</i>	101
5.1	<i>Two level atom scheme.</i>	104
5.2	<i>Bloch sphere</i>	107
5.3	<i>Illustration of a coherent state polarized along \hat{J}_x.</i>	109
5.4	<i>Shot-noise and squeezed limited interferometric sequence</i>	112
5.5	<i>Illustrating fringes of the shot-noise and squeezed limited interferometric sequence</i>	113
5.6	<i>Schematic of the interaction between the system and the measurement device.</i>	115
5.7	<i>Three level system considered for the QND Hamiltonian.</i>	117
5.8	<i>Sequential description of the non demolition measurement</i>	121
5.9	<i>Scheme of the Mach-Zehnder interferometer considered.</i>	124
5.10	<i>Squeezing function</i>	126
5.11	<i>Simulation of the atomic wavefunction collapse in a Mach-Zehnder measurement for $N_{\text{at}} = 100$ and $\phi = 10^{-2}$.</i>	129
5.12	<i>Long time behavior, the continuity breaks down</i>	130
5.13	<i>Scheme of the lossy Mach-Zehnder</i>	131

5.14	<i>Scheme of the Mach-Zehnder with a sensitivity increased by the cavity.</i>	133
5.15	<i>Schematic of the detection of a photon in a superposition of two modes.</i>	135
5.16	<i>Schematic of the detection of a photon in a superposition of two modes.</i>	135
5.17	<i>Detection probability of a phase φ</i>	138
5.18	<i>Measurement strength $M_l^{(2)}$ and center n_l of the squeezing function $\left f_{N_p}^{(j,l)}(n)\right ^2$</i>	140
5.19	<i>Simulation of the atomic wavefunction collapse under an heterodyne measurement for $N_{\text{at}} = 100$ and $\phi = 10^{-2}$.</i>	142
5.20	<i>Comparison of the Mach Zehnder interferometer and the heterodyne detection.</i>	144
5.21	<i>An heterodyne detection seen as an homodyne detection of the RF field.</i>	144
5.22	<i>Simulation of the atomic wavefunction collapse into Schrödinger cats for a Mach-Zehnder interferometer.</i>	146
5.23	<i>Description in the plane (n_1, n_2) of the entanglement of two clouds.</i>	147
5.24	<i>Representation of the Dicke state rotation</i>	148
5.25	<i>Mean value of $\langle \hat{J}_z \rangle$ for a collective Zeno effect.</i>	149
6.1	<i>Schematic view of a population sensitive heterodyne measurement.</i>	153
6.2	<i>Phase transfer from the optical range to the microwave range.</i>	154
6.3	<i>Presentation of the laser frequency configurations considered to probe of the atomic population.</i>	155
6.4	<i>Set-up of the single-pass non-destructive measurement.</i>	159
6.5	<i>Scheme of the optical detector.</i>	160
6.6	<i>Noise power spectral density of the detector.</i>	160
6.7	<i>Linearity after demodulation of the signal on the fast photodetector.</i>	161
6.8	<i>Signal-to-noise as a function of the ratio $w_{\text{ph}}/w_{\text{at}}$.</i>	164
6.9	<i>Spectroscopy on the MOT</i>	165
6.10	<i>Destructivity as a function of probe detuning.</i>	166
6.11	<i>Non-demolition measurement of the atomic population in $F = 2\rangle$ when Rabi oscillations are driven in the atomic sample.</i>	168
6.12	<i>Dependence of the Rabi oscillation parameters from the probe detuning.</i>	169
6.13	<i>Spin-echo sequence.</i>	172
6.14	<i>Variance of the signal $\delta V^2 = \delta S^2$ as a function of its mean value $\langle V \rangle = \langle S \rangle \propto N$.</i>	176
6.15	<i>Scheme of the Pound-Drever-Hall like measurement method.</i>	178
6.16	<i>Complete locking scheme foreseen for the QND measurement.</i>	178
7.1	<i>The Zerodur vacuum system with the integrated linear cavity.</i>	182
7.2	<i>Compact opto-mechanical design.</i>	183
7.3	<i>Optical system of the Raman laser experiment.</i>	184
7.4	<i>Frequency scheme and spatial modes of the Raman laser.</i>	185
7.5	<i>Threshold of the laser</i>	186
7.6	<i>Output power of the cavity when the Raman pump laser is scanned across the resonance condition.</i>	187
7.7	<i>Beatnote of the TEM_{10} and TEM_{01} modes.</i>	188
7.8	<i>Absolute frequency drift as a function of the effective atom number for (a) red and (b) blue detuned light.</i>	189
7.9	<i>Laser threshold shape as a function of the detuning Δ.</i>	190
B.1	<i>Bessel function of a phase modulation.</i>	200

C.1	<i>Locking the alignment of the cavity.</i>	204
-----	---	-----

Introduction

In physics as in every day life, it is by gathering information about the systems that surrounds us that an understanding of their behavior can be obtained. Looking at the ball, a goalkeeper can predict the trajectory and catch it. But what if, by looking at the ball, we were actually fixing its trajectory? Would you call that cheating?

For many years before quantum physics arise, it was strongly believed that objects were Newtownian and had well determined properties such as a definite position and velocity, and that the constituents of matter were well described by point-like particles. With the elaboration of quantum physics a real revolution [Bitbol 97] occurred, and a complete reversal in the interpretation of the world has been operated. The concept of object itself and the properties it holds had to be redefined [Bitbol 99].

From its very beginning, quantum physics has been disturbing physicists, and even its founding fathers were skeptical and in a sense overcome by their discovery. For most of them it was only an intermediate description that should be further completed. In 1911, Einstein who had himself introduced with M. Planck the quanta of energy to explain the black body radiation was insisting on: "the provisional nature of this description (quanta) which does not seem to be reconcilable with the experimentally verified consequences of the wave theory". But the theory was in march, and in 1925 Schrödinger was already introducing his master equation and the powerful description of a quantum system that is the wavefunction. Despite the many remaining conceptual difficulties, the strength of the formalism, and its ability both to precisely calculate experimental values ([Nez 93]) and to predict so many classically unexpected but observed behaviors made it an unavoidable theory of modern research.

Among the well known achievements of the theory, was the prediction in 1924 that below a critical temperature, a macroscopic number of particles would accumulate in the ground state of the system and form a Bose-Einstein condensate. Sixty years later the experimental achievement was realized at NIST and MIT [Anderson 95, Davis 95]. If quantum mechanics has experienced such a progress, it is partially thanks to the development of a proper experimental system of study: cold atoms. Since the advances of optical cooling in the 80's that were rewarded in 1997 by the Nobel Prize of Steven Chu, Claude Cohen-Tannoudji and William D. Phillips [Cohen-Tannoudji 97], cold atom physics proved to be a very adapted system to experiment the quantum predictions such as the superfluid- Mott insulator transition [Greiner 02, Jördens 08] or the BEC-BCS crossover [Bourdel 04, Bartenstein 04, Greiner 03], which even extended the success of the theory to interacting particles.

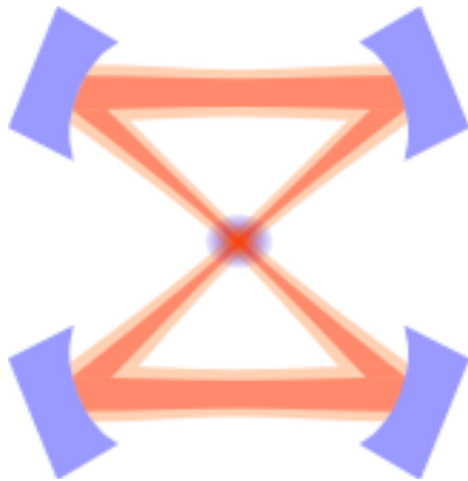
These many experimental achievements represent as many votes in favor of the quantum theory but the theoretical concepts are still troublesome. At the very heart of the disturbance is actually the measurement process itself. In 1925, Einstein, Podolsky and Rosen raised their well known paradox [Einstein 35] that opened the way for the proposal of Bohm to complete the theory by hidden variables [Bohm 52]. But this attempt failed [Bell 66] and the experimental proof [Aspect 82, Rowe 01, Fattal 04, Weihs 98] was brought that the theory was complete. Nevertheless, it did not end the debate since if it proves that entangled states exist, it does not

explain why such states are not observed for macroscopic objects. This point was raised by E. Schrödinger in 1935 with his famous cat experiment, where he imagined a cat following quantum rules that would be in a superposition of states *dead* and *alive*. A partial answer was brought in 1981 with the theory of decoherence [Zurek 81]. This theory states that for each interaction with the environment, some information is taken from the system and the coherence of the superposition collapses. The numerous interactions of a macroscopic object with its environment make it quickly lose its coherence and it shortly becomes a statistical mixture. The cat is either dead or alive but not in a superposition of states. Among the great achievements of the theory of the decoherence was its ability to reconcile the non-linearity of the projection postulate with the linear evolution described by the Schrödinger equation. But some questions on the measurement remain, and among them is the final state of the cat: dead or alive? Does it depend on the observer, or is it dead in one realization of the world and alive in another? These considerations on the measurement process itself, *i.e.* the extraction of information from the system towards the environment, may fill the gap between the quantum world description and our classical perception of it. In that perspective cold atoms offer the possibility to study macroscopic entangled state of a few million atoms in a very controllable and toy model environment. Many questions have already been addressed in quantum optics to deeply understand the measurement process [Brune 96, Haroche 08], and I believe that cold atoms present an alternative to further study the measurement process and the decoherence of macroscopic non-classical states.

Another interesting feature of cold matter is the ability to measure the coherence of a superposition by using the large de Broglie wavelength (\sim hundred nm) that atoms exhibit at low temperature. The first demonstration of cold atomic trapping [Chu 85] triggered the analogy between atomic physics and optics, and soon the wave nature of atoms was exploited to realize Young slits experiment with atoms [Carnal 91]. In 1991, was first demonstrated the ability to coherently separate the internal and external atomic states [Kasevich 91], paving the way to cold atom interferometry technique. In the last 20 years, atomic interferometers have been extensively applied in different geometries to realize precise measurement of time and inertial constants [Riehle 91]. Pushed to their limits, devices such as clocks [Santarelli 99], gyrometers [Gauguet 09] and magnetometers [Wasilewski 10] have reached the shot-noise classical limit. For now, the sensitivity of these devices can be further pushed by increasing the number of particles. But as the recent progresses of gravitational wave detectors have shown [Goda 08], sooner or later, the Standard Quantum Limit [Caves 80a] of cold atom interferometers will be reached, and the use of quantum engineered states such as spin-squeezed states [Kitagawa 93] will be unavoidable. The generation of spin-squeezed state involves a non-linear evolution of the state. In that perspective, the non-linearity of particle interactions can be exploited, but up to now it has only been able to entangle a few thousands particles [Esteve 08, Gross 10, Riedel 10]. A real alternative is actually the non-linearity associated to the renormalization of a state during a Quantum Non-Demolition (QND) measurement [Caves 80b]. Using this method, atomic spin-squeezed states have been recently achieved [Appel 09b, Schleier-Smith 10b] and already allowed a sensitivity enhancement in atomic clocks [Louchet-Chauvet 10, Wineland 92] beyond the projection noise limit. Up to now, only a small amount of squeezing has been obtained on small samples, leaving room for improvement...

Context of the thesis The work presented in this manuscript has been led between march 2007 and january 2011 in the group: "Optique Atomique" of the Charles Fabry Laboratory. The

experiment started in Orsay in 2006 and I joined it in march 2007 after it had moved to its new location in Palaiseau. When we started, spin-squeezing in cold atomic samples had not yet been achieved, and the international competition was strong. Our goal in this project named BIARO, for Bose Einstein condensate for Atom Interferometry in a high finesse Optical Resonator, was to construct an experiment suitable to push forward the performance of atom interferometers.



Two directions were guiding our work: the first consisted in using new types of atomic source such as Bose Einstein condensates in bouncing gravimeters [Impens 06], and the second was the creation of measurement induced spin-squeezed ensembles [Kuzmich 98]. For that purpose, we decided to implement a new type of folded high-finesse cavity doubly resonant at 1560 nm and 780 nm, that would serve the two purposes. Using 1560 nm light, we would be able to trap atoms in the fundamental mode of the cavity and eventually to reach the degeneracy regime by evaporation. On the other side, the enhanced coupling at 780 nm would benefit to the Quantum Non-Demolition measurement process and allow a better extraction of the information while minimizing the probe effect on the sample. The construction of this experiment raised

many technical challenges with the implementation and operation of a complex folded cavity geometry in an ultra-high vacuum environment.

Outline of the thesis

The first chapter will introduce the topics of atom interferometry using non classical states of matter. After a brief overview of the first matter wave interferometers that were realized, we will present the basics of cold atom interferometer and compare their present performance with the one of classical apparatus that measure the same inertial constants. We will then review the experiment that have been attempted to increase the sensitivity of atom interferometers using non-classical states. Finally we will detail the two prior objectives of this experiment which will allow us to justify for the design chosen.

In the second chapter, we describe the experimental apparatus that has been designed and realized to manipulate cold atomic samples. The main blocks of the experiment are detailed. The optical bench that generates the 780 nm frequencies used to trap, cool and manipulate the atoms has been designed in a compact and versatile way. The vacuum block is composed of a two dimensional magneto-optical trap (MOT) chamber and a science chamber in which the 3D MOT is operated. Because of the unusually large size of the vacuum chamber, we developed, a long range high aperture and diffraction limited optical system.

The third chapter is entirely dedicated to the high-finesse cavity that is at the heart of the experiment. We first expose the reasons of our choice of geometry and present a few test that were carried out before the geometry was decided. The chosen geometry is analyzed and characterized in details including its geometrical and spectral features. In an optical cavity, the mode profile can usually be calculated from the geometrical properties (length, radius of curvature). In our case, the cavity is close to the instability regime where the modes are very

sensitive to imperfections of the geometry. An in-situ nondemolition measurement of the optical mode based on atomic tomography is presented as well as an estimation of the intracavity losses. The locking procedure of the 1560 nm laser on the cavity and its performances that are of key importance for the trapping of atoms are detailed.

The fourth chapter presents our experimental procedure and achievements towards the obtainment of a quantum degenerate gas. We start this chapter by a few theoretical remarks on Bose Einstein condensation to point out the relevant experimental parameters that have to be optimized. In a second part, we present the characteristics of the dipole trap realized by the cavity mode and demonstrate our ability to load and trap atoms in the crossing region of the cavity. The perspectives raised in this chapter include the opportunity to use the transverse modes to generate exotic potentials, and the possibility to engineer the differential light-shift.

The fifth chapter gives a theoretical presentation of the Quantum Non-Demolition measurement that leads to spin squeezed systems. At first we introduce the Bloch sphere description of two level systems and extend this approach to a many body situation. The effect of the atomic shot noise in an interferometer is shown, as well as the potential gain in the use of spin-squeezed states. The basics of QND measurements to realize spin-squeezed states are given and we show that the dispersive measurement foreseen in our case has indeed a QND character. In a last step, we introduce a wavefunction formalism based on the partial projection of the atomic state, which we developed to dynamically follow the evolution of the state towards a highly squeezed state. It relies on a precise description of the measurement apparatus and is applied in the cases of a Mach-Zehnder interferometer and of an heterodyne detection. Interestingly, this method proved adapted to the description of the formation of Schrödinger cats and of the entanglement of separated clouds.

In the sixth chapter we present the frequency modulation technique that we developed to realize the QND measurement. The low sensitivity to noise of frequency modulation spectroscopy is detailed and it is shown that the detector is a key element in the achievement of high signal-to-noise ratio. Such a detection, that has been implemented in our set-up, has been characterized and special care was taken to understand the effects such as spontaneous emission and light-shift of the probe on the atomic sample. This detection tool was used in single pass to follow non-destructively the internal state evolution of an atomic sample that undergoes an interferometric sequence.

The last chapter is dedicated to the work that was realized during my stay in the group of Pr. Kasevich in Stanford. During this time we discovered and set-up a Raman lasing process between a Raman pump and a cavity mode. A key element that drove our attention is the very high finesse of the cavity, that in principle should make possible the achievement of ~ 100 mHz linewidth. In this chapter we give the main characteristics of the lasing process including the laser threshold, the gain bandwidth, laser linewidth, and an interesting feature that is an atomic population dependence of the laser absolute frequency.

Introduction to non-classical interferometry

Contents

1.1	Atom interferometric measurement	6
1.1.1	The concept	6
1.1.2	State of the Art	7
1.2	The international context of non-classical state preparation.	9
1.2.1	Measurement induced spin squeezing in a Mach Zehnder interferometer	10
1.2.2	Measurement/Cavity induced spin squeezing at MIT	11
1.2.3	Measurement induced spin squeezing in Stanford	13
1.3	The initial orientation of the experiment	14
1.3.1	New sources for new types of gravimeter	14
1.3.2	Pushing forward the quantum	15

This project of using non-classical states in atom interferometers emerged from a dual interest of the SYRTE at Observatoire de Paris which measure physical constants such as time or gravity with high precision using cold atoms interferometers and the groupe d'Optique Atomique at Institut d'Optique that takes interest in the quantum properties of these cold atomic clouds.

This naturally led the two groups to collaborate and to develop a new experimental apparatus that would enable as well to probe the physics of non-classical states predicted by quantum mechanics as to make the proof of principle of their usefulness for the enhancement of the sensitivity of atom interferometers. Therefore, the ambition of this project was to realize an atom interferometric measurement that would scale with a sensitivity better than $1/\sqrt{N_{\text{at}}}$ that is the Heisenberg limit of a classical source of N_{at} atoms.

In the following of this chapter, we will introduce the topics of atom interferometry and the state of the art achieved in these systems. In a second part, we will detail the initiative and the achievement that have been obtained in the world in the enhancement of the sensitivity of atom interferometers by the use of non-classical states of matter. The physical interest and the international context in which this experiment was led will be given and will explain the technical and physical choice realized. This chapter does not have the pretension to teach the reader on the precise physics of atom interferometers with non-classical states but merely to introduce this topic that is at the heart of the experimental apparatus developed. A formalized approach of the generation of non classical-states is given in chapter 5.

1.1 Atom interferometric measurement

Very soon after the introduction of Matter Wavepacket by Schrodinger, experiments have been performed to prove that atomic interferences could be observed in the same way than optical interferences. In this prospect, the scattering of matter waves of electrons [Davisson 27] and neutrons [Halban 36] on the periodic structure of crystals were observed in 1927. These scattering processes that can be interpreted as the interference of multiple path, are completely equivalent to the coherent scattering of a laser beam on a grating or to the scattering of X-Ray on crystal structures [Von Laue 15]. After a few more years and an improved control of the experimental apparatus, this was the two wave interferences of electrons [Marton 52] (1952) and neutrons [Maier-Leibnitz 62] (1962) that were achieved. In the same time, the well known technique of Ramsey interferometry [Ramsey 50] (1950) that coherently manipulates internal states was introduced and is still used nowadays to perform the best measurement of time [Itano 82].

In 1991, the first proof of principle of a coherent transfer of momenta [Kasevich 91] to a cold atomic cloud opened a new way to the measurement of inertial constants with a high precision. Previous measurement of the acceleration of gravity g had for example already been realized with a jet of neutron [Colella 75], but the possibility to perform these same interferometric experiments with a cold atomic cloud that has no initial velocity allowed to lengthen the interrogation time with the inertial field and to increase then the measurement sensitivity.

1.1.1 The concept

The physics of cold atoms inertial sensors usually involve two wave interferences and can be understood by analogy with their optical equivalent which are the Mach Zehnder and Michelson interferometers. Similarly to optics, different point of views can be adopted to understand these interferometers. Indeed, one can consider either a *particle* description in which the state of a single atom after the first beam splitter is in a coherent superposition of the two outputs $1/\sqrt{2}(|O_1\rangle + |O_2\rangle)$ or a *wave* description in which a single wave of amplitude A_0 is splitted in two coherent waves of amplitudes $A_0/\sqrt{2}$. The combination of these two descriptions is well known as the wave/particles duality. In atomic interferometers, the rôle of light and matter are exchanged with respect to optical interferometers. For optical systems, the light is manipulated by material objects such as mirrors and beam splitters while in atomic systems, the cloud of cold atoms is coherently controlled by laser beams as schematized in figure 1.1. For atom interferometer, the detection is even optical.

In practice, two types of atomic interferometers can be distinguished : the *atomic clocks* which can be essentially seen as interferometers realized by a coherent manipulation of the internal atomic state and the *inertial sensors* such as gravimeters or gyrometers which involve a coherent manipulation of the external degree of freedom. As previously mentioned, the coherent manipulation of the external degree of freedom of cold atoms has been a crucial breakthrough for atomic interferometers [Riehle 91, Keith 91] and was first realized a coherent two photon excitation [Kasevich 91] known as stimulated Raman transition. The transfer of momenta is essential for inertial sensors. It allows to separate in space and time the trajectories of the two arms of the interferometer and then to generate an interaction with the inertial field that is different for each arm. This differential effect is measured by the interference of the two trajectories.

In the case of an atomic clock, the interferometer usually realized is a Ramsey-Bordé

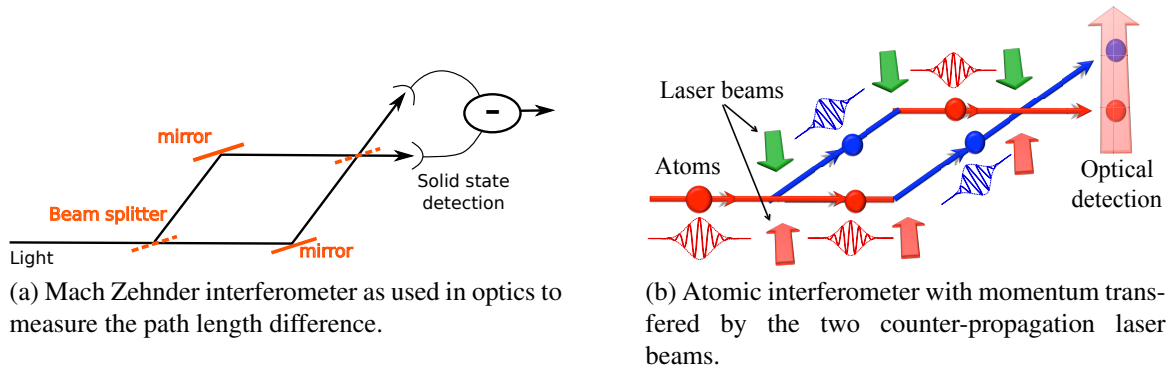


Figure 1.1: *Analogy between optical and atomic interferometer*

The atom interferometers can be understood in comparison with their optical analogues with reversed rôle for light and matter. In atomic interferometers, the matter (Atoms) is manipulated by laser beams. The atoms being massive particles and therefore not constrained to travel at light speed, they can probe inertial forces with long interaction times and are then very sensitive to inertial fields.

interferometer that consists of two beam splitting pulses. These pulses create a superposition of the internal state with a momentum transfer only linked to the microwave wavevector $\hbar k_{\text{MW}} \ll \hbar k_{\text{optical}}$. The interference pattern is ruled by the phase accumulated $\Delta\varphi_{\text{clock}}$ by the atoms in the rotating frame of the microwave source that turns at ω and that generates the beam splitting pulses, *i.e.*

$$\Delta\varphi_{\text{clock}} = (\omega_0 - \omega)T \quad (1.1)$$

, where ω_0 is the angular frequency of the atomic transition addressed and T is the interrogation time of the interferometer. By reading the interferometer output, one obtains a measurement of the atomic transition that is used as a frequency standard.

In the case of a gravimeter, it was shown in 1989 [Bordé 89] that, due to the external inertial field, the phase accumulated in a $\pi/2 - \pi - \pi/2$ interferometer could be expressed by:

$$\Delta\varphi_{\text{gravitation}} = \mathbf{k}_{\text{eff}} g T^2 \quad (1.2)$$

, where \mathbf{k}_{eff} is the wavevector associated with the momentum transfer of the beam splitter and T the time between two pulses. This effect of the gravitational inertial field can be either interpreted as the action of the Hamiltonian $\mathbf{H}_g = m\mathbf{g}r$ along the trajectories [Bordé 89] or in the free falling frame of reference, by the phase imprinted by the laser pulses [Antoine 03].

1.1.2 State of the Art

The achievement of atomic interferometers should be first compared to the classical analogous that realize the same measurement. If we focus for example on the case of gravimeters, different apparatus that rely on classical physics have been developed. For comparison with the following apparatus, the sensitivity obtained at Syrte - Observatoire de Paris for their *absolute* atomic fountain gravimeter is $1.4 \times 10^{-8} \text{ g.Hz}^{-1/2}$.

One of the first precision measurement of gravity has been realized in 1855 [Kater 18] using a pendulum of tunable length. The oscillation period depending on the length of the pendulum

and on g , and using two different length, the value of g could be obtained with an accuracy of $10^{-5}g$.

Other mechanical devices such as Lacoste-Romberg gravimeter relying on the use of zero effective length spring were developed [LaCoste 67, Riccardi 02] and allowed to reach sensitivity down to $10^{-10} \text{ g.Hz}^{-1/2}$. Nevertheless, these static gravimeter are not absolute and very much influenced by the aging of the spring ($10^{-8} \text{ g.Hz}^{-1/2}$ per day).

Another, more recent technic but still not absolute uses the levitation induced by the Meissner effect in supra-conductor [Prothero 68, Goodkind 99]. In these system, the position of a macroscopic object levitating over a supra-conductor is measured. When the inertial environment of the gravimeter is changed, the position of the object is modified which indicates on the variation of g . This modern measurement reaches the tremendous sensitivity of $10^{-12} \text{ g.Hz}^{-1/2}$ but need the use of a complex cryogenic system and suffer from drift of 10^{-10} g/day . Nevertheless, these systems are very adapted for the measurement of tiny variation of the earth structure [Courtier 00] and are thus very useful for geophysical studies.

Up to now the best absolute evaluation of g are realized by measuring an object in free fall. The more commonly used system is a free falling corner cube [Faller 67, Marson 86, Niebauer 95] that closes one arm of a Michelson interferometer. Recording, during the free fall, the fringes displacement at the output of the Michelson directly measure the position of the cube versus time. The sensitivity of this interferometer to the phase and then to g is given by $\Delta\varphi_{\text{cube}} = 2\mathbf{k}gT^2$ where \mathbf{k} is the wavevector of the light used in the interferometer. These corner cube systems involve the same physics of free falling object than the atomic interferometers. In addition, the sensitivity of both systems scales similarly with the interrogation time (see equation 1.2). Hence, to be able to compare the performances of these two systems, it is crucial to determine how these system are affected by noise or systematic bias and how far these noises can be controlled.

It is also interesting to study the state of the art of atom interferometers themselves with respect to the classical prediction given for the scaling of their sensitivity. It is well known in optics that the classical sensitivity of an interferometer is given by the optical shot noise. In these single particle interferometers, each photon interferes with itself and can be detected on one or the other output ports. As each photon follows a path *independent* from the other photons, the difference of the photocurrents at the outputs will exhibits a Poissonian noise. This "shot noise" is linked to the number of photon N_{ph} involved in the measurement and scales as $\sqrt{N_{\text{ph}}}$. The same consideration can apply for atom interferometers that have then a sensitivity proportional to $\sqrt{N_{\text{at}}}$.

This atomic shot noise limit has now been reached in the recent apparatus that have been developed in the context of cold atoms interferometers [Santarelli 99]. This type of performance is depicted on figure 1.2 that describes the sensitivity of the detection of an atomic clock. The sensitivity scales here as $\sqrt{N_{\text{at}}}$ which is the signature of shot noise. Similar performances have been obtained for the measurement of rotations using a gyroscope interferometer [Gauguet 09]. From figure 1.2, two solutions can be adopted to increase the sensitivity per run. One can either increase the atom number or overpass the classical limit of the shot noise using non-classical states such as squeezed states. Obviously a combination of the two approaches, that is a highly squeezed sample that contains a high atom number, is not forbidden and would actually guarantee the best sensitivity per run.

At this point, it is interesting to remark that if today, the sensitivity of falling corner cube and atomic interferometer are comparable, the road map of non-classical (quantum) states give a strong interest for the future of atomic interferometer. It is indeed clear that the benefit in

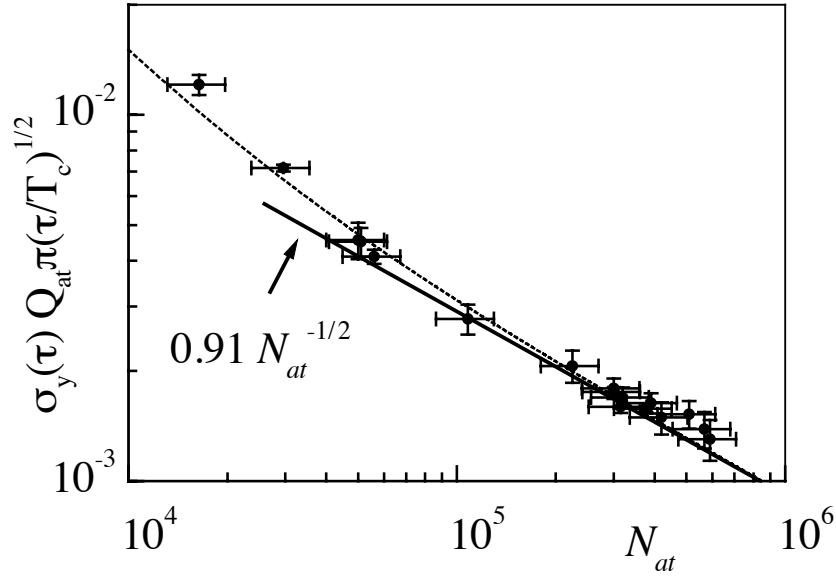


Figure 1.2: *Detection sensitivity of an atomic clock limited to the shot noise.*

The data presents the sensitivity of an atomic clock of Caesium operated in the BNM-LPTF at Observatoire de Paris. The plain curve has the form $\alpha \sqrt{N_{at}}$ with $\alpha = 0.94$ that was adjusted on the data. This dependence in $\sqrt{N_{at}}$ is the signature of atomic shot noise. Data extracted from [Santarelli 99] with the authorization of the authors.

using quantum mechanics will not apply to a macroscopic object such as a corner cube.

1.2 The international context of non-classical state preparation.

From the previous section, it appears that the independence of the particles in a single particle interferometer such as a Mach-Zehnder interferometer is the key issue. Breaking the independence require to introduce correlations between the particles. Rephrasing with the vocabulary of quantum mechanics: the goal is to transform the separable state of independent particles into an entangled state or squeezed state of reduced uncertainty for the measurement of the "path length difference" of the two interfering arms.

It is well known in quantum optics [Thorne 78, Caves 81] that such a transformation needs a non-linearity to occur. Different methods can be applied to generate such a non-linearity including the inter-atomic interactions [Esteve 08, Gross 10, Riedel 10], an atom-cavity field interaction [Schleier-Smith 10b] or a Quantum Non-Demolition measurement (QND) [Appel 09b, Louchet-Chauvet 10, Schleier-Smith 10b, Teper 08].

Up to now, the inter-atomic interaction squeezing has been realized in double well and multi well experiment but does only concern atomic cloud with a "low" number of particles ($\approx 10^3$). It therefore does not really represents an alternative for today's classical interferometers that are still more sensitive even if they operate in the classical limit. Nevertheless, these experimental achievements use with ingenuity the atomic interactions that are usually considered as harmful for the operation of atomic interferometers and have even proven that an increased sensitivity

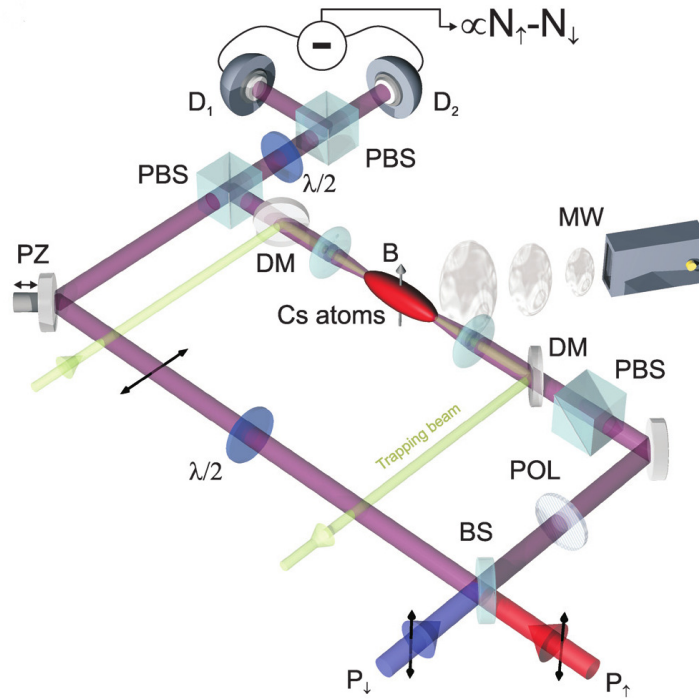


Figure 1.3: *Schematic of the Mach Zehnder interferometer used in the group of Eugen Polzik*

The measurement of the atomic is realized in this experiment by its effect on the path length difference of the interferometer. The interferometer is operated with two colors, each probing one of the two hyperfine levels (figure 1.4a) and in a configuration that suppress common noise of the path length to the level of the difference of frequency of the two laser ($\approx 6.8GHz$). The figure presented here are extracted with permission of the author from [Appel 09b]

could be achieved.

In the following, we will describe a few international experiments that represented in 2007 the main attempt for the generation of large atom number and squeezed atomic cloud. The technical limitation of the sensitivity of each apparatus will be raised. In the last part, we will sum up the main idea of the experimental apparatus that has been constructed and operated during this thesis.

1.2.1 Measurement induced spin squeezing in a Mach Zehnder interferometer

One of the pioneer group to take interest in the implementation of Quantum Non Demolition measurement for spin squeezing was the group of Eugen Polzik in the Netherlands. Their work followed the proposal of Kuzemich, Bigelow and Mandel [Kuzmich 98] that stated that a far of resonance measurement of the index of refraction induced by a two level atomic system was realizing a Quantum Non Demolition measurement [Caves 81] of the difference of population of these two levels. Therefore, such a measurement squeezes the observable of the population difference and reduces, for example, the uncertainty in the outcome of an atomic interferometer.

To realize such a measurement, the Dutch group setted up an optical Mach Zehnder interferometer in which the atoms are placed in one arm of the interferometer (see figure 1.3). The measurement of the interferometer outcome indicate on the phase difference of the two arms and

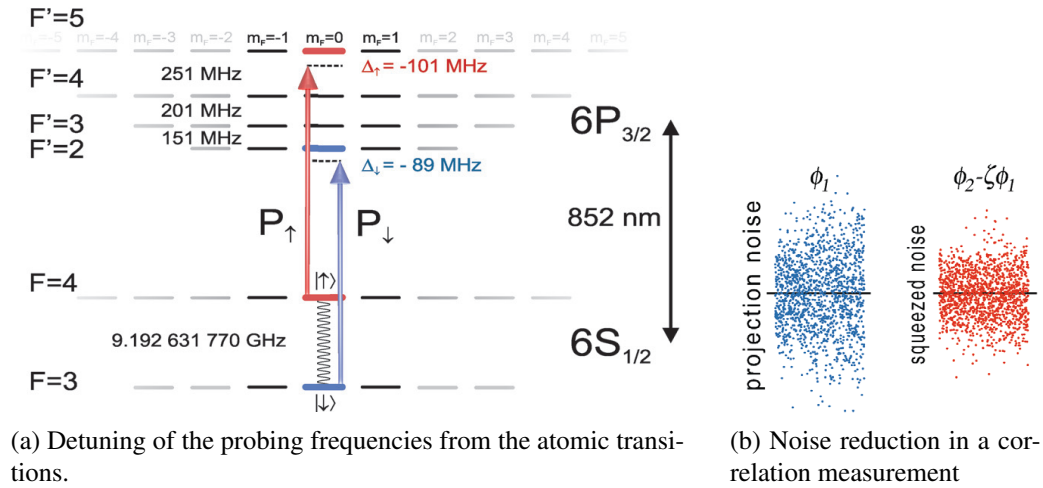


Figure 1.4: Atomic projection reduction in a two color probing

(a) Each probing laser address one of the hyperfine transition. The sum of photocurrent generated is proportional to the population difference between the hyperfine ground states. (b) The population difference noise is estimated by applying two successive pulses. In an ideal measurement, the first pulse measure a phase within the initial atomic projection noise and the second pulse remeasure in principle exactly the same phase. This effect is depicted here by a visible reduction of the noise between the individual phase observable ϕ_1 and the correlated observable $\phi_2 - \zeta\phi_1$

then on the refractive index induced by the atoms. A first all fibered version of the interferometer was unsuccessful in reaching the high sensitivity required to clearly distinguish the atomic noise. A second attempt was realized in 2007 by a dynamically stabilized free space interferometer operated close to the zero path length difference. A clever operation of the interferometer in a bi-frequency design [Saffman 09], allowed to overpass the last technical challenges of path length fluctuations and to reach measurement of the population difference (figure 1.4) below the atomic shot noise in 2009 [Appel 09b]. In this bi-frequency (f_1 and f_2) design, the atomic index of refraction is measured with respect to the optical wavelength, whereas the path length fluctuations are common mode and contribute only with respect to the microwave wavelength ($c/(f_1 - f_2)$).

While realizing a very good measurement almost insensitive to path length fluctuations, this system still suffer from its fairly "low" optical depth ($OD \approx 50$) that intrinsically limits the achievable amount of squeezing. In addition, the measurement is realized in DC, which makes it perturbed by low frequency noise of the environment such as $1/f$ noises.

1.2.2 Measurement/Cavity induced spin squeezing at MIT

1.2.2.1 Non demolition measurement by cavity transmission measurement

In the group of Vladan Vuletic at MIT, another experimental apparatus was developed to perform the same type of non-demolition measurement. In this system, the atoms are placed in the center of a linear high Finesse Fabry Perot cavity ($\mathcal{F} \approx 100000$) and trapped with a far of resonance light at 851 nm. The index of refraction, induced by the population difference, shifts the cavity resonance frequency. Adjusting a laser on half fringe of the transmission yields in a

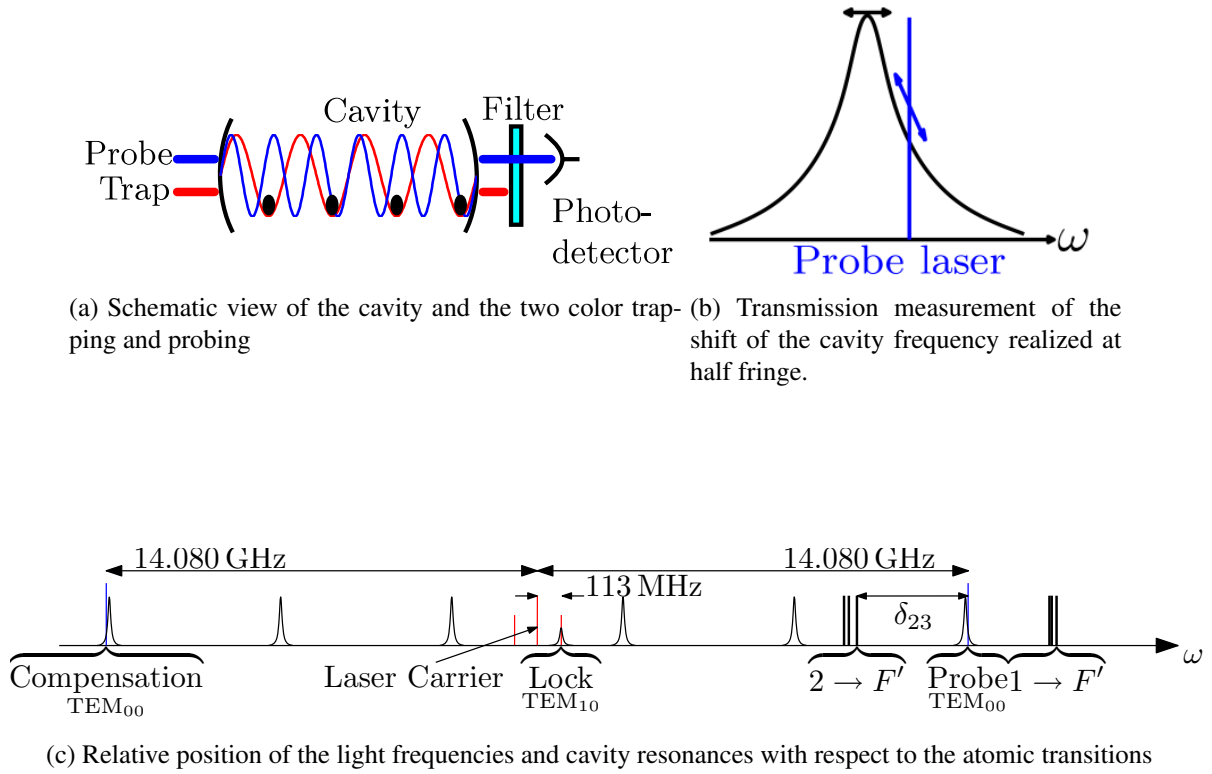


Figure 1.5: *Probing the population difference by a measurement of the transmission of a cavity.*

The hyperfine state population difference is measured by the frequency shift it induces on a resonance of the cavity that is tuned in between the two hyperfine states. A far from resonance twin beam (Compensation) allows a common rejection of the cavity length fluctuations on the transmitted power while preserving the effect of the difference of population. The locking of the probing to the resonance is realized by a sideband lock to a higher transverse mode of the cavity.

transmitted intensity that is proportional to the population difference of the two levels (figure 1.5b). A number of interesting technical choices made for the locking procedure can be seen in figure 1.5c and are detailed in [Schleier-Smith 10c]. The two main points are the locking on higher transverse mode that does not perturb the measurement and the use of a second beam that compensate for cavity path length fluctuations.

This system takes advantage of the high optical depth that is reached in the optical resonator. Nevertheless, the trapping and the probing being realized at two different wavelength yield in an inhomogeneous coupling of the probing standing wave. Indeed, the atoms are spread in the antinodes of the dipole trap which position does not correspond to the antinodes of the probe (see figure 1.5a). This complicate the analysis of the atomic noise and intrinsically lower the strength of the measurement. Similarly to the Dutch experiment, this transmission measurement is also realized in DC and suffer then from the same sensitivity to low frequency noise.

1.2.2.2 Non linearity in the Atom - cavity coupling.

In the research led on this apparatus it appeared in a second step that a stronger squeezing mechanism could be implemented. This mechanism rely on the dual interaction between atoms

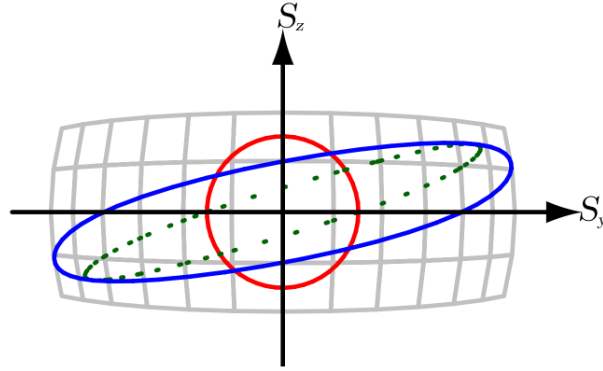


Figure 1.6: *Shearing effect of a coherent state*

The non linearity of the atom cavity coupling is strictly equivalent to the twisting hamiltonian that was first introduced in [Kitagawa 93]. This causes the transformation from the coherent state (red) to an elongated and squeezed state.

and photons. On one hand, the photons light shift the atomic transition and on the other hand, the atoms shift the cavity resonance frequency via their index of refraction. This dual mechanism was both first understood [Schleier-Smith 10a] and observed [Leroux 10] in the MIT group. The physics can be sum-up in the following. We consider for simplicity that the cavity is tuned such that for a zero difference of population of the two eigenstates, the cavity resonance is unshifted. For a positive atom number difference ($\Delta N > 0$), the cavity is shifted for example such that more photons enter the cavity, leading to a light shift effect that furthermore depends on the absolute value of $|\Delta N|$. In reverse, for $\Delta N < 0$, less photons enter the cavity and a low light shift is observed. Hence, within the initial Poissonian distribution of a coherent superposition of atom number difference, a shearing effect as described on figure 1.6 can be observed. Indeed, for $\Delta N > 0$ and $\Delta N \gg 1$ a large rotation angle is predicted while none will appear for $\Delta N = 0$. As a matter of fact this system mimics the Twisting Hamiltonian that was first proposed by Kitagawa and Ueda [Kitagawa 93] for the generation of squeezed states.

1.2.3 Measurement induced spin squeezing in Stanford

In parallel, the group of Mark Kasevich in Stanford published in 2008 [Teper 08] their experimental work on the measurement of atomic noise. The apparatus developed also consists of a linear cavity, but does not involve trapping since the atoms are released from a MOT and in free fall during the measurement. An important feature of this apparatus is its measurement process, that consists to measure the phase of the probe while it is reflected by the cavity (figure 1.7a). The dispersive profile of the cavity is imprinted on the probing light. This profile depends on the relative position of the probe frequency with respect to the cavity resonance frequency and is proportional to the difference of population. An experimentally interesting feature of this detection is that it realizes an AC detection insensitive to low frequency noise. In addition it takes advantage of a strong local oscillator that helps to reach the optical shot noise for the detection (see chapter 6). Nevertheless, this system suffers from the low optical density of a magneto-optical trap.

The results obtained in 2008 is presented on figure 1.7b and shows a noise increase of the antisqueezed quadrature. No clear signature of squeezing could have been seen in this pioneer experiment.

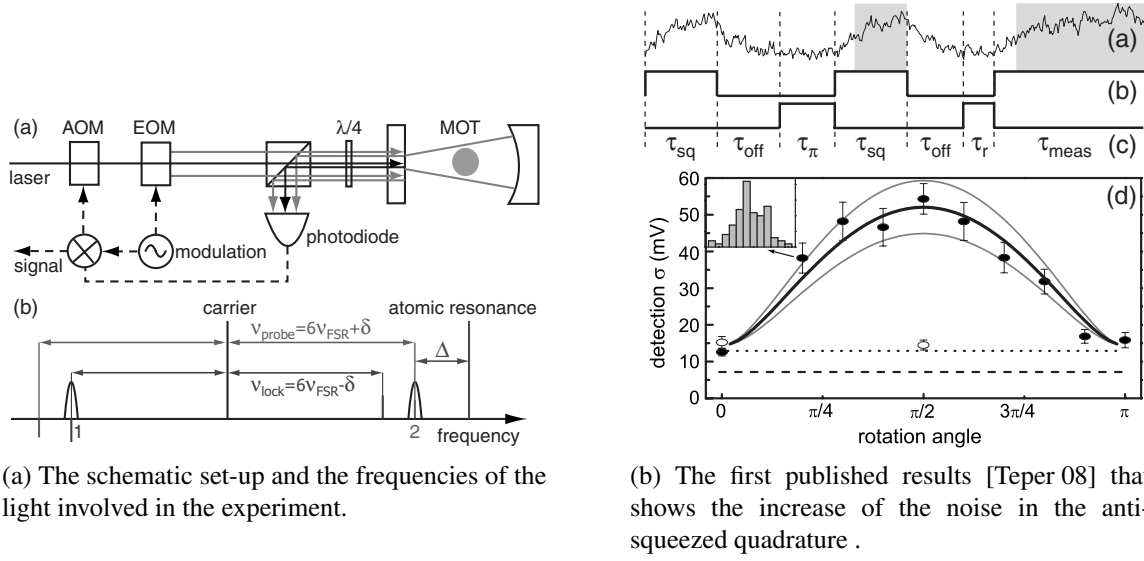


Figure 1.7: *Heterodyne Non demolition measurement apparatus developed at Stanford.*

The frequency modulation spectroscopy involved in this experiment allows to reach an optimal detection limited to the optical shot noise and insensitive to path length fluctuations. The schematic and results presented here are extracted from [Teper 08] and presented here with the authorization of the authors.

1.3 The initial orientation of the experiment

As previously mentioned, this experiment emerged from the will to try new types of interferometers involving ultra-cold atomic gas and to create an apparatus that would push forward the sensitivities of atomic interferometers. In this last perspective, we choose to follow the Quantum Non-Demolition approach that scales very well with high atom number.

1.3.1 New sources for new types of gravimeter

A gravimetric experiment that was foreseen and that uses ultra-cold atomic sources was issued from a proposal of Impens *et al* [Impens 06] and consisted in a bouncing gravimeter. In this proposal, an ultra-cold gas is released from a trap at $t = 0$, after a free fall of time T , a first Raman pulse stops the cloud while a second one send it back in its original place. As the efficiency of the Raman pulses depend on the energy momentum dispersion relation, the number atoms addressed by the pulse depend on the "phase matching condition" : $\mathbf{p} = \hbar\mathbf{k}$. This condition is perfectly satisfied for a kick at time $T = \hbar\mathbf{k}_{\text{eff}}/(mg)$. Measuring the optimal kicking time that keeps the atoms after N repetitions allows then to evaluate g [Hughes 09].

Regarding the experimental realization, our main concern was to reach degeneracy of the cold cloud in a compact environment and using low electrical power. This, to demonstrate, for example, the possible implementation of such a system in space application. An optical trapping and evaporation in an optical cavity were chosen to satisfy this condition. The trapping wavelength was chosen at 1560 nm to match with the requirements of the Quantum Non-Demolition measurement (see section 1.3.2). For the implementation of the Raman pulses, we decided to phase lock two independent lasers and we designed the vacuum chamber with a large optical access on the vertical. Interestingly, a Non-Demolition measurement of the atoms that have

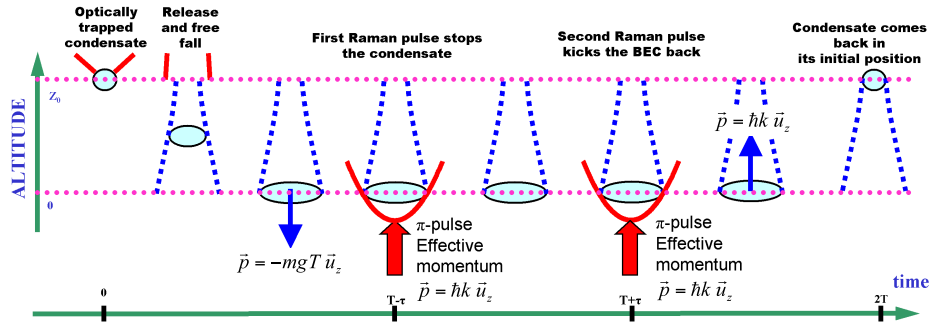


Figure 1.8: A bouncing gravimeter sequence

Pulse sequence of a bouncing gravimeter as proposed by Impens *et al* [Impens 06]. A condensate is suddenly released from a trap, starts to fall and is stopped and reversed by the use of two optical kicks (Counter-propagating Raman transition). The obtention of a levitating sample by the use of well timed kicks then realizes a measurement of gravity.

bounced could also be an interesting feature to implement in this scheme and would allow to increase the repeatability of the sequence.

1.3.2 Pushing forward the quantum

Concerning the measurement induced spin-squeezing, different options were still considered when I started on the project. It was clear that a cavity resonant at 780 nm would help to increase the atom-light coupling and then to increase the signal-to-noise of the measurement, but the exact experimental realization was still to be determined. In addition, we wanted to trap the atoms in the cavity mode. As previously stated, this will allow to use low power laser for the evaporation and will also automatically guaranty the alignment of the probe on the atomic mode (mode of the same cavity). To avoid the mismatch of the position of the atoms and the maxima of the probe that is inherent to a linear cavity, we opted for a traveling wave cavity geometry. Looking for an evaporation in the cavity, a tight confinement of the mode in all direction was needed. In a three mirrors geometry, this can only be obtained by focusing the mode, but the Rayleigh range associated with the longitudinal variation of the beam does not allow for a tight trapping (except if the focus is almost λ , but then the trapping region is very small). It was then necessary to implement a four mirrors cavity geometry with two crossing arms. This lead us to the cavity presented in figure 1.9.

To realize the Non Demolition measurement, we decided to implement a frequency modulation spectroscopy realized at 780 nm in our ring cavity. This scheme benefits from the far off resonance strong local oscillator which helps to reach an optically shot noise limited detection. In addition, this method of detection takes also advantage of the atom-light cavity coupling enhancement that increases the signal-to-noise ratio. As will be shown in chapter 6, this method realizes in principle the optimal measurement of very low photon flux and is also insensitive to optical path (cavity) length fluctuations. Our choice of measurement induced spin-squeezing and not, for example of interaction induced spin-squeezing relies on the scaling of the process with the number of particles. Indeed, as the optical shot noise does not depend on the number of atoms, the measurement induced spin-squeezing is very suitable to realize spin-squeezing of larger and larger sample for which the atomic noise is ever increasing. To realize the measure-

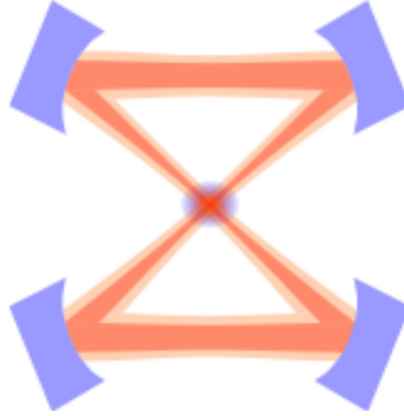


Figure 1.9: *The four mirror cavity geometry.*

The geometry of the cavity arise from a compromise to reach degenerate cold atom sample trapped in the mode of the cavity while being able to measure with a strong enhancement factor.

ment, our goal is to trap atoms in the 1560 nm radiation injected in one of the cavity mode, to cool by evaporation and to nondestructively measure the trapped atoms by using light injected in the 780 nm mode of the cavity. Experimentally, the choice of 1560 nm radiation for the trapping that is the half frequency of 780 nm radiation allows to refer the cavity length to the atomic transition of Rb⁸⁷ while limiting spurious interaction with the atomic sample.

Experimental set-up

Contents

2.1	Optical bench	17
2.1.1	Extended cavity diode lasers	17
2.1.2	Laser frequency	19
2.1.3	Scheme of the optical bench	21
2.1.4	Laser locks	23
2.2	Apparatus for cold atom trapping	29
2.2.1	Cooling and trapping of atoms	29
2.2.2	Two dimensional Magneto-Optical Trap	31
2.2.3	Ultra High vacuum set up	35
2.3	Imaging system	39
2.4	Summary	43

In this chapter we present the experimental apparatus in its main blocks, namely the optical and laser system, the vacuum set-up, and the imaging system. As this manuscript is the first doctoral thesis on the experiment, the description of the technical aspects of the experiment are rather detailed. I hope that this chapter will be a useful reference for new students who have to learn about this experiment.

In the first part we detail the generation of all the laser frequencies that are used in this experiment. The lasers themselves are presented as well as the different locking procedure implemented among which are atomic spectroscopy, frequency, and phase lock. In the second part, we give information about the geometry of the vacuum set-up and its use to create a 2D and a 3D magneto-optical trap (MOT). One of the peculiarity is the implementation of the 3D MOT coils under vacuum. In the last part, we describe and show the characterization of the imaging system that has a long working distance (~ 30 cm) and a high numerical aperture (0.13).

2.1 Optical bench

2.1.1 Extended cavity diode lasers

The laser system mounted in this experiment relies on extended cavity diode lasers in a linear configuration which have been first introduced in [Lucas-Leclin. 98]. A full characterization of the laser has been realized at Syrte - Observatoire de Paris and an exhaustive study can be found in [Cheinet 06, Baillard 06, Lucas-Leclin. 98]. In the following, we will just remind the main

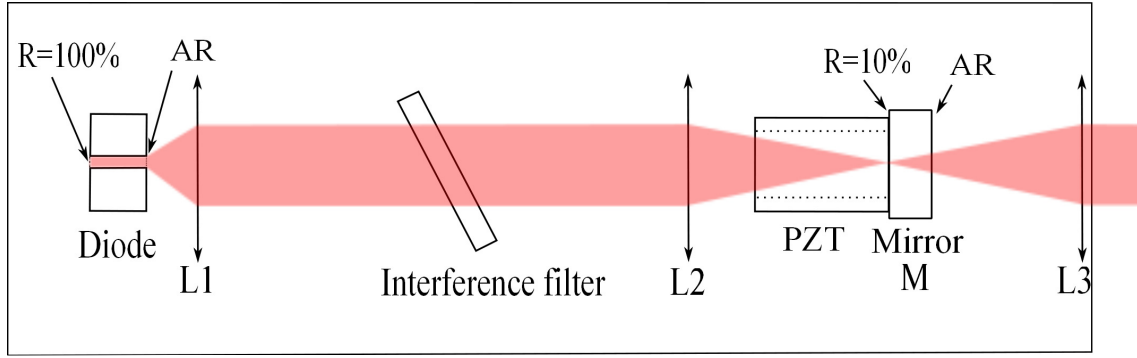


Figure 2.1: *Scheme of the extended cavity diode.*

The front plane of the diode is imaged on a 10% reflecting mirror that guarantees the necessary feedback. An interference filter is used in the configuration to narrow the gain profile. The output beam is re-collimated by L3.

characteristics of these lasers, schematically shown in figure 2.1.

The laser emitter is a diode laser (Eagle Yard, mod. EYP RWE 0790). The front side is anti-reflection coated while the back side is totally reflecting and is used as one of the two mirrors of the cavity. The diverging beam from the diode is collimated by an aspherical lens of 4.5 mm focal length ($L1$) and refocused on the out-coupling mirror with an aspherical lens ($f = 18$ mm) ($L2$). This results in a cat's eye configuration on the out-coupling mirror which confers its geometrical stability to the laser. Indeed, the lens $L2$ conjugates the output plane of the diode with the out-coupling mirror (M), and it makes the system independent of the mirror position and much less sensitive to alignment. The lens $L3$ (18 mm focal) is used for the collimation of the beam

In the extended cavity is placed an interference filter (Research Electro-optics) with a band-pass window of 0.3 nm. This filter allows to considerably reduce the gain window of the diode and ensures a monomode behavior of the diode laser. The central wavelength of the filter can be finely tuned by tilting the filter, that changes the multilayer interspacing. Since laser diodes have considerable round trip gain, it is enough to feedback only 10 % with the out-coupling mirror. The use of an anti-reflecting diode reduces considerably the mode competition between the diode and the cavity. Nevertheless, it obliges to maintain a low intra-cavity power to preserve the anti-reflecting coating of the diode. Indeed, for an intracavity power exceeding 1 W, the antireflection coating (situated on a focal point) usually gets damaged.

In order to tune the emitting frequency of the laser, the length of the cavity, and then the position of the longitudinal modes of the cavity, is controlled by a piezo electric-tube on which is glued the mirror M. The frequency lock is realized by a low bandwidth feedback applied on the piezo and a high frequency one applied on the current (see section 2.1.4.2). The temperature stabilization of the laser is ensured by two peltiers elements: one guarantees the stability of the ensemble and especially the length of the cavity, and the other stabilizes the temperature of the diode itself.

The measurement of the laser linewidth is presented in figure. 2.2 [Baillard 06]. It is ob-

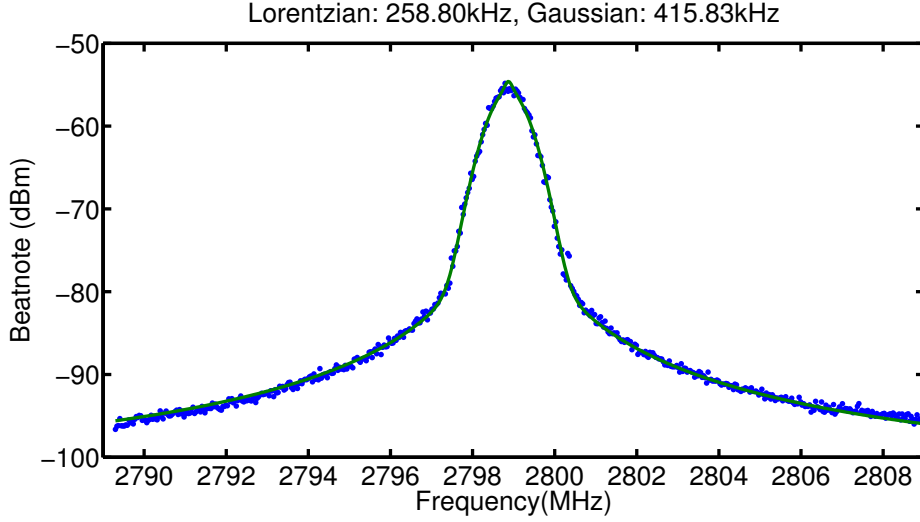


Figure 2.2: *Beatnote of two extended cavity diodes.*

Two ECDL are beated on a fast photodiode (Hamamatsu, mod. G4176). The lasers are respectively the repumper (locked to ^{87}Rb) and the QND laser (see 2.3, locked on the repumper). The amplified frequency is analyzed on a spectrum analyzer with 30 kHz resolution bandwidth (RBW). The green plain curve is a fit of the tail by a Lorentzian of 258 kHz (FWHM). The center is fitted by a Gaussian of 416 kHz standard deviation.

tained by the analysis of the beatnote of two "identical" ECDL, after locking the beatnote to a local oscillator. The beatnote is detected on a fast photodiode (Hamamatsu, mod. G4176). The Lorentzian fit of the tail indicates a linewidth of 258 kHz (FWHM) that corresponds to the convolution of the two Lorentzian. The Lorentzian linewidth of a single laser being then 124 kHz. The low frequency noise is fitted by a Gaussian of 416 kHz standard deviation for the two lasers. It corresponds to non-fundamental processes such as the feedback noise or thermal fluctuations. Hence, one laser has a Gaussian linewidth of 294 kHz. These values vary for each laser but it gives a good idea of the general linewidth properties.

2.1.2 Laser frequency

In this section, we will describe the laser frequency stabilization and the tunability needed in the experiment. This will be helpful to understand the implementation of the optical bench. Figure 2.3 shows the atomic structure of ^{87}Rb and the laser optical frequencies involved in our bench.

This experiment aims at the non-classical improvement of atomic interferometers. As a consequence, we need laser radiation to trap and cool the atoms (780 nm), to create a far off resonance dipole trap (1560 nm), to squeeze by nondemolition measurement (780 nm), and to perform the interferometric sequence (Raman beams at 780 nm).

- The trapping and cooling of the atoms in the 2D and 3D MOT involve 2 lasers at different frequencies. The cooling laser is tuned slightly on the red of the closed optical transition $|5^2S_{1/2}, F=2\rangle \rightarrow |5^2P_{3/2}, F_p=3\rangle$ while the repumping laser is tuned on the $|5^2S_{1/2}, F=1\rangle \rightarrow |5^2P_{3/2}, F_p=2\rangle$ transition. Because of the differential light shift at 1560 nm which will be discussed in section 3.2.5.2, the cooling laser requires the pos-

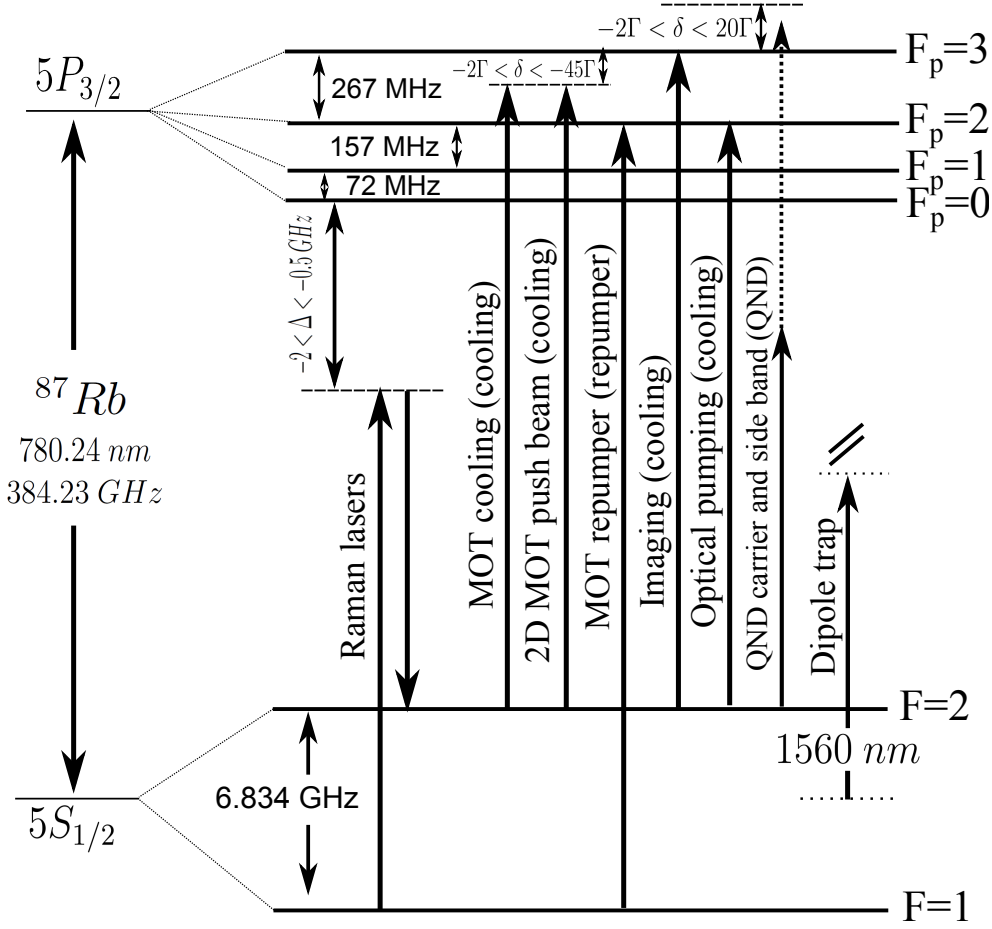


Figure 2.3: Atomic transition and lasers frequencies.

All the laser frequencies used in the experiment are presented. In brackets is the laser from which the radiation is generated

sibility to be frequency shifted by a few hundred MHz. This allows to tune the cooling laser on the $|5^2S_{1/2}, F=2\rangle \rightarrow |5^2P_{3/2}, F_p=2\rangle$ transition.

- Based on the study of 2D MOT operation [Cheinet 06, Müller 07, Riis 90, Nellesen 90], we decided to have the same frequencies for all the beams operating the 2D and 3D MOT. Hence the push beam is 2.5Γ detuned from the cycling transition. This is not optimal to maximize the 2D MOT atomic flux, but simplifies the optical bench design with an acceptable loss of efficiency.
- To image the cloud by the fluorescence technique, we decided to use the MOT beams themselves. During such imaging, the beams frequency is tuned on resonance with the $|5^2S_{1/2}, F=2\rangle \rightarrow |5^2P_{3/2}, F_p=3\rangle$ transition.

The cooling radiation is also used to perform absorption imaging on a different axis. As the MOT and the absorption imaging beam are never present at the same time on the atoms, it is not a problem to use the same laser source for the two purposes. Thanks to a versatile lock the cooling laser can be easily shifted to realize off-resonance absorption imaging.

- Since we want to maximize the number of atoms in a non magnetic-sensitive atomic state (atomic interferometer), a linearly polarized optical pumping on the transition $|5^2S_{1/2}, F = 2\rangle \rightarrow |5^2P_{3/2}, F_p = 2\rangle$ is implemented using the radiation of the cooling laser. This optical pumping allows to accumulate the atoms in the $|5^2P_{3/2}, F_p = 2, m_F = 0\rangle$ atomic state that is insensitive to magnetic field at first order.
- In order to trap the atom in a non dissipative trap, we use far detuned radiation (1560 nm) injected in the optical mode of a cavity. The 1560 nm laser is locked to the fundamental mode of the cavity. As the radiation is far off-resonance, the absolute frequency of the mode of the cavity is a priori not a critical parameter. Nevertheless, as the cavity is also used to perform the nondemolition measurement, the cavity resonances have to be referenced to the ^{87}Rb atomic lines. This involves that the length of the cavity has to be controlled, and then that the exact frequency of the 1560 nm radiation has to be referenced to the ^{87}Rb atomic frequency reference.
- To perform atom interferometry (e.g. Ramsey-Bordé type interferometer), and to coherently control the internal atomic state, we choose to implement stimulated Raman transition induced by far detuned two photon transitions. To enable the transition, the two lasers need to be coherent with respect to each other and with a frequency difference equal to the fundamental hyperfine splitting that is 6.834 GHz. The detuning Δ from the atomic transition depends on the optical power available and on the diameter of the beams. In typical experimental configurations that are a few hundreds mW power available over ~ 1 cm beam waist, the detuning is generally in the GHz range.
- Different frequency configurations were considered for the nondemolition measurement. In order to keep versatility to our design, we decided to dedicate a specific extended cavity diode laser for this purpose. This diode can be easily tuned for a few GHz and is referenced to an atomic transition.

2.1.3 Scheme of the optical bench

The optical bench has been designed to be compact. The optical system to generate the cooling and repumping radiation holds only on a 60×60 cm breadboard. The beam height is 4 cm above the table. To minimize the spacing between the optical elements, all the mounts are glued on the table.

In this optical bench two independent extended cavity diode lasers are implemented: a repumper, locked by saturated absorption (see section. 2.1.4.1) on the cross over $|F = 1\rangle \rightarrow |F_p = 1, 2\rangle$ of ^{87}Rb and a cooling laser on the red of $|F = 2\rangle \rightarrow |F_p = 3\rangle$. The repumper is frequency shifted on the $|F = 1\rangle \rightarrow |F_p = 2\rangle$ transition by an acousto-optic modulator which is furthermore used as a fast controller for the light intensity. The cooling laser is first injected in a 1 W diode tapered amplifier (Eagle Yard : mod. EYP TPA 0780) and frequency locked to the repumper (see section. 2.1.4.2). The relative beatnote lock implemented allows a tunable control of the laser frequency. The strong beam is separated, controlled in amplitude and injected in different fibers for the MOT operations, the absorption imaging, and the optical repumping.

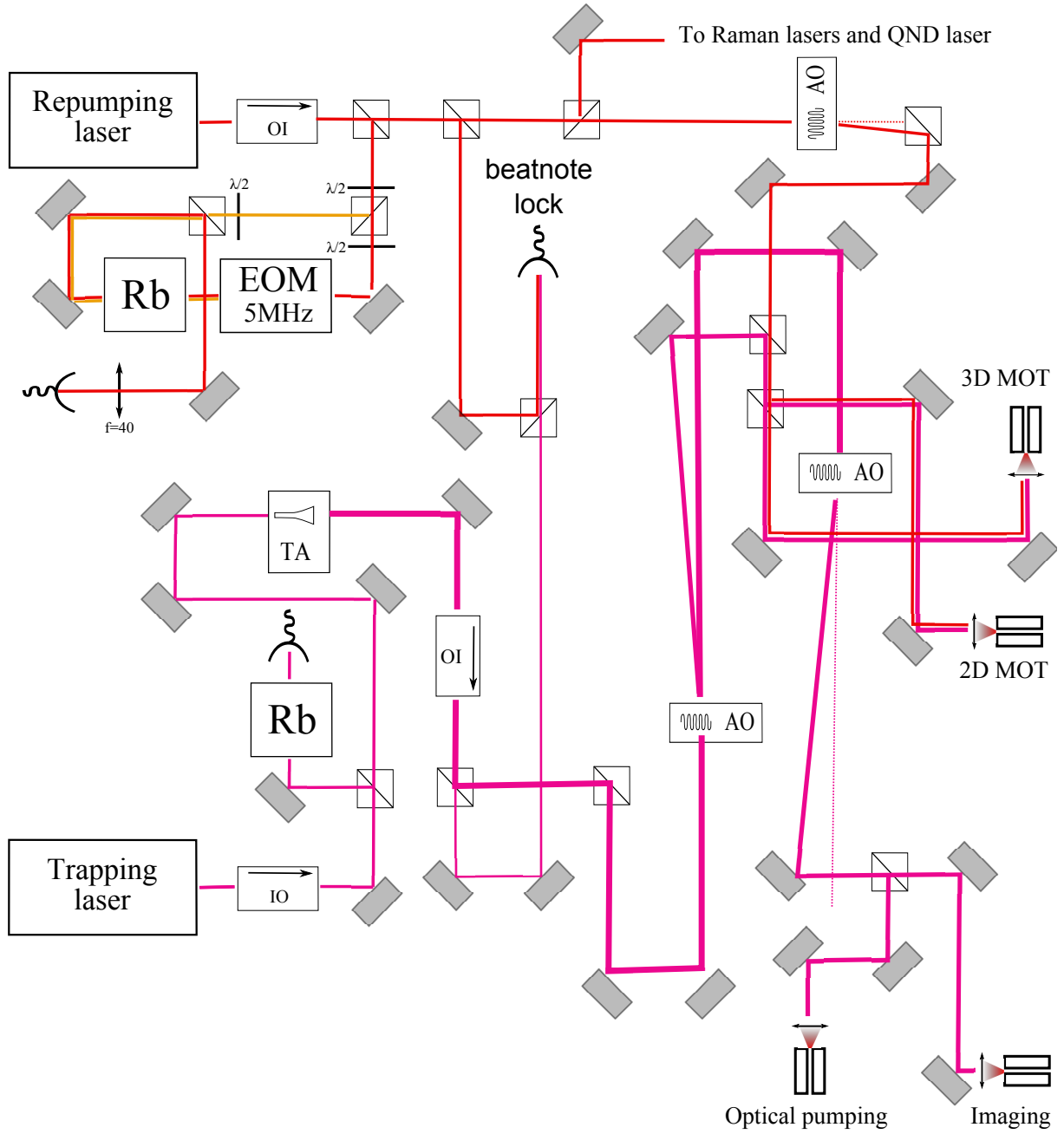
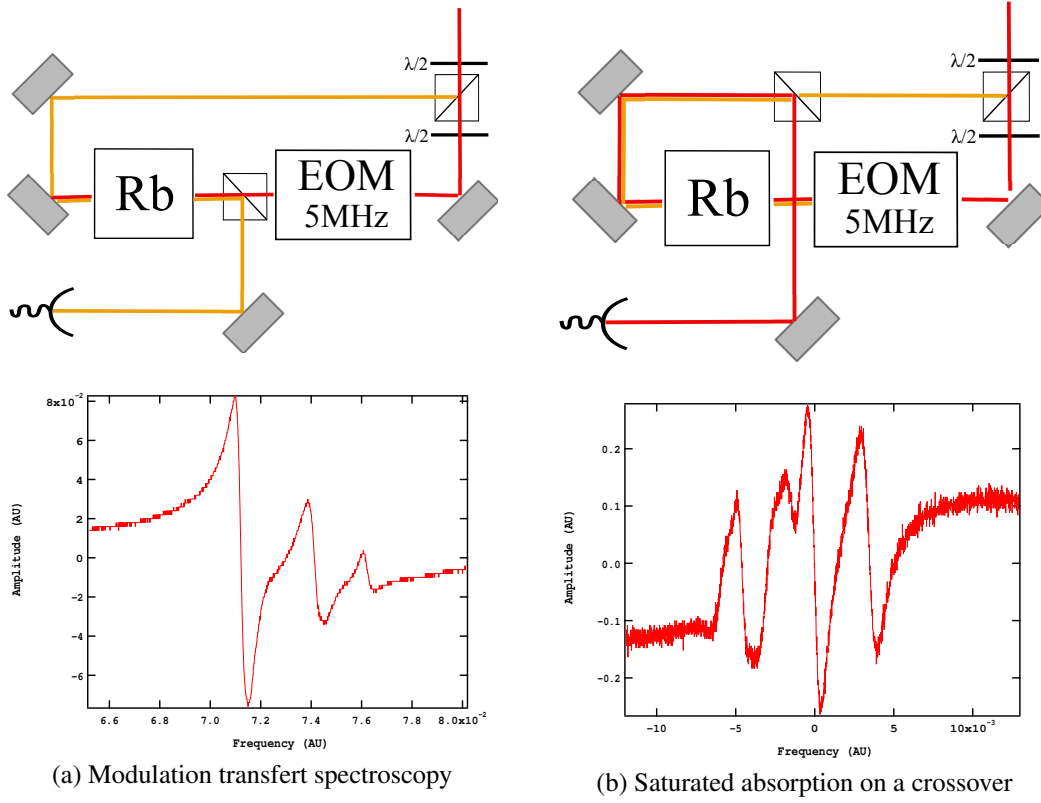


Figure 2.4: *Scheme of the optical bench.*

The cooling radiation is amplified and split to be used to cool, image and optically pump the atoms. The repumper is spectroscopically locked on the ^{87}Rb transition. Small fractions of the beams ~ 2 mW, are used for the frequency lock of the cooling laser on the repump laser. The repumper and cooling radiations are geometrically overlapped before being injected in the fibers toward the 2D and 3D MOT. For the sake of clarity, the optical wave plates have been intentionally removed from the scheme.

Figure 2.5: *Saturated absorption*

(a) The modulation that is present on the strong pump is transferred onto the weak probe. On the error signal below, only the atomic lines can be seen and not the crossover. (b) The modulation is directly applied on the probe and the pump is used to saturate the transition for the right velocity class of atoms. The error signal is not as clean but the crossovers are present.

2.1.4 Laser locks

2.1.4.1 Saturated absorption on a cross over.

In order to stabilize the laser frequency, one needs an absolute frequency reference. As the final purpose of the experiments is to control the atomic state, it is common to use the atomic transition lines themselves as a frequency standard. The main problem in doing so is the existence in a gas at room temperature of the Doppler broadening of the atomic transitions. At room temperature the apparent linewidth of atomic state are about $2\pi \times 500 \text{ rad.s}^{-1}$, which is much more than the natural linewidth $\Gamma = 2\pi \times 6 \cdot 10^6 \text{ rad.s}^{-1}$ of the atomic transition $|5S\rangle \rightarrow |5P\rangle$. Nevertheless, using Doppler free spectroscopy techniques [Bennett 62, MacAdam 92] such as saturated absorption, this enlargement can be circumvented..

To extract an error signal, we proceed with an heterodyne detection. Two main techniques to insert the modulation are commonly adopted. The first consists to modulate the Zeeman splitting of the magnetic sublevels with an external magnetic field. Because of the coils inductance, magnetic fields cannot be modulated very fast, and the feedback bandwidth is limited to a few kHz. The second method that we chose is a phase modulation introduced directly on the optical beam [Shirley 82, Bjorklund 80]. The usual scheme of this method is presented in figure 2.5a.

The principle of the modulation transfer spectroscopy is to modulate the refractive index of the cloud with a phase modulated pump beam (red in figure 2.5a). This modulation of the refractive index, which depends on the relative position of the laser frequencies with respect to the atomic lines, creates a phase modulation on the probe beam. Because the modulation is fully transferred by the atoms, it is a spectroscopically sensitive measurement. Nevertheless, the modulation is applied on the atomic transition that the pump frequency is addressing. Hence, it is not possible to use this technique for a crossover where the pump and the probe are addressing two different transitions.

To circumvent this difficulty, we use an alternative method where the phase modulation is directly applied on the probe (figure 2.5b). The pump is used to modify the atomic population between ground and excited state when the two lasers are addressing the same atoms. This method does not depend on which atomic transition is addressed and work even for a crossover. The error signal detected for one and the other methods are presented in figure 2.5.

Using this method, the repumper laser is locked on the $|F = 1\rangle \rightarrow |F_p = 1, 2\rangle$ crossover. The feedback is realized by a double integrator feedback scheme as presented in figure 2.6.

2.1.4.2 Beat note frequency lock

As shown previously, the repumper is fixed with respect to the atomic lines. In order to guarantee a high tunability of the cooling laser for the molasses and loading phases, it is locked with respect to the repumper via a beatnote technique.

The basic idea is to observe the beating frequency between the repumper and the cooling radiation on a fast photodetector (Hamamatsu, mod. G4176-03). The beating frequency is the difference of frequency between the two lasers ($\Delta\omega \approx 6.8$ GHz). Mixing this signal with a stable (fluctuations $\ll \Gamma$) microwave generator (YIG, mod. LPO-0408), the frequency is down converted in between 0 and 512 MHz. After a division by 512, the signal is proportionally converted to a voltage through a frequency to voltage converter (FVC, 1 MHz = 10 V). The signal is then low pass filtered to avoid residual signal modulation at 1 MHz which passes through the FVC, and a controllable reference voltage is subtracted. The error signal obtained is doubly integrated: the fast part of the feedback is applied on the current and the low frequency feedback is applied on the piezo. The double integrator scheme ensures that the piezo is always dominating at DC.

The main advantage of this scheme is its versatility and capture range. Changing the reference voltage, one changes the frequency of the laser over approximately 400 MHz. The full range (512 MHz) is not available since the FVC does not work at low frequencies (< 200 kHz).

When the dipole trap is operated, the cooling frequency needs to be shifted by 250 MHz in 1 ms. Extended cavity diode laser are done to work with a zero average current correction. When the reference voltage is quickly ($\tau \approx 1$ ms) changed in a two integrator scheme, all the short time corrections are applied on the current. This creates an instability in the laser and makes it more sensitive to mode-hop. In order to improve the speed at which the frequency can be corrected, we implemented a feedforward on the feedback loop of the piezo. This feedforward is actually equivalent to a peaked gain at $f \approx \frac{1}{\tau}$ in the transfer function of the piezo. With such a proportional feedback, the error signal on the current is kept centered on zero. With this method, we were able to change the frequency by $60 \Gamma = 360$ MHz in 1 ms.

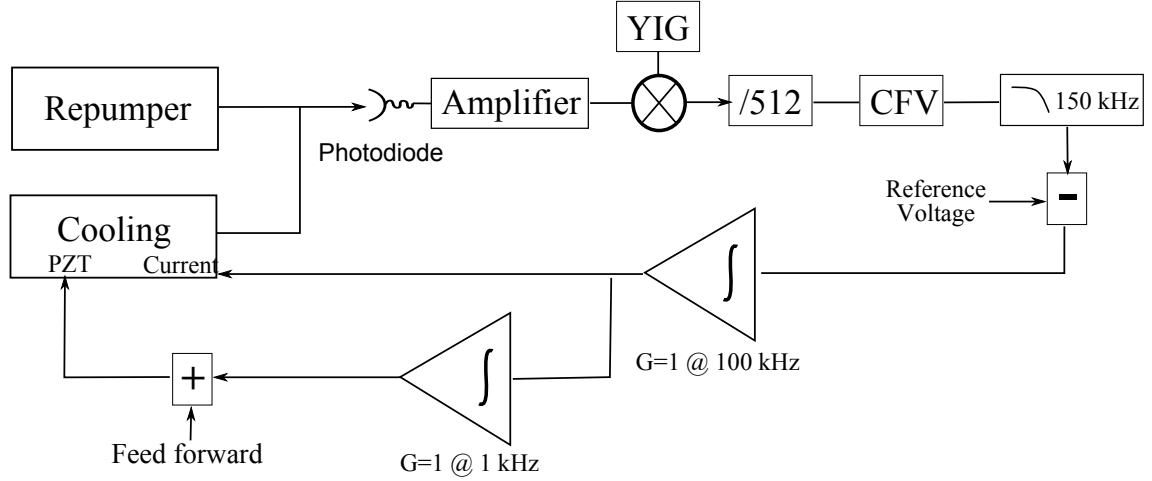


Figure 2.6: Scheme of the beatnote lock.

The beatnote detected on the photodiode is down converted in the range 0-1 MHz and linearly converted to a voltage. The further subtraction of a reference voltage gives the error signal that is integrated and fed on the piezo and the current of the laser.

2.1.4.3 Raman phase lock

Since the experiment is designed to realize sub-shot noise atom interferometry, a Raman bench was mounted for the coherent manipulation of the atoms. In the following, we introduce the coherent manipulation of atoms by two photons Raman transition [Cheinet 06] and emphasize on their sensitivity to the laser phase noise. The performance of the implemented phase lock of two independent lasers is then detailed.

Two photon transitions

To realize an atomic interferometer, it is necessary to coherently drive the atoms in a superposition state. This coherent manipulation is the equivalent of the beam splitter in optics. The superposition can be created by a microwave field oscillating at the frequency difference between the two states, but this interaction transfers only a small momentum $p_{\text{MW}} = h/\lambda_{\text{MW}}$ to the atom. It is then not adapted to generate the spatial separation of the two arms of the interferometer that is needed for the measurement of inertial forces. The solution was demonstrated in 1991 [Kasevich 91] and takes advantage of a two photons transition. The implementation of two photons Raman transition has been a real breakthrough for atom interferometry since the momentum of the two photons are transferred to the atoms: $p_{\text{opt}} = 2h/\lambda_{\text{opt}} \gg p_{\text{MW}}$.

If we consider the case of a three level system, and if we neglect the light-shift induced by the Raman beams, the evolution of a system $|\psi_{\text{at}}\rangle = c_f(0)|f\rangle + c_e(0)|e\rangle$ is given by [Cheinet 06]:

$$c_f(t) = \left[\cos\left(\frac{\Omega_R t}{2}\right) c_f(0) - ie^{i\phi^0} \sin\left(\frac{\Omega_R t}{2}\right) c_e(0) \right] e^{-i\omega_f t} \quad (2.1)$$

$$c_e(t) = \left[-ie^{-i\phi^0} \sin\left(\frac{\Omega_R t}{2}\right) c_f(0) + \cos\left(\frac{\Omega_R t}{2}\right) c_e(0) \right] e^{-i\omega_e t} \quad (2.2)$$

where $\Omega_R = \Omega_1 \Omega_2 / (2\Delta)$ is the Rabi frequency of the two photons transition and Ω_i the one

photon Rabi frequency of each laser. The energies of both hyperfine state are $\hbar\omega_f$ and $\hbar\omega_e$ and $\phi^0 = \phi^2 - \phi^1$ is the phase difference between the two lasers.

This expression shows that during the coherent transfer, the phase difference of the lasers is transferred onto the atomic state. As the interferometer measures the phase difference between the two internal states, the noise on the phase difference between the laser will have a direct impact on the sensitivity of the interferometer. To reach high precision measurement, this noise has then to be kept as low as possible.

Phase lock of Raman beams

As previously mentioned, the two Raman lasers have a frequency difference equal to the ground state hyperfine splitting (6.8 GHz) and a well defined relative phase. To get such a phase relation between the lasers, two different methods are commonly used:

- The two phase related frequencies can be obtained by the generation of sidebands around a carrier. This has been for example demonstrated with an acousto-optic modulator in [Bouyer 96]. In this case, the phase correlation is automatically fulfilled if optical path length fluctuations are well controlled. This technique, which is quite efficient, lacks versatility in the tunability of the phase difference between the two lasers that can only be tuned by changing the optical path.
- Instead, we decided to set two independent lasers. The frequency and phase relation between the lasers is ensured by a locking procedure that is presented in figure. 2.7. The master laser (Raman 1: R1) is frequency locked to the $|F = 1\rangle \rightarrow |F' = 1, 2\rangle$ cross over via the repumper laser (noted: Rep). This frequency lock is done using a Phase Locked Loop (PLL, Analog device: mod. ADF4108). In this numerical electronic device, the frequency of the signal, which oscillates at the frequency difference of the lasers ($\Delta f = f_{R1} - f_{Rep}$) is numerically rescaled and compared to a quartz reference to obtain an error signal. With this method, the absolute frequency of the master f_{R1} can be placed anywhere close to the repumper ($\Delta f < 8$ GHz). Contrarily to what seems to indicate its generic name, the PLL device is here used for a frequency lock and not for a phase lock. In recent years, the technology of PLL (bandwidth and compactness) has been optimized for the need of telephony, where they are used to lock Voltage Controlled Oscillator frequencies. Their application to laser locking is recent and detailed in [Banerjee 06, Appel 09a].

As described in figure 2.7, the slave laser (Raman 2: R2) is phase-frequency locked to the master laser. This lock consists in down converting the laser frequency difference ($\Delta f = f_{R1} - f_{R2} = 6.834$ GHz) around 200 MHz, by mixing the beatnote signal with a reference frequency. This down converted signal is frequency compared to a tunable Local Oscillator ($f_{LO} \approx 200$ MHz) in a phase-frequency detector (ON Semiconductor, mod. MC100EP40). The error signal obtained is feedback on the laser as described in figure 2.7. The resulting beatnote presented in figure 2.8b shows that the residual phase noise is below $10 \mu\text{rad.Hz}^{-1/2}$ at 10 kHz and reaches $3 \mu\text{rad.Hz}^{-1/2}$ at 100 kHz.

Microwave frequency chain

A critical part in the lock of Raman lasers is the quality of the microwave reference. Actually,

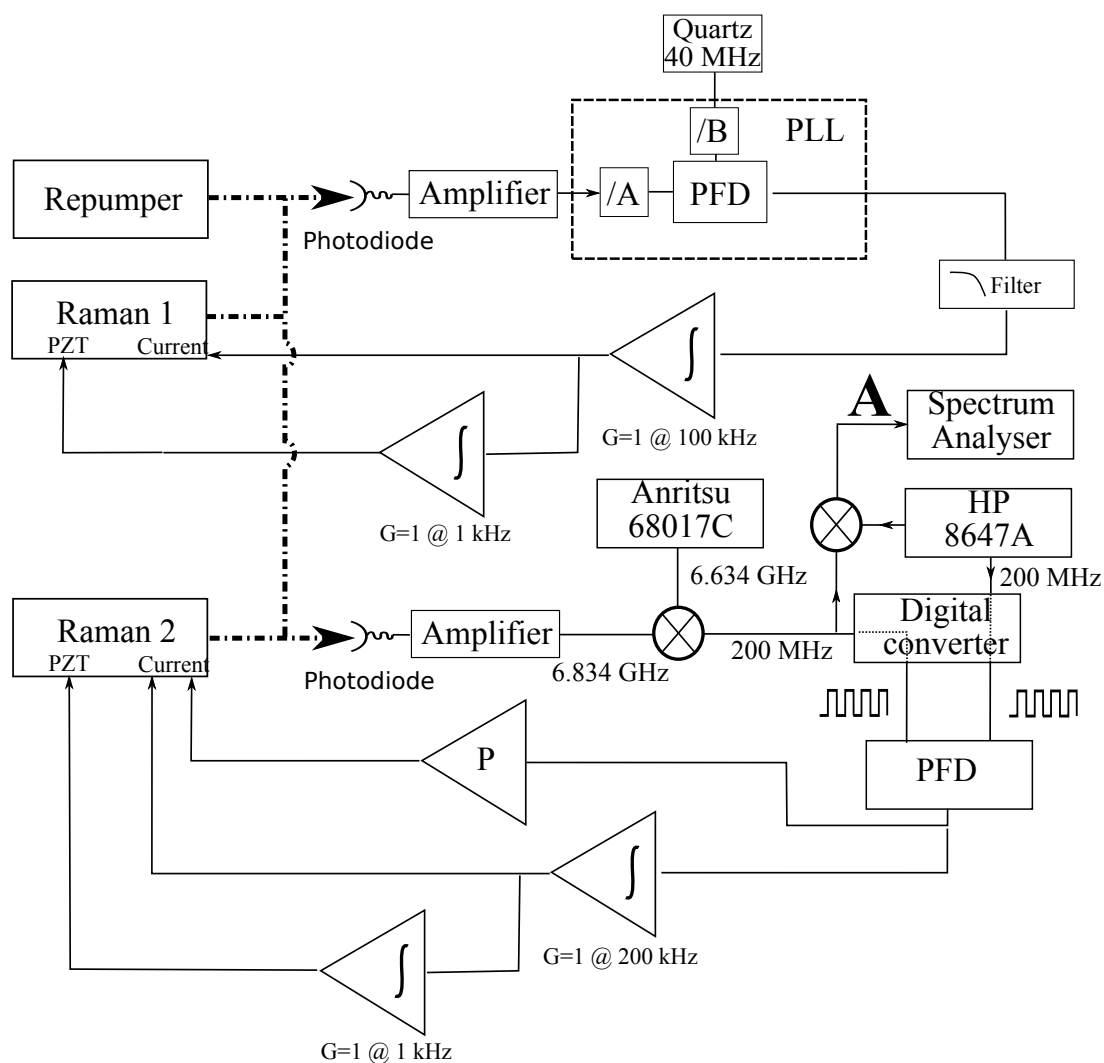
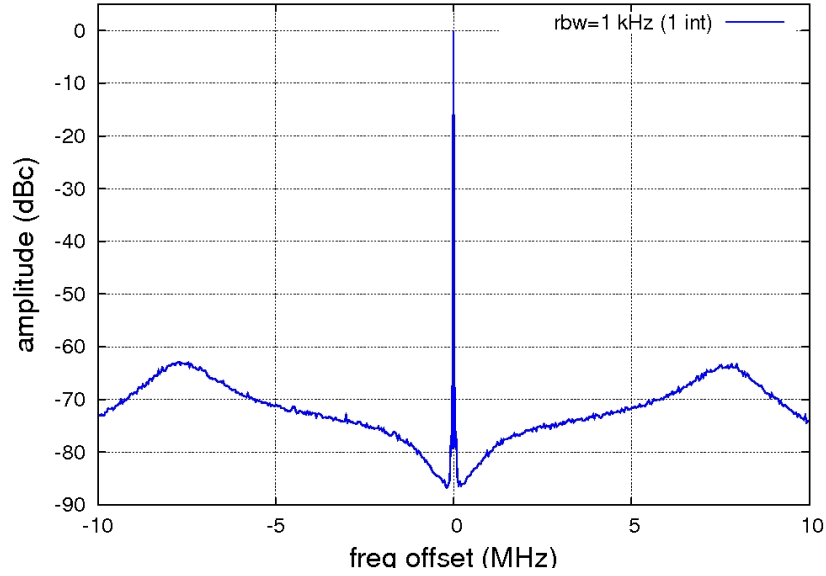
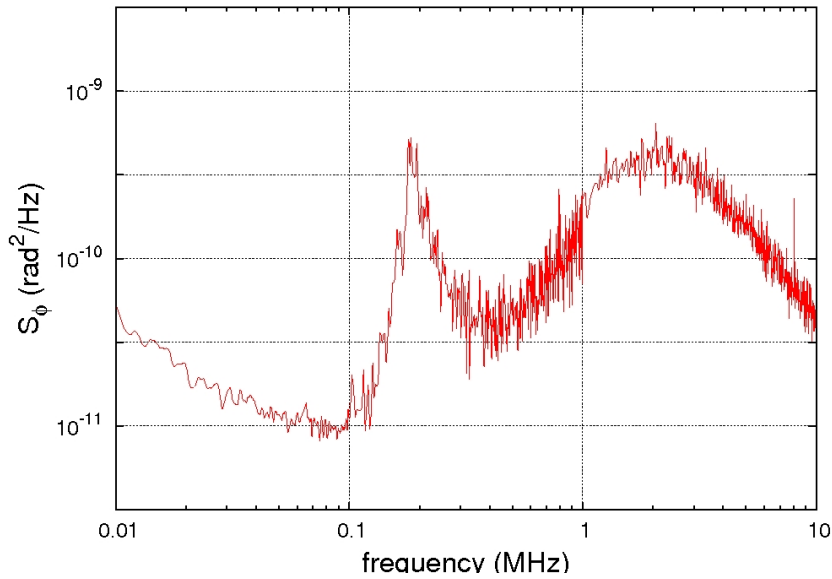


Figure 2.7: Scheme of the frequency and phase lock of the Raman beams

A frequency lock between Raman1 and Repumper is first realized by the mean of a Phase Locked Loop. The phase lock between Raman 2 and Raman 1 is done using a phase frequency detector (PFD).



(a) Optimization of the bandwidth of the phase lock: BW= 7GHz



(b) Optimization of the phase noise close to the carrier

Figure 2.8: *Phase lock beatnote*

This spectrum is obtained by a demodulation with the HP synthesizer (point A in figure 2.7). The demodulation is introduced to suppress the phase noise of the synthesizers and to look only for the residual phase noise of the lock.

a high quality (high gain, high bandwidth) phase lock will copy the noise of the microwave source on the Raman phase difference. The noise spectrum of figure 2.8 is measured relatively to the microwave source, and shows that the phase noise performances of the lock are close to standard performances. Nevertheless, the atoms will be sensitive to the absolute phase noise and not to the relative one. It is then important to use a clean microwave source to drive the atomic transition.

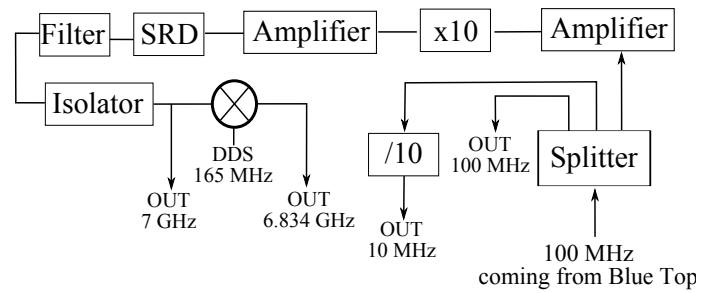
In that purpose, we designed in collaboration with the Syrte our own microwave reference (figure. 2.9b). The basis of the design is a very low noise commercial $5 \times 2 = 10$ MHz crystal reference (table 2.9a) on which a second 100 MHz reference is phased locked.

On one side, this 100 MHz frequency is divided by 10. The resulting 10 MHz are used as our common reference for the electronics in the lab.

On the other side, it is multiplied by 10, amplified and sent to a non linear device (step recovery diode, mod. HP 33005C). The 7th harmonic (7 GHz) is filtered (Bandpass cavity filter, mod. BP7000-70-6CS) and used as the reference microwave. In order to create a tunable frequency around 7 GHz, the signal is mixed with a synthesiser tuned around 160 MHz and referenced to the 10 MHz output of the chain. All the phase noise of the chain is then ensured by the quality of the reference crystal.

Frequency offset	Phase noise
1 Hz	-113 dBc/Hz
10 Hz	-143 dBc/Hz
100 Hz	-163 dBc/Hz
1 kHz	-170 dBc/Hz

(a) Reference noise of the Blue top crystal.



(b) Scheme of the Microwave frequency chain. SRD: Step recovery diode

Figure 2.9: *Microwave frequency chain*

On the left hand side are given the performance of the crystal measured by the manufacturer, and on the right side is presented the electrical scheme that we implemented.

2.2 Apparatus for cold atom trapping

In this section, we will detail the apparatus where cold atomic sample are generated. The underlying physics for cooling and trapping of atoms is briefly exposed. In a second part, we present the vacuum and optomechanical design of our 2D and 3D MOT which are generated in two different vacuum chambers.

2.2.1 Cooling and trapping of atoms

Laser cooling techniques have been developed and pushed forward in the 80's. This led to the Nobel Prize of Steven Chu, Claude Cohen-Tanoudji and William D. Philipps in 1997. The key idea of laser cooling is to use the radiative pressure exerted by light to slow down atoms. In

this section we will limit our explanation to the 1D case, and introduce the main notions of these techniques. For further details on atoms cooling and trapping, one can refer to [Chu 85, Metcalf 03, Metcalf 01, Adams 97].

2.2.1.1 Cooling atoms

Because of the Doppler effect, two counter-propagating lasers with angular frequency ω will be absorbed differently depending on the relative atoms' velocity direction and modulus with respect to the optical beams. If the lasers are tuned to the red of the atomic transition ($\omega < \omega_0$), the atoms absorb preferentially from the beam counter-propagating its displacement. Because of the momentum transfer associated with this absorption, the atoms are slowed down. A graph of this dissipative force (F_{dop}) is presented on figure 2.10a.

$$F_{\text{dop}} = F_0 \left(\frac{\Gamma^2/4}{(\omega - kv - \omega_0)^2 + \Gamma^2/4} - \frac{\Gamma^2/4}{(\omega + kv - \omega_0)^2 + \Gamma^2/4} \right) \quad (2.3)$$

where $\Gamma = 2\pi \times 6.066 \cdot 10^6 \text{ rad.s}^{-1}$ is the natural linewidth of Rubidium. One can see in figure 2.10a that the force is opposed to the atomic velocity, which makes it equivalent to a friction force.

Remark

- The model presented before is based on a two levels atom. The cooling mechanisms actually rely on the existence of a cycling transition that allows to repeat the process of absorption. In ^{87}Rb , the transition ($|F = 2\rangle \rightarrow |F_p = 3\rangle$) is a good candidate. Nevertheless the cooling laser can still excite the $|F = 2\rangle \rightarrow |F_p = 2\rangle$ transition. From $|F_p = 2\rangle$, the atoms can spontaneously decay to $F = 1$ where they will no more be sensitive to the cooling laser. $|F = 1\rangle$ is then called a dark state. An extra laser, called repumper is needed to bring atoms back in the cycling transition.
- In addition, this description does not take into account the heating term due to the spontaneous emission linewidth. This effect limits in principle the lowest temperature achievable to the Doppler temperature $T_{\text{c,dop}}$:

$$T_{\text{c,dop}} = \frac{\hbar\Gamma}{2k_B} = 144 \text{ } \mu\text{K}, \quad (2.4)$$

which corresponds to a mean kinetic energy per particule of $\hbar\Gamma/2$

2.2.1.2 Trapping

In order to gather a cold sample of atoms, a velocity dependent force that cools the atoms is not sufficient. It is also necessary to make the force position dependent. For that purpose, the atom-magnetic field interaction is used (Zeeman effect). Hence, the energy of the atoms is modified through an interaction between an external field (B) and the atomic magnetic moment (μ). In the case of a magnetic splitting smaller than both the fine and the hyper-fine structure [Steck 10], the interaction Hamiltonian is $H_B = \mu_B g_F \frac{m_F}{\hbar} \cdot B_z$, where $\mu_B = \frac{e\hbar}{2m_e c}$ is the Bohr

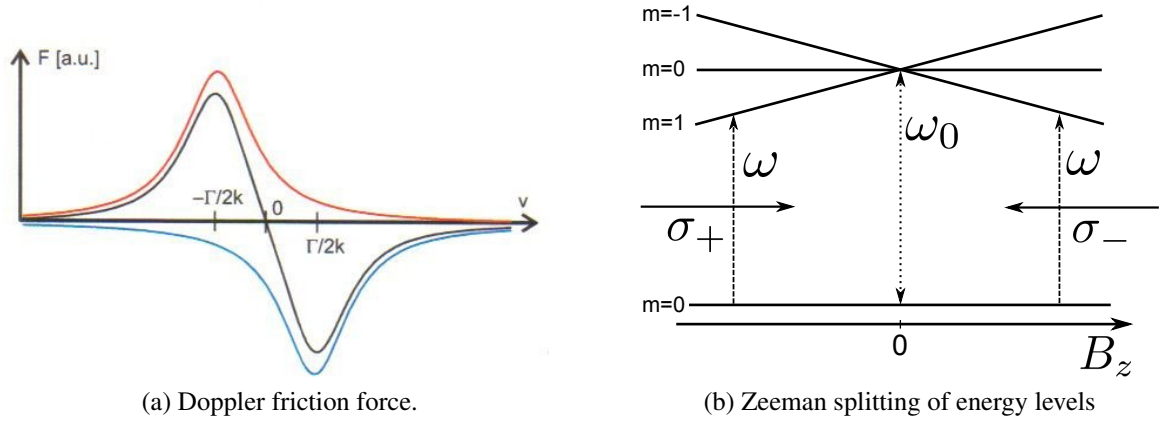


Figure 2.10: Cooling and Trapping mechanism

magneton and g_F is the Landé factor ($g_F = 1/2$ for $F = 2$ and $g_F = 2/3$ for $F_p = 3$). The splitting energy of an $|F, m_F\rangle$ level is then:

$$\Delta E_{F, m_F} = \langle F, m_F | H_B | F, m_F \rangle = \mu_B g_F m_F B_z \quad (2.5)$$

We consider now a magnetic field $\mathbf{B} = aze_z$ and two counter-propagating and circularly polarized optical beams (figure 2.10b). Because of selection rules [Cohen-Tannoudji 96], a σ_+ beam authorizes only the $|g, m = 0\rangle \rightarrow |e, m = +1\rangle$ transition, and a σ_- authorizes the $|g, m = 0\rangle \rightarrow |e, m = -1\rangle$ transition. For an atom in $z > 0$, this interaction brings the atom closer to resonance for the σ_- beams and takes it out of resonance for the σ_+ beams. The radiation pressure pushes the atom in the direction $z=0$ which creates the central force desired for trapping.

In order to create such a linear dependence of the magnetic field, two coils in an anti-Helmholtz configuration are commonly adopted. The quadrupolar field has the required linear dependence in the 3 directions of space. The polarization of the six beams trapping beams is adjusted to match with the direction of the gradient.

2.2.2 Two dimensional Magneto-Optical Trap

To produce the source of atoms for the 3D magneto-optical trap, different methods were proposed and tested. Among them, chirped optical cooling lasers [Ertmer 85] or white light slower [Hoffnagle 88] can be mentioned. The methods which are now the most commonly adopted are:

- Dispensers are the easiest way to create a controlled vapor. They consist in a metallic filament that contains solid Rubidium. In this filament can circulate a current. By Ohm dissipation, the filament is heated and the Rubidium sublimates, creating the desired vapor. This technique is the simplest to increase the Rubidium vapor pressure but it has the drawback that the atoms are not well collimated towards the trapping region and thus the background pressure increases when dispensers are turned on. A high pumping rate is needed to quickly recover the vacuum that allows the evaporation process to occur.

- A Zeeman slower allows to extract a directed atomic beam from a hot vapor [Phillips 85]. This hot but directed atoms are slowed down by a laser counter-propagating the atomic direction. A gradually decreasing or increasing magnetic field allows to compensate for the decreasing Doppler shift linked with the slowing down of the atoms, such that the counter-propagating light stays on the red side of the atomic transition. This technique is very efficient and allow to separate by differential vacuum the high pressure chamber (oven) from the high-vacuum chamber. The main drawback of the method is the place needed for the Zeeman slower (few meters).
- 2D-MOT loading is a technique that creates a slow jet of atoms that can circulate in between two chambers that are separated by a differential vacuum stage. This technique has been chosen in our set-up for its compactness and is described in the next section. For a detailed analysis of 2D-MOT processes, one can refer to [Metcalf 01].

2.2.2.1 Principle

The technique involved in a 2D-MOT relies on the cooling mechanism described in section 2.2.1. As shown in figure 2.11a, two pairs of counter-propagating and circularly polarized beams are applied in two transverse directions (x and y). Following the description given in section 2.2.1 the atoms will be slowed down in these two directions. Using two pairs of coils in anti-Helmholtz configuration, a gradient is created on x and y with a zero of field at equal distance of the coils. Using two pairs of coils as presented in 2.11a, the residual gradient on z is cancelled at first order. Atoms passing through the region of the beams will be trapped and cooled along x and y , but free to escape along the longitudinal direction z . This creates a jet of atoms along z , with a low divergence due to the transverse cooling. To force the atoms in only one longitudinal direction, a push beam is added to reverse the velocity of atoms propagating in the undesired direction and push them towards the 3D-MOT region.

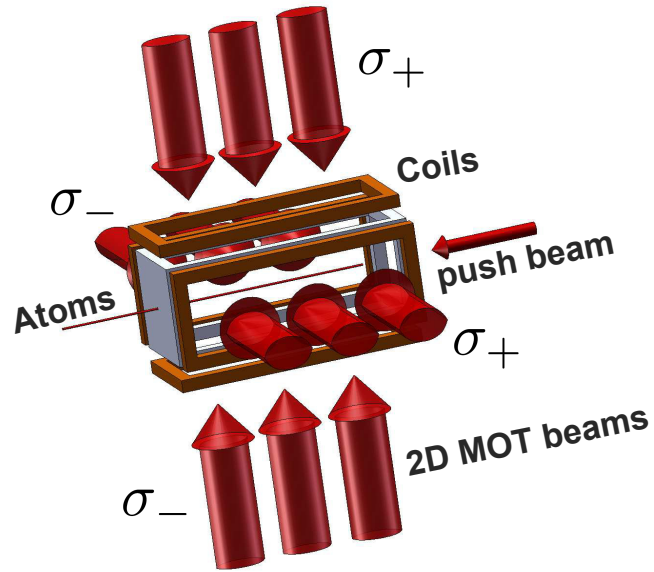
2.2.2.2 Design

Vacuum

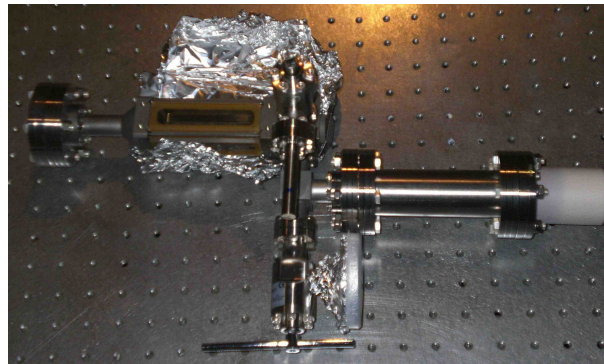
The titanium vacuum chamber of the 2D-MOT and the whole opto-mechanical system are presented in figure 2.11b and 2.11c. The design is inherited from the Syrte where our 2D-MOT has been assembled.

The Rubidium (1 g) is inserted in a glass cell which in turn is placed in a titanium finger. Once the system is under vacuum, the glass cell is broken by a mechanical pressure on the titanium finger and the Rubidium vapor is free to reach the 2D MOT chamber. The finger is usually kept at room temperature but can be heated to increase the 2D MOT flux.

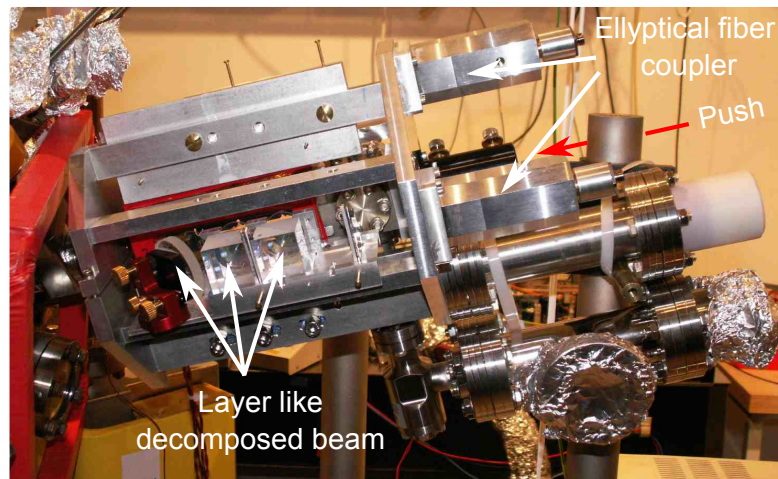
The windows ($15 \times 5 \text{ cm}^2$) for the cooling laser are elongated to allow for a long trapping region. For compactness reasons, the windows are glued to the titanium mount. A small hole (2 mm diameter and 2 mm long) followed by a 5 cm long graphite piece with a conical hole (1.5 mm input diameter, 5 mm output diameter) ensures the differential pressure operation of the 2D MOT chamber and the science chamber. The slow jet of atoms reaches the 3D MOT region through this hole. The vacuum of the two chambers can be isolated by an all metal CF16 valve. On the 2D MOT side, the vacuum was primarily pump to 10^{-6} mbar, before a 50 l/s getter pump



(a) Schematic of the 2D MOT.



(b) Vacuum part of the 2D MOT



(c) Opto-mechanics assembled around the 2D MOT

Figure 2.11: *Two dimensional magneto-optical trap*

Two pairs of counter-propagating beams decomposed over three region each generate a slow jet of atoms that escape through a hole in the vacuum chamber. A push beam helps the atoms to escape the 2D MOT chamber towards the 3D MOT region.

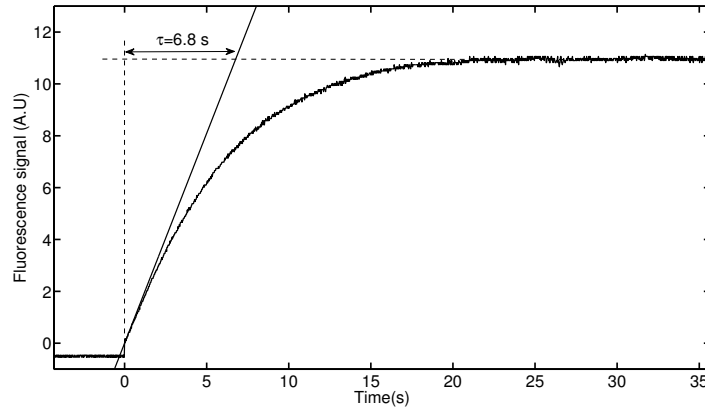


Figure 2.12: *Loading of the 3D MOT.*

The trapping beams of the 3D MOT are suddenly turned on, and the fluorescence of the MOT is measured on a photodiode.

was started (SAES getters, mod. C50-St707). The vacuum on this side is maintained to about 10^{-8} mbar with the getter alone.

Light and coils

As explained in 2.1.3, the light used for the 2D MOT is composed of repumper and cooling radiations which are injected in the same fiber. The light is split in 3 with a commercial device (Schäfter + Kirchhoff, mod. 1×3) to create 2 cooling beams containing each 20 mW of cooling and ~ 0.5 mW of repumper, and 1 push beam made of 0.5 mW of cooling and $\sim 10^{-2}$ mW of repumper.

In order to create a long layer of light to cover the windows, the cooling beams are elliptically shaped with an aspect ratio of 2 and a beam waist of 10 mm on the long axis. As can be seen in figure 2.11c, the layer is generated by the juxtaposition of three of these elliptical beams. The circularity of the polarization is ensured by a rotating quarter wave plate. Each of these $6 = 2 \times 3$ beams is retroreflected by a mirror on top of which is glued a 1 inch quarter wave plate.

The magnetic gradient needed for the trapping is generated out of 2 pair of rectangular coils ($15 \times 5 \text{ cm}^2$). Only one pair is really needed, but using 2 pairs ensures the symmetry of the two transverse trapping direction and cancel at first order the residual longitudinal gradient. Each coil is composed of 100 turns of 1 mm diameter wires. All the coils are operated in series with 1.5 to 2 A. The zero of magnetic field is adjusted on the axis of the hole using independent adjustable resistances in parallel to the coils (few percent adjustability).

Performance

Using the adjustability of the magnetic field and power cited above, this 2D MOT loads the 3D MOT with more than 5×10^8 at/s. We were able to fully load 3D MOT of a few 10^9 atoms in about 3 s.

2.2.3 Ultra High vacuum set up

The design of the main chamber, the cavity and the coils were carried out as an ensemble. All the drawings have been realized on Solidworks. The design of the 2D MOT and the main chamber are independent except for a CF16 flange that links the two. All the mechanical pieces were realized in non-magnetic material. The chamber is completely done in 316LN stainless steel. The closest mechanics to the atoms were done in titanium, bronze beryllium or copper.

2.2.3.1 Main chamber

The main chamber is designed to reach ultra high vacuum and contains the optical cavity as well as the MOT coils. Hence, it has a high volume compare to standard UHV chambers. It is a cylinder with inner diameter of 25 cm and height of 30 cm. The cavity and the coils are mounted on the CF250 top flange, which is turned upside down to close the vacuum chamber (see figure 2.13). This chamber includes as many optical ports as possible considering the optical access left by the cavity and the coils. In particular, there are four CF100 windows (2 on the vertical and 2 on the horizontal), 13 CF40 and 1 CF16. A precleaning of the cavity was realized by baking the chamber to 350°C with only blank flanges for 1 week. A second precleaning was realized at 200°C with the windows for 2 weeks. As described in 2.2.3.2, the coils had their own precleaning. The cavity with the coils were inserted and the vacuum started with a turbo pump mounted behind an all metal valve. When a vacuum of about 10^{-6} mbar was reached, two (out of four) 50 l/s getter pumps and two 20 l/s ion pumps were started. The valve of the turbo pump was then closed and the turbo pump removed to avoid vibrations. The chamber was baked to 80°C for 2 weeks to prevent damages on the piezo-electric elements of the cavity. To avoid magnetic fields, no gauge was installed on the chamber and the two ion pumps are shielded. The sum of the two ion pump currents is below 0.5 μ A, which is probably the leakage current. We have no precise value for the residual vacuum pressure, but the life time of the MOT is about 20 s (see figure 2.16).

2.2.3.2 Coils under ultra high vacuum

Because the science chamber contains the cavity, it has big dimensions. Hence, if the coils had been out of the vacuum chamber, we should have used about 50 A to generate the 3D MOT gradient. This would have unnecessarily constrained the experiment. To avoid such a problem, the coils have been inserted in the science chamber itself. The design is presented in figure 2.15 and the drawings are given in appendix G. The V shaped design of the copper (OFHC) mounts, that can be seen in figure 2.15b allows for a maximal optical access. To guarantee the overlap of the cavity center and the zero of magnetic field, the supports of the coils are fixed on the titanium (TA6V type) plate of the cavity. In this configuration, the coils and the mirror of the cavity are both referenced to the same mechanical piece (titanium plate) which helps to achieve the previously mentioned geometrical overlap.

When the coils are supplied, a thermal distortion of the cavity plane could appear. To prevent for such an effect, the coils supports were attached to the titanium plate with machor ceramics which are thermally insulating and UHV compatible. To allow for the thermal dissipation to occur, the coil supports are linked to the science chamber via copper braids which avoid mechanical constraints.

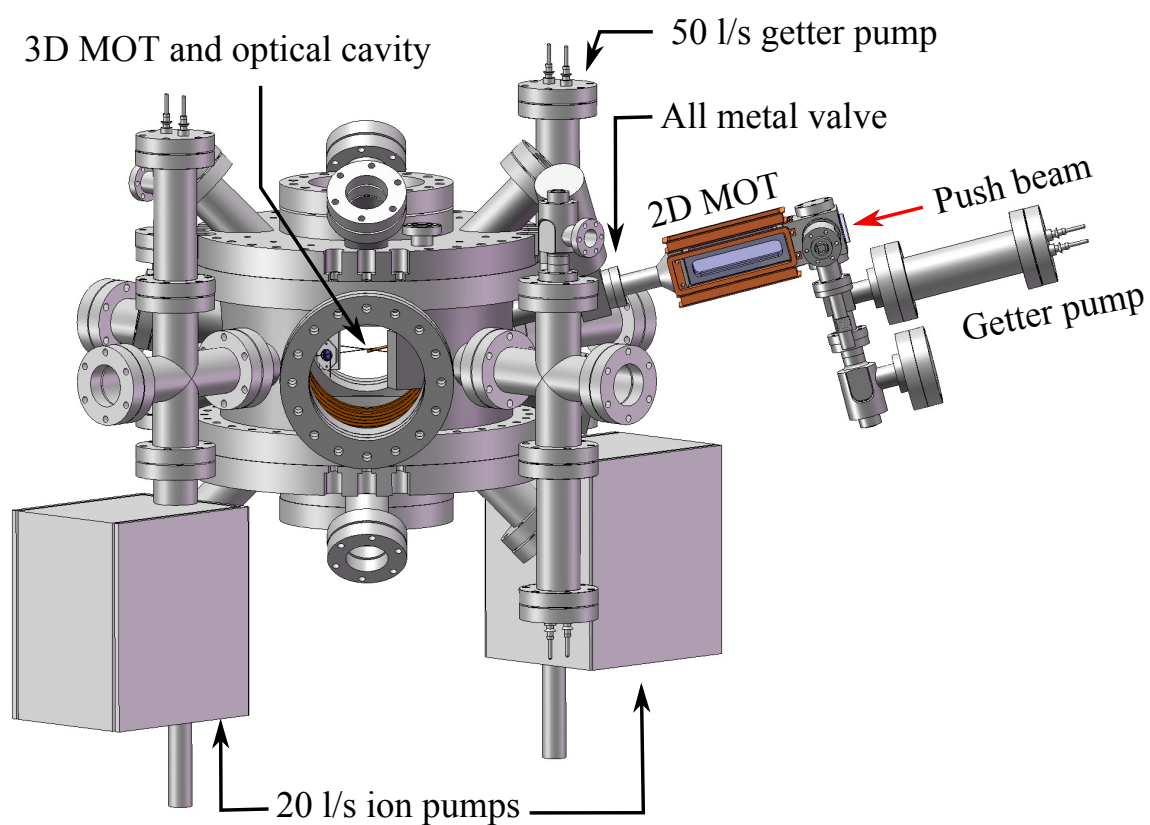


Figure 2.13: *Overview of the complete vacuum system*

The 2D MOT compact design is on the right and the science chamber containing the ultra-high finesse cavity is on the left.

The winding of the coils are made of kapton insulated copper wires. Their section is 2.44×1.2 mm. The wires are glued together to the support to guarantee the robustness. The glue is Epotek H77 and was heated up to 180°C under nitrogen to dry. Each coils has 116 turns with radii between 50 and 77.5 mm and distances to the MOT between 16 and 38.5 mm. Considering the full geometry, we have $2.2 \text{ Gcm}^{-1}\text{A}^{-1}$ and the coils are operated with 4 A. To avoid Eddy currents, the copper support are cut.

To carry the current in and out of the chamber, a CF16 electrical feedthrough in 316L stainless steel with 8 pins has been installed on the vacuum chamber. To avoid heating on the feedthrough, each way of the current is split onto two pins of the flange. Each pin can handle 15 A with 1 kV.

Before the coils were included in the main chamber, they were baked to 200°C for 2 months to allow for a maximal degassing. This long degassing time was mainly attributed to the air that is captured deep in the coil wiring and that has then a low conductivity towards the pump. A vacuum of $4 \cdot 10^{-10}$ mbar was then reached at room temperature with no current in the coils and with a 100 l/s pump behind 50 cm of a CF40 elbowed tube.

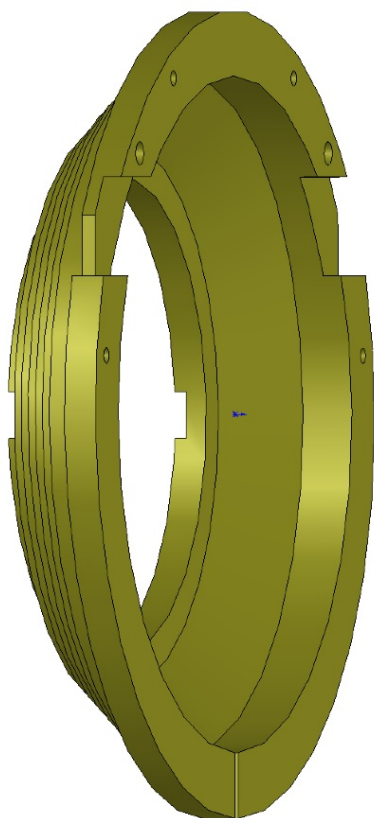
Remark: In order to create a bias field for optical pumping or Rabi oscillations, we have the possibility to switch the coils from anti-Helmholtz to Helmholtz configuration. In that case, the coils create a bias field of 17.4 GA^{-1} at the position of the MOT.

To compensate for external parasite magnetic fields (e.g. earth fields), we settled the so called compensation coils. These coils are three pairs of coils mounted in Helmholtz configuration. Each pair of coils compensate for the field in one of the three direction of space such that the residual magnetic field is null. Hence when the 3D MOT coils are turned off, optical molasses and subdoppler cooling can be performed in a zero magnetic-field environment. Along the vertical, they create 31.8 GA^{-1} , in the axis of the 3D MOT coils they create 17.3 GA^{-1} and in the last direction they create 34.4 GA^{-1} .

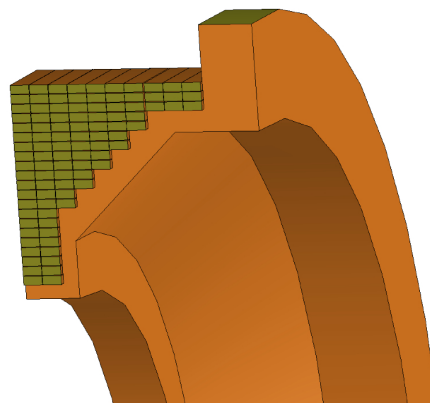
2.2.3.3 Magneto-optical trap

In this section, we describe the optical arrangement and characteristics of the 3D MOT. As presented in section 2.1.3, the two necessary frequencies for the trapping and cooling are injected in the same polarization maintaining fiber. To send the radiation from the three directions of space, the light is split in 3 different fibers using 1x3 splitter (Schäfter + Kirshoff). Each retro-reflecting beam contains 0.5 mW of repumper and 20 mW of cooling and is collimated to be sent on the atoms. The collimator are commercial couplers (Schäfter + Kirshoff, mod. 60FC-M75) directly fixed on the chamber itself. These couplers are composed of an achromat lens to collimate the light with a 6.75 mm waist, followed by a quarter wave plate to create left or right circularly polarized light. To simplify the set-up, we choose to retro-reflect the MOT beams with a 2 inch quarter wave plate followed by a 2 inch mirror.

Remark 1: This choice of retroreflected MOT beams simplifies the implementation since no intensity balance is required. At the same time, it becomes critical to reach low temperature in optical molasse, with the shadow effect on the first path that unbalances the power of the retroreflection.



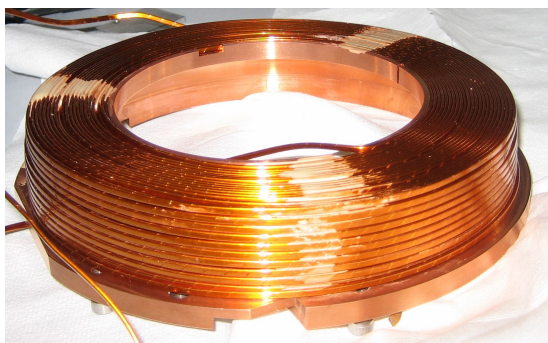
(a) Coils support.



(b) Disposition of the wire

Figure 2.14: *The copper support of the coils*

The V shape allows beams at 45° to access the atomic sample. The supports are directly attached to the titanium plate of the cavity.



(a) One of the two 3D MOT coils.



(b) Front surface of the coils

Figure 2.15: *UHV coils support*

The coils are wound on a copper support and are made of 116 winding each. The windings are glued together to the support by epotek H77.

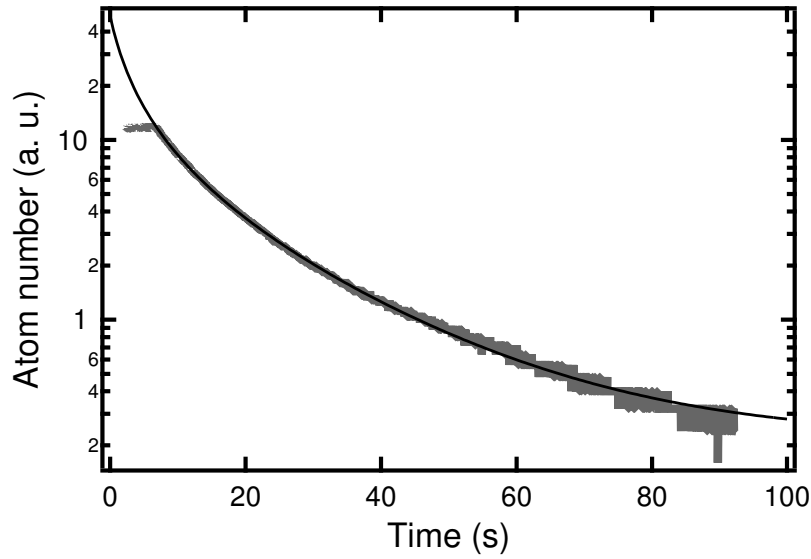


Figure 2.16: *Life time of the 3D MOT.*

The 2D MOT is turned off and the decay of the fluorescence of the 3D MOT atoms is measured.

Remark 2: For more versatility, we have recently implemented a 3D MOT configuration using 6 independent beams. The splitting in 6 beams is done by 1×2 fiber splitters (Oz optics).

2.2.3.4 The optical cavity

The optical cavity properties are detailed in chapter 3. Figure 3.4 shows a picture of the mechanical layout that gives an idea of the involved geometry for the cavity and of the mechanical connection between the 3D MOT coils and the cavity plane. Essentially, the cavity is composed of four mirrors placed at the corners of a square of 90 mm diagonal. Some of the mirror mounts can be actuated under vacuum for a precise alignment on the atoms.

2.3 Imaging system

The strong interaction of Rb atoms with optical light is of great interest. It allows for all the trapping and cooling process previously mentioned but can also be used to image the atoms. When a laser that is resonant with an atomic transition is shined on the atomic cloud, it is partially absorbed by the atoms, and a shadow appears on the transmitted beam. Recording this shadow is called an absorption imaging. The optical system which images this atomic shadow on the CCD is presented in section 2.3.0.5. Another possibility to record an image of the sample is to collect the light scattered by the atoms, hence realizing a fluorescent imaging.

2.3.0.5 Imaging system

Our imaging system can be used with two different overall magnifications $\times 1$ and $\times 4$ which are described in figure 2.18a. The first stage of the optical system is a side object tele-centric

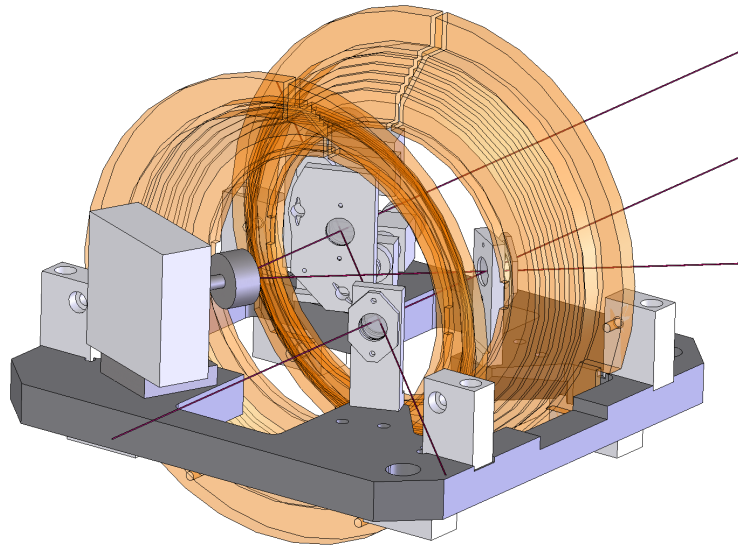


Figure 2.17: *Mechanical design of the cavity*

Four mirrors hold at the corners of a 90 mm diagonal square. The mirror mounts are referenced to a 15 mm thick titanium plate on which are also fixed the coils

telescope described in the next paragraph. The first lens of the telescope is placed at 220 mm from the atomic ensemble. The image created by the telescope is taken by a microscope objective x5 or x20 (Zeiss, mod. Fluar) which are infinity-corrected followed by a microscope lens tube which images the atomic cloud on the sensor of the camera (Apogee). Using the x5 objective, the point spread function of the system is limited by the microscope objective x5 to about $\varnothing = \frac{2.44\lambda}{NA} = 38 \mu\text{m}$ in the object plane ($NA=0.05$) and the depth of field is $312 \mu\text{m}$. Using the x20 objective, the point spread function of the system is limited by the telescope to about $\varnothing = 13 \mu\text{m}$ in the object plane ($NA=0.13$) and the depth of field is $46 \mu\text{m}$. The adjustment of the focus is realized by micro-positioning the microscope objective.

Telecentric objective

The two-side tele-centric telescope (Schneider optics, mod. Xenoplan1:5) has been characterized on the Zygo laser interferometer of the Institut d'Optique, Graduate School. The telescope has an input numerical aperture of 0.13 (output $NA = 0.65$) and a magnification of 1/5 with a working distance of $270 \pm 75 \text{ mm}$. As shown on figure 2.19, the telescope is actually diffraction limited on all its numerical aperture. The test has been realized at 632 nm with $NA = 0.125$. The Strehl factor of this telescope is 0.945 on axis, 0.937 out of axis by 2 degree and 0.997 for half the full NA and out of axis by 2 degree.

Technical notes:

- Telecentric telescope Xenoplan 1/5 : NA 0.13, working distance (WD) $270 \pm 75 \text{ mm}$.
- Microscope objective Zeiss Fluar x5 : NA 0.25, WD 12.5 mm, Transmission (T) > 85%.
- Microscope objective Zeiss Fluar x20 : NA 0.75, WD 0.6 mm, Transmission (T) > 90%.

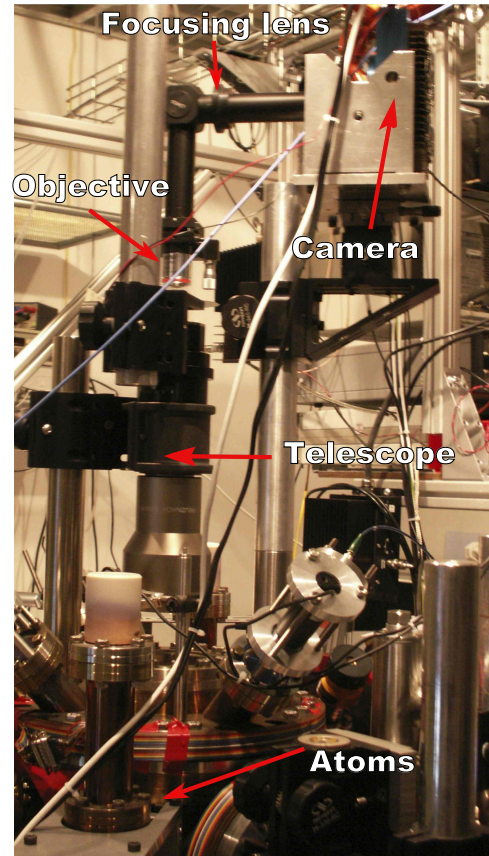
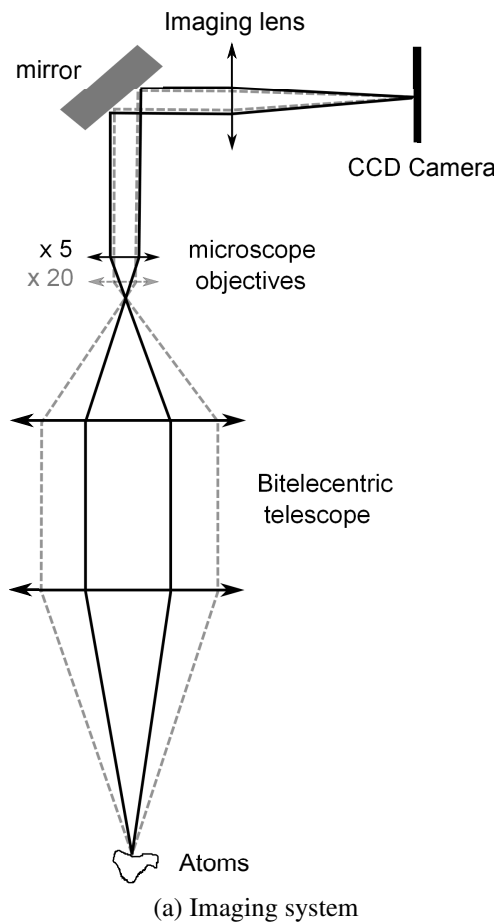


Figure 2.18: *Imaging system.*

The imaging system is made of a telecentric objective that transports the image out of the vacuum chamber. The image created is conjugated with the CCD plane by a microscope objective. This configuration allows to switch easily from an overall magnification of 1 to 4 simply by changing the microscope objective.

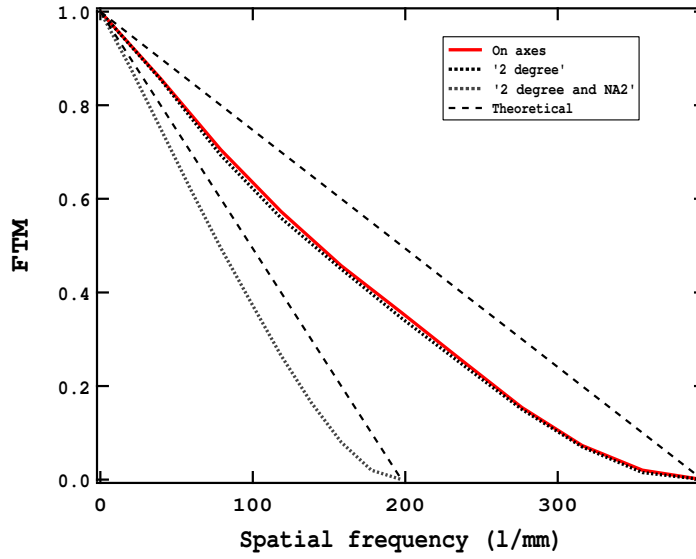


Figure 2.19: *Modulation Transfer Function of the telescope.*

The dashed line are theoretical prediction and the dotted and plain lines are measurement realized on axis and 2° off axis. The MTF of the telescope shows that it is very close to be diffraction limited on all its aperture.

- Lens tube edmund optics : focale 164.5 mm, WD 120 ± 10 mm.

2.3.0.6 Absorption imaging

In most of the experiment described in the following, the detection of the atoms is realized with an absorption imaging. This technique measures the local optical density of the cloud integrated along one direction z .

The atomic cross section for atoms on the cycling transition ($|F = 2, m_F = 2\rangle \rightarrow |F_p = 3, m_F = 3\rangle$) is given by [Steck 10]:

$$\sigma = \frac{3\lambda^2}{2\pi} \frac{1}{1 + \left(\frac{2\delta}{\Gamma}\right)^2 + I/I_{sat}} \quad (2.6)$$

where $\Gamma = 2\pi \cdot 6.066 \cdot 10^6 \text{ rad.s}^{-1}$ is the natural linewidth, $I_{sat} = 1.67 \text{ mW.cm}^{-2}$ is the saturation intensity, and δ the angular frequency detuning of the probe with respect to the atomic transition.

In our experiment, the quantization axis is not well determined. Hence it is not possible to define a σ + polarization of the light and the absorption cross section is reduced by a factor 2.13 [Steck 10].

Using a Beer Lambert law for the intensity, one finds :

$$I(x, y) = I_0(x, y) e^{-\sigma \int \rho(x, y, z) dz} \quad (2.7)$$

$$\rho = \frac{N_0}{(2\pi)^{3/2} \sigma_x \sigma_y \sigma_z} e^{-\left(\frac{x^2}{2\sigma_x^2} + \frac{y^2}{2\sigma_y^2} + \frac{z^2}{2\sigma_z^2}\right)} \quad (2.8)$$

where ρ is the atomic density that is assumed to have a Gaussian distribution and N_0 the number of atoms of the cloud.

After the integration over the propagation axis and the integration of the 2D image on one direction (y), one finds the optical density profile:

$$\int \ln \left(\frac{I(x, y)}{I_0(x, y)} \right) dy = -\sigma \frac{N_0}{\sqrt{2\pi}\sigma_x} e^{-\left(\frac{x^2}{2\sigma_x^2}\right)} = \sum \ln \left(\frac{I(x, y_i)}{I_0(x, y_i)} \right) \delta y \quad (2.9)$$

where δy is the pixel size.

Fitting the projected image, one obtains the number of atoms N_0 as well as the size of the atomic cloud (σ_x).

The evolution of the size of the cloud after a time-of-flight is governed by the initial momentum distribution of the atoms in the cloud and characterizes the temperature of the cloud:

$$\sigma_x^2(t_{tof}) = \sigma_x^2(t_{tof}) + \frac{k_B T}{m} t_{tof}^2 \quad (2.10)$$

This expression is valid for sufficiently diluted cloud ($\rho a^3 \ll 1$) and for non degenerated samples with a Maxwell-Boltzmann distribution. ρ is the atomic density and $a = 5.77$ nm the s-wave scattering length.

2.4 Summary

In this chapter, we have presented the main technical characteristics of the experimental apparatus.

We have described the extended cavity diode laser used in the experiment and shown the different locking circuit that have been realized. The reference laser is the repumper laser which is locked by saturation spectroscopy. The other lasers are locked to the repumper using beatnote techniques in a versatile way. An optical bench to drive two photons Raman transitions and involving a phase lock has also been realized.

The vacuum system consists of a titanium made 2D MOT chamber and a non-magnetic stainless steel science chamber where the high finesse cavity sits. Special coils have been designed to be mounted under vacuum.

The imaging set-up has been designed and implemented to be situated at 30 cm from the atomic sample while keeping a high numerical aperture (NA=0.13). The system has been characterized and is diffraction limited for this numerical aperture.

CHAPTER 3

The high finesse cavity

Contents

3.1	The considered geometries	46
3.1.1	Different possible geometries... but a common description	46
3.1.2	Triangle and star geometry	47
3.2	The Butterfly geometry	52
3.2.1	The a priori cavity properties	52
3.2.2	The gaussian mode : TEM_{00}	55
3.2.3	Cavity alignment	61
3.2.4	Transverse mode study, an indication of the anisotropy	64
3.2.5	Measurement of the optical profile	65
3.2.6	Cavity parameters at 1560 nm.	74
3.2.7	Losses of the cavity	75
3.3	Locking of the 1560 nm laser to the cavity	78
3.3.1	The cavity: a low pass frequency filter	78
3.3.2	Pound Drever Hall Method	79
3.3.3	Locking a Koheras fiber laser to the cavity	82
3.3.4	Opto-mechanical injection of the cavity	83
3.4	Summary	83

The high finesse cavity is at the heart of our experimental apparatus and is its peculiar element. The four mirrors geometry in a crossed configuration makes it quite specific to trap atoms. Since it is a novel geometry for cold atoms experiment, a care has been given to properly understand its characteristics. The cavity has been chosen to be resonant both at 1560 nm and 780 nm. The radiation injected in the cavity at 1560 nm has the purpose to trap the atoms in a far off-resonance optical dipole trap (FORT). As the waist chosen for the optical mode geometry are about 100 μm , a finesse of a few thousands is enough to create a trap with a depth of a mK using laser power that are only in the range of 1 W. On the contrary the 780 nm resonance that is used to enhance the quality of the nondemolition measurement, should in principle always benefit from a higher finesse (see for example section 5.3.4.2 or 6.3 or [Lye 03]). In that context, we searched for a manufacturer that could make the highest finesse possible at 780 nm (~ 100000) with the constraint of keeping a finesse of a few thousands at 1560 nm.

The choice of a trapping with a radiation at 1560 nm that is the double of 780 nm was not fortuitous and was led by the idea to reference the 780 nm cavity resonance to the ^{87}Rb lines using the 1560 nm lock. This locking of the cavity length that is still prospective in our current

set-up is detailed in section 6.3. In this perspective, locking the cavity length at a frequency for which the finesse is "low" may seem problematic to perform a measurement at a high finesse (low linewidth) frequency. Actually if it is true that the absolute frequency stability of a lock is proportional to the cavity finesse, it is important to remember that it is also proportional to the square root of the optical power used to extract the error signal. Hence in our present case (see section 6.3 for details), the low frequency at 1560 nm can be compensated by a higher optical power which should in principle allow to approach the optimal situation where all the cavity length fluctuations are cancelled.

In this chapter, we will present a detailed study which has been led on the cavity. At first, we will discuss the intrinsic properties of the geometries that have been considered for the experiment. We will then focus and describe in detail the features of the chosen configuration and its experimental realization. We introduce at first the formalism for the description of optical cavities and apply it to derive the fundamental mode profile as well as the stability conditions. The expected and measured spectrum of the transverse modes are then compared and give informations on the astigmatism in the cavity. The fundamental mode of the cavity that is used for the trapping of atoms is characterized via an indirect measurement of the divergence of the output mode, but also via an in-situ nondemolition measurement that uses the atoms as a sensor. At last we detail the locking procedure that has been realized.

3.1 The considered geometries

In this section, we present the three geometries that have been foreseen in the experiment. We first give some qualitative arguments to understand their behavior, and briefly describe the experimental characterizations that were led before our final choice was made (section 3.1.2). The description of the butterfly cavity that has been finally implemented is given in detail in section 3.2.

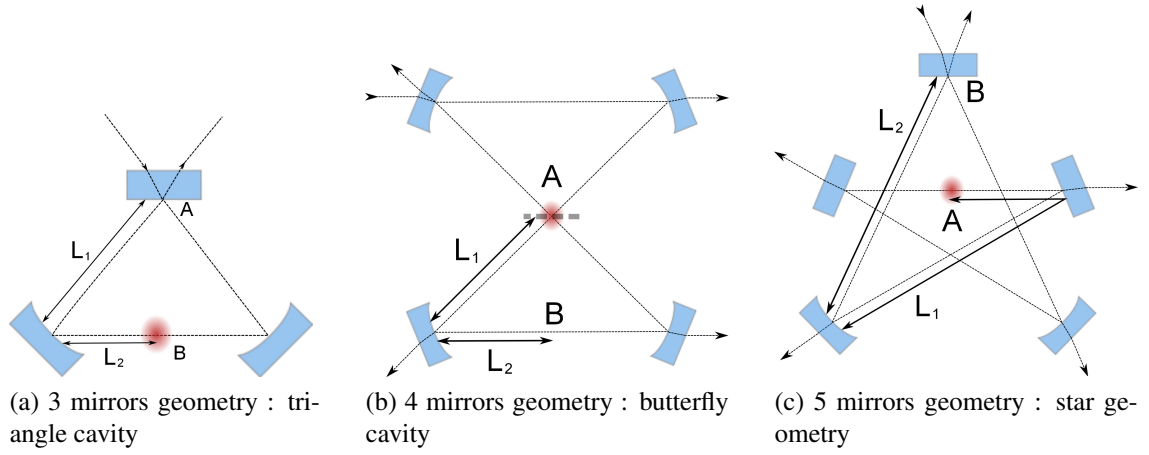
The geometries were analyzed in regard of the following requirements:

- the ability to switch between running and standing waves in the resonator. Hence, linear cavity were excluded of the discussion,
- the possibility to reach high confinement in the dipole trap which involves to aim at small cavity mode waists. The confinement of a trap plays a crucial role to reach a high atomic density and then to start the evaporation process that leads to the condensation,
- the optimization of the loading of atoms from the MOT to the dipole trap. This is obtained by creating a good overlap between the MOT volume and the cavity mode with the use of large cavity mode waist, that is contradictory with the previous point.

These requirements led us to study the geometries presented in the following section and to look for the best compromise possible.

3.1.1 Different possible geometries... but a common description

Given the requirement of high confinement and our will to use traveling waves, we compared the 3 mirrors geometry (figure 3.1a, called triangle), the 4 mirrors geometry (figure 3.1b, called butterfly), the 5 mirrors geometry (figure 3.1c, called star). The position of the atoms in these different geometries is represented by the red spot.

Figure 3.1: *Geometry considered for the cavity*

In the following of this section, we forget about the astigmatism of the cavity that will be discussed in section. 3.2.2.2.

As the plane mirrors are only folding the space, it is clear in figure 3.1 that the star geometry and the triangle geometry are quite equivalent. But there is one major difference: in the triangle geometry, the atoms are placed at the closest waist from the curved mirrors while it is the reverse for the star geometry.

The butterfly geometry can also be brought back to the triangle case considering that the upper part of the cavity is the symmetric of the lower one. A plane mirror placed at the center would preserve the mode geometrical properties.

Studying the stability of the 3 mirrors configuration, one can see that there exists actually two different stability regimes that lead to an inverted ratio of the waist in A and B:

- $f = \frac{R}{2} > L_1$. In that condition, the waist in A is smaller than in B. This condition would be the one to apply for 3.1b and 3.1c to have the tightest confinement on the atoms.
- $f = \frac{R}{2} < L_2$. In that condition, the waist in B is smaller than in A. This condition would be optimal for 3.1a.

More generally, it can be intuitively understood by the fact that the waist in A and B are reciprocally imaged by the curved mirrors. The smallest waist is the one whose distance from the curved mirrors is closer to the focal length.

3.1.2 Triangle and star geometry

In this section, we describe the coupling efficiency that can be reached in the triangle and star geometries, and determine the finesse of such cavities.

3.1.2.1 Coupling efficiency

Looking to the stationary equation for the propagation of the electric field at each interface, we calculate the inner and transmitted field in the cavity. In the following, the results will be

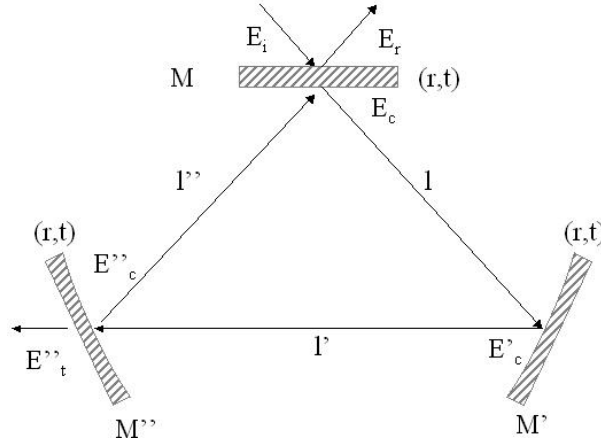


Figure 3.2: Notation for the electric field in the cavity.

The reflection and transmission r and t are considered to be identical for all the mirrors.

presented in two columns. The first describes the triangle geometry and the second the star geometry.

Definition:

The field amplitude reflexion, transmission and losses of the mirrors are noted r , t and κ respectively. The cavity reflection and transmission are noted (R, T) in amplitude and $(\mathcal{R}, \mathcal{T})$ in intensity. We note \mathcal{E}_i and \mathcal{E}_r the complex amplitude of the incident and reflected electric field on the mirror M and \mathcal{E}_c the complex amplitude in the cavity (see figure 3.2).

In the stationary limit, we have:

Triangle cavity	Star cavity
$\mathcal{E}_c = t \mathcal{E}_i + r^3 \mathcal{E}_c e^{ikL}$ $\mathcal{E}_r = tr^2 \mathcal{E}_c e^{ikL} - r \mathcal{E}_i$	$\mathcal{E}_c = t \mathcal{E}_i + r^5 \mathcal{E}_c e^{ikL}$ $\mathcal{E}_r = tr^4 \mathcal{E}_c e^{ikL} - r \mathcal{E}_i$

(3.1)

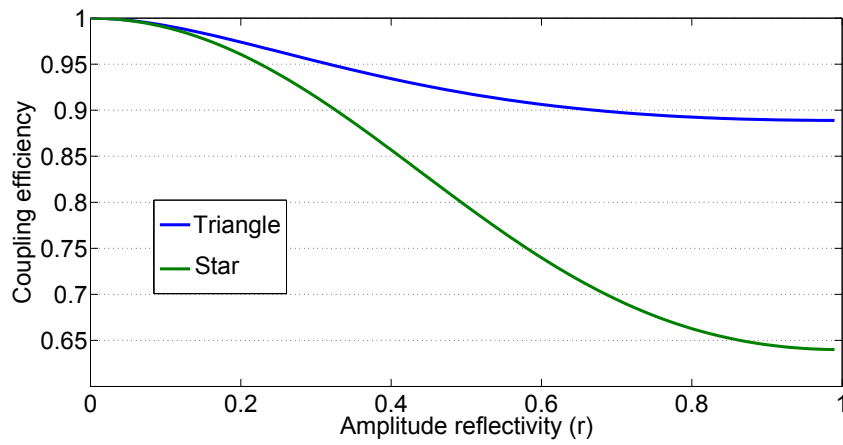
Solving these equations, one finds the reflectivity (\mathcal{R}) and transmission (\mathcal{T}) coefficients, which should verify $\mathcal{R} + \mathcal{T} = 1$ for a lossless cavity.

Triangle cavity	Star cavity
$\mathcal{R} = \left \frac{\mathcal{E}_r}{\mathcal{E}_i} \right ^2 = r^2 \frac{1+r^2-2r \cos(kL)}{1+r^6-2r^3 \cos(kL)}$ $\mathcal{T} = \left \frac{\mathcal{E}_t}{\mathcal{E}_i} \right ^2 = \frac{t^4 r^2}{1+r^6-2r^3 \cos(kL)}$	$\mathcal{R} = r^2 \frac{1+r^6-2r^3 \cos(kL)}{1+r^{10}-2r^5 \cos(kL)}$ $\mathcal{T} = \frac{t^4 r^6}{1+r^{10}-2r^5 \cos(kL)}$

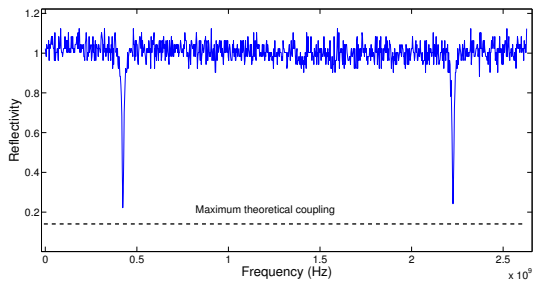
(3.2)

The coupling efficiency (\mathcal{C}) is defined as the part of the energy which is not reflected, i.e. $\mathcal{C} = 1 - \mathcal{R}$. It can be experimentally easily estimated by measuring the reflected power in and out of resonance.

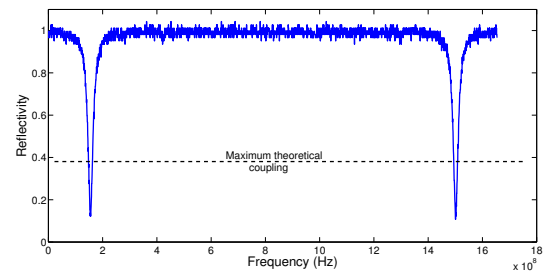
From 3.3a, the coupling efficiency increases for a decreasing reflectivity. Indeed, in the low reflectivity limit, we are approaching the free space condition where all the light is transmitted (no mirrors), i.e. the coupling converge to 1.



(a) Coupling efficiency as a function of the reflectivity of the mirror.



(b) Reflectivity of the triangle cavity.



(c) Reflectivity of the star cavity.

Figure 3.3: *Reflectivity of the cavities in p polarisation*

The theoretical limit to the coupling efficiency is presented in dashed line on the figures.

In the high mirror reflectivity limit, figure. 3.3a shows that the more mirrors are involved, the lower the coupling efficiency. In the case of the Fabry-Perot cavity, the coupling efficiency is 100% whatever the mirrors reflectivity. This happens because the transmission of the first mirror perfectly matches the reflection of the second mirror. In other terms, the contrast of the interference on the first mirror is full: the cavity is impedance matched for the propagation of light. For additional mirrors added in the cavity, the contrast of the coupling interference on the first mirror is lowered and part of the light is reflected. In our experimental realization, this property was well verified for the triangle geometry but not for the star geometry that exhibits a higher coupling than expected (see figure. 3.3c). Our explanation holds on the angle of incidence on the mirrors and on the calculation that assumes identical reflectivity for the mirrors. The mirrors used were treated to have an optimal reflection for an angle of incidence of 0° . In the case of the star geometry realized experimentally, the input mirror had an angle of incidence of 45° while the others had about 20° . The high angle of incidence on the in-coupling mirror probably lowers its reflectivity, and allows to approach the case of impedance matching ($r_1 \approx r_2 \cdot r_3 \cdot r_4 \cdot r_5$).

The coupling efficiency obtained experimentally for the triangle and star geometries were respectively 80% and 87%.

3.1.2.2 Finesse

Another important characteristic of a cavity is its ability to store the light, or in other terms the average number of turns that a photon realizes before it exits the cavity. This parameter is called the finesse of the cavity. The finesse is related to the average propagation distance in the cavity over the length L of the cavity. It is also the ratio of the frequency distance between two adjacent longitudinal modes (Free Spectral Range - FSR) over the width of the cavity transmission.

$$\mathcal{F} = \frac{\Delta\nu_{FSR}}{\delta\nu_{cav}}, \quad (3.3)$$

where $\Delta\nu_{FSR} = c/L$ is the FSR frequency, and $\delta\nu_{cav}$ is the spectral width of the cavity transmission, which is linked to the coherence length of the cavity and is inversely proportional to the decay time τ of the cavity.

In equation 3.2, the denominator D defines the width of the cavity resonance ($\delta\nu_{cav}$) and can be rewritten as:

$$\boxed{\begin{array}{l} D = (1 - r^3)^2(1 + m_1 \sin^2(kL/2)) \\ m_1 = \frac{4r^3}{(1-r^3)^2} \end{array} \quad \begin{array}{l} D = (1 - r^5)^2(1 + m_2 \sin^2(kL/2)) \\ m_2 = \frac{4r^5}{(1-r^5)^2} \end{array}} \quad (3.4)$$

The linewidth of the cavity is measured at half width at half maximum (HWHM) of the resonance line and corresponds to the condition:

$$k \frac{L}{2} = \frac{\pi L}{c} \left(\nu \pm \frac{\delta\nu_{cav}}{2} \right) \approx p\pi \pm \frac{1}{\sqrt{m}}. \quad (3.5)$$

The cavity linewidth and the free spectral range are then given by:

$$\delta\nu_{cav} = 2\pi \frac{2c}{\sqrt{m}L\pi}, \quad (3.6)$$

$$\Delta\nu_{FSR} = 2\pi \frac{c}{L}. \quad (3.7)$$

Combining these two results, one obtains the finesse in the form:

$$\mathcal{F} = \frac{\pi}{2} \sqrt{m} \quad (3.8)$$

Such a definition of the finesse shows that it is an increasing and unbound¹ function of the reflectivity. Even if the coupling efficiency gets down with reflectivity, it is always profitable to increase the reflectivity of the mirror if the losses of the cavity can be neglected. Considering the specifications of the mirrors, the finesse were calculated to be 417 and 250 for the triangle and star cavities respectively. Their experimental measurements gave 60 for both geometries. This discrepancy is essentially attributed to the mirrors that were not taken at their specified angle of incidence (AOI).

Remark: The cavities have also been tested in s polarization (\perp to the cavity plane) for which they give finesse of 160 and 105 with coupling efficiency of 41% and 28% for the triangle and the star geometries respectively. This polarization dependence of the mirrors is linked to the nonzero angle of incidence that allows to differentiate the two polarizations (Fresnel coefficients).

3.1.2.3 Optical beam dimensions

We focus now on the size of the single trapping beam of the triangle and star geometries. All the relevant definitions for Gaussian beams are given in section 3.2.2.1.

To perform an evaporation in a atomic trap requires high atomic densities. To reach these densities, a tight trapping of the atoms has to be obtained. In the case of an optical dipole trap, the trapping frequencies are mostly determined by the beam size which should be typically below 200 μm . Hence, for a tight trapping in the transverse direction, the waist (w) should be less than 200 μm . The characteristic length for the confinement in the longitudinal direction of a Gaussian beam is called the Rayleigh range $z_R = \pi w^2 / \lambda$. To respect the same condition on the dimension in the longitudinal direction, *i.e.* $z_R < 200 \mu\text{m}$, the waist of the beam would actually be limited to 10 μm at 1.56 μm . This waist dimension would be a priori technically feasible but would require to operate the cavity close to the unstable limit of the concentric geometry. Indeed, in this limit, the waist at the center of the cavity approaches the diffraction limit ($w \approx \lambda/2$). There are nevertheless some drawbacks to such a situation.

- Beams with small waist, are highly diverging $\theta \propto \lambda/w_0$. Hence, the mirrors need to be close to the cavity center so that they can be used under high numerical aperture while preserving the beam from aberrations. This proximity of the mirrors constrains the optical access needed for all the cooling and trapping operation. In that perspective, the star configuration has the advantage to have its tightest waist the furthest from the mirrors.
- To operate a cavity close to an instability limit is technically difficult since the length of the cavity becomes a very critical parameter. For example, during the bake out the system for degassing, the cavity length may change so that the cavity becomes unstable.

¹Only true in a lossless cavity as will be discussed in 3.2.7

- When considering to obtain a quantum degenerate sample in a cavity, a crucial parameter is to reach high densities. For that, not only the trapping frequencies are important parameters but also the number of atoms loaded from the MOT into the dipole trap formed by the cavity mode. Regarding this second constraint, a dipole trap with a waist of $10\text{ }\mu\text{m}$ is completely unadapted to load atoms from a MOT that has typical dimensions of a few hundred μm .

Considering these geometrical arguments, we converged to the crossing cavity geometry (see figure 3.3b) in which the Rayleigh range does not play any role. The strong constrain on the waist dimension, *i.e.* $w \approx 10\text{ }\mu\text{m}$, is then removed. This geometry allows at the same time for high trapping frequencies in all directions, and for a high volume of capture with waist of the cavity beam that can be about $100\text{ }\mu\text{m}$. On the other hand, this geometry has the drawback that interferences between the two arms can appear in the crossing region. The pattern of the interference is linked with the position of the mirrors and will then shake with acoustic noise, inducing heating of the atomic sample. To avoid the interference, we use light polarized in the plane of the cavity and we finely adjust the angle between the two crossing arms to 90° . A second drawback is due to the fact that for the butterfly cavity all the waists are positioned inside the cavity while the triangle and star cavities have waists on the plane mirrors. This geometrical difference makes mode matching more difficult to achieve.

3.2 The Butterfly geometry

In this section we present a detailed analysis of the cavity used in the experiment. We give its mechanical design and describe the geometrical properties of the mode and the spectral response of the cavity. A last part is dedicated to present the locking scheme of the $1.5\text{ }\mu\text{m}$ laser to the cavity.

3.2.1 The a priori cavity properties

3.2.1.1 Geometry and mechanical design

The cavity adopted for this experiment is a four mirror cavity with two arms crossing at its center as presented in figures 3.1b and 3.4a.

The cavity, shown in 3.4, is made up of four mirrors placed at the corners of a square with a diagonal of 90 mm . All the mechanical components of the cavity are realized in titanium to maintain a low magnetic environment for the trapped atoms. The size of the cavity results from a compromise to maximize the optical access while minimizing the cavity mode to ensure a tight trapping. For a polarization in the cavity plane, the square geometry enables a 90° crossing angle which avoids an interference pattern in the crossing region. The mirrors are all identical and are plane-concave with a radius of curvature $R = 100\text{ mm}$. They have a diameter of $1/2\text{ inch}$. With the notations of figure 3.1b, we are in a configuration where $L_1 \sim f = R/2$ which corresponds to a concentric cavity. Considering in addition the astigmatism, we are actually very close to the concentric cavity case for the horizontal direction (see figure 3.14).

All the parts are tightly mounted on a 15 mm thick titanium plate, which gives its stability to the mechanical design. Two mirror mounts allow an axial degree of freedom (θ_y) for air

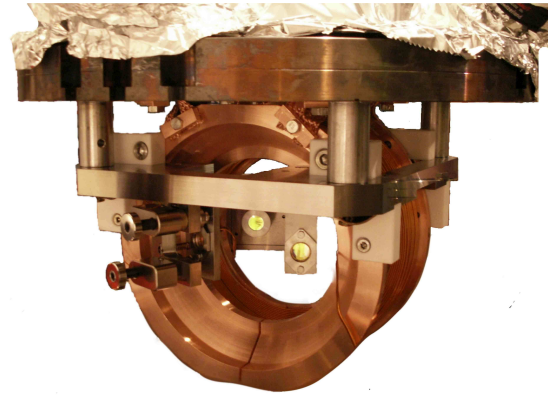
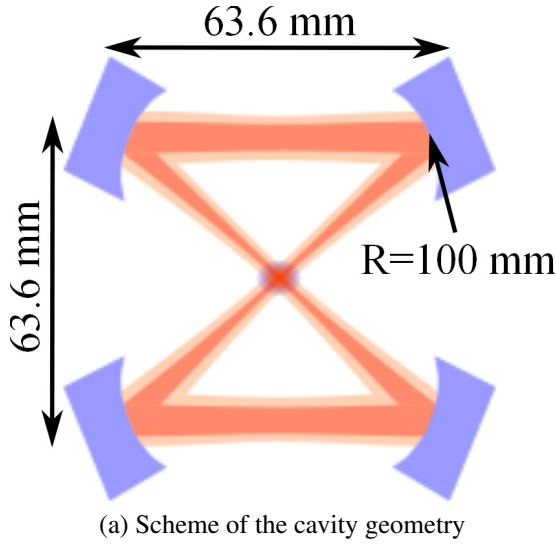


Figure 3.4: *The crossed cavity configuration*

The cavity is a square of 90 mm diagonal, and all the mirror mounts are mechanically referenced to titanium supporting plate. Under vacuum, two mounts are completely fixed whereas the two others can be piezo actuated. One mount realizes the coarse alignment and the other one gives the fine adjustment of the cavity length.

alignment but are completely fixed once under vacuum 3.5a. One mount (figure 3.5b) is hold with an exact constraint design (point-line-plane), in which the screws are newfocus picomotors (Newfocus, mod.4301). These linear actuator can be driven under vacuum and allow for a coarse alignment of the cavity, necessary to vertically overlap the two crossing arms. The last mount (figure 3.5c) is adapted from a nano positioning system (Madcitylabs, mod. M3Z) ; it is a 3 axis (θ_x, θ_y, z) piezo actuated titanium mount with maximal angular displacement of 2 mrad and translation of 50 μm . It allows for a fine adjustment of the cavity crossing angle and for a dynamical control of the cavity length (20 Hz - bandwidth).

To fix the mirrors in these mounts, the mirrors are inserted in an adjusted hole and compressed onto a front reference plane. In each mount a care was given to mechanically reference this front plane. Following the study presented in section. 3.2.3.2, the position tolerance was fixed to $T_0 = 100 \mu\text{m}$ and an angle tolerance of $\theta = 100 \mu\text{rad}$ was accepted

To avoid mechanical distortion on the mirrors, special o'ring string have been designed and fabricated in Bronze-Beryllium which is a non-magnetic and elastic material. These o'ring compress the mirror from the back (see figure 3.5a).

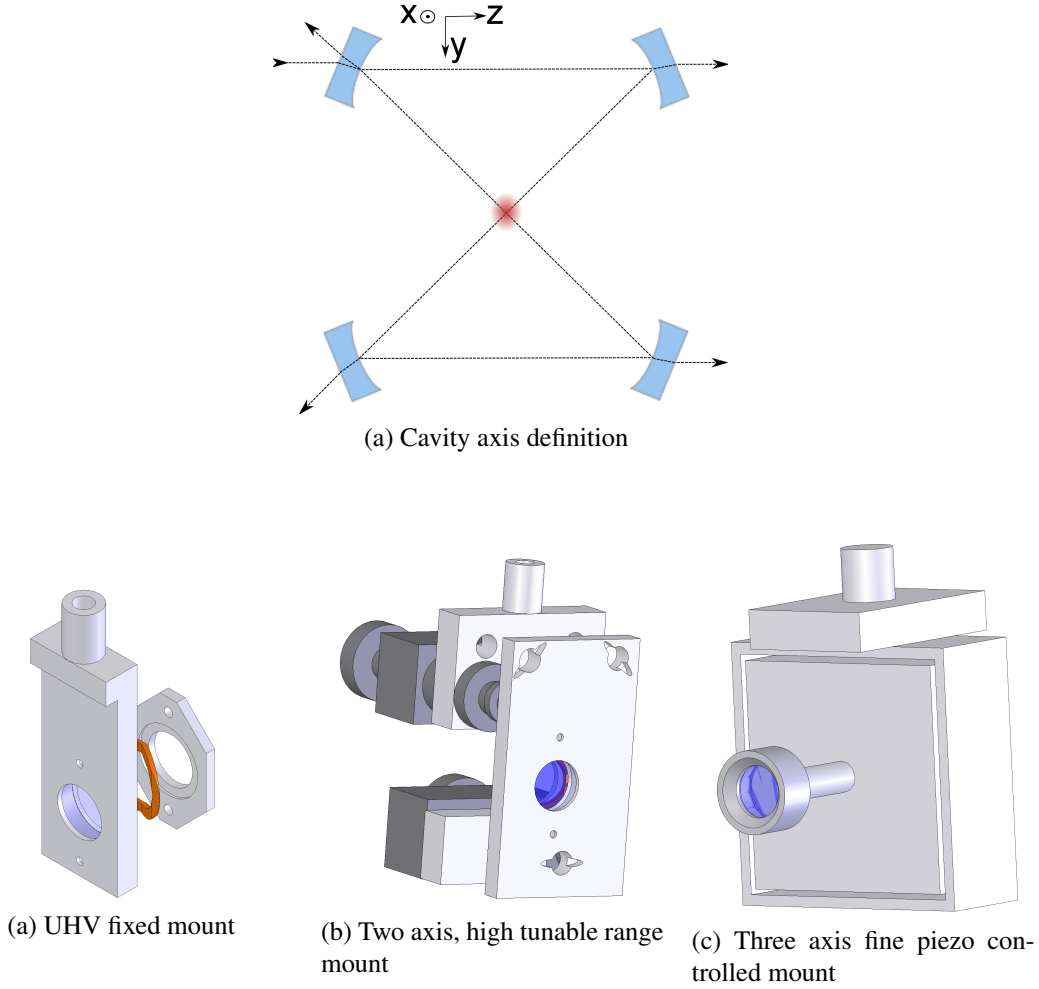


Figure 3.5: *UHV mirror mount mechanics.*

Under vacuum, two mounts are completely fixed (a). Among the two others, one is actuated by picomotors and gives a coarse alignment of the cavity whereas the other is actuated by piezo element and give a continuous and fine adjustment.

3.2.1.2 Mirror datasheet

The high reflectivity mirrors were ordered from ATFilms. On the back side, the surface is plane and is anti-reflection coated at both 1560 nm ($r^2 = 0.03419\%$) and 780 nm ($r^2 = 0.07929\%$). The front is a concave surface with 100 mm radius of curvature. It has a superpolish finish (roughness $< 5 \text{ \AA}$). The transmission of the front side is $t^2 = 0.03776\%$ at 1560 nm and $t^2 = 0.001545\%$ at 780 nm.

These are manufacturer measured data on a dark background, i.e. the high quality reflexion is measured by the transmission leaks.

3.2.1.3 Coupling efficiency and finesse expression

The formalism used in 3.1.2 is applied to model the coupling mechanism of the field in the cavity. In a stationary limit, one has:

$$\mathcal{E}_c = t \mathcal{E}_i + r^4 \mathcal{E}_c e^{ikL}, \quad (3.9)$$

$$\mathcal{E}_r = tr^3 \mathcal{E}_c e^{ikL} - r \mathcal{E}_i. \quad (3.10)$$

This leads to a field $(R(\omega), T(\omega))$ and intensity $(\mathcal{R}(\omega), \mathcal{T}(\omega))$ coefficients of the form:

$$\begin{aligned} R = \frac{\mathcal{E}_r}{\mathcal{E}_i} &= \frac{t^2 r^3 e^{ikL}}{1 - r^4 e^{ikL}} - r & \mathcal{R} &= \left| \frac{\mathcal{E}_r}{\mathcal{E}_i} \right|^2 = \frac{r^2}{1 + r^8 - 2r^4 \cos(kL)} \\ T = \frac{\mathcal{E}_t}{\mathcal{E}_i} &= t \frac{\mathcal{E}_c}{\mathcal{E}_i} = \frac{t^2}{1 - r^4 e^{ikL}} & \mathcal{T} &= \left| \frac{\mathcal{E}_t}{\mathcal{E}_i} \right|^2 = \frac{t^4}{1 + r^8 - 2r^4 \cos(kL)} \end{aligned} \quad (3.11)$$

where $k = \omega/c$ is the wavevector of the light.

The maximal coupling that can be achieved if all the mirrors are identical is:

$$\mathcal{C} = 1 - \mathcal{R}(\omega) = 1 - r^2 \frac{1}{(1 + r^2)^2} \approx 75\%. \quad (3.12)$$

As in section 3.1.2.2, the denominator D of equation 3.11:

$$D = (1 - r^4)^2 (1 + m \sin^2(kL/2)), \quad (3.13)$$

where:

$$m = \frac{4r^4}{(1 - r^4)^2}, \quad (3.14)$$

leads to the expression of the finesse:

$$\mathcal{F} = \frac{\pi \sqrt{m}}{2} = \frac{\pi r^2}{1 - r^4} = \mathbf{4160} \text{ at } 1560 \text{ nm} \quad \text{and} \quad \mathcal{F} = \mathbf{101\,668} \text{ at } 780 \text{ nm}. \quad (3.15)$$

The value given in 3.12 and 3.15 are theoretical values calculated from the specifications. They have to be compared to the measured ones which are presented in section 3.2.6.

3.2.2 The gaussian mode : TEM₀₀

Gaussian profiles and more generally Hermite-Gauss or Laguerre-Gauss beams are very useful in optics. They have the property to be self consistent, which means that during their propagation, they change size but not shape. In addition, it is possible to prove with Huygens integral formalism [Nicolas 05], that they also conserve their shape while going through a linear optical system.

3.2.2.1 Definition of the cavity modes

In this section, we will give some definitions and formulas relevant to the context of this manuscript. All the following formulas on Gaussian beams can be derived directly from the Helmholtz equation of propagation of field in free space:

$$\left(\nabla - \frac{1}{c^2} \frac{\partial^2}{\partial t^2} \right) E(\mathbf{r}, t) = 0. \quad (3.16)$$

In the case of a time separable electric-field $E(\mathbf{r}, t) = A(x, y, z) e^{i(\omega t - \mathbf{k} \cdot \mathbf{z})}$, the wave equation 3.16 simplifies to its equivalent on the field spatial amplitude:

$$(\nabla + k^2) A(x, y, z) = 0. \quad (3.17)$$

In the paraxial approximation ($\frac{\partial A}{\partial z} \ll kA$ and $\frac{\partial^2 A}{\partial z^2} \ll k^2 A \equiv \sin(\theta) \ll 1$), the expression 3.17 becomes:

$$\left(\nabla_{\perp} A - 2ik \frac{\partial A}{\partial z} \right) = 0. \quad (3.18)$$

If the x and y coordinates can be further separated, which is true for an astigmatic cavity, the complex amplitude of the electric field is found to be the Hermite-Gauss functions:

$$E = E_0 \frac{w_0}{w(z)} \varphi_m \left(\frac{\sqrt{2}x}{\omega(z)} \right) \varphi_n \left(\frac{\sqrt{2}y}{\omega(z)} \right) e^{\left(-i \frac{k(x^2+y^2)}{2q(z)} \right)} e^{(-ikz + i(m+n+1)\zeta(z))}, \quad (3.19)$$

where

$$\varphi(\xi) = \frac{H_m(\xi)}{\sqrt{2^m m!} \sqrt{\pi}} e^{\left(-\frac{\xi^2}{2} \right)}, \quad (3.20)$$

$$H_n(x) = e^{\frac{x^2}{2}} \left(x - \frac{d}{dx} \right)^n e^{-\frac{x^2}{2}}, \quad (3.21)$$

and H_m is the n^{th} Hermite polynomial with $H_0(x) = 1$, $H_1(x) = 2x$ and $H_2(x) = 4x^2 - 1$.

With this formalism, the fundamental mode is a Gaussian mode that takes the form of:

$$E = E_0 \frac{w_0}{w(z)} e^{\left(-i \frac{k r^2}{2q(z)} \right)} e^{(-ikz + i\zeta(z))} \quad (3.22)$$

$$= E_0 \frac{w_0}{w(z)} e^{\left(-\frac{r^2}{w^2(z)} \right)} e^{\left(-ikz - i \frac{r^2}{2R(z)} + i\zeta(z) \right)}. \quad (3.23)$$

In equations 3.19 to 3.23, we have used the following definitions:

- $q(z) = \left(\frac{1}{R(z)} - \frac{i\lambda}{\pi w^2(z)} \right)^{-1}$ is the complex curvature of the beam,
- $R(z) = z \left(1 + \left(\frac{z}{z_r} \right)^2 \right)$ is the wave front curvature,

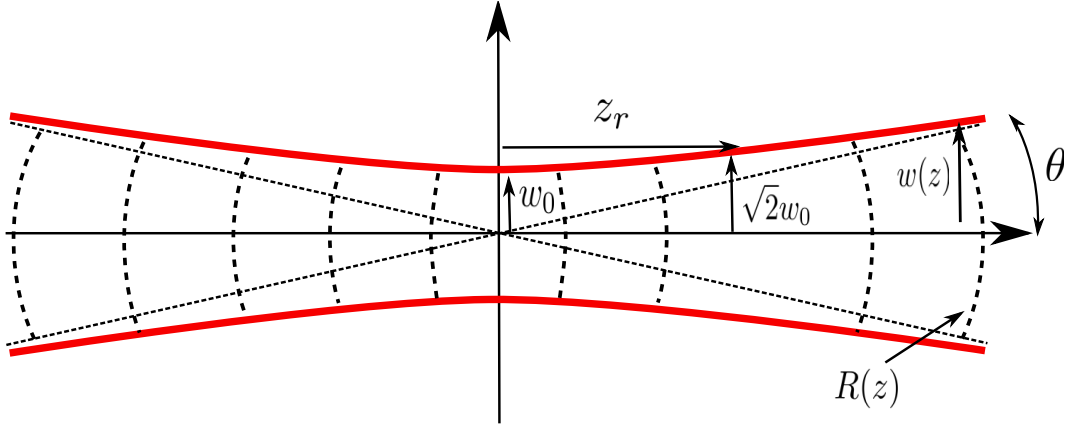


Figure 3.6: Gaussian beam profile and definitions

- w_0 is the beam waist at the focus and $w(z) = w_0 \sqrt{1 + \left(\frac{z}{z_r}\right)^2}$ the beam waist at distance z ,
- $z_r = \frac{\pi w_0^2}{\lambda}$ is the Rayleigh range,
- $\zeta(z)$ is the Gouy phase of the mode [Gouy 90b, Gouy 90a].

The intensity $I(z, r) = \epsilon_0 n c \frac{|E(r, z)|^2}{2}$ of the fundamental mode writes:

$$I(r, z) = I_0 \left(\frac{w_0}{w(z)} \right)^2 \exp \left(-\frac{2r^2}{w^2(z)} \right) \quad (3.24)$$

where I_0 stands for the maximum intensity at the center of the beam, and is linked to the power P_0 through $I_0 = \frac{2P_0}{\pi w_0^2}$

Remark 1: Harmonic oscillator

When the field complex amplitude $A(x, y, z) = B(x, z).C(y, z)$ is transversally separated, it is possible to show [Steuernagel 05] that the paraxial approximation of the Helmholtz equation is equivalent to the Schrödinger equation of the harmonic oscillator. It is then not surprising that the profile of the optical mode corresponds to the space profile of the harmonic oscillator eigenstates.

Remark 2: Useful formula for beams characterization

In the context of Gaussian beams, we give here some useful formula for the waist characterization when realizing a Foucaultage. The Foucaultage consists to cut progressively part of the beam and to measure the remaining and normalized power:

$$P_r(z) = \frac{\int_{x=-\infty}^{+\infty} \int_{y=a}^{+\infty} I(x - x_0, y - y_0, z) dx dy}{P_0}. \quad (3.25)$$

Deriving this signal, one re-obtains the Gaussian profile. For an intensity profile centered in (x_0, y_0) , and using equation (3.24), the expression 3.25 can be simplified in:

$$P_r(z) = \frac{1}{2} \left(1 + \operatorname{erf} \left(\frac{\sqrt{2}(y - y_0)}{w(z)} \right) \right), \quad (3.26)$$

where $\operatorname{erf}(z)$ is the error function defined as:

$$\operatorname{erf}(a) = \frac{2}{\sqrt{\pi}} \int_{y=0}^a \exp(-y^2) dy. \quad (3.27)$$

3.2.2.2 ABCD Matrix study

The Gaussian beams introduced in the previous section are self consistent profile, and the only parameter to be determined during their propagation is their complex radius of curvature $q(z)$.

Introduction to the ABCD formalism

The ABCD formalism introduced in [Kogelnik 66] expresses the idea that the geometrical propagation parameters (y, α) evolve linearly when the light propagates through passive optical systems (fig. 3.7a). They can thus be expressed using a matrix formalism (3.7). In the context of optics, it is called the ABCD formalism. Such a formalism makes the beam rays calculation very systematic and easy to implement.

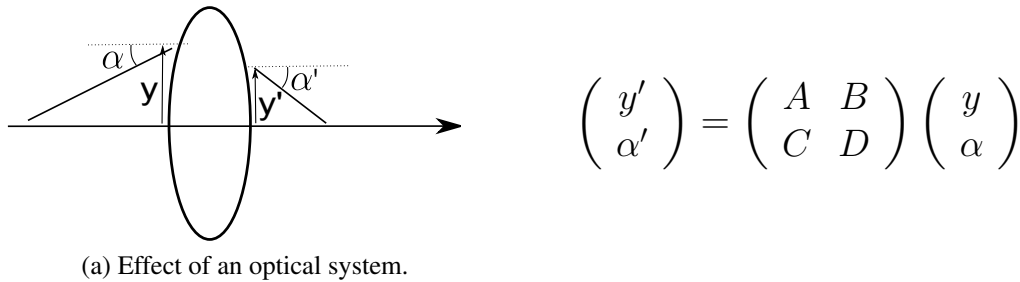


Figure 3.7: ABCD formalism

As an example, we give in 3.1 two commonly used matrices: the free space and lens matrices.

Free space	Lens
$\begin{pmatrix} 1 & L \\ 0 & 1 \end{pmatrix}$	$\begin{pmatrix} 1 & 0 \\ \frac{-1}{f} & 1 \end{pmatrix}$

Table 3.1: Commonly used ABCD matrices.

The propagation of an electric field can be calculated using the Huygens-Fresnel integral :

$$E(x', y') = \frac{i}{\lambda L} \int_{\Pi} E(x, y) \frac{\exp(-ikMM')}{MM'} dx dy \quad (3.28)$$

which describes the fact that each point in space is emitting a spherical wave.

Using the Huygens integral of equation. 3.28 on a Gaussian beam $E(x, y)$ for which the transverse direction (x', y') can be calculated from ABCD laws, it is possible to derive [Siegman 86] a formula for the evolution of the complex curvature q_f introduced in 3.2.2:

$$q_f = \frac{Aq_i + B}{Cq_i + D} \quad (3.29)$$

where A , B , C and D are the element of the propagation matrix through the system and q_i is the initial complex radius of curvature. To determine the Gaussian properties of a beam after propagation, one first calculates the ABCD matrix of the optical system by multiplying all the individual matrices and applies 3.29 to obtain the beam properties at the output.

Off axis mirrors

A concave mirror of radius of curvature R acts as a lens of focal length $f = R/2$ that also modifies the direction of the optical axis. This does not make any difference for the beam profile but allows to recycle the space.

As it can be seen on figures 3.8a and 3.8b, when a mirror is taken off axis by an angle θ , the focal distance is no more $R/2$ but depends on the direction with respect to the plane of incidence. The optical profile will have a focal $f_x = R/(2 \cos \theta)$ for the x direction (\perp to the incident plane) and $f_y = R \cos(\theta)/2$ for the y direction (\parallel to the incident plane). This is illustrated on figure 3.8 and makes the cavity strongly astigmatic. This astigmatism of the mirror purely results from geometrical considerations and is strictly equivalent to the astigmatism of a tilted lens.

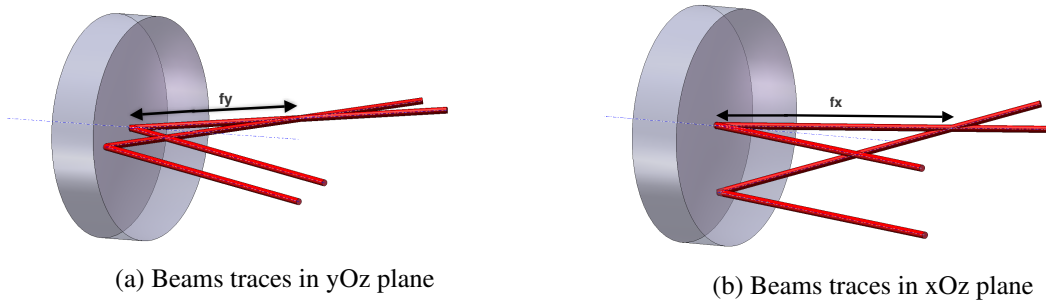


Figure 3.8: Ray traces

Off axis mirrors are astigmatic. The ray traces show that the focal (crossing) point of parallel traces depend on the direction with respect to the plane of incidence (orthogonal, xOz or parallel yOz).

yOz plane

$$f_y = \frac{R}{2} \cos(\theta)$$

xOz plane

$$f_x = \frac{R}{2 \cos(\theta)}$$

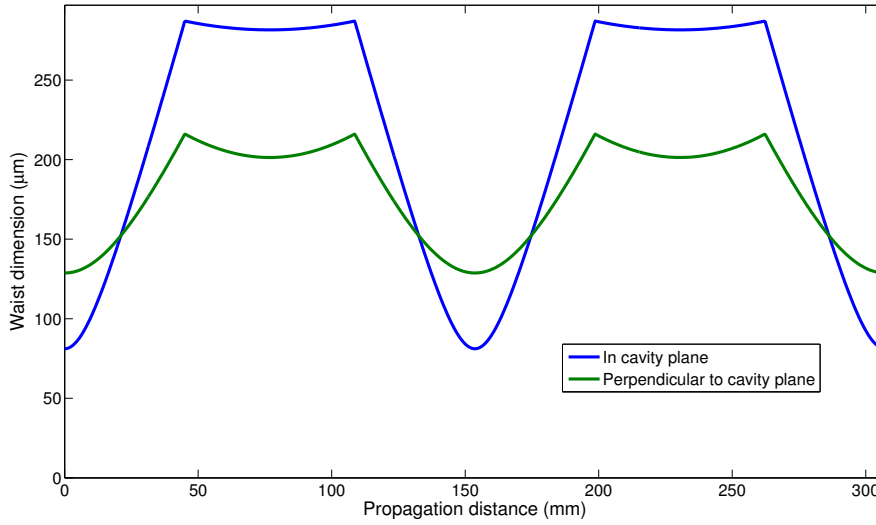


Figure 3.9: Profile of the beam along the optical axis for 1560 nm radiation.

These profile are obtained by applying the ABCD formalism in which is including the correction of focal due to the nonzero angle of incidence. The astigmatism arises from the astigmatism of off-axis reflection on curved mirrors.

Waist profile of the fundamental mode

It has been shown that the complex radius of curvature $q(z)$ could be expressed from $q(0)$ and the propagation matrix:

$$M(z) = \begin{pmatrix} A & B \\ C & D \end{pmatrix}. \quad (3.30)$$

Since the profile is auto imaged by the cavity mirrors, we have :

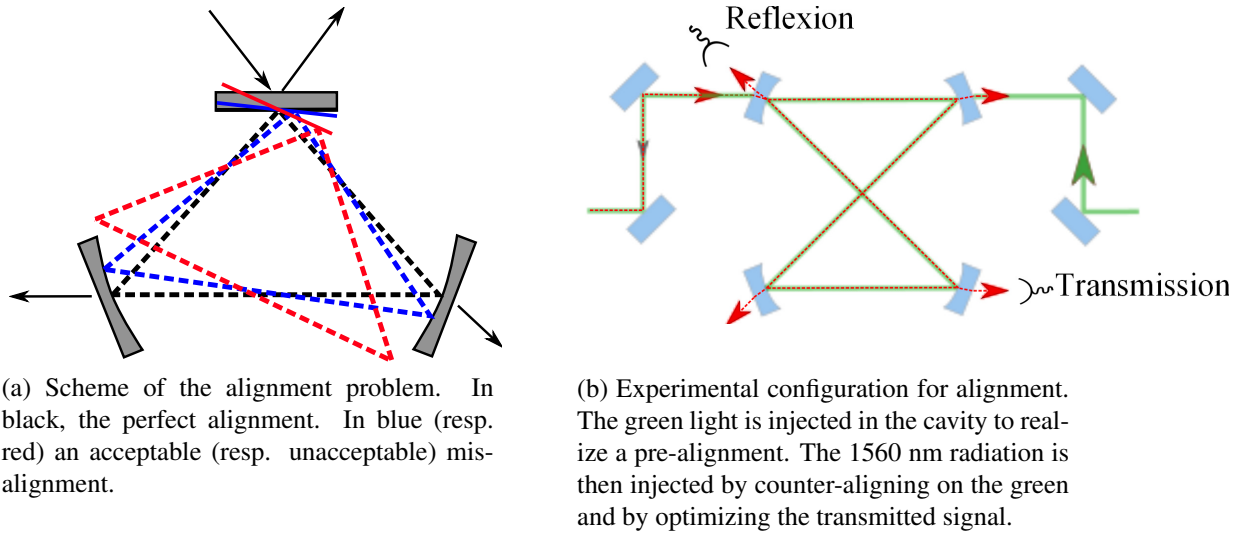
$$q(L_c) = q(0) = \frac{Aq(0) + B}{Cq(0) + D} \quad (3.31)$$

where A , B , C and D are the matrix coefficients of one round trip in the cavity starting from $z = 0$.

The expression 3.31 determines the size of the waist at any place in the cavity. Figure 3.9 shows the beam profile for the two eigen-directions of the cavity (\perp and \parallel to the cavity plane). Because the mirror focal length is smaller in the cavity plane, the cavity gets closer to instability in this direction (part 3 of figure. 3.14). As can be seen in figure 3.9, the beam waist is smaller in the cavity plane.

For a 1560 nm radiation, this calculation allows us to predict a priori a waist in the cavity plane of $w_{\parallel} = 81 \mu\text{m}$ and $w_{\perp} = 128 \mu\text{m}$ perpendicular to this plane. This gives Rayleigh ranges of $z_{r,\parallel} = 13.2 \text{ mm}$ and $z_{r,\perp} = 34 \text{ mm}$ respectively.

For 780 nm wavelength, the same calculation gives $w_{\parallel} = 57.4 \mu\text{m}$ and $w_{\perp} = 91 \mu\text{m}$. The Rayleigh range are the same as the one given at 1560 nm.

Figure 3.10: *Alignment and injection of the cavity*

3.2.3 Cavity alignment

In the initial study that has been led on the cavity, one of the key elements considered was the inaccessibility of the cavity once under vacuum, and the complicate geometry that has many degrees of freedom. In particular, we analyzed the alignment of the cavity injection as being a critical experimental parameter. The procedure used for the alignment of the cavity is first described in section. 3.2.3.1, and the sensitivity of the optical axis to misalignment is then estimated.

3.2.3.1 Alignment procedure

In a non-confocal cavity only one optical axis exists. This axis is defined by the optical ray which overlaps after one turn. The first constraint in the alignment is to make sure that such an axis exists and stands **on** the mirror (see figure 3.10b).

Once this first constraint is fulfilled, it becomes sufficient to align the injection beam on this axis to couple light in the cavity. For a cavity under vacuum the windows limit the optical access and make the prealignment more critical. More details on the coupling are given in section C at the end of this chapter.

Experimentally, we used the configuration described in figure 3.10b. A visible green laser was used to realize a prealignment of the cavity: the cavity mirrors are rotated such that the green light overlaps after one turn. The green light is not coupled on resonance in a cavity mode, we only take advantage of the low reflectivity in the green to have a visible beam in the cavity. For the alignment, we took advantage of the degree of freedom given by the mechanical design (section 3.2.1.1). Once the cavity was close to be aligned and because the mirror have some reflection at 532 nm (about 90%), it was possible to distinguish the structure of a cross in the transmitted mode, that indicates the injection of the transverse modes. The structure was modified until it became point-like which indicates the end of the prealignment. The 1560 nm laser was injected in counter-propagation with the green (figure 3.10b) outside the cavity to the obtain the first 1560 nm signal in transmission. It is then directly this transmission signal that is

$$\begin{array}{c}
\text{Back in the OOAF} \\
\hline
\text{Action of the mirror in its own frame} \\
\hline
\text{TDMF} \\
\hline
\text{OOAF} \\
\hline
\end{array}
\begin{pmatrix} y' \\ \alpha' \\ T_x \\ \theta_x \end{pmatrix} = \begin{pmatrix} 1 & 0 & 1 & -R \\ 0 & 1 & 0 & 0 \\ 0 & 0 & 1 & 0 \\ 0 & 0 & 0 & 1 \end{pmatrix} \begin{pmatrix} 1 & 0 & 0 & 0 \\ \frac{-1}{f_x} & 1 & 0 & 0 \\ 0 & 0 & 1 & 0 \\ 0 & 0 & 0 & 1 \end{pmatrix} \begin{pmatrix} 1 & 0 & -1 & R \\ 0 & 1 & 0 & 0 \\ 0 & 0 & 1 & 0 \\ 0 & 0 & 0 & 1 \end{pmatrix} \begin{pmatrix} y \\ \alpha \\ T_x \\ \theta_x \end{pmatrix}$$

$$= \begin{pmatrix} 1 & 0 & 0 & 0 \\ -\frac{1}{f} & 1 & -\frac{1}{f} & -\frac{R}{f} \\ 0 & 0 & 1 & 0 \\ 0 & 0 & 0 & 1 \end{pmatrix} \begin{pmatrix} y \\ \alpha \\ T_x \\ \theta_x \end{pmatrix}$$

Table 3.2: ABCD formalism for a misaligned mirror.

optimized.

3.2.3.2 Stability of the optical axis

In this section we focus on the sensitivity of the optical axis position to misalignments (translation or rotation) of the mirrors. This study was realized because the cavity is mounted and used under vacuum. In addition, the cavity mirrors are about 20 cm from the vacuum windows. It is then crucial to ensure that the mode position, in other word the optical axis, is close to the theoretical cavity axis and stands in the windows aperture.

This study defines the mechanical requirements (planarity and parallelism) that constrain the cavity realization. It also gives some clues on the type of deformation that can be expected for our concentric geometry.

To lead this analysis, we adapted the ABCD formalism to take into account the possible rotation and translation of the cavity mirrors. The cavity is completely unfolded using the procedure of figure. 3.11b. In addition, a ray (y, α) arriving on a mirror that has been translated and rotated by (T_x, θ_x) will exit as (y', α') with respect to the original optical axis. In the ABCD formalism, it can be formally written as in table 3.2.

where OOAF and TDMF stand respectively for the Original Optical Axis Frame and the Tilted and Displaced Mirror Frame.

Since the position of the mirror is completely defined by that of its center of curvature, it is possible to show that the translation of a mirror is in first approximation equivalent to a rotation around its center, and the link between the two is the radius of curvature. Figure 3.11a illustrates this equivalence.

In order to be sure to take into account the worst misalignment possible, we scan the mirrors rotation $(+\theta_0, 0, -\theta_0)$ and translation $(+T_0, 0, -T_0)$ in both direction for all mirrors. For rotation, the error angle considered is $\theta_0 = 100 \mu\text{rad}$. For translation, we considered $T_0 = 100 \mu\text{m}$. These

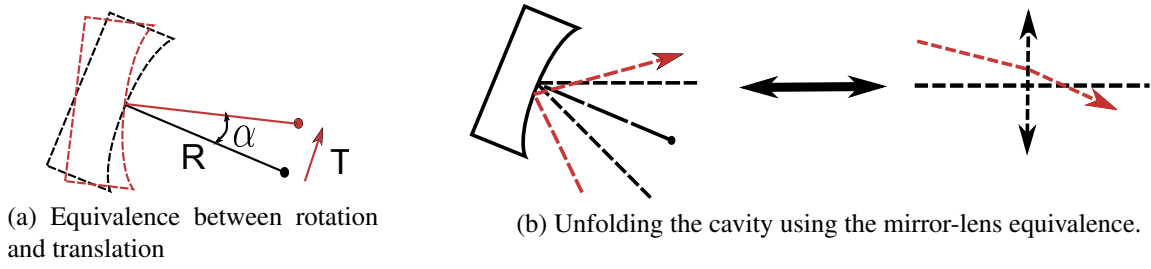
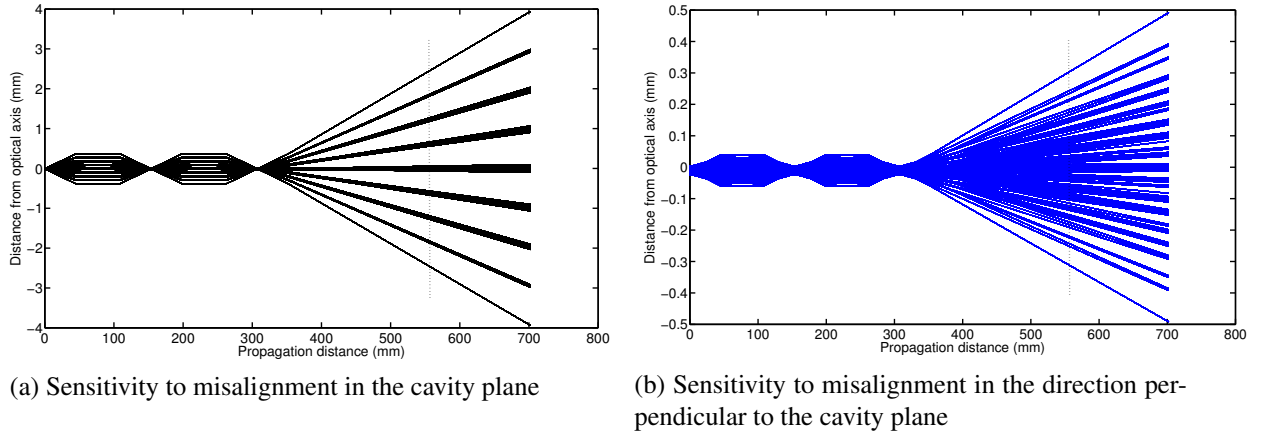


Figure 3.11: Translation and rotation of a mirror

Figure 3.12: Trajectory of the mode compared to the theoretical optical axis. The curve are obtained for $\theta_0 = 100 \mu\text{rad}$ and $T_0 = 0 \mu\text{m}$.

values were chosen because they are standard mechanical achievable precision.

In figure 3.12, the mode position is presented when only rotation ($\theta_0 = 100 \mu\text{rad}$) misalignments of the mirrors are permitted. We note that in the worst combination, the displacement of the optical axis is below $500 \mu\text{m}$ on the mirror, and below 3mm on the output vacuum windows (CF 40). Thus rotational misalignment are not critical. Figure 3.12a shows the trajectories in the horizontal plane which appear to be degenerate. The horizontal direction is the closest to the instability regime, and the transverse modes are close to be degenerate with the next fundamental mode (see figure 3.14).

In figure 3.13, the optical path for all possible rotations and translations of the mirrors are traced. The result shows a much stronger displacement on the mirrors (few mm) as well as on the vacuum windows (below 3cm) than for the pure rotational misalignment. The cavity is then much more sensitive to translational misalignment than rotational one. This is due to the fact that a rotation α is equivalent to a translation *via* $T = R\alpha \approx 10 \mu\text{m}$.

In the figures, we see that at the center of the cavity, where the atoms are situated, the two directions have different behaviors. In the horizontal (*i.e.* cavity plane, figure. 3.13a), the optical axis always passes through the same point while on the vertical (figure. 3.13b) it is more spread. This means that for a misalignment in the vertical, the two crossing beam can be one over the other. On the other hand, for an horizontal misalignment, the two beams will always cross at

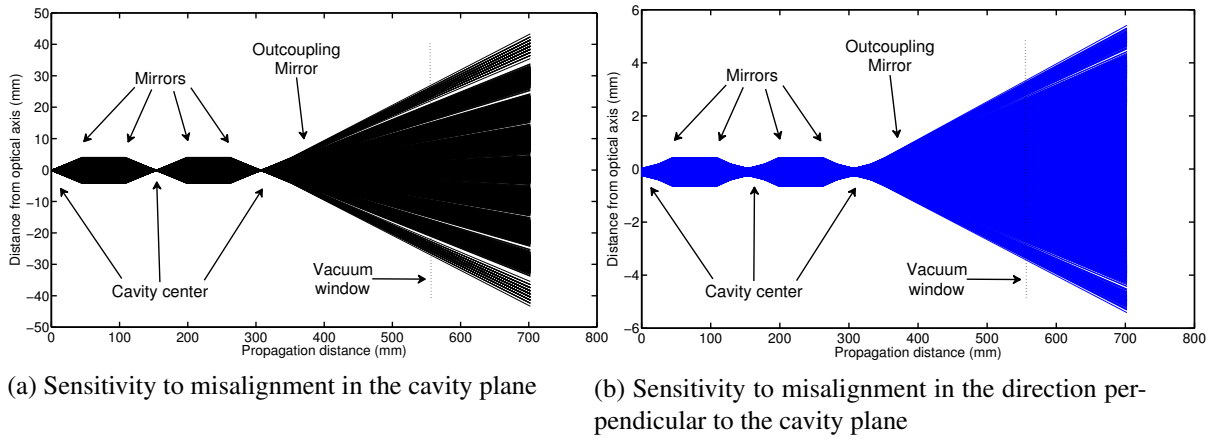


Figure 3.13: Trajectory of the mode compared to the theoretical optical axis. The curves are obtained for $\theta_0 = 100 \mu\text{rad}$ and $T_0 = 100 \mu\text{m}$.

the center of the configuration but the crossing angle will be modified.

3.2.4 Transverse mode study, an indication of the anisotropy

3.2.4.1 Gouy phase of the transverse modes

The Gouy phase $\zeta(z)$ [Gouy 90b] accumulated when propagating through the focus is related to the waist size. The tighter the beam is focused, the higher will be the Gouy phase. Since the beam focus is controlled by the cavity geometry, the Gouy phase is linked to the geometrical parameters.

A reinterpretation of the Gouy phase in terms of Heisenberg like inequalities in [Feng 01] makes quite understandable the dependance of the Gouy phase with the transverse mode numbers. Indeed, the higher transverse modes have smaller lobes. As a consequence, their divergence and then the Gouy phase are increased.

A possibility to study the geometrical properties of the cavity is to look for the transverse mode spectrum (see figure 3.14). This spectrum is related to the Gouy phase acquired by the mode while traversing the beam focus and are then determined by the cavity geometry parameters through [Siegman 86]:

$$\nu_{p,m,n} = \frac{c}{2\pi L} \left(2p\pi + (m + \frac{1}{2})\text{Arg} \left(A_m + \frac{B_m}{q_m} \right) + (n + \frac{1}{2})\text{Arg} \left(A_n + \frac{B_n}{q_n} \right) \right), \quad (3.32)$$

where p is the longitudinal mode order, m and n are the two non degenerate transverse mode orders (horizontal and vertical), A_m , B_m factors refer to the ABCD matrix element in the m direction and q_m is the complex radius of curvature of the beam. A , B and q are completely determined by the geometrical properties of the cavity (length, angle and mirrors radius of curvature).

3.2.4.2 A correction on the astigmatism

To measure the transverse mode cavity spectrum, the cavity length is scanned for a fixed frequency of the injection laser. Since the cavity is astigmatic, the transverse modes are Hermite-Gauss modes. To obtain the blue curve of figure 3.15a a vertical misalignment of the injection

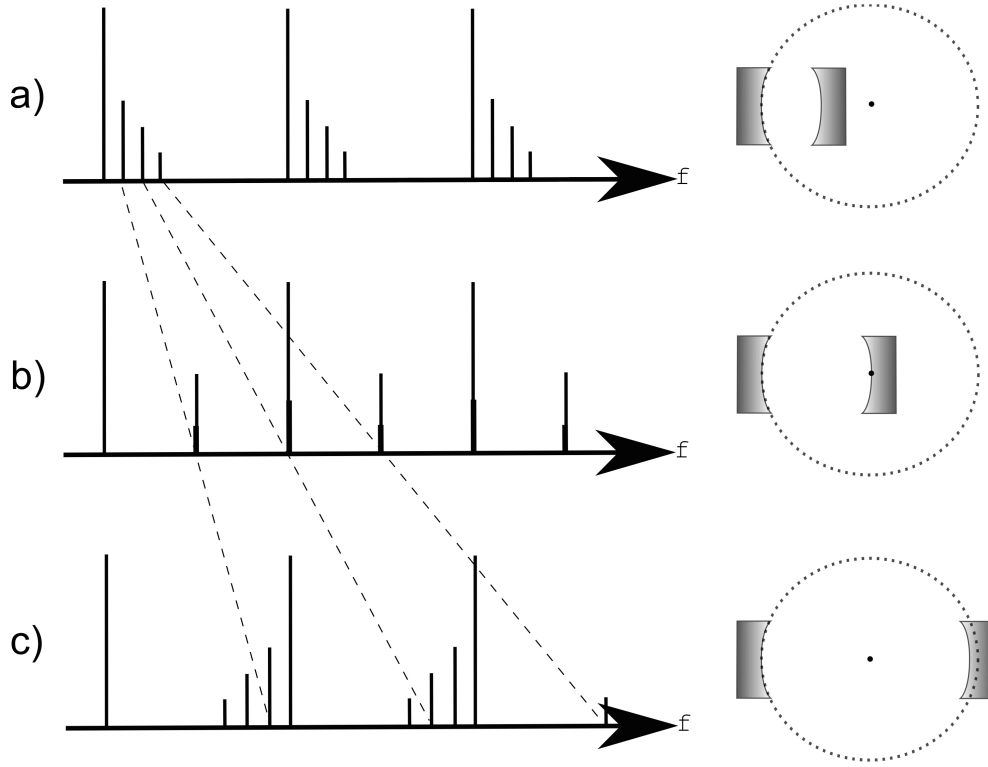


Figure 3.14: *Transverse mode frequency position*

The position of the high order transverse modes of the cavity are shown for different cavity geometries. From up to down, the coplanar, confocal or Fabry Perot and concentric cavity.

is voluntarily applied to create a mode overlap with the TEM_{0m} transverse modes. Doing the same in the horizontal direction, we obtained the TEM_{n0} modes which correspond to the black curve.

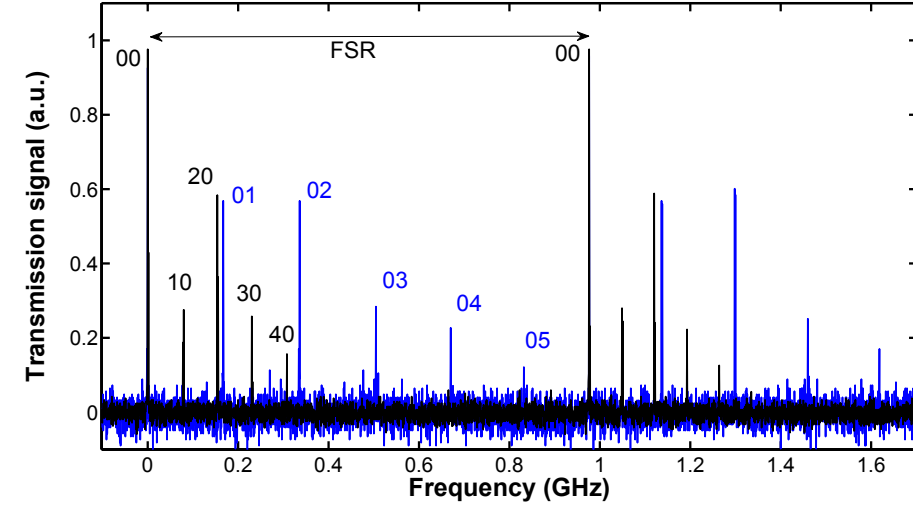
The horizontal mode inter-spacing is 78.9 MHz and the vertical is 164.6 MHz.

On figure 3.15b the experimental data for the relative frequencies (red cross) are presented as well as the a priori calculation (red dashed) based on 3.32.

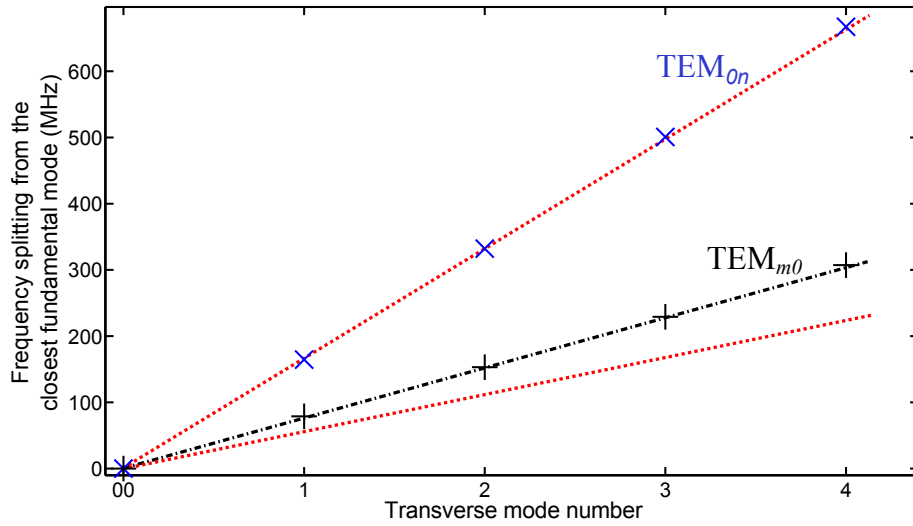
The discrepancy of the horizontal splitting is corrected by a phenomenological factor α_{\parallel} that, for example, accounts for aberrations. This factor is applied on the horizontal effective radius of curvature $R_{\parallel} = \alpha_{\parallel} R \cos \theta$, and is adjusted on the slope of the data giving $\alpha_{\parallel} = 1.020(5)$ (black curve in 3.15b). In the adopted quasi-concentric configuration, the parallel direction is the closest one to the instability regime. A 2% deviation of α_{\parallel} induces a noticeable frequency shift as it can be seen in 3.15b. Including this correction for the astigmatism, we infer a horizontal waist $\omega_{\parallel} = 93.1 \mu\text{m}$ to be compared with $98(1) \mu\text{m}$ found using a tomographic measurement [Brantut 08a, Bertoldi 10] and reported in section 3.2.5.2. The vertical waist is calculated to be $\omega_{\perp} = 129.8 \mu\text{m}$. The corresponding Rayleigh ranges are $z_r^{\parallel} = 17.46 \text{ mm}$ and $z_r^{\perp} = 33.9 \text{ mm}$.

3.2.5 Measurement of the optical profile

The trapping of atoms being realized in the cavity, it is essential to precisely know the cavity mode size. As we are close to instability regime, where the geometrical mode properties diverge a calculation of the size is not sufficient. To that purpose, we first realize an indirect



(a) Cavity transmission.



(b) Transverse splitting

Figure 3.15: *Transverse mode splitting*

(a) The cavity transmission signal when the cavity length is scanned for an horizontal (black, " TEM_{m0} ") and vertical (blue, " TEM_{0n} ") misalignment of the injection beam. (b) Frequency splitting of the transverse mode relative to the closest fundamental mode. The red dashed lines represents eq. 3.32 when only the off axis incidence on the mirrors is taken into account. The black dashed-dotted line includes furthermore the correction factor α_{\parallel} as presented in the text.

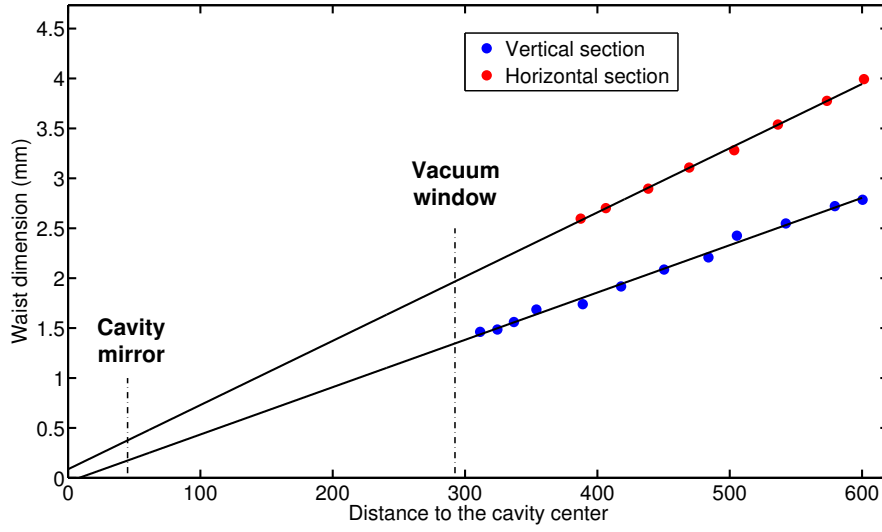


Figure 3.16: *Divergence of the beam measured on a diagonal output.*

The waist is extracted using the equation: 3.26. The vertical divergence is of 4.7 mrad while the horizontal 6.4 mrad. These values are extracted from the fit of the slope.

measurement of the mode given by the divergence of the transmitted profile. To complete this measurement, we realized a direct nondestructive measurement of the mode using the atoms as a sensor.

3.2.5.1 Indirect measurement: the divergence of the mode

When radiation is injected in the cavity, the transmitted mode has the profile of the intracavity mode that further propagated through the diverging transmission mirror. Therefore, the measurement of the transmitted mode waist and divergence gives information on the intra cavity mode characteristics.

The divergence of a beam is linked to its waist through:

$$\tan(\theta) = \frac{\lambda}{\pi w_0}. \quad (3.33)$$

Realizing a Foucaultage of the transmitted beam with a chopper, we measured the waist as a function of distance as presented in figure. 3.16. The waist are calculated using equation 3.26.

The divergence in the cavity plane is $\theta_{\parallel} = 6.4$ mrad and perpendicularly to this plane we have $\theta_{\perp} = 4.7$ mrad. The waist extracted from this measurement are $w_{\parallel} = 77 \mu\text{m}$ and $w_{\perp} = 104 \mu\text{m}$. Considering in addition, the diverging lens effect f of the out-coupling mirror, we find $w_{\parallel} = 95.7 \mu\text{m}$ for $f_{\parallel} = -f_0 \times \cos(22.5^\circ)$ and $w_{\perp} = 125.6 \mu\text{m}$ for $f_{\perp} = -f_0 / \cos(22.5^\circ)$.

In these formula, $f_0 = 200$ is the focal length of the mirror in transmission which is calculated from the refractive index and the radius of curvature: $f_0 = -R/(n - 1)$. These values are in good agreement with the prediction from the ABCD matrix calculation that was giving: $w_{\parallel} = 81 \mu\text{m}$ and $w_{\perp} = 128 \mu\text{m}$.

3.2.5.2 A direct nondestructive measurement of the optical profile

In situ measurement of cavity modes are tricky to realize. Indeed, a destructive measurement such as a Foucaultage for example cannot be done in a cavity. When the mode start to be destructively measured, this create losses in the cavity that prevent the coupling of the injected radiation. For *in-situ* measurement, one needs then to perform a nondestructive measurement.

In this section, we present a nondestructive measurement of the optical field in the cavity that uses the differential light shift that 1560 nm light induces on the imaging transition $|5^2S_{1/2}, F = 2\rangle \rightarrow |5^2P_{3/2}, F_p = 3\rangle$.

Light shift in the optical dipole trap

Under the influence of the dipolar interaction, the atomic state energy are shifted by:

$$\Delta E = -\frac{1}{2}\text{Re}(\alpha)E^2 = -\frac{\text{Re}(\alpha)I}{2\epsilon_0 c}, \quad (3.34)$$

where α is the atomic polarizability which describes the atom-light coupling strength, E is the rms value of the electric field and I the optical intensity. For a spatially dependent intensity, one obtains a spatially dependent light-shift.

The exact expression of the polarizability is derived in appendix D and takes the form:

$$\alpha_\mu \approx \frac{1}{\hbar} \sum_k \frac{|\langle k | \hat{d} | \mu \rangle|^2 \omega_{k,\mu}}{\omega_{k,\mu}^2 - \omega^2}, \quad (3.35)$$

where k designs all the possible transient states coupled by the light, $\omega_{k,\mu} = (E_k - E_\mu)/\hbar$ is the algebraic transition frequency and $\langle k | \hat{d} | \mu \rangle$ is the dipole element between k and μ .

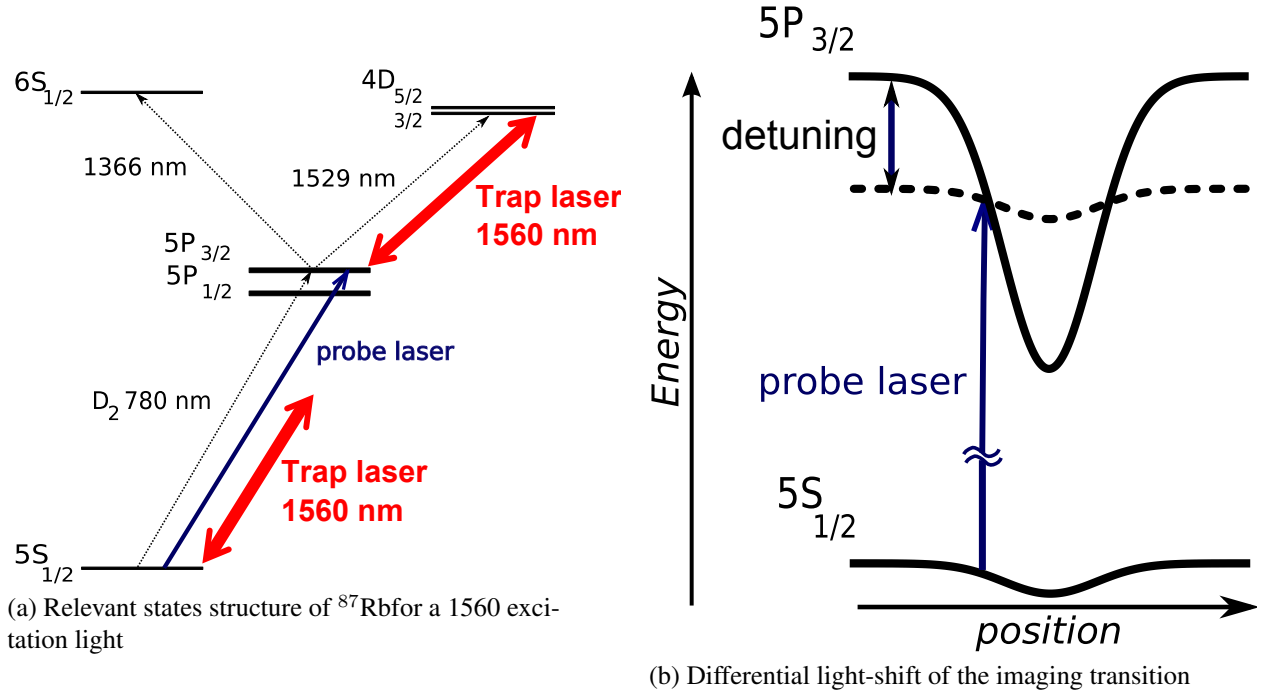
The atomic structure relevant for our discussion is presented in figure 3.17a. From the ground states $5^2S_{1/2}$, and for a radiation at 1560 nm, only the D_2 and D_1 lines need to be considered. For these transitions, we have $\omega < \omega_k$, and the ground state will be down shifted for a maximum of the intensity. A Gaussian beam will be trapping atoms in the ground state (figure 3.17b).

On the other hand, if it was only for the D-lines, the state $5^2P_{3/2}$ should be blue shifted (expelling the atoms) at this same maximum. Actually, for the polarizability of $5P_{3/2}$, one should also consider the transitions to the $4^2D_{3/2}$ and $4^2D_{5/2}$ states which are at 1529 nm and which have dipole elements similar to the one of the D-lines (table 3.3). As the excitation frequency is also red detuned for this transition, the state $5^2P_{3/2}$ is red shifted by the 1560 nm radiation. In addition, the proximity of these 1529 nm resonances, makes the light-shift of the $5^2P_{3/2}$ states large compare to the one of the $5^2S_{1/2}$ state. The resulting differential light-shift structure is presented in figure 3.17b.

In the case of a 1560 nm radiation and using for the calculation all the relevant transitions, we find (scalar) polarizabilities :

$$\alpha_{5^2S_{1/2}}^s = 6.8253 \cdot 10^{-39} \text{ Jm}^2/\text{W}, \quad (3.36)$$

$$\alpha_{5^2P_{3/2}}^s = 3.2550 \cdot 10^{-37} \text{ Jm}^2/\text{W}. \quad (3.37)$$

Figure 3.17: *Differential light shift structure.*

The 1560 nm radiation is close to the frequency of the transition from $5^2P_{3/2}$ to 4^2D states, which strongly shifts the state $5^2P_{3/2}$ to the red. Hence a differential light-shift is created on the imaging transition by the 1560 nm radiation.

Table 3.3: *Dipole elements relevant in the context of 1560 nm radiation*

The data are extracted from [Steck 10, Arora 07, Safronova 06, Clement 08] and are given in units of ea_0 where e is the electron charge and a_0 the Bohr radius.

Transition	λ [nm]	d [ea_0]
$5S_{1/2} \rightarrow 5P_{1/2}$	794.979	4.221
$5S_{1/2} \rightarrow 5P_{3/2}$	780.241	5.956
$5P_{3/2} \rightarrow 6S_{1/2}$	1366.875	6.047
$5P_{3/2} \rightarrow 4D_{1/2}$	1529.261	3.633
$5P_{3/2} \rightarrow 4D_{5/2}$	1529.366	10.899

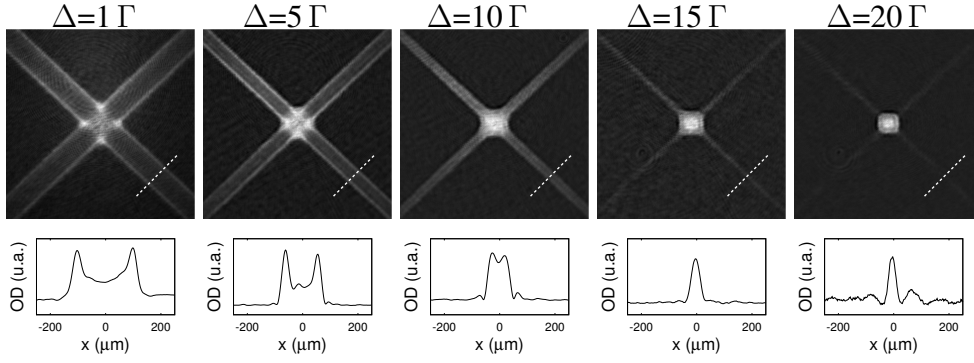


Figure 3.18: *Tomographic images of the fundamental*

(Top) Tomographic images of the optical potential setting the probe frequency to different detuning with respect to the D_2 line. (Bottom) Integral optical density obtained by projecting the upper images on the 45° dashed line crossing one arm of the cavity.

This leads to a polarizability ratio (β) of:

$$\beta = \frac{\alpha_{5^2P_{3/2}}}{\alpha_{5^2S_{1/2}}} = 47.7. \quad (3.38)$$

Under the influence of the 1560 nm radiation, the imaging transition has an energy:

$$\hbar\omega_{S,P} = \hbar\omega_0 + \frac{\text{Re}(\alpha_{5^2S_{1/2}})I}{2\epsilon_0 c} - \frac{\text{Re}(\alpha_{5^2P_{3/2}})I}{2\epsilon_0 c} \quad (3.39)$$

$$= \hbar\omega_0 + \frac{\text{Re}(\alpha_{5^2S_{1/2}})I}{2\epsilon_0 c} (1 - \beta). \quad (3.40)$$

Optical tomography of the Gaussian mode

We will show now how such a differential light shift can be used for the measurement of the modes profiles. The atoms released from the MOT are used as sensors of the light intensity. From expression 3.40, it appears clearly that the imaging transition is frequency shifted depending on the light intensity. Therefore, a probe tuned off resonance by δ (see figure 3.17b) and on the red of the transition will be resonant with atoms that are in a position of space where the light intensity I verifies:

$$\hbar\delta = \frac{\text{Re}(\alpha_{5^2S_{1/2}})I}{2\epsilon_0 c} (1 - \beta) \quad (3.41)$$

As a consequence, by changing the detuning of the probe beam with respect to the D_2 transition it is possible to bring into resonance atoms placed at different positions in the optical potential [Brantut 08a].

This method provides the isopotentials of the crossed dipole trap, as shown in figure 3.18, where the 1560 nm laser is locked to the fundamental transversal mode (TEM_{00}). In each shot, the probe detuned by δ is absorbed by the atoms with potential energy $U(\mathbf{r}) = \text{Re}(\alpha)I(\mathbf{r})/(2\epsilon_0 c) = \hbar\delta/(\beta - 1)$ in the ground level; for this atomic class the probe is shifted into resonance because of the local light shift. The optical density was projected on an axis parallel to one cavity arm (figure. 3.18, lower row), and the relative profile fitted to obtain the distance of the couples

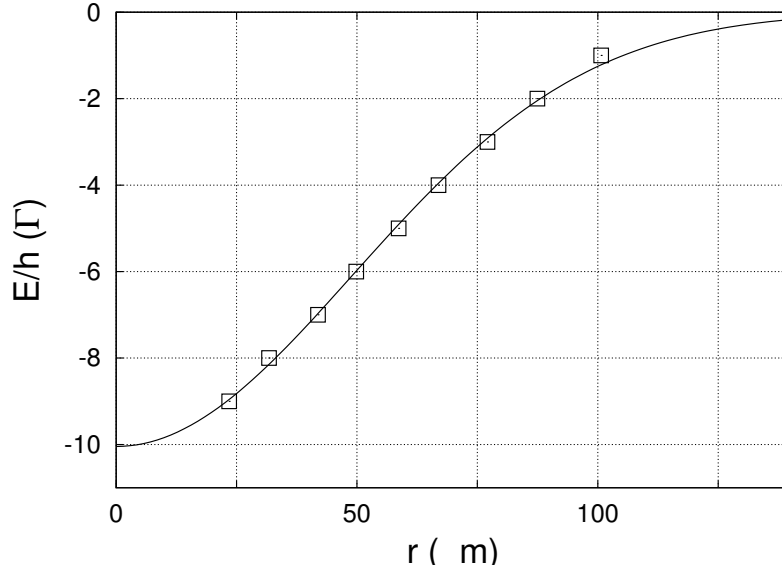


Figure 3.19: *Tomographic profile of the fundamental*

Optical potential depth when the 1560 nm laser is locked to the fundamental transversal mode of the optical resonator. The measurement was obtained by projecting the signal relative to one arm of the cavity. The result of the fit with the first Hermite-Gauss mode is shown with a continuous line.

of isopotential lines. Plotting the position of these isolines versus the probe detuning provides the cavity mode profile, as shown in figure 3.19, and the fit with the first Hermite-Gauss mode gives a waist $w = 98(1) \mu\text{m}$. This is in good agreement with the result obtained in section 3.2.4, where a correction on the astigmatism was applied: $w_{\parallel} = 96 \mu\text{m}$ and $w_{\perp} = 128 \mu\text{m}$.

Optical tomography of the transverse modes

The characterization previously led on the Gaussian mode can easily be extended to other Hermite-Gauss modes. In order to properly inject the higher excited modes of the cavity, phase masks are inserted in the path of the gaussian beam. A $(0 - \pi)$ phase mask projects the gaussian mode with a 79% overlap on the first transverse mode TEM_{01} (see figure. 3.20a). In the same way a $(0 - \pi - 0)$ phase mask will project on the second transverse mode TEM_{02} (see figure. 3.20b), with a maximum overlap of 68%.

Since the imaging is realized from the top, the injected transverse modes are the horizontal ones. The figures 3.21 and 3.22 show the absorption image which are obtained on the first and second transverse mode.

Looking to the isopotential distance as a function of detuning, we were able to retrace their profiles which are given on figure 3.23. The dashed lines on figure 3.23 represent the fitted

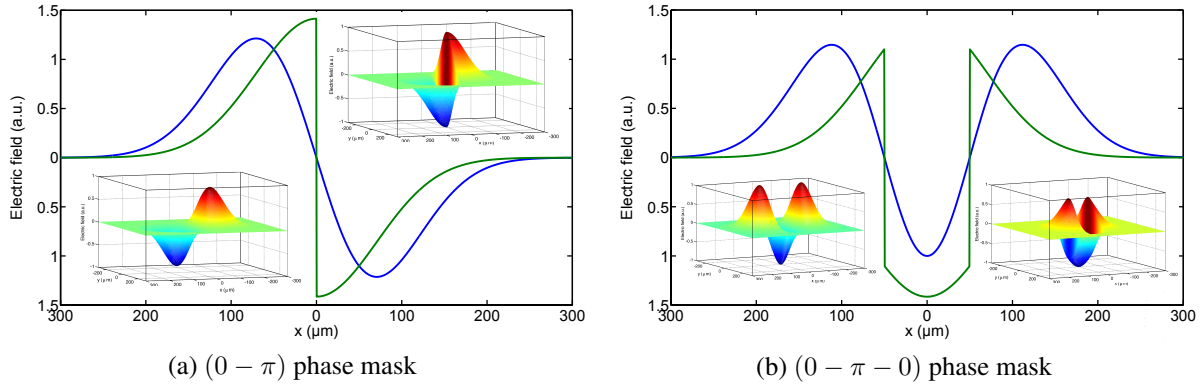


Figure 3.20: *Phase mask transformation.*

Abrupt phase transition can be used to approximate high order Hermite-Gauss mode. A $(0 - \pi)$ (resp $(0 - \pi - 0)$) phase mask essentially project the Gaussian input beams on the TEM_{01} (resp. TEM_{02}) Hermite-Gauss mode.

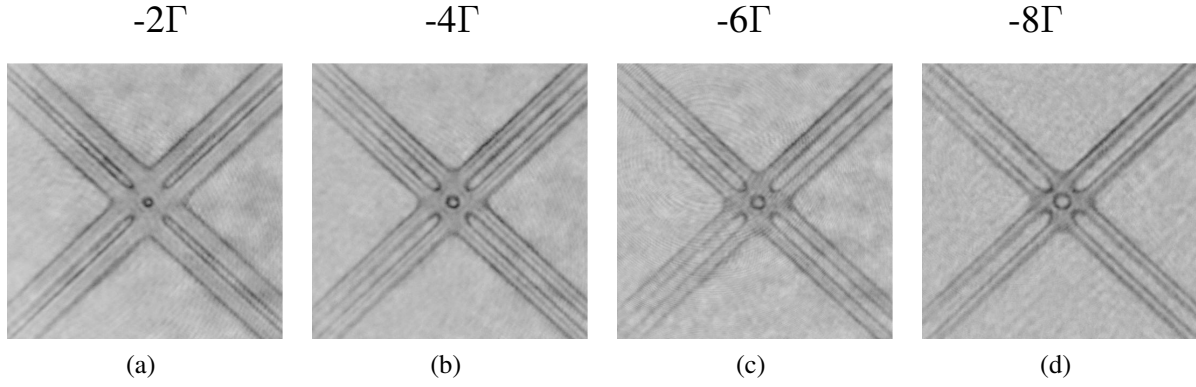


Figure 3.21: *Tomographic absorption images of the TEM_{01}*

The images are realized with off resonance absorption image on atoms in the MOT when the TEM_{01} mode was injected in the cavity. The image are realized for a detuning of 2Γ (a), 4Γ (b), 6Γ (c), 8Γ (d).

Hermite Gauss modes which are given by:

$$TEM_{01}(x) = U_0 \int_y e^{-\frac{2y^2}{w_y^2}} x e^{-\frac{2x^2}{w_x^2}} dy \quad (3.42)$$

$$= U'_0 x e^{-\frac{2x^2}{w_x^2}} \quad (3.43)$$

$$TEM_{02}(x) = U'_0 \left(\frac{4x^2}{w_x^2} - 1 \right) e^{-\frac{2x^2}{w_x^2}} \quad (3.44)$$

These fits give a waist of $101(1) \mu\text{m}$ for the TEM_{01} and $99.8(4) \mu\text{m}$ for the TEM_{02} , in agreement with the measurement of the fundamental waist: $w = 98(1) \mu\text{m}$.

In principle the precision of this measurement is given by the local intensity gradient and can thus be very high. Nevertheless, in practice, this method is limited by the fact that a minimum number of atoms are necessary for the imaging of each trench.

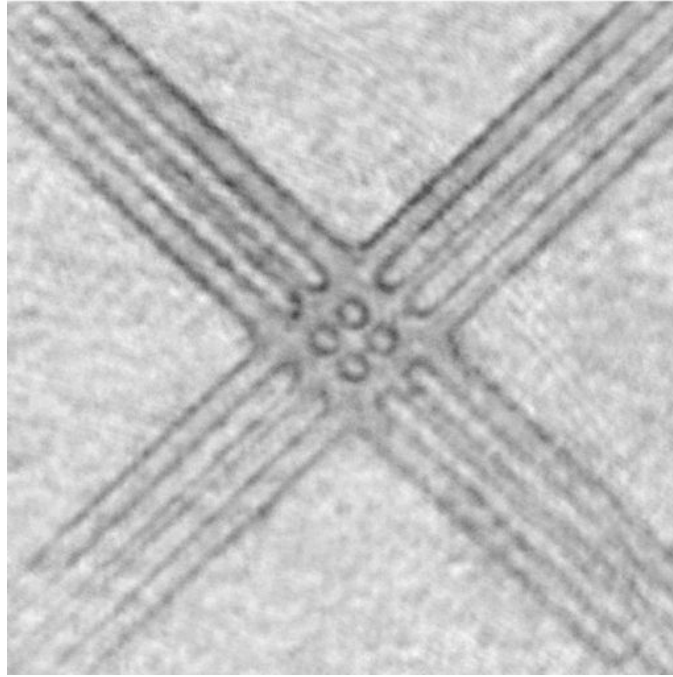
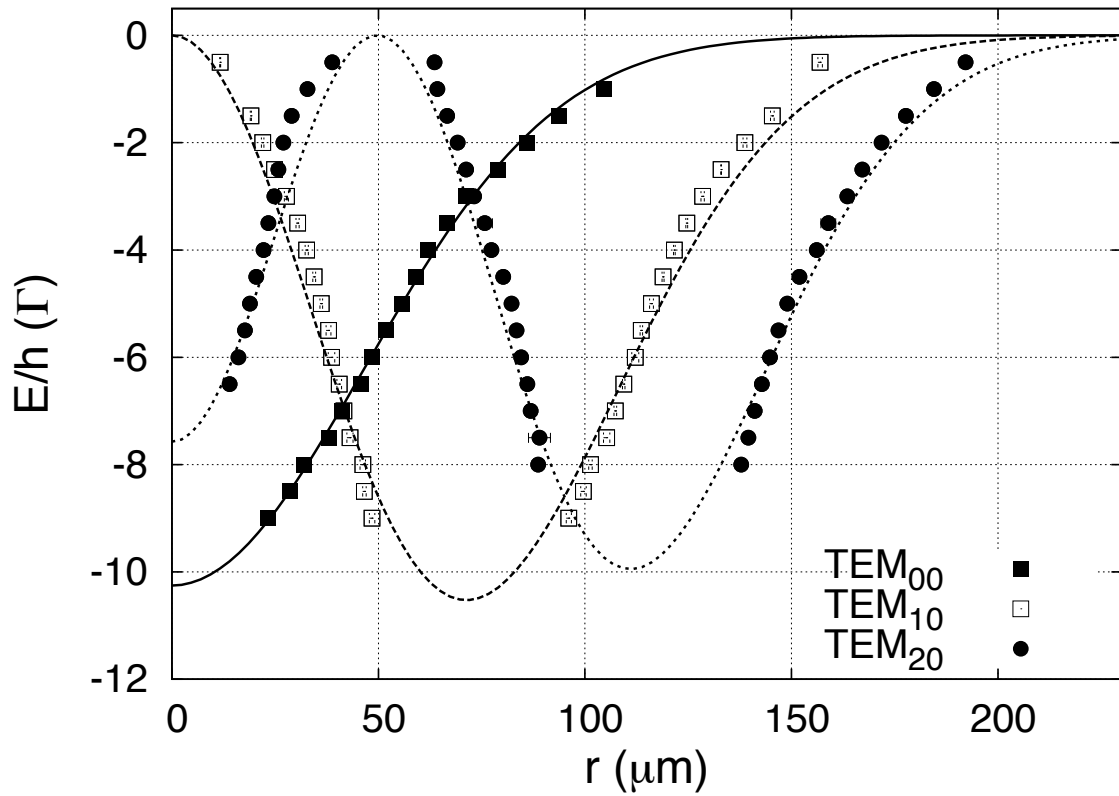
Figure 3.22: Tomographic absorption images of the TEM_{02} .

Figure 3.23: Tomographic profiles of the first modes.

Optical potential depth induced by the laser at 1560 nm locked to the first three transversal modes of the cavity. Each series of points is fitted with the corresponding Hermite-Gaussian mode.

3.2.6 Cavity parameters at 1560 nm.

In addition to the geometrical properties characterized in the previous section, the spectral features of the cavity that are the Free Spectral Range (FSR) and the linewidth are of first importance.

3.2.6.1 Free spectral range

The Free Spectral Range is the frequency distance between adjacent cavity modes. It is proportional to the inverse of the cavity length (equation 3.45).

In order to measure precisely the FSR we have realized a spectroscopic measurement. The length of the cavity is scanned over three cavity lines and we observe the transmission of the cavity when the input light is phase modulated (1 carrier and 2 sidebands). To obtain the FSR, the frequency of the phase modulation is arranged so that the sidebands are resonant with the cavity for the same cavity length as the carrier. In that case the modulation frequency corresponds to an integer number of FSR. In the measurement, the sidebands were injected two FSR away from the carrier for a modulation of 1952.4 MHz, which gives:

$$\Delta\nu_{\text{FSR}} = 2\pi \frac{c}{L} = 2\pi \times (976.2 \pm 0.05) \text{ rad.MHz} \quad (3.45)$$

For a perfect square cavity, the FSR measured corresponds to a diagonal of 90.010(5)mm and we were expecting 90mm from the design.

Polarization As the mirrors are used off-axis, the two orthogonal polarizations acquire a different phase at the reflection (Fresnel coefficients). This does not change the FSR, but modifies the resonant condition. The two polarizations are non-degenerate, and they are frequency split by 68 MHz. When a laser is locked on the cavity, only one polarization goes through, and the other one is completely reflected.

3.2.6.2 Linewidth

To measure the linewidth of the cavity resonance, different methods were used. A commonly adopted method is the ring down method, which consists to suddenly turn off the injection of the cavity and measure the decay time τ . The linewidth is given by $\delta\nu = 2/\tau$ in rad.s^{-1} where τ is the decay time. This method did not prove to be very precise in our case since the finesse at 1560 nm is not very high and the decay time is of the order of 1 μs which is difficult to measure without any artifact due to the nonzero extinction time of the injected radiation [Lawrence 99].

As a consequence, to get a precise estimation, the linewidth has been measured by a spectroscopic method. The cavity and the laser are free running. A sideband is added to the laser frequency with an EOM and its transmission through the cavity is measured while the sideband is swept across the resonance. The sweeping is precisely controlled by a synthesizer, so that the abscissa of figure 3.24 is very well known. In principle, it could be better to lock the laser on the cavity, but in that case, the transmission of the sideband has to be distinguished from the transmission of the carrier (bright background measurement). In addition, it did not reveal necessary in our case since the sideband is swept with frequency velocity of 12 MHz/ms and no substantial relative displacement of the laser frequency with respect to the resonance occurs in this lapse of time.

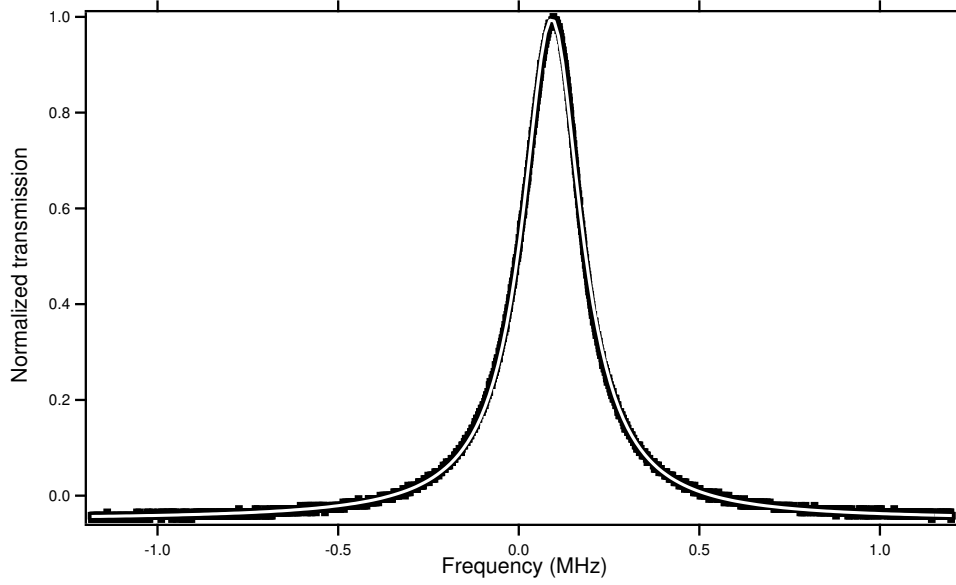


Figure 3.24: *Linewidth of the cavity at 1560 nm*

The black curve is a measurement of the cavity linewidth while sweeping the frequency across the resonance. The white line is a Lorentzian fit on the data with a width of $2\pi \times 546 \cdot 10^3 \text{ rad.s}^{-1}$.

This measurement gives a cavity linewidth (FWHM) of:

$$\delta\nu = 2\pi \times 546 \cdot 10^3 \text{ rad.s}^{-1} \quad (3.46)$$

This linewidth measurement, together with the measurement of the FSR gives a finesse :

$$\mathcal{F} = \frac{\delta\nu_{\text{FSR}}}{\delta\nu} = 1788 \quad (3.47)$$

which has to be compared with the theoretical value $\mathcal{F}_{\text{theo}} = 4160$.

The difference between the two indicates that the mirrors are not as good as expected from the specification. Two possible reasons for this discrepancy:

- The reflectivities of the mirrors are lower than the specified values
- The losses in the cavity are of primary importance and should be taken into account.

Remark: To have the expected Lorentzian profile for the transmission signal, it is important to sweep adiabatic with respect to the loading and emptying of the cavity. The relevant time for the emptying is the decay time τ , while for the loading, it is $\sqrt{L/c} \times \tau$. The physics of the loading and emptying is well described in [Lawrence 99, Rohde 02].

3.2.7 Losses of the cavity

The low finesse that has been measured in the previous section raises questions about the losses of the cavity.

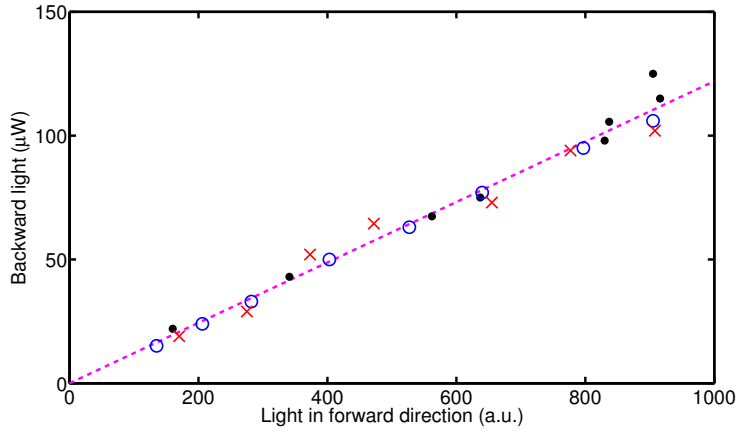


Figure 3.25: *Reversed light in the cavity as a function of the forward intensity*

The transmitted light in the two directions is monitored while the injection is misaligned vertically (black dots), and horizontally in the two direction (red cross and blue circle). The magenta dashed line is adjusted on the data, and shows a proportionality relation.

3.2.7.1 Backward propagating light

When the 1560 nm radiation is coupled into the cavity, some light propagates in the reverse direction. For 90 mW of transmitted power in the forward direction, about 100 μW can be measured in the reverse direction. Some external parameters can slightly (a few percent) change this ratio. Among these parameters is for example the presence of optical elements in the transmitted path. This backward propagating light might principally arise from two sources. Either it comes from some backscattering after the transmission on the in-coupling mirror (solution 1), or or it comes from some optical back reflexion on external optics (e.g. vacuum windows) after the reflection on the in-coupling mirror that would recouple in reverse into the cavity (solution 2).

We distinguish these two possibilities since the beam reflected by the cavity is the most intense ($\sim 5\text{W}$) of the experiment and is then the first suspect. To disentangle the two, we look at the power in the reverse direction as a function of the power in the forward direction (in transmission) while the injection beam is misaligned. In transmission on the in-coupling mirror, the spatial mode is filtered by the cavity. In the case of solution 1, the reduction of intensity due to the misalignment in the forward and backward direction should be proportional. On the contrary, in the case of solution 2, no linearity is expected since the light in the forward and the backward direction correspond to two independent spatial mode-matching condition which are disentangled by the displacement. The result presented in figure 3.25 shows a linear behavior (solution 1). It suggests that the solution 1 is correct and that the backward light is either due to intracavity scattering or to optical back reflection in the transmitted beam. A high scattering is astonishing considering the expected surface quality of the mirrors but the reduction of the finesse observed support this conclusion. The next section presents the effect of intracavity scattering on the cavity finesse.

3.2.7.2 Loss effects in a cavity

Comparing the theoretical finesse given in section 3.2.1.3 $\mathcal{F}_{theo} = 4160$ with the measured one of $\mathcal{F} = 1788$ highly suggests that the cavity is more lossy than expected. In the following,

we will try to evaluate the scattering on the mirrors by incorporating in the equation of section 3.2.1.3 a scattering in field amplitude κ . The scattering is considered to be the same on every mirror. We have $r^2 + t^2 + \kappa^2 = 1$. The equation 3.11 remains valid but it is no more possible to replace t^2 by $1 - r^2$. From the equation 3.11 on the transmitted intensity, it is clear that the expression of the finesse is unchanged :

$$\mathcal{F} = \frac{\pi r^2}{1 - r^4} \quad (3.48)$$

The finesse measurement gives then the mirror reflectivity :

$$r^2 = \sqrt{1 - \frac{\pi}{\mathcal{F}}} \approx 1 - \frac{\pi}{2\mathcal{F}} = 99.91\% \quad (3.49)$$

This fixes the "losses" to $t^2 + \kappa^2 = 1 - r^2 = 9.24 \cdot 10^{-2}$. In the following, we will express the scattering κ relatively to the transmission by defining $x = \kappa^2/t^2$. From equation 3.48, the mirror transmission can be expressed in terms of the finesse and this parameter x by:

$$t^2 = \frac{\pi}{2(1+x)\mathcal{F}}. \quad (3.50)$$

The maximum cavity coupling (\mathcal{C}) efficiency 3.12, when the radiation is on-resonance becomes:

$$\mathcal{C} = 1 - \mathcal{R} = 1 - \left| \frac{t^2 r^3}{1 - r^4} - r \right|^2 \quad (3.51)$$

$$= 1 - \left[1 - \frac{1}{2(1+x)} + \frac{\pi}{4\mathcal{F}} \left(\frac{3}{2(1+x)} - 1 \right) \right]^2, \quad (3.52)$$

and the intra-cavity power P_{intra} can be expressed on one hand as a function of the input power P_{in} and the effective cavity coupling (measured) and on the other hand by the output power P_{out} .

$$P_{\text{intra}} = \frac{\mathcal{C}_{\text{eff}}}{\mathcal{C}} \frac{\mathcal{F}}{2(1+x)\pi} P_{\text{in}} \quad (3.53)$$

$$= \frac{1}{t^2} P_{\text{out}} \quad (3.54)$$

$$= \frac{2(1+x)\mathcal{F}}{\pi} P_{\text{out}}. \quad (3.55)$$

From our spectroscopic measurement, we have the value of the finesse \mathcal{F} , and the output power can be easily recorded. To obtain a value of the losses, the intracavity power still needs to be determined. As previously mentioned, it is usually a difficult parameter to measure since the presence of power in the cavity rely on a interference effect. In addition, in our case, the cavity is under vacuum and the mode volume is completely out of reach.

Fortunately, the 1560 nm radiation offers a solution with the differential light-shift it creates on the atoms. For an output power $P_{\text{out}} = 5.1$ mW, we measured a differential light shift in one

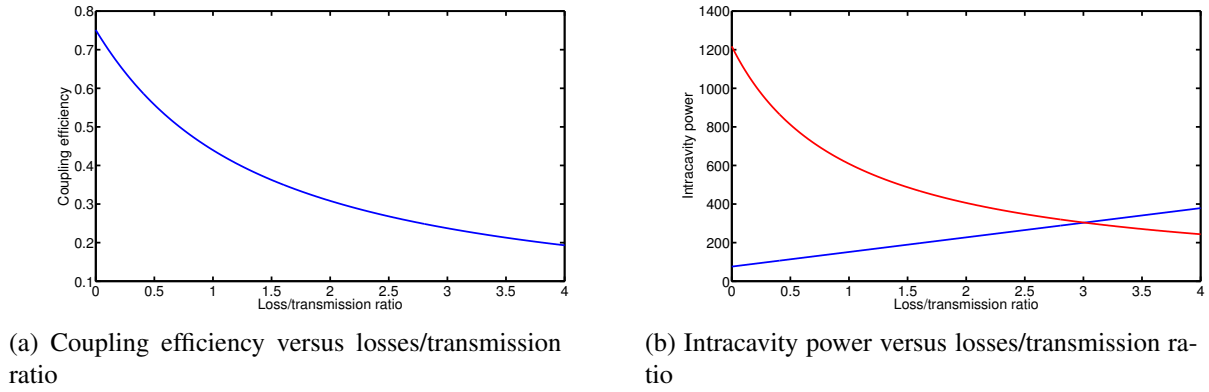


Figure 3.26: *Effect of the losses on the cavity response.*

Losses in the cavity reduce both the contrast of the coupling interference (lower coupling efficiency) and the finesse of the cavity (lower intra-cavity power).

arm that is $\Delta E = 11 \Gamma$. Using the expression of the polarizability given in 3.35, we extract the input intensity and power:

$$I_{\text{intra}} = \frac{2\epsilon_0 c \Delta E}{\alpha_{5P_{3/2}} - \alpha_{5S_{1/2}}} = 2.26 \times 10^8 \text{ W/m}^2, \quad (3.56)$$

$$P_{\text{intra}} = \frac{\pi w_x w_y I_{\text{intra}}}{2} = 14.3 \text{ W}, \quad (3.57)$$

where $w_x = 98 \mu\text{m}$ and $w_y = 128 \mu\text{m}$ are the two transverse waists.

The losses over transmission ratio is then:

$$x = \frac{\pi P_{\text{intra}}}{2\mathcal{F}P_{\text{out}}} - 1 = 1.46 \quad (3.58)$$

With this value, we obtain a maximum coupling efficiency of $\mathcal{C} = 36\%$. Experimentally we obtained $\mathcal{C} = 35\%$.

This ratio $x = 1.46$ indicates that the losses on the mirrors are really important and superior to the mirror transmission. The finesse at 780 nm has not been measured yet, but it might be heavily affected by these losses.

3.3 Locking of the 1560 nm laser to the cavity

3.3.1 The cavity: a low pass frequency filter

"A cavity is a low pass frequency filter": As I am used to say, it is a property that is very well known from people who know it. In this section, we will give some evidence about this statement [Fox 03].

In transmission of the cavity, this property is obvious since any photon that comes in, will be delayed by the number of round trips it has made before it exits. Thus any information is delayed by the $\tau = 2/\gamma = \mathcal{F}L/(\pi c)$, where γ is the linewidth of the cavity in rad.s^{-1} . In

reflection, this property is less clear since photons do not appear to transit through the cavity (which is not true).

We consider a Fabry Perot with mirror reflectivity r , transmittivity t and without losses ($r^2 + t^2 = 1$). The cavity length is L . We consider an input field E_{in} at frequency $\omega_0 = 2\pi pc/L$, *i.e.* exactly on resonance with the cavity. At $t = 0$, the frequency of the input is suddenly changed by $\delta\omega$ and we take $\delta\omega \ll \gamma$ such that the transmitted and reflected amplitude are not changed.

We consider time steps of length $\delta t = L/c$, such that the reflected field E_r after N steps can be written as:

$$E_r(N\delta t) = rE_{\text{in}} - tr^2 \sum_{k=0}^{\infty} r^{2k} E_{\text{in}}(N-1-k) \quad (3.59)$$

$$\begin{aligned} &= re^{i(\omega_0+\delta\omega)N\delta t} - tr^2 \left(\sum_{k=0}^{N-1} r^{2k} e^{i(\omega_0+\delta\omega)(N-1-k)\delta t} + \sum_{k=N-1}^{\infty} r^{2k} e^{i\omega_0(N-1-k)\delta t} \right) \\ &= re^{i\delta\omega N\delta t} \left((1 - r^2 e^{i\delta\omega\delta t}) \sum_{k=0}^{N-1} r^{2k} e^{i\delta\omega k\delta t} \right) \left(1 - \frac{t^2 e^{-i\delta\omega\delta t}}{1 - r^2 e^{-i\delta\omega\delta t}} \right). \end{aligned} \quad (3.60)$$

The last term in equation 3.60 is the reflection coefficient of the cavity for $\omega = \omega_0 + \delta\omega$ in the steady state regime. Indeed, this last term is the long term limit of equation 3.60 since

$$(1 - r^2 e^{i\delta\omega\delta t}) \sum_{k=0}^{N-1} r^{2k} e^{i\delta\omega k\delta t}, \quad (3.61)$$

converges to 1 for $N \rightarrow \infty$.

In addition, as we have $\delta\omega \ll \gamma$, it gives $1 - r^2 = \pi/\mathcal{F}$ and the first term of the sum in 3.61 can be approximated to 1. For small N , equation 3.61 can be simplified to: $N\pi/\mathcal{F}$. It results that the reflected signal builds up in time with a rate :

$$\frac{1}{\tau} = \frac{\pi c}{\mathcal{F}L} = \frac{\gamma}{2}. \quad (3.62)$$

This proves that even in reflection, the Pound Drever Hall scheme gives an error signal which is low pass filtered by the cavity ($f_c = \gamma$).

The same formalism can be applied in the case of a phase jump and would show that the cavity is actually a high pass filter for phase. This is the expected result since the frequency is the derivative of the phase.

3.3.2 Pound Drever Hall Method

The Pound Drever Hall scheme [Drever 83a, Black 01, Bjorklund 83] is a very efficient method to determine if a laser is on-resonance with a cavity line, and is naturally used to generate an error signal to lock lasers to cavities and vice versa. The essential idea is to create sidebands on the incoming laser and to compare on a fast detector the phase of the reflected sidebands to the phase of the on-resonant carrier. If the carrier is not perfectly on-resonance, it accumulates a phase per turn that is slightly different from $2n\pi$ and that is summed over the number of turns. The PDH scheme compare this phase shifted carrier with the reflected sidebands, and gives the error signal.

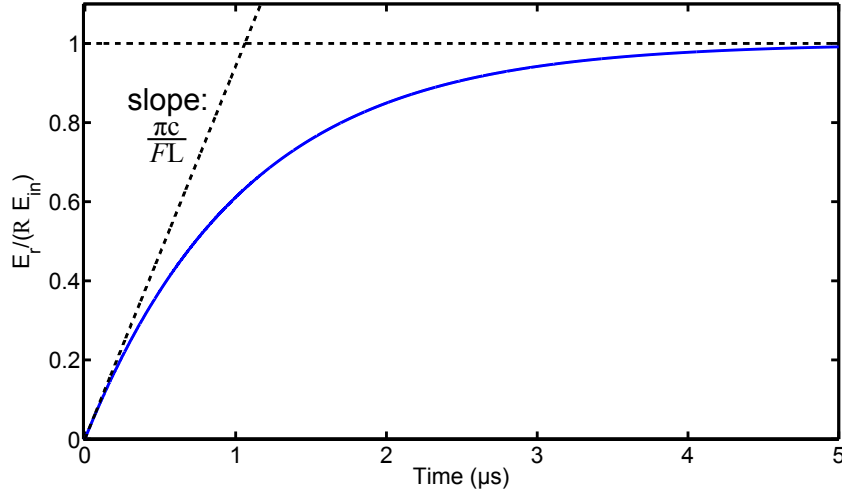


Figure 3.27: *The cavity as a low pass frequency filter*

The ratio of the instantaneous reflected field over the steady state reflected field is given as a function of time. The ratio increases linearly with a slope $\pi\gamma$ and saturates to one. The curve is given for a finesse $\mathcal{F} = 10000$ and a length $L = 10$ cm

The PDH method present the advantage to be applicable to cavities, independently of its finesse. Indeed, the resonance linewidth of the cavity reduces with the finesse, but at the same time, the sensitivity of the detection increases since the number of turns per photon increases.

Details on phase and frequency modulation are given in B.

In order to suppress most of the common mode noise, the sidebands are created by phase modulating the beam. The effect of residual amplitude modulation is discussed in section 6.1.3.1. Experimentally, the phase modulation is applied using an electro-optical modulator (EOM).

After reflection on the cavity the different frequency components of the light have experienced a phase shift Φ_i and a reduction of amplitude A_i . The field reflectivity $R(\omega) = A(\omega)e^{i\Phi(\omega)}$ has been given in 3.2.1.3:

$$E = E_0 e^{i\omega_0 t} \left(J_0(\beta) |R(\omega_0)| e^{i\Phi_0} + J_1(\beta) |R(\omega_0 + \Omega)| e^{i(\Omega t + \Phi_1)} + J_{-1}(\beta) |R(\omega_0 - \Omega)| e^{-i(\Omega t - \Phi_{-1})} \right). \quad (3.63)$$

Assuming that the two sidebands are far enough from resonance, so that they are completely reflected ($|R(\omega_0 + \Omega)| = |R(\omega_0 - \Omega)| = 1$) and that they experience the same phase shift ($\Phi_1 = \Phi_{-1}$), one obtains the simplified expression:

$$E \approx E_0 e^{i\omega_0 t} \left(|R(\omega_0)| e^{i\Phi_0} + \beta \left(e^{i(\Omega t + \Phi_1)} - e^{-i(\Omega t - \Phi_{-1})} \right) \right). \quad (3.64)$$

The current i_{ph} generated on the photodetector is then:

$$i_{\text{ph}} = \eta |E|^2 = \eta E^* E \quad (3.65)$$

$$= \eta E_0^2 \left(\frac{|R(\omega_0)|^2 + 2 * \beta^2}{2} + |R(\omega_0)| \beta \left(e^{i(\Omega t + \Phi_1 - \Phi_0)} - e^{i(\Omega t + \Phi_0 - \Phi_{-1})} - \beta^2 e^{i(2\Omega t + \Phi_1 - \Phi_{-1})} \right) + c.c. \right) \quad (3.66)$$

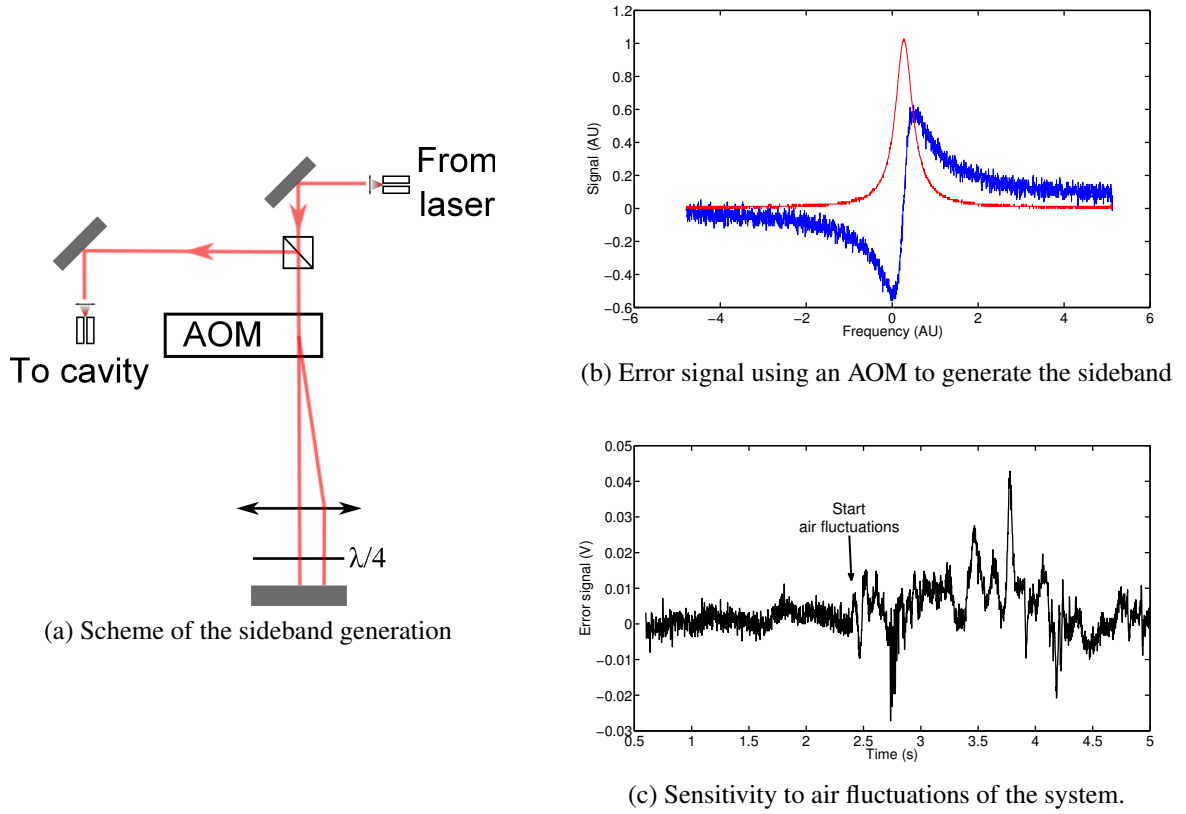


Figure 3.28: PDH like error signal with an amplitude modulator.

After demodulation with a local oscillator $LO = e^{i(\Omega t + \Phi_{LO})} + c.c.$ and DC filtering, one obtains the error signal S ,

$$S = \eta_{mixer} i_{ph} LO \quad (3.67)$$

$$= \eta_{mixer} \eta E_0^2 |R(\omega_0)| \beta \left(e^{i(\Phi_1 - \Phi_0 - \Phi_{LO})} - e^{i(\Phi_0 - \Phi_{-1} - \Phi_{LO})} \right) + c.c. \quad (3.68)$$

Using a demodulation phase $\Phi_{LO} = \pi/2$, we have $e^{i(\Phi_1 - \Phi_0 - \Phi_{LO})} + c.c. = 2 \sin(\Phi_1 - \Phi_0)$, and the demodulated signal becomes:

$$S = 2\eta_{mixer} \eta E_0^2 |R(\omega_0)| \beta (\sin(\Phi_1 - \Phi_0) - \sin(\Phi_0 - \Phi_{-1})) \quad (3.69)$$

$$\approx 2\eta_{mixer} \eta E_0^2 |R(\omega_0)| \beta (\Phi_1 + \Phi_{-1} - 2\Phi_0). \quad (3.70)$$

Equation 3.70 shows the comparison of the phase shift of the different frequency components that was mentioned at the beginning of the section.

The feedback signal is integrated in a double stage proportional integrator similar to that used for laser locking (see figure 2.6) [Fox 03]. The low frequency correction is applied on the piezo of the laser for long term stability and the fast correction is realized via a double pass acousto-optic modulator.

Interlude: PDH with an acousto-optic modulator

In the experiment, we currently use a phase modulator (EOM) to realize the Pound Drever Hall lock. Nevertheless, it is interesting to notice that the Pound Drever Hall method is a very

general method which compares the phase of two frequency components. Actually, when the project started, we first used an AOM in double pass as presented in figure 3.28a to generate one sideband. The light sent on the cavity was containing two frequency components separated by twice the modulation frequency. The local oscillator was doubled for the demodulation. The signal S after demodulation writes: $S \propto \sin(\Phi_0 - \Phi_1)$ where Φ_0 and Φ_1 are the phases accumulated in reflection on the cavity, and have dispersive shapes when the cavity resonance is crossed (see figure 3.28b). Such a system was easy to implement but was also lacking stability. As a matter of fact, the beams are not on the same path between the AOM and the retro-reflection mirror. As can be seen in figure 3.28c, due to air fluctuations the frequency components of the beam accumulate different phases which are indistinguishable from the phases induced by the cavity and the error signal is then perturbed by these fluctuations. This problem of differential fluctuations seen by the frequency components also applies to the heterodyne nondemolition measurement (chapter 6) for which the sensitivity has to be pushed to an optimum.

3.3.3 Locking a Koheras fiber laser to the cavity

At 1560 nm, that is a telecommunication wavelength, two kind of lasers are commonly used: Distributed feed back (DFB) diode and DFB fiber lasers (see for example [Zeller 10]). The diode technology has a laser linewidth of a few MHz but offers the possibility to fast correct the frequency (high bandwidth). On the contrary, the DFB fiber lasers have linewidths that can be as low as a few kHz but have only low feedback capabilities ($BW < 10$ kHz).

In our experiment, the delay in the 5W fiber amplifier that is 30 m long, intrinsically limits the closed loop bandwidth to 2.5 MHz ($\pi/2$ phase delay). As the DFB diode has a linewidth bigger than the cavity resonance, the feedback bandwidth should be higher than the laser linewidth ($\times 5$) so as to narrow the laser linewidth with respect to the cavity resonance. With the delay previously mentioned, this is obviously not possible. The use of a DFB diode has then naturally been eliminated to the profit of a DFB fiber laser (NKT photonics).

This laser has a specified linewidth of 1 kHz and an output power of about 100 mW. In order to give the feedback loop more bandwidth, we inserted a double pass acousto-optic modulator before the high power amplifier (see figure. 3.29a). Using this scheme we obtained 250 kHz bandwidth essentially limited by the propagation of the acoustic wave in the TeO_2 crystal for which the propagation velocity of the two eigen-polarizations are 4.2 mm/ μs and 0.6 mm/ μs).

The noise power spectral density (PSD) of the relative frequency between the laser and the cavity as well as the relative intensity noise of the transmitted power are presented in figure. 3.29b.

The noise spectral density shows the servo-bump of the fast AOM correction loop placed at about 250 kHz, and stays below the $0.1 \text{ Hz/Hz}^{1/2}$ level between 10 Hz and 10 kHz. Below 100 Hz the frequency noise is dominated by a $1/f$ component with $0.1 \text{ Hz/Hz}^{1/2}$ at 10 Hz.

The intensity noise of the radiation field in the cavity was measured evaluating the Fast Fourier Transform (FFT) of the transmission signal (PD2 in figure. 3.29a). As shown on the lower spectrum of figure. 3.29b, the intensity noise PSD is always below $10^{-9} \text{ Hz}^{1/2}$ with respect to the DC level, except for narrow peaks in the acoustic band (important in relation to parametric excitation of the atom in the optical trap) and close to 1 MHz. The integral value of the relative intensity noise PSD between 1 Hz and 10 kHz amounts to $2.8 \cdot 10^{-6} \text{ dBc}$.

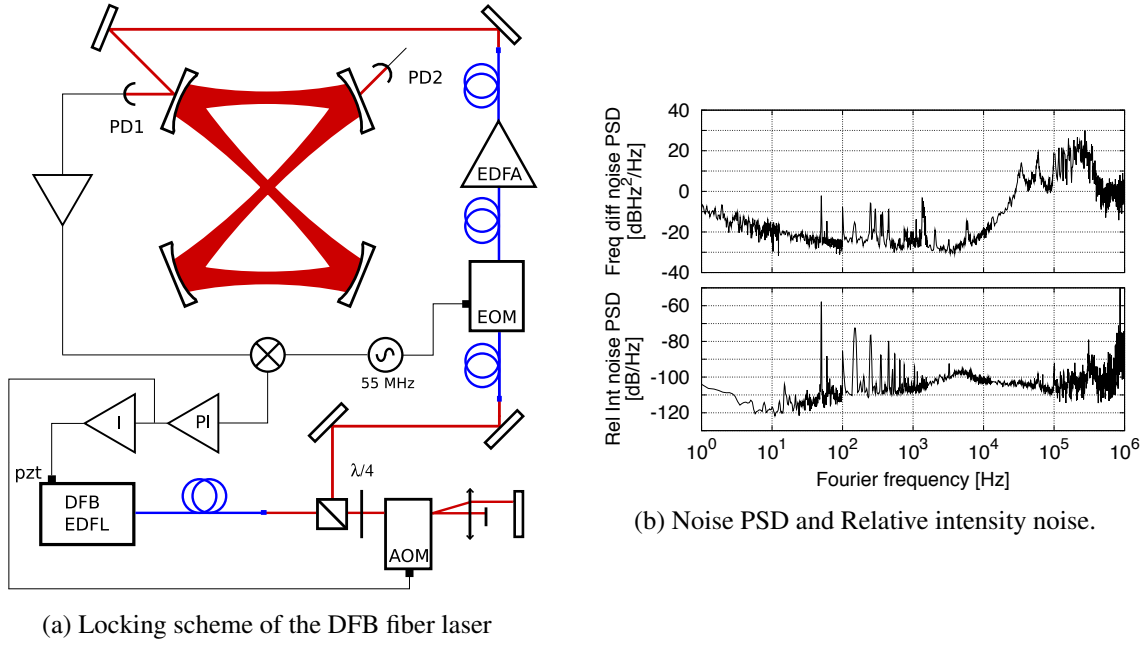


Figure 3.29: *Locking scheme and noise of the laser*

The noise intensity is measured in transmission on the cavity. The relative frequency noise is deduced from the Pound-Drever Hall signal and rely on a calibration of the error signal.

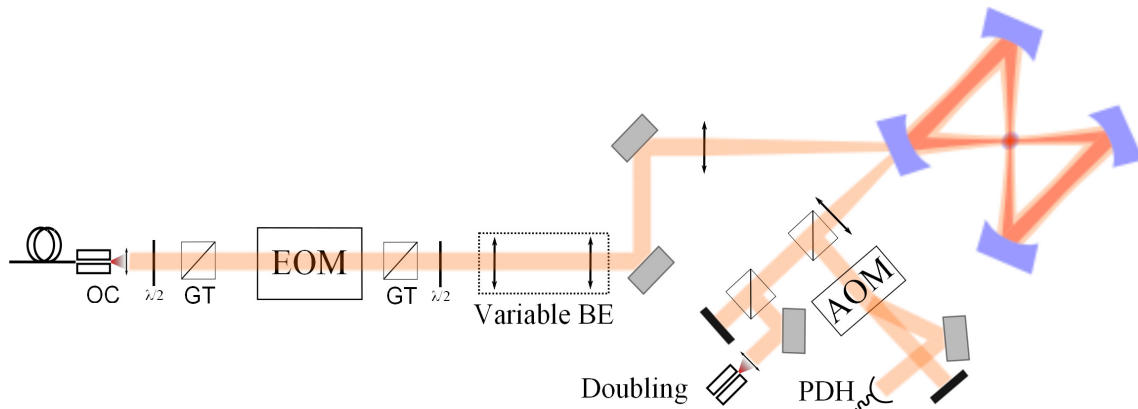
3.3.4 Opto-mechanical injection of the cavity

As it has been described in section 3.4b, the reference plate of the cavity is fixed to the upper flange of the vacuum chamber. In order to stabilize the pointing injection and to optimize the cavity coupling we designed a mechanical system directly attached to the vacuum chamber, and not to the optical table. For beam stability, the optical path from fiber output to the vacuum window has been made as short as possible. The path includes a Glan-Thompson polarizer to purify the polarization after the fiber, an amplitude modulator (EOM between two crossed polarizers, Conoptics) to control the beam intensity, a beam expander, two position adjustable mirrors and a coupling lens. In this set-up, The Glan-Thompson polarizers allow to achieve high extinction ratio of the amplitude modulator. Since the power is changed during the experimental sequence, a low power AOM has been inserted before the PDH photodiode to maintain a constant power on this one. The scheme and a picture of the opto-mechanical system are presented in figures 3.30a and 3.30b.

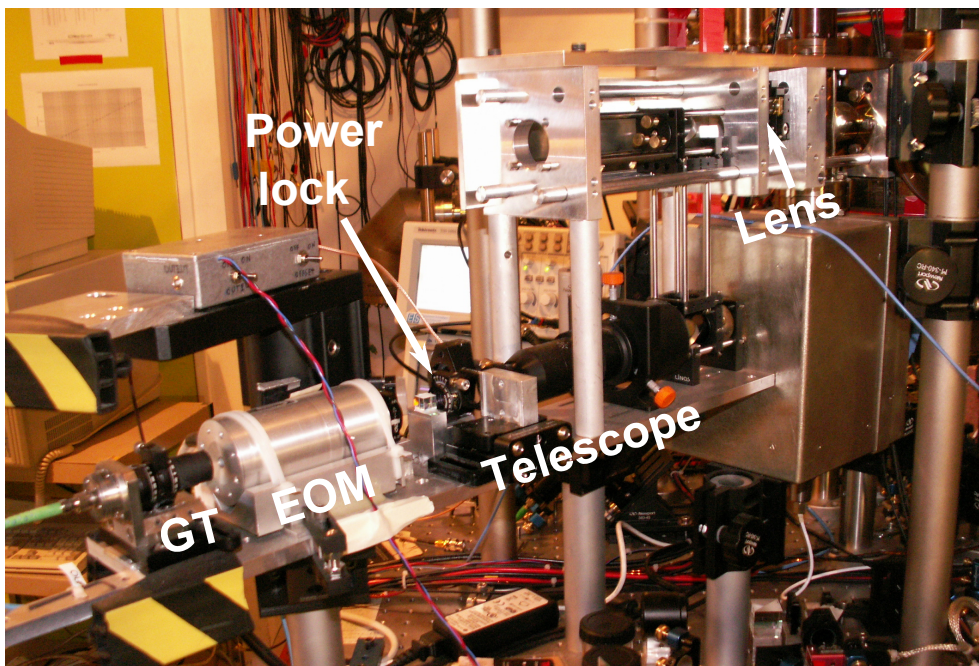
3.4 Summary

In this chapter we have presented a detailed characterization of the bi-frequency cavity used in the experiment. In particular, we have emphasized the criteria that led our choice of geometry. The cavity implemented has been carefully analyzed, and we have especially shown:

- The cavity has a four mirrors geometry which gives it a significantly different behavior with respect to a Fabry Perot resonator. The coupling efficiency for example is quite reduced in this configuration.



(a) Optical control of the light before the injection in the cavity.



(b) Picture of the mechanical injection of the cavity.

Figure 3.30: *Cavity injection opto-mechanics.*

The amplified fiber laser output is filtered in polarization (GT: Glan Thompson polarizer) and its power is controlled an amplitude modulator (EOM: Electro Optic Modulator used as an intensity controller). The mode matching is realized by a variable beam expander (BE) and a tilted lens doublet.

- The optical profile has been calculated and measured with different methods, including a transverse mode spectrum analysis and an *in situ* nondemolition measurement which relies on the differential ac-Stark shift induced by the 1560 nm light on ^{87}Rb atoms. All the methods agree within 10% and give horizontal and vertical waists of $95 \pm 5 \mu\text{m}$ and $128 \pm 5 \mu\text{m}$ respectively.
- The spectral characteristics of the cavity were measured with precise spectroscopic techniques which gave a linewidth of $2\pi \times 546 \cdot 10^3 \text{ rad.s}^{-1}$ at 1560 nm. At 780 nm, the linewidth has not been measured but the expected finesse $\mathcal{F} = 100\,000$ would lead to a resonance linewidth of about $2\pi \times 10 \cdot 10^3 \text{ rad.s}^{-1}$.
- The losses in the cavity can be inferred from the measurement of the intracavity power. It was shown that in our experiment the losses κ are essentially due to absorption and scattering on the surface of the mirrors. These losses are of the same order of magnitude than the mirror transmission t ($\kappa = 1.5 t$).
- The locking scheme of the 1560 nm laser is achieved using a Pound Drever Hall technique that allows to fast correct the frequency with an acousto-optic modulator in double pass.

Atomic samples trapped in a high finesse cavity

Contents

4.1	Introduction to Bose Einstein condensation	87
4.1.1	Saturation of the excited states	88
4.1.2	Effect of the interactions	89
4.2	Trapping atoms in a crossed optical cavity	90
4.2.1	Trapping cold atoms	92
4.2.2	Perspectives	99
4.3	Summary	101

Atom interferometers, such as a Ramsey-Bordé sequence [Riehle 91], rely on single particle interference. As this interferometers are operated close to the zero path length difference, the coherence of the source essentially presents no interest. In that perspective, atom interferometers do not take advantage of ultra-cold or condensed samples. Nevertheless, different geometries of the interferometers such as the bouncing gravimeter can be considered [Impens 06] and benefit for example of the low divergence of a condensate [Robert-de Saint-Vincent 10, Hughes 09].

In addition, as discussed in section 6.1.6, the density and number of atoms are of primary importance for the realization of efficient Quantum Non Demolition (QND) measurement valuable for the improvement of atom interferometers. In the set-up that we exploit, high number of particles ($\sim 10^7$) are trapped and automatically overlapped with the QND probe, hence realizing a situation close to an optimum for the generation of highly squeezed states.

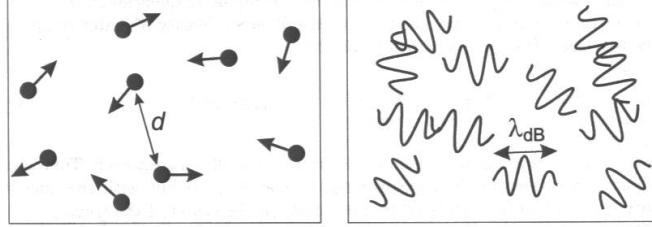
In the following, we will first theoretically introduce the subject of Bose Einstein condensation and raise the experimental parameters of concerns for the experimentalist. Secondly, we present the characteristics of the dipole trap that is realized by the fundamental mode of the cavity, and describe the loading procedure as well as the properties of the trapped cloud. At last we present the perspectives of cavity trapping that include the possibility to use the transverse modes to generate exotic potentials, and to use a second radiation at 1529 nm to engineer the differential light shift.

4.1 Introduction to Bose Einstein condensation

The Bose Einstein condensation corresponds to the transition where a macroscopic number of particles accumulates in the ground state of the system. In classical physics, particles are described as points, and the only relevant distance is the inter-atomic distance $d = n^{-1/3}$. On the other hand, in quantum mechanics, particles are formalized by wavefunctions which have an

extent given by the de Broglie wavelength $\lambda_{dB} = h/\sqrt{2\pi m k_B T}$.

For particles that are far enough from each other, the idea of particles that have a sort of radius given by λ_{dB} is easily acceptable. But how to interpret a case where the atoms are so close to each other that the wavefunction have to overlap? Particles can no more be distinguished from each other and the system crosses the critical point of the Bose Einstein condensation.



4.1.1 Saturation of the excited states

The bosonic character of the particles is of first importance in the process. Indeed, it is this character that allows the particles to overlap, and that even stimulates the overlap. This can be expressed through the statistics of the energy occupation of the bosons in a trap.

We consider a three dimensional harmonic trap in the form:

$$V(\mathbf{r}) = \frac{1}{2}m(\omega_x^2 x^2 + \omega_y^2 y^2 + \omega_z^2 z^2), \quad (4.1)$$

which admits a discrete set of energy levels:

$$\epsilon_{n,m,p} = \hbar(n\omega_x + m\omega_y + p\omega_z). \quad (4.2)$$

For Bosons at a temperature T , the number of particles in the state of energy $\epsilon_{n,m,p}$ is given by the Bose distribution:

$$N(\epsilon_{n,m,p}) = \frac{1}{e^{\frac{\epsilon_{n,m,p} - \mu}{k_B T}} - 1} \quad (4.3)$$

Tautologically, the number of atoms in the ground state N_0 is the number of atoms which are not in the excited states:

$$N_0 = N - \sum_{n,m,p \neq 0} N(\epsilon_{n,m,p}), \quad (4.4)$$

and, for the trap of concern, the number of atoms in the excited state is actually limited [Dalfovo 99] to:

$$\sum_{n,m,p \neq 0} N(\epsilon_{n,m,p}) = \zeta(3) \left(\frac{k_B T}{\hbar \bar{\omega}} \right)^3, \quad (4.5)$$

where $\zeta(n)$ is the Rieman function and $\bar{\omega} = (\omega_x \omega_y \omega_z)^{1/3}$ is the geometrical average of the trapping frequencies.

This is the so-called saturation of the excited states. If the number of particles N is increased above this value, for a given temperature T , the atoms have to accumulate in the ground state of the harmonic oscillator.

The critical temperature for the apparition of such a behavior can be expressed as a function of the number of atoms N . It is obtained when N exceeds the excited states population limit in equation (4.5):

$$T_c = \frac{\hbar\bar{\omega}}{k_B} \left(\frac{N}{\zeta(3)} \right)^{1/3} = 0.94 \frac{\hbar\bar{\omega}}{k_B} N^{1/3} \quad (4.6)$$

We notice that this expression confirms the comparison previously proposed. Indeed, the transition corresponds to the point where individual wavepackets start to overlap, *i.e.* when the phase-space density verifies:

$$D = n_0 \lambda_{dB}^3 \sim 1, \quad (4.7)$$

where n_0 is the atomic density at the center of the trap.

The atomic density of the thermal part (excited states) follows a Maxwell-Boltzman distribution ($n(\mathbf{r}) = n_0 \exp(-V(\mathbf{r})/k_B T)$) which has a width:

$$\sigma = \left(\frac{k_B T}{m\bar{\omega}} \right)^{1/2} \quad (4.8)$$

In the harmonic potential, the ground state wave function is given by:

$$\phi_0(\mathbf{r}) = \left(\frac{m\bar{\omega}}{\pi\hbar} \right)^{3/4} \exp\left(-\frac{m}{2\hbar}(\omega_x x^2 + \omega_y y^2 + \omega_z z^2)\right) \quad (4.9)$$

resulting in a density of the condensed part that is $n(\mathbf{r}) = N|\phi_0(\mathbf{r})|^2$, and an extension of the ground state:

$$a_{ho} = (\hbar/m\bar{\omega})^{1/2}. \quad (4.10)$$

For a gaz below T_c , the density distribution shows a bimodal distribution, with the thermal Gaussian on the outerpart and the condensed fraction in the center.

4.1.2 Effect of the interactions

The statistical behavior previously described in the case of a non-interacting gas effectively shows the apparition of a macroscopic population in the ground state of the harmonic oscillator. Nevertheless, to determine the wavefunction extension and the atomic density, the interactions have to be taken into account. In the case of dilute gas, where the scattering length ($a=5.3$ nm) is small compared to the interatomic distance $n^{-1/3}$, the interactions can be accounted by a mean repulsing field in the form: $V_{rep} = g_{rep}n(\mathbf{r}, t) = g_{rep}|\Psi(\mathbf{r}, t)|^2$ where $g_{rep} = 4\pi\hbar^2 a/m$.

The evolution of the wavefunction $\Psi(\mathbf{r}, t)$, is then governed by the Gross Pitaevskii equation:

$$i\hbar \frac{\partial}{\partial t} \Psi(\mathbf{r}, t) = \left(-\frac{\hbar^2 \nabla^2}{2m} + V_{ext}(\mathbf{r}) + g_{rep} |\Psi(\mathbf{r}, t)|^2 \right) \Psi(\mathbf{r}, t). \quad (4.11)$$

Looking for the ground state, we have a time independent problem, and the wavefunction can be separated in:

$$\Psi(\mathbf{r}, t) = e^{-i\frac{\mu}{\hbar}t} \varphi(\mathbf{r}), \quad (4.12)$$

where $\varphi(\mathbf{r})$ is the amplitude of density that verifies:

$$\mu\varphi(\mathbf{r}) = \left(-\frac{\hbar^2\nabla^2}{2m} + V_{ext}(\mathbf{r}) + g|\varphi(\mathbf{r})|^2 \right) \varphi(\mathbf{r}) \quad (4.13)$$

The chemical potential μ is the energy that it would cost to take one atom out of the condensate wavefunction.

Thomas-Fermi regime

In the case of large particles number, the interaction energy overcomes the kinetic energy : $N \gg a_{ho}/a_s$, and we enter the Thomas-Fermi regime. The wavefunction in this regime has a simple solution:

$$\varphi(\mathbf{r}) = \begin{cases} \sqrt{\frac{\mu - V_{ext}(\mathbf{r})}{G}} & \text{if } \mu \geq V_{ext}(\mathbf{r}) \\ 0 & \text{otherwise} \end{cases}$$

With the interactions, the atomic density in an harmonic trap takes the form of an inverted parabola:

$$n(\mathbf{r}, t) = |\Psi(\mathbf{r}, t)|^2 = |\varphi(\mathbf{r}, t)|^2 \quad (4.14)$$

$$= \frac{\mu - V_{ext}(\mathbf{r})}{g} \quad (4.15)$$

$$= n_0 \max \left(1 - \left(\frac{x}{R_x} \right)^2 - \left(\frac{y}{R_y} \right)^2 - \left(\frac{z}{R_z} \right)^2, 0 \right). \quad (4.16)$$

The radii of the parabola are:

$$R_i = \sqrt{\frac{2\mu}{m\omega_i^2}}, \quad (4.17)$$

and the normalization of the atomic density to the total number of particles N gives the chemical potential expression:

$$\mu = \frac{\hbar\omega_{ho}}{2} \left(\frac{15Na}{a_{ho}} \right)^{2/5} \quad (4.18)$$

4.2 Trapping atoms in a crossed optical cavity

In the description given above we show that Bose Einstein condensation can be reached if one is able to obtain a phase-space density (atomic density and temperature) that fulfills equation 4.7. Practically, it means that the temperature of the sample should be decreased and/or the density should be increased. For an experimentalist, the obvious question is how such a regime can be reached. The answer was given back in the 90's and is called the evaporation process. Removing the particles of the sample which have the highest energy allows to reduce the mean energy per particles and thus to increase the phase-space density. This technique has been efficiently applied in the case of magnetic traps [Anderson 95, Davis 95, Bradley 95] and optical dipole trap [Barrett 01]. In the following, we focus on the specific case of the dipole potential that is created by the modes of our optical cavity.

4.2.0.1 The optical dipole potential

In order to trap the atoms in a non-dissipative potential, we use the spatially dependent light shift created by the Gaussian profile of the fundamental cavity mode. In annexe D, we derived a complete expression for the polarizability. In our case of concern, the driving field at 1560 nm is very far from the D_1 and D_2 transitions (see annexe A). Hence, the hyperfine splitting can be neglected and the polarizability of the hyperfine ground state becomes:

$$\alpha_{F=1,2} = \frac{1}{\hbar} \left(\frac{\omega_0}{\omega_0^2 - \omega^2 + i\Gamma \frac{\omega^3}{\omega_0^2}} \sum_{F', m'_F, q} \left| \langle J' = 1/2, F', m'_F | \hat{d}_q \cdot e_q | J, F, m_F \rangle \right|^2 \right. \\ \left. + \frac{\omega_1}{\omega_1^2 - \omega^2 + i\Gamma \frac{\omega^3}{\omega_1^2}} \sum_{F', m'_F, q} \left| \langle J' = 3/2, F', m'_F | \hat{d}_q \cdot e_q | J, F, m_F \rangle \right|^2 \right), \quad (4.19)$$

where $\omega_0 = 2\pi c/\lambda_0$ and $\omega_1 = 2\pi c/\lambda_1$ are the transition frequencies of the D_1 ($\lambda_0 = 794.98$ nm) and D_2 lines ($\lambda_1 = 780.03$ nm) respectively.

From the symmetry of the dipole operator [Steck 10], we have:

$$\alpha_{F=1,2} = \frac{1}{\hbar} \left(\frac{\omega_0}{\omega_0^2 - \omega^2 + i\Gamma \frac{\omega^3}{\omega_0^2}} \frac{(J' = 1/2 \| d \| J)^2}{2J + 1} + \frac{\omega_1}{\omega_1^2 - \omega^2 + i\Gamma \frac{\omega^3}{\omega_1^2}} \frac{(J' = 3/2 \| d \| J)^2}{2J + 1} \right) \quad (4.20)$$

where $(J' = 1/2 \| d \| J) = 4.228ea_0$ and $(J' = 3/2 \| d \| J) = 5.97ea_0$ are the reduced dipole elements given in [Arora 07]. Using the definition of the linewidth that is [Grimm 00]:

$$\Gamma = \frac{\omega_0^3}{\pi\epsilon_0\hbar c^3} \frac{(J' = 1/2 \| d \| J)^2}{2J' + 1} \sim \frac{\omega_0^3}{3\pi\epsilon_0\hbar c^3} \frac{(J' = 3/2 \| d \| J)^2}{2J' + 1} \quad (4.21)$$

we finally find:

$$\alpha_{F=1,2} = \frac{\pi\epsilon_0 c^3}{\omega_0^3} \left(\frac{\Gamma\omega_0}{\omega_0^2 - \omega^2 + i\Gamma \frac{\omega^3}{\omega_0^2}} + \frac{2\Gamma\omega_1}{\omega_1^2 - \omega^2 + i\Gamma \frac{\omega^3}{\omega_1^2}} \right) \quad (4.22)$$

Hence, atoms in the hyperfine ground state will be transversally trapped by a Gaussian intensity profile I in an optical potential given by:

$$U = -\text{Re}(\alpha_{F=1,2}) \frac{I}{2\epsilon_0 c} \quad (4.23)$$

Because the real part of α is positive, this potential is indeed trapping for a maximum of intensity.

In our experimental configuration which consists of two Gaussian modes that cross at 90° , the optical potential is given by:

$$U = -\text{Re}(\alpha_{F=1,2}) \frac{P_0}{\pi\epsilon_0 c w_h w_v} e^{-2\frac{z^2}{w_v^2}} \left(e^{-2\frac{x^2}{w_h^2}} + e^{-2\frac{y^2}{w_h^2}} \right) = U_0 e^{-2\frac{z^2}{w_v^2}} \left(e^{-2\frac{x^2}{w_h^2}} + e^{-2\frac{y^2}{w_h^2}} \right). \quad (4.24)$$

where $w_h \sim 98 \mu\text{m}$ and $w_v \sim 128 \mu\text{m}$ are the waists of the cavity mode, and $U_0 = -\text{Re}(\alpha_{F=1,2})P_0/(\pi\epsilon_0 c w_h w_v)$ is the potential depth of one arm.

Close to the bottom of the trap, U can be approximated by an harmonic potential U_{har} :

$$U_{\text{har}} = U_0 \left(1 - 4\frac{z^2}{w_v^2} - 2\frac{x^2}{w_h^2} - 2\frac{y^2}{w_h^2} \right) = U_0 - \frac{m\omega_z^2 z^2}{2} - \frac{m\omega_x^2 x^2}{2} - \frac{m\omega_y^2 y^2}{2} \quad (4.25)$$

where

$$\omega_x = \omega_y = \sqrt{\frac{4U_0}{mw_h^2}}, \quad \text{and} \quad \omega_z = \sqrt{\frac{8U_0}{mw_v^2}} \quad (4.26)$$

are the trapping frequencies.

The value of the depth and the trap frequencies are given in table 4.1, for the experimental value usually achieved:

Parameters	Full power	Loading
Power at one output P_{out}	80 mW	8mW
Intracavity power in one arm P_{intra}	228 W	22.8W
Intracavity intensity in one arm I_{intra}	$11.9 \times 10^9 \text{ W.m}^{-2}$	$1.19 \times 10^9 \text{ W.m}^{-2}$
Depth in one arm U_0	$1.47 \times 10^{-26} \text{ J}$	$1.47 \times 10^{-25} \text{ J}$
Depth in one arm U_0	3.69Γ	0.369Γ
Depth in one arm U_0	1.1 mK	0.11 mK
Horizontal trapping frequencies ω_x	$2 \pi 1.04 \text{ kHz}$	$2 \pi 329 \text{ Hz}$
Vertical trapping frequencies ω_z	$2 \pi 1.13 \text{ kHz}$	$2 \pi 356 \text{ Hz}$

Table 4.1: *Relevant parameters for our trap configuration.*

In the table 4.1, the intracavity power is computed using equation (3.55).

Scattering

From the expression of the polarizability in equation 4.22, we can derive the scattering rate of an atom at the position \mathbf{r} of the potential:

$$\Gamma_{\text{scatt}} = \frac{\text{Im}(\alpha_{F=1,2})I(\mathbf{r})}{\hbar\epsilon_0 c} \quad (4.27)$$

In our specific case, in the center of the trap that is operated at full power, this makes a scattering rate that is $\Gamma_{\text{scatt}} = 1.6 \text{ event.s}^{-1}$. The full power is only conserved for a few ms before the power is ramped down for the evaporation, and this rate should not play any role in the evaporation.

4.2.1 Trapping cold atoms

4.2.1.1 Loading the dipole trap

We focus now on the transfer of atoms from the MOT to the dipole trap. This process is among the most critical to achieve a Bose Einstein condensate [Barrett 01] in an all optical evaporation.

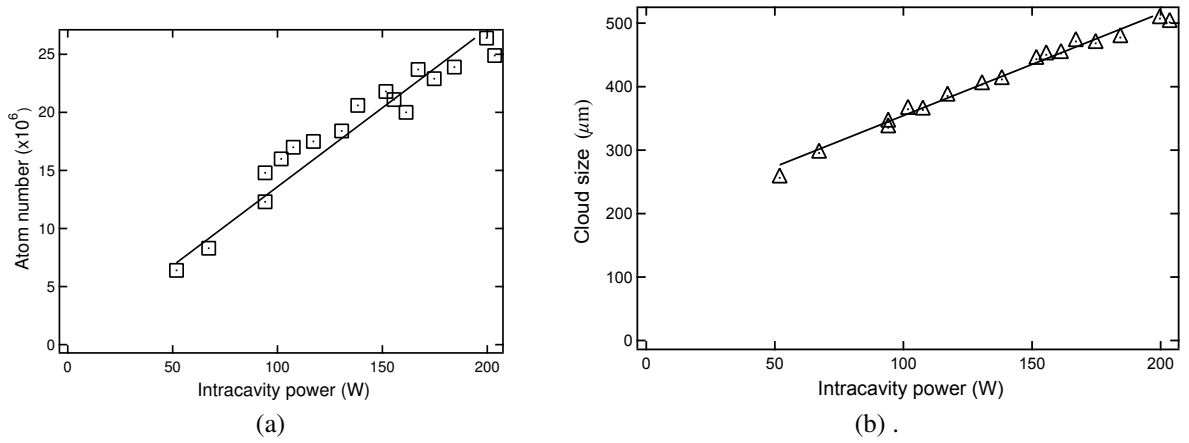


Figure 4.1: *Atoms loaded in the dipole trap.*

(a) Number of atoms kept in the dipole trap after 1 s of trapping as a function of the intracavity optical power. (b) Temperature of the atoms in the dipole trap measured by the cloud size after a time of flight expansion and given as a function of the intracavity power.

Contrarily to magnetic traps that uses an RF knives to adjust the potential depth, optical traps uses directly the finite depth of the trap for the evaporation. Hence, to lower the temperature, it is directly the optical power that is lowered. But this reduces the trapping frequencies, and lowers the efficiency of the evaporation. In such an evaporation, an efficient loading is essential to start with the highest phase-space density possible ($\sim 10^{-3}$). Actually, it is mainly thanks to a high loading efficiency that the first all optical BEC was achieved [Barrett 01].

The first parameter that optimizes the loading is the overlap of the MOT (few 100 μm) with the dipole trap ($\sim 100 \mu\text{m}$). In addition, to maximize the phase-space density in equation (4.7):

$$D \propto N \left(\frac{\bar{\omega}}{T} \right)^3, \quad (4.28)$$

the trapping frequencies should be as high as possible. In equation 4.28, $\bar{\omega} = (\omega_x \omega_y \omega_z)^{1/3}$ is the geometrical average of the trapping frequencies. Equation 4.26 shows that either the power should be increased or the waist should be lowered. To increase the power is not an ideal solution. Atoms loaded in the arms of the optical potential acquire the energy of the depth of the trap when they fall in the trapping region. Hence, the thermalized sample has a temperature that scales linearly with the potential depth. On the other hand, the trapping frequencies scale as the square root of the depth (equations 4.26), meaning in equation 4.28 a loss of phase-space density. A better solution is to lower the waist but it is in contradiction with the optimization of the mode overlap. Our chosen optical waist of 100 μm results from a compromise to keep an efficient loading with frequencies in the kHz range.

Differential light shift: the induced Dark MOT

As it has been previously mentioned in section 3.2.5.2, the 1560 nm light not only creates a dipole trap for the atoms, but also shifts the state $5^2P_{3/2}$ which is part of the cycling transition for laser cooling. This induces some subtleties since the coupling of the atoms to the cooling light is

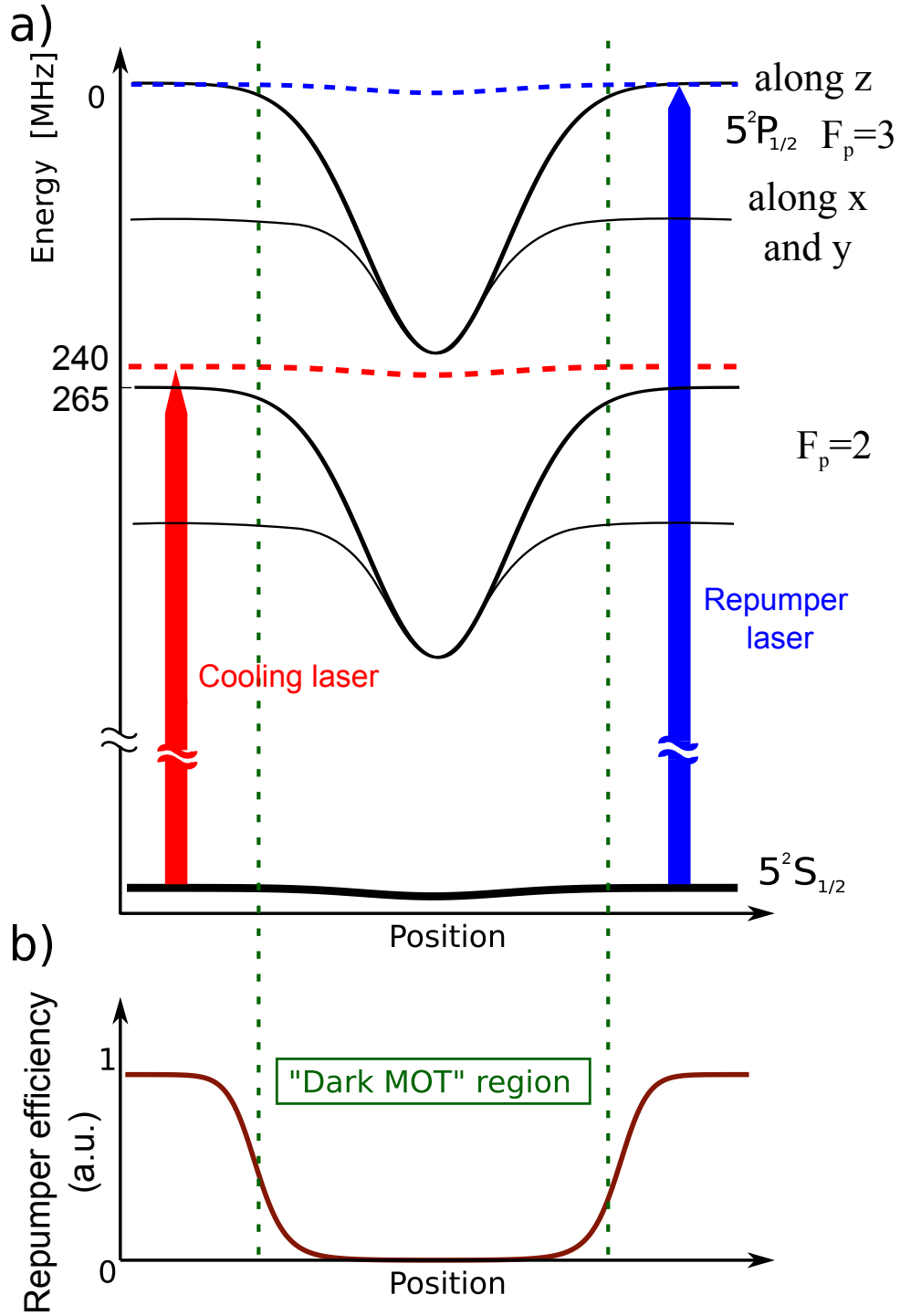


Figure 4.2: Scheme realized to load the dipole trap.

In the center of the trap the repump light is far from resonance, and the atoms accumulate in $|F = 1\rangle$. The depth of the trap during the loading is chosen such that the cooling laser can be in between the transition to the hyperfine state $|F_p = 2\rangle$ and $|F_p = 3\rangle$ whatever the position of the atoms in the trap.

now dependent on their position in the trap [Griffin 06]. In [Clément 09, Clement 08], different methods are presented to efficiently load a trap at 1560 nm. The more efficient took advantage of this differential light shift to create an induced Dark MOT in the trap. The principle of this method [Clement 08] is schematically presented in figure 4.2 and is applied in our experimental sequence:

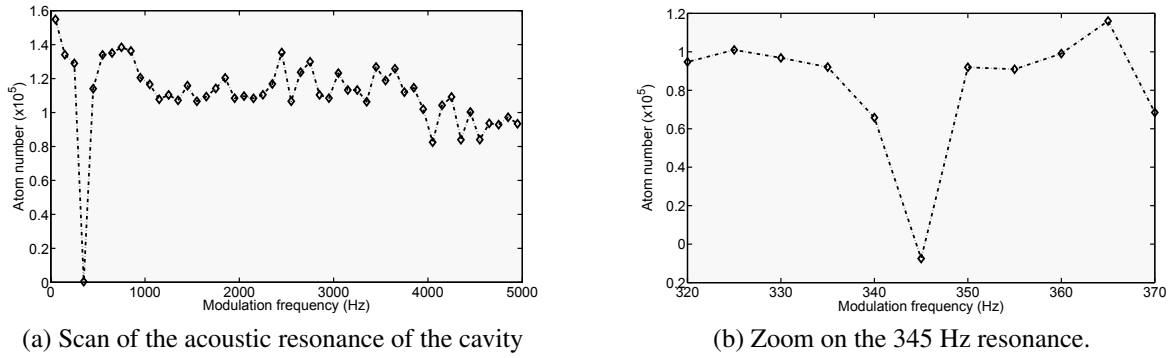
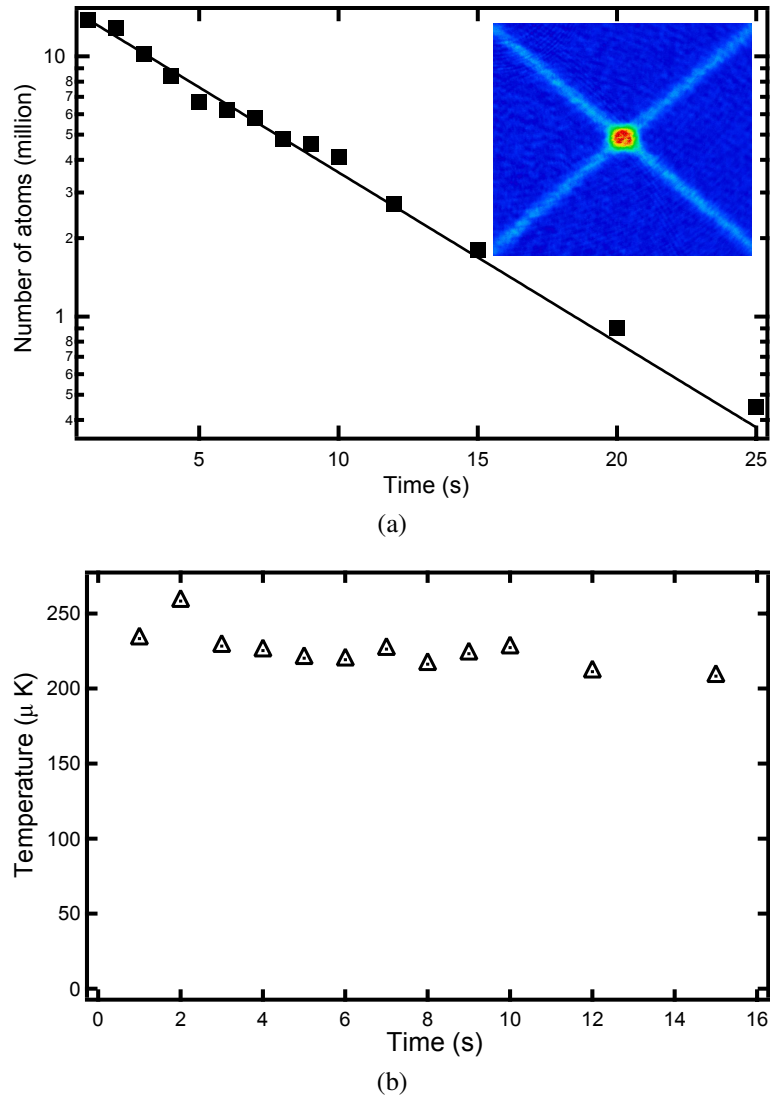
- A 3D MOT of about 10^{10} atoms is loaded from the 2D MOT source. For the loading, the depth of the far off resonance dipole trap (FORT) starts at $\sim 110 \mu\text{K}$.
- A compressed MOT phase [Petrich 94] is operated by detuning the MOT beams to 5Γ from the atomic resonance for 50 ms. The cloud is compressed and the atomic density increases in the FORT region.
- The cooling beams are further detuned to 40Γ for 100 ms. At this detuning, the cooling radiation is on the red-side of the $|F = 2\rangle \rightarrow |F_p = 3\rangle$ transition for any position of the atoms in the trap. Indeed, the depth of the FORT during the loading is fixed to $\sim 110 \mu\text{K} = 35\Gamma$, such that there still exists a frequency range where the cooling laser can be in between the $|F = 2\rangle \rightarrow |F_p = 3\rangle$ and $|F = 2\rangle \rightarrow |F_p = 2\rangle$ transitions even in the presence of the strong differential light shift (see figure 4.2). Moreover, in the FORT region the repump light is out of resonance and the atoms accumulate in the $|F = 1\rangle$ hyperfine state, realizing in this way a dark SPOT MOT [Ketterle 93] induced by the 1560 nm light shift.
- Finally, the cooling radiation and the MOT coils are turned off (cooling and repumper lasers), and the power in the FORT can be either kept constant or ramped up. In figure 4.4, we see for example the number of atoms present after 1s for different final power in the FORT.

At the end of the loading sequence about 20 million atoms are loaded in the crossing region of the dipole trap that has been raised to full power, and the temperature of the cloud is about $230 \mu\text{K}$ (see figure 4.4b).

Remark: As the dipole trap is operated in the cavity, the 1560 nm light cannot be turned on and off at will. To be able to repeat the sequences, the laser needs to stay locked all the time. Actually, the stability of our set-up allows us to turn the power off for a few ms during which the images of the sample are taken. When the laser is turned on again, it automatically re-locks.

4.2.1.2 Keeping cold atoms...

In the history of the experiment, the trapping of atoms in the mode of the cavity has been quickly achieved. Nevertheless, in the early stage of the experiment the dipole trap had a lifetime of about 100 ms. Some fundamental limiting processes such as two photon Raman transitions, molecular recombination or two photon excitations were suspected but all of them are orders of magnitude away to generate such an effect. As a matter of fact, the heating rate limiting the trap lifetime proved to be linked to the retroreflected light mentioned in section 3.2.7.1. In principle this light is phase related to the forward propagating field, and the interference pattern between the backward and the forward traveling field should be fixed. Nevertheless, the acoustic environment in the laboratory as well as the noise on the piezo that controls the length of the cavity cannot be ignored.

Figure 4.3: *Acoustic resonance of the cavity.*Figure 4.4: *Free evaporation in the trap.*

Atom number (a) and temperature (b) in the dipole trap as a function of time when the power in the dipole trap is kept constant.

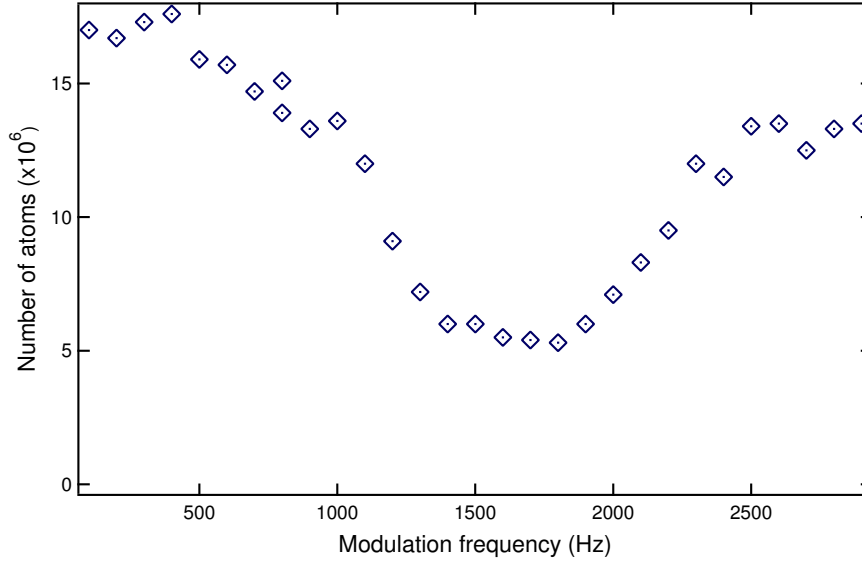


Figure 4.5: *Trapping frequencies measurement by parametric excitations.*

A fluctuation of the intensity of the dipole trap is induced and the losses of atoms are measured as a function of the excitation frequency.

In figure 4.3 the atom number kept in the dipole trap is presented as a function of the frequency of an acoustic wave excitation. It clearly exhibit a resonance at 345 Hz, which is attributed to a mechanical resonance of the cavity. In the natural environment of the lab, there is no specific excitation at this peculiar frequency, and the losses are essentially linked to the background acoustic noise and the residual noise of the piezo-elements that control the cavity length.

The backward reflected light is lowered by adjusting the position of the cavity mirrors, and the noise on the piezo elements of the cavity have been passively filtered to lower the displacement of the residual fringes.

After such an optimization, the trapping time of the dipole trap reached 6.6 s. As shown in figure 4.4a, it is limited by one body collisions with the residual background gas as indicated by the exponential decay. After thermalization in the full trap, the sample temperature is 230 μ K, leading to a temperature to trap depth ratio $k_B T/U_0 \sim 4.8$. No increase of the temperature can be seen in figure 4.4b, which indicates that the evaporation can be started. The phase-space density before any evaporation is 9.2×10^{-5} . As the ratio η is small compare to other experiment (~ 10 in [Clément 09]), it should be possible to lower further the initial temperature and then to increase the initial phase-space density.

Using the tomographic characterization of the cavity mode, we were able to precisely measure the waist of the mode, which gives us the horizontal trapping frequency. For the vertical trapping frequency equation 4.26 gives an estimate, but it relies on the assumption that the two arms are well crossed on the vertical. At a high trap depth, this parameter is measured in-situ by parametric excitations (see figure 4.5). For a low trap depth, they are estimated by time-of-flight measurement that are extrapolated to 0.

Parametric excitation To measure the trapping frequencies, we induce a modulation of the intensity of the dipole trap and observe the number of atoms that remain in the trap. Experi-

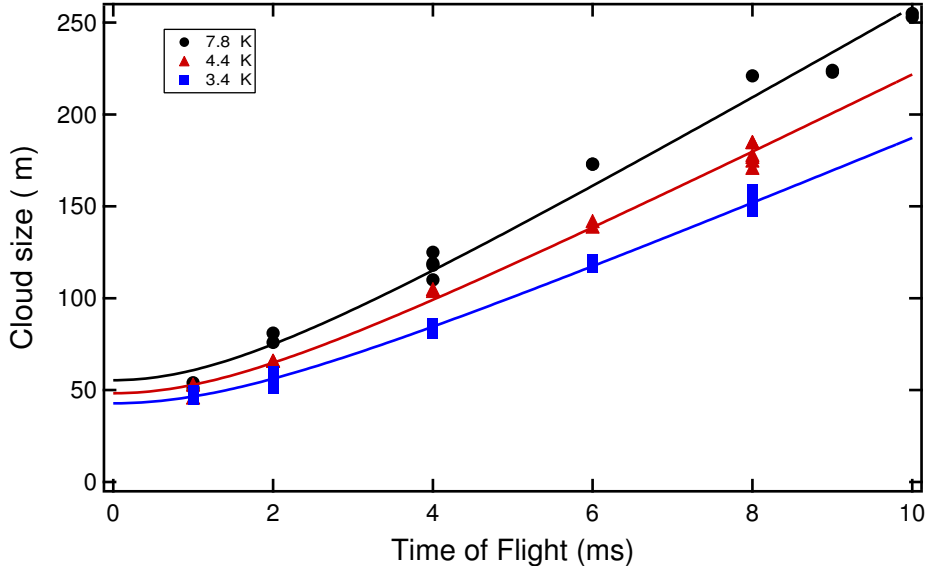


Figure 4.6: *Trapping frequencies measurement by time of flight expansion.*

The time of flight expansion gives the temperature and its extrapolation to 0 gives the initial rms size.

mentally, atoms are loaded in the dipole trap as described in section 4.2.1.1. The intensity of the dipole laser is increased and after the thermalization, a modulation is applied to the intensity of the laser. It was shown in [Gehm 98, Savard 97] that due to the parity of the excitation, the excitation resonances are twice the trapping frequencies. The result obtained is presented in figure 4.5 and is centered around 1.6 kHz, leading to trap frequencies of 800 Hz. This value is small compared to our expectation (1.1 kHz). In addition, the resonance in figure 4.5 is quite large compare to similar measurements [Brantut 08b]. A default in the alignment of the two arms is suspected to be the reason of both the enlargement and the low frequencies. This point is presently under study.

Time-of-flight measurement In the case of small trap frequencies, the method of parametric excitation cannot be applied because its resonance is too large. In order to estimate the frequency, we proceed to a time of flight expansion of the cloud as presented in figure 4.6. Extrapolating the expansion towards 0, and using equation 2.10, we obtain the initial rms size of the cloud σ_0 , the temperature T and the atom number N . The initial density at the center of the cloud for a thermalized sample is :

$$n_0 = \frac{N}{(2\pi\sigma_0^2)^{3/2}} = \frac{Nm^{3/2}\omega_h^2\omega_v}{(2\pi k_B T)^{3/2}} \quad (4.29)$$

Hence, the geometrical averaged frequency is given by:

$$\bar{\omega} = \frac{1}{\sigma_0} \sqrt{\frac{k_B T}{m}}. \quad (4.30)$$

The data presented in figure 4.6 are obtained after reduction of the trap depth to three different values of the intracavity power that correspond to final temperature of 7.8, 4.4 and 3.4 μ K. The frequency obtained from equation 4.30, are respectively: $\bar{\omega}_1 = 2\pi \ 78.5 \text{ Hz}$, $\bar{\omega}_2 = 2\pi \ 67.8 \text{ Hz}$

and $\bar{\omega}_3 = 2\pi \cdot 67.1$ Hz. The expected ratio calculated from the final power are $(\bar{\omega}_1/\bar{\omega}_2)_{\text{exp}} = 1.12$ and $(\bar{\omega}_1/\bar{\omega}_3)_{\text{exp}} = 1.38$, and the measured one are $(\bar{\omega}_1/\bar{\omega}_2)_{\text{meas}} = 1.16$ and $(\bar{\omega}_1/\bar{\omega}_3)_{\text{meas}} = 1.7$. This tends to indicate that the sample at 3.4 μK was not yet thermalized.

In addition, the first set of data at 7.8 μK , was realized for a trap depth $\sim 1/38$ times lower than the full trap depth. Using equation 4.26, we find that at full power the trapping frequencies should be $\bar{\omega} = 484$ Hz, which is contradictory with the measurement realized by the parametric excitation. This discrepancy is attributed to the effect of the gravity that modifies the shape of the potential for low potential depths.

At the end of these sequences, the phase-space density obtained are $D_1 = 2.8 \times 10^{-4}$, $D_2 = 9.1 \times 10^{-4}$ and $D_3 = 1.5 \times 10^{-3}$. These values are still far from the critical value of 1. Current efforts are oriented to reach a lower temperature in the trap at full depth.

4.2.2 Perspectives

Recent progress in the experiment allowed the trapping of a large number of atoms (10^7) on long time scales (5 s), opening the way to the Bose-Einstein condensation in the mode of the cavity. This is presently the main goal. Up to now we obtained an efficient loading, and more work is needed to lower the temperature, which may require some initial cavity cooling [Vuletic 00] and to optimize the evaporation process [Wu 97, Luiten 96]. In addition, to the condensation in the fundamental mode, it could be very interesting to couple the condensate to higher modes of the cavity that present multiple extrema of the intensity. This would open the way to the creation of scalable trap array. Interestingly, based on the 1560 nm differential light shift, the use of different wavelengths could allow to engineer the atomic state.

4.2.2.1 Higher modes trapping

As shown in figure 4.7, trapping in these higher modes has already been achieved. These multi-trap geometry can be raised at any time in an experimental sequence, and could be superimposed to the fundamental mode, allowing to condense and to split the cloud or on the contrary to condense in a multi-trap geometry and to regroup the condensate in the fundamental mode. The modes are transverse modes of the cavity, they are non-degenerate, and apart from each other by several tenth of MHz. The local beatnote between the modes is modulated at this frequency difference and the dynamics of the atoms should not be affected by it, and will only react to the average potential.

4.2.2.2 Engineering the light shift

As described for the loading procedure, the 1560 nm creates a strong light shift on the D_2 line that is used for the cooling. This prevents the loading of the trap at full trap depth. One solution considered to overcome this difficulty, is to use a laser at 1529 nm injected in the cavity, and that compensate for the differential light shift [Griffin 06]. Indeed, as this radiation is blue detuned but close to the $5^2P_{3/2} \rightarrow 5^2D_{3/2,5/2}$ transitions, it creates on the $5^2P_{3/2}$ an opposite effect with respect to 1560 nm light. In addition, as the wavelength (1560 nm and 1529 nm) are close, the profile of the modes are similar and the engineered light shift can reproduce very well a magic wavelength. Figure 4.8 represents the differential light shift between the ground state $5^2S_{1/2}$ and the excited state $5^2P_{3/2}$ when such a compensation is realized. It shows that the residual differential light shift can be cancelled in one point (e.g. at the center), but the overall

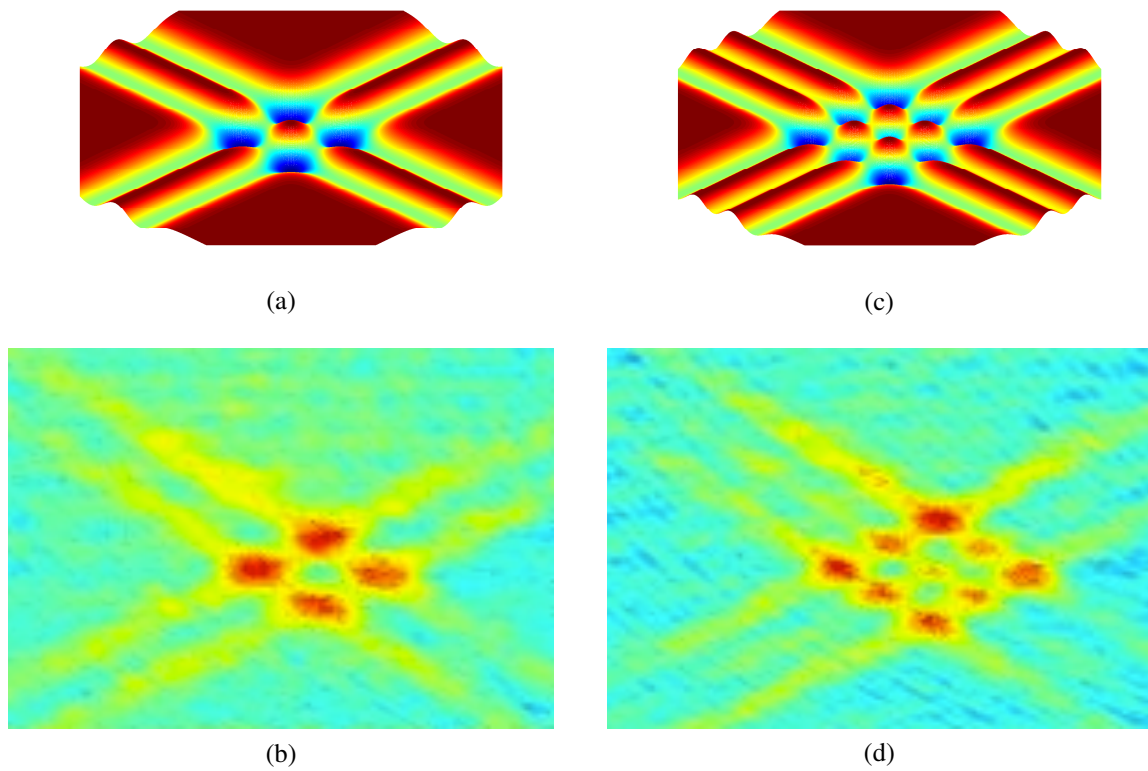


Figure 4.7: *Trapping in the transverse modes.*

In (b) and (d) two clouds are shown that were trapped in the TEM_{01} and TEM_{02} transverse modes respectively. In (a) and (c) are the potentials calculated for the corresponding Hermit-Gauss modes.

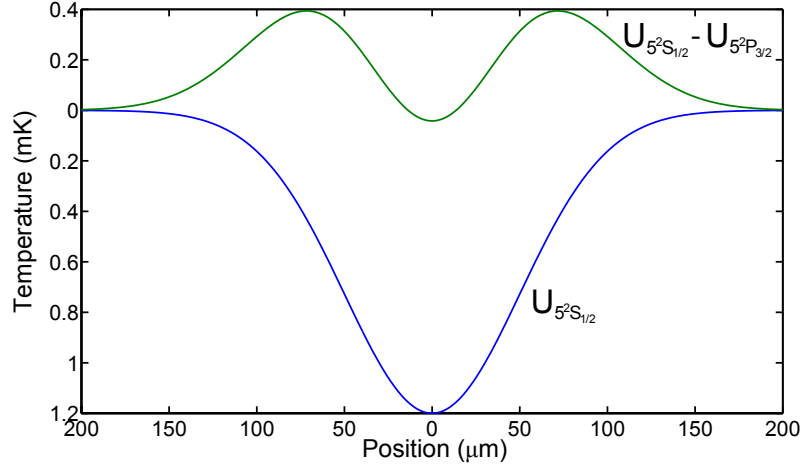


Figure 4.8: *1529 nm compensation of the light shift.*

The dipole trap shape of the ground state is presented in blue (below) and the residual differential light shift of the excited state is in green (above).

shape will still present light shift fluctuations of the order of the ground state depth ($\sim \Gamma$ at full power). The curves in figure 4.8 are given for a power of 200 W of the 1560 nm radiation concentrated in 100 μm waist. The 1529 nm radiation was adjusted to a power of 2.36W in $100\sqrt{1.529/1.56} = 98 \mu\text{m}$ waist.

The light shift of the excited state that is created by the 1560 nm alone is of the order of 1.2 GHz. To control the engineered light shift suppression, for example, at better than the inhomogeneity on the cloud size, requires a relative power stability of the 1529 nm light with respect to the 1560 nm light that is $\delta P/P \sim 5 \times 10^{-3}$.

We underline that this compensation may actually be very valuable for the realization of the dispersive nondemolition measurement. Indeed, it allows to uniformly couple the atoms to the probing light, independently of their position.

Some work in this direction has been already realized with the locking of the 1529 nm to a test cavity. For this lock we developed a frequency control through a serrodyne procedure [Johnson 10] that appears to be promising.

4.3 Summary

In this chapter we have presented the work realized in the direction of the trapping of cold atoms in the modes of the cavity. We first introduced the parameters relevant for the description of an ultra cold atomic sample and showed that a dipole trap at 1560 nm realized in the fundamental mode of the cavity was suitable for such a purpose.

In the second part, we described the loading procedure of the trap that needs to take into account for the differential light shift of the excited state. We showed that about 20 million atoms are loaded in the crossing region of the dipole trap. After a reduction of the effect of the backward propagating light, a lifetime of 6.6 s was obtained in the dipole trap. The trapping frequencies that are of primary importance for the condensation were measured by parametric excitation and time of flight evaluation.

At last we present the possibility to use the higher transverse modes to trap in different geometries. In addition, to compensate for the differential light shift induced by the 1560 nm

radiation we consider the injection of 1529 nm radiation that would allow to engineer the differential light shift.

Atomic squeezing induced by Quantum Non-Demolition measurement: theory

Contents

5.1	Introduction to the Bloch sphere	104
5.1.1	Coherent manipulation of a single two level system	104
5.1.2	The rotation operators and the Bloch sphere	106
5.1.3	Extension to the many body system	108
5.1.4	Shot noise in atomic interferometry	111
5.2	Quantum Non-Demolition measurement	114
5.2.1	Global measurement	114
5.2.2	Element of theory	114
5.2.3	Optical phase detection	119
5.3	Quantum trajectories in a wavefunction analysis of the squeezing process	121
5.3.1	Background formalism	121
5.3.2	The Mach-Zehnder interferometer	122
5.3.3	Long term behavior	128
5.3.4	The Mach-Zehnder including losses and in an optical cavity	130
5.3.5	The heterodyne measurement	134
5.3.6	Comparison between the Mach-Zehnder interferometer and the heterodyne measurement	143
5.3.7	Comment on the photon by photon versus single pulse measurement	143
5.3.8	Perspectives	145
5.4	Summary	149

The measurement in quantum mechanics is at the same time one of the simplest and one of the most complex principles. Indeed, when looking to the formalism it looks fairly simple, since it is composed of easily applicable rules. When measured, a physical system is projected on an eigenvector of the measured variable, that is the observable. In this way, a repeated measurement on the system should always give the same result. The description of systems as wavefunctions and the possibility to project the wavefunction on a single state (the eigenstate) is at the heart of the wave-particle duality. But it is also one of the most disturbing fact in quantum mechanics: our world and the behavior of system are quantum, and described by a wavefunction that can exhibit different results in the same situation. In the quantum mechanical description of

the measurement process, physical objects acquire properties that were not intrinsically present before the measurement.

In this chapter, we will not answer these deep questions but merely try a modest approach to address the problem of partial measurements on practical devices. The measurement that has been described above is the ideal projective measurement that requires an infinite signal-to-noise to be able to fully distinguish between eigen-vectors. Obviously, a measurement device does not have such a signal-to-noise and some care should be taken when treating it.

In a first part, we will describe the physical system that is composed of N two level atoms and introduce some formalism for its description. This formalism is then applied to show the influence of the atomic shot-noise on the performance of atomic interferometers. In a second part, we will give some elements of the theory of Quantum Non-Demolition (QND) measurement and show that the dispersive measurement foreseen in our experiment is indeed QND. In the last part, we introduce a wavefunction formalism that allows us to describe the partial projection of the atomic wavefunction photon after photon. This description is particularly useful to understand the dynamical collapse of the atomic state that leads to the creation of a squeezed state.

5.1 Introduction to the Bloch sphere

In this section, we will introduce the Bloch sphere formalism, which is convenient to describe the coherent manipulation of atoms or to represent squeezed states. In that purpose, we will start from the Hamiltonian which holds clear evidence of the physics, and derive the proper set of operators for the description of the evolution: the Pauli matrices.

5.1.1 Coherent manipulation of a single two level system

As described in figure. 5.1, we consider here the case of a two level atom ($|g\rangle, |e\rangle$) driven by an off-resonant electro-magnetic field $E = A_0 \exp i(\omega t + \phi)$, with angular frequency ω and phase ϕ . We will use in the following a semi-classical description where the atoms are quantized and the field is classical. The atomic state evolves with respect to the Hamiltonian \mathcal{H} :

$$\mathcal{H} = \mathcal{H}_{\text{at}} + \mathcal{H}_{\text{I}}, \quad (5.1)$$

where \mathcal{H}_{at} describes the free evolution of the atoms and \mathcal{H}_{I} the atom-field interaction.

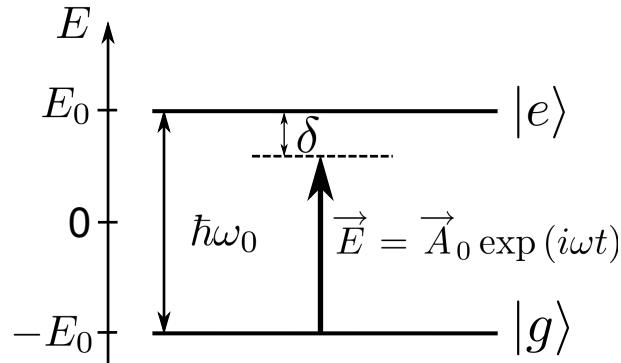


Figure 5.1: *Two level atom scheme.*

The two levels have energies $\pm E_0 = \pm \hbar\omega_0/2$. The driving field \mathbf{E} is frequency detuned by $\delta = \omega - \omega_0$ from the atomic transition.

The zero of potential energy is chosen in between the two states. The atomic free evolution is described by the Hamiltonian :

$$\mathcal{H}_{\text{at}} = \hbar\omega_0\hat{j}_z, \quad (5.2)$$

where $\hat{j}_z = \frac{1}{2}(|e\rangle\langle e| - |g\rangle\langle g|)$ is an observable of the atomic state. It measures the difference of population between e and g.

As developed in many quantum mechanics textbook [Cohen-Tannoudji 96, Aspect 06], the atom - field coupling that arises from the interaction of the individual charged particle that constitute the atom, can be expanded and limited to its first term: the electric-dipole interaction. In this approximation, the (charged) electron follows the oscillation of the electric field. Its wavefunction can oscillate back and forth in between eigenstates: the spherical harmonic wavefunctions. The Hamiltonian of the interaction is

$$\mathcal{H}_I = -\hat{\mathbf{D}} \cdot \mathbf{E}, \quad (5.3)$$

where $\hat{\mathbf{D}} = e \cdot \hat{\mathbf{r}}$ is the dipole operator.

Two states with identical parity being not coupled by $\hat{\mathbf{r}}$, the diagonal terms are null. The coupling of this two level system can thus be simplified to:

$$\hat{\mathbf{D}} = \begin{pmatrix} 0 & d_{eg} \\ d_{eg}^* & 0 \end{pmatrix} \quad (5.4)$$

$$= d_{eg} |e\rangle\langle g| + d_{eg}^* |g\rangle\langle e|, \quad (5.5)$$

where $d_{eg} = \langle e | \hat{\mathbf{D}} | g \rangle$ is the dipole element between $|e\rangle$ and $|g\rangle$.

The interaction Hamiltonian is then:

$$\mathcal{H}_I = - \left(d_{eg} \hat{j}_+ e^{-i(\omega t + \phi)} + d_{eg}^* \hat{j}_- e^{i(\omega t + \phi)} \right) A_0, \quad (5.6)$$

where $\hat{j}_+ = |e\rangle\langle g|$ and $\hat{j}_- = |g\rangle\langle e|$ are the raising and lowering operators that describe the transfer from one state to the other.

In the rotating frame of the electric field, the interaction Hamiltonian is $\tilde{\mathcal{H}}_I = U^\dagger \mathcal{H}_I U$ with $U = e^{i\omega \hat{j}_z t}$. In this frame, the lowering and raising operators are $\tilde{\hat{j}}_\pm U^\dagger \hat{j}_\pm U = \hat{j}_\pm e^{\pm i\omega t}$, and we have:

$$\tilde{\mathcal{H}}_I = - \left(d_{eg} \hat{j}_+ e^{-i\phi} + d_{eg}^* \hat{j}_- e^{i\phi} \right) A_0 - \hbar\omega \hat{j}_z \quad (5.7)$$

$$= -d_{eg} \left(\cos(\phi) (\hat{j}_+ + \hat{j}_-) + \sin(\phi) (\hat{j}_+ - \hat{j}_-) \right) A_0 - \hbar\omega \hat{j}_z. \quad (5.8)$$

Defining

$$\hat{j}_x = \frac{1}{2} (\hat{j}_+ + \hat{j}_-) = \frac{1}{2} (|e\rangle\langle g| + |g\rangle\langle e|), \quad (5.9)$$

$$\hat{j}_y = \frac{-i}{2} (\hat{j}_+ - \hat{j}_-) = \frac{-i}{2} (|e\rangle\langle g| - |g\rangle\langle e|) \quad (5.10)$$

we obtain the Jaynes-Cummings Hamiltonian [Jaynes 63] in the semi-classical limit:

$$\mathcal{H} = \hbar\delta\hat{j}_z + \hbar\Omega \left(\cos(\phi)\hat{j}_x + \sin(\phi)\hat{j}_y \right) \quad (5.11)$$

where $\delta = \omega_0 - \omega$ is the angular detuning of the field with respect to the atomic transition, and $\Omega = -2d.A_0/\hbar = \Omega_R$ is the on-resonance Rabi frequency which includes the coupling strength d as well as the field amplitude A_0 .

In the expression 5.11 of the Hamiltonian, the set of operator $(\hat{j}_x, \hat{j}_y, \hat{j}_z)$ appears as essential to describe the evolution of the atomic system.

The phase ϕ of the electric field is arbitrarily defined at $t = 0$, but latter value of the phase will then be related to this initial definition.

5.1.2 The rotation operators and the Bloch sphere

To describe the effect of the Hamiltonian 5.11 on an atomic system, we will determine the evolution of the density matrix. The trace of the density matrix being normalized to one, only 3 parameters are necessary to parametrize the density matrix $\hat{\rho}_{\text{at}}$. Decomposed in the $(\mathbb{1}, \hat{j}_x, \hat{j}_y, \hat{j}_z)$ basis, the density matrix takes the form:

$$\hat{\rho}_{\text{at}} = \frac{\mathbb{1}}{2} + \mathbf{n} \cdot \hat{\mathbf{j}} \quad (5.12)$$

where $\mathbf{n} = n_x \mathbf{e}_x + n_y \mathbf{e}_y + n_z \mathbf{e}_z$ contains the decomposition information of the density matrix. The vector \mathbf{n} is called the Bloch vector. It is the mean value of $2\hat{\mathbf{j}}$, and is then included in a sphere of radius 1.

In order to understand the effect of the Hamiltonian (5.11) on $\hat{\rho}_{\text{at}}$, we focus on the specific case of an on-resonance excitation with initial electro-magnetic phase $\phi = 0$. In this case the Hamiltonian simplifies to:

$$\hat{\mathcal{H}} = \hbar\Omega\hat{j}_x. \quad (5.13)$$

After an interaction time t , the density matrix in the interaction frame is rotated by the evolution operator $e^{-\frac{i\hat{\mathcal{H}}t}{\hbar}}$:

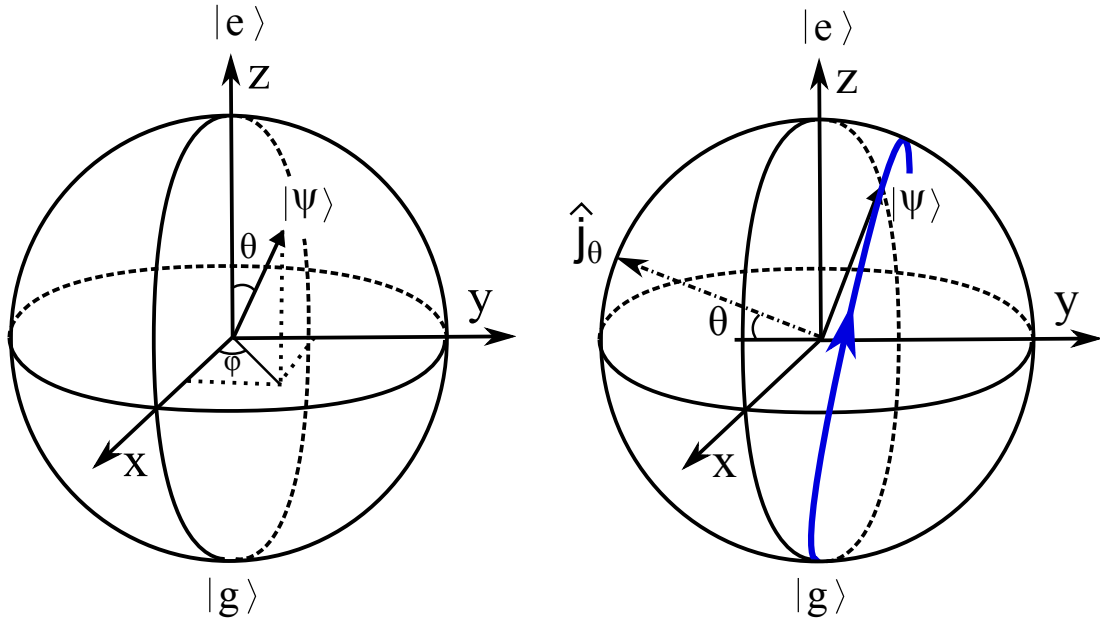
$$\hat{\rho}_{\text{at}}(t) = e^{-\frac{i\hat{\mathcal{H}}t}{\hbar}} \hat{\rho}_{\text{at}} e^{\frac{i\hat{\mathcal{H}}t}{\hbar}} = e^{-i\Omega t \hat{j}_x} \hat{\rho}_{\text{at}} e^{i\Omega t \hat{j}_x} \quad (5.14)$$

$$= \frac{1}{2} \left(\mathbb{1} + 2n_x \hat{j}_x + 2(n_y \cos(\Omega t) - n_z \sin(\Omega t)) \hat{j}_y + 2(n_z \cos(\Omega t) + n_y \sin(\Omega t)) \hat{j}_z \right), \quad (5.15)$$

where we have used:

$$e^{-i\Omega t \hat{j}_x} = \cos\left(\frac{\Omega t}{2}\right) \mathbb{1} - i \sin\left(\frac{\Omega t}{2}\right) \hat{j}_x \quad (5.16)$$

The Hamiltonian $\mathcal{H} = \hbar\Omega\hat{j}_x$ generates then a rotation of the Bloch vector representation of the density matrix around the x axis with angular frequency Ω (see equation (5.15)). Under such an evolution, the measurement of the atomic state: $\langle \hat{j}_z \rangle$ (projection of the Bloch vector on the z -axis) would exhibit the well known Rabi oscillations.



(a) Any superposition state of a two level system can be described on the Bloch sphere by a unitary vector. The probability of $|\Psi\rangle$ to be in $|1\rangle$ is $\cos^2 \theta$, and the coherence between the two level has a phase φ .

(b) The interaction with the electro-magnetic field couples state $|0\rangle$ and $|1\rangle$ and rotates the Bloch vector around makes the \hat{j}_θ .

Figure 5.2: Bloch sphere

(a) Representation of a two level atom on the Bloch sphere, (b) Rotation of $|0\rangle$ induced by the momentum operator \hat{j}_θ .

Generalization

This rotation property on the Bloch sphere is not only limited to \hat{j}_x , but is obtained for any linear combination of the set of operator $(\hat{j}_x, \hat{j}_y, \hat{j}_z)$. Indeed, the Hamiltonian $\mathcal{H} = \hbar\Omega_1\hat{j}_x + \hbar\Omega_2\hat{j}_y + \hbar\Omega_3\hat{j}_z$ generates a rotation of the Bloch vector around $\mathbf{e}_\alpha = \frac{1}{\sqrt{\Omega_1^2 + \Omega_2^2 + \Omega_3^2}}(\Omega_1\mathbf{e}_x + \Omega_2\mathbf{e}_y + \Omega_3\mathbf{e}_z)$ with angular frequency $\Omega_{\text{eff}} = \sqrt{\Omega_1^2 + \Omega_2^2 + \Omega_3^2}$.

These operators \hat{j} that were derived from the interaction Hamiltonian are named the Pauli matrices:

$$\hat{\sigma}_x = 2\hat{j}_x = \begin{pmatrix} 0 & 1 \\ 1 & 0 \end{pmatrix} \quad \hat{\sigma}_y = 2\hat{j}_y = \begin{pmatrix} 0 & -i \\ i & 0 \end{pmatrix} \quad \hat{\sigma}_z = 2\hat{j}_z = \begin{pmatrix} 1 & 0 \\ 0 & -1 \end{pmatrix} \quad (5.17)$$

that were first introduced to describe the evolution of two-level systems.

In the following, we will prefer the \hat{j} notations (and not the $\hat{\sigma}$), which are commonly adopted in the context of spin 1/2 equivalent systems.

The \hat{j} operators verify the commutation relations of angular momentum operators:

$$[\hat{j}_x, \hat{j}_y] = i\hat{j}_z, \quad [\hat{j}_z, \hat{j}_x] = i\hat{j}_y, \quad [\hat{j}_y, \hat{j}_z] = i\hat{j}_x. \quad (5.18)$$

Because of this rotation property of the Hamiltonian, the Bloch sphere is very well adapted

to describe the atomic state evolution. Indeed, for any state, the evolution can be very easily analyzed or computed by simple rotations on the Bloch sphere.

A few physical situations

- We consider the situation of a free evolution of an atomic system that may be latter excited by a driving field that is detuned by $\delta = \omega - \omega_0$. The Hamiltonian of the system is:

$$\mathcal{H} = \hbar \delta \hat{j}_z, \quad (5.19)$$

and the Bloch vector rotates with angular frequency δ around the z axis. The simple interpretation is that during a free evolution that lasts for a time T , the field accumulates a phase $\phi = \delta T$. This phase will only be revealed by a later interaction between the microwave field and the atom through the Hamiltonian (5.11). In other terms, the phase is measured if the interferometer is closed.

- The driving field is applied with a small detuning $\delta\omega$, compare to the Rabi frequency $\Omega_R \gg \delta\omega$, and the Hamiltonian simplifies to:

$$\mathcal{H} = \hbar \Omega_R \hat{j}_y. \quad (5.20)$$

This corresponds to a rotation around the y axis of the Bloch sphere.

5.1.3 Extension to the many body system

In sections 5.1.1 and 5.1.2, we have discussed the evolution of a single particle that interacts with an electro-magnetic field. Now the purpose is to extend the formalism introduced to the case of a cloud of N_{at} two levels atoms. Before any correlations have been introduced in the system, the cloud starts as an ensemble of independent two level atoms. The many-body Hamiltonian describes then the evolution of each atoms independently:

$$\mathcal{H} = \sum_{i=0}^N \left(\hbar \delta \hat{j}_z^{(i)} + \hbar \Omega \left(\cos(\phi) \hat{j}_x^{(i)} + \sin(\phi) \hat{j}_y^{(i)} \right) \right) \quad (5.21)$$

The collective momentum operators are defined as the sum over all the individual contributions:

$$\hat{J}_x = \sum_{i=0}^N \hat{j}_x^{(i)}, \quad \hat{J}_y = \sum_{i=0}^N \hat{j}_y^{(i)}, \quad \hat{J}_z = \sum_{i=0}^N \hat{j}_z^{(i)}. \quad (5.22)$$

\hat{J}_z is an observable since it measures the population difference between the two atomic levels. The definitions (5.22) should be regarded carefully. Each $\hat{j}^{(i)}$ operator working in a different Hilbert space, the contracted notation $\hat{j}^{(i)}$ actually stands for $\left(\hat{j}^{(i)} \otimes \mathbb{1}^{(j)} \right)_{j \neq i}$.

The commutation relation hold for these global operators:

$$\left[\hat{J}_x, \hat{J}_y \right] = i \hat{J}_z, \quad \left[\hat{J}_z, \hat{J}_x \right] = i \hat{J}_y, \quad \left[\hat{J}_y, \hat{J}_z \right] = i \hat{J}_x, \quad (5.23)$$

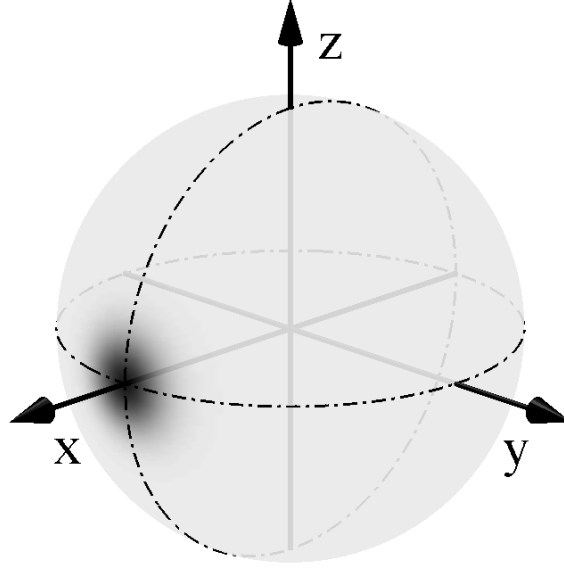


Figure 5.3: *Illustration of a coherent state polarized along \hat{J}_x .*

This representation does not mean that the collective vector has an unknown position on the sphere since any pure state is well defined by one point on the surface of the Bloch sphere. In the present case, the Bloch vector is well defined and pointing along x. The uncertainty represented comes from the projection of the wavefunction on the quasi continuum of eigenstates of \hat{J}_z , i.e. the variance of \hat{J}_z is nonzero.

and the associated Heisenberg inequalities are:

$$\Delta \hat{J}_x \Delta \hat{J}_y = \frac{\langle \hat{J}_z \rangle}{2}, \quad \Delta \hat{J}_z \Delta \hat{J}_x = \frac{\langle \hat{J}_y \rangle}{2}, \quad \Delta \hat{J}_y \Delta \hat{J}_z = \frac{\langle \hat{J}_x \rangle}{2}. \quad (5.24)$$

Similarly to the momentum analysis, the set formed by $\hat{J}^2 = \sum_{k=x,y,z} \hat{J}_k^2$, \hat{J}_z is a complete set of commuting observable (C.S.C.O., [Cohen-Tannoudji 86]). Regarding many-body system, this statement should be taken carefully since it only applies to the symmetrized form of the state, which mean that we are in a second quantization formalism where the particle exchange permutation invariance is assumed. The eigenstate of this C.S.C.O. are the $|J, n\rangle$ vectors which verify:

$$\hat{J}^2 |J, n\rangle = J(J+1) |J, n\rangle, \quad (5.25)$$

$$\hat{J}_z |J, n\rangle = n |J, n\rangle. \quad (5.26)$$

A state $|J, n\rangle$ is called a Dicke state. The set of all the Dicke state forms a basis for the symmetrized states.

Remark:

To actually regard the set \hat{J}^2 and \hat{J}_z as a C.S.C.O., we have neglected the external degree of freedom of the atoms. In the case of a measurement on a Bose Einstein condensate this would be totally acceptable since all the atoms are in the same external wavefunction. Regarding a thermalized sample the question of the legitimacy of such a reduction may be questioned. In

our specific case of a dispersive measurement, the measurement is independent of the external degree of freedom (position and velocity), and the description can be reduced to the internal state.

The coherent state

To familiarize with the Dicke states, we detail now the decomposition of the coherent state in the Dicke basis. In our present context, we call a coherent state $|\Psi\rangle$, the state given by N_{at} independent atoms all in a balanced superposition of the two levels $|f\rangle$ and $|g\rangle$:

$$|\Psi\rangle = \bigotimes_{i=1}^{N_{\text{at}}} \left[\frac{1}{\sqrt{2}} (|f\rangle_i + |g\rangle_i) \right] \quad (5.27)$$

$$= \frac{1}{2^{\frac{N_{\text{at}}}{2}}} \sum_{k=0}^{N_{\text{at}}} \sum_{\sigma} |f\rangle_{\sigma(1)} \cdots |f\rangle_{\sigma(k)} |g\rangle_{\sigma(k+1)} \cdots |g\rangle_{\sigma(N_{\text{at}})} \quad (5.28)$$

where the sum is done over all the possible permutations. Experimentally, this state is obtained by the application of a $\pi/2$ pulse on atoms that are all in the same initial state. The Bloch representation of the coherent state is given in figure 5.3.

The collective basis $|n\rangle$ is obtained by symmetrizing and normalizing the state $|f\rangle^{N_{\text{at}}/2+n} |g\rangle^{N_{\text{at}}/2-n}$ ($n = k - N_{\text{at}}/2$):

$$|n\rangle = \frac{1}{\sqrt{C_{N_{\text{at}}}^{N_{\text{at}}/2+n}}} \sum_{\sigma} |f\rangle_{\sigma(1)} \cdots |f\rangle_{\sigma(N_{\text{at}}/2+n)} |g\rangle_{\sigma(N_{\text{at}}/2+n+1)} \cdots |g\rangle_{\sigma(N_{\text{at}})} , \quad (5.29)$$

and the coherent state decomposition becomes:

$$|\Psi\rangle = \sum_{n=-N_{\text{at}}/2}^{N_{\text{at}}/2} c_n |n\rangle = \frac{1}{2^{\frac{N_{\text{at}}}{2}}} \sum_{n=-N_{\text{at}}/2}^{N_{\text{at}}/2} \sqrt{C_{N_{\text{at}}}^{N_{\text{at}}/2+n}} |n\rangle \quad (5.30)$$

The initial coefficients of the distribution are:

$$c_n = \frac{1}{2^{\frac{N_{\text{at}}}{2}}} \sqrt{C_{N_{\text{at}}}^{N_{\text{at}}/2+n}} \quad (5.31)$$

For $N \gg 1$ and $n \ll N/2$, the binomial distribution is very well approximated by a normal distribution. This is the Moivre-Laplace theorem which gives:

$$c_n = \frac{1}{2^{\frac{N_{\text{at}}}{2}}} \sqrt{C_{N_{\text{at}}}^{N_{\text{at}}/2+n}} \approx \frac{1}{(\pi N_{\text{at}}/2)^{1/4}} e^{-\frac{n^2}{N_{\text{at}}}} \quad (5.32)$$

The initial distribution of the coherent state after a $\pi/2$ pulse follows a normal distribution centered on 0 and with variance $\frac{N_{\text{at}}}{2}$. The initial variance of \hat{J}_z is:

$$\Delta \hat{J}_z^2 = \langle \Psi | \hat{J}_z^2 | \Psi \rangle = \sum_{n=-N_{\text{at}}/2}^{N_{\text{at}}/2} c_n^2 n^2 \langle n | n \rangle = \frac{N_{\text{at}}}{4} \quad (5.33)$$

Contrarily to the case of the single atom Bloch sphere where the eigenvalues are only the poles, for $N_{\text{at}} \gg 1$ the collective Bloch sphere eigenvalues form almost a continuum in between the poles. For this reason, the coherent state can be represented as a density of distribution as depicted in figure 5.3.

In the cases that will be discussed later on, and that apply to atom interferometry, the initial atomic state correspond to N_{at} atoms all starting in their lower state. This corresponds to the Dicke state $|J = N_{\text{at}}/2, n = -N_{\text{at}}/2\rangle$. The total angular momentum $J = N_{\text{at}}/2$ being conserved during the coherent interaction, latter manipulations of the state preserve J . The Dicke states will then only be depicted by their projection on z , namely:

$$|J = N_{\text{at}}/2, n\rangle = |n\rangle \quad (5.34)$$

For independent particles, all the single body results can be directly extended to the many body system. It is particularly true for the evolution of the system that can be completely described in terms of rotation on the sphere, which has now a radius of $N_{\text{at}}/2$. The rotation on this extended Bloch Sphere is a complex problem of algebra, especially concerning the evolution of the variance. Details can be found in [Arecchi 72], where the rotations are treated in details.

5.1.4 Shot noise in atomic interferometry

Atomic energy levels are at the same time very well defined, but also very sensitive to their environment. Measuring the exact energy of a transition $E_0 = \hbar\omega_0$, can thus be either a way to properly define the time $T = 2\pi/\omega_0$ or to precisely measure perturbing effects. Atomic interferometers [Kasevich 91], and especially atomic clocks [Santarelli 99] must be placed in this context of energy/frequency measuring devices.

Because atoms are massive particles compared to photons, they are sensitive to inertial forces. Atomic accelerometer [Gouët 08] and gyroscope [Gauguet 09] are part of the devices that allow to measure inertial constants.

As it is well known for optical interferometers, the ultimate limit for a classical system is the optical shot noise, that describes the independence of particles that can go in one or the other output port of the interferometer. For uncorrelated particles, this results in a Poissonian noise that limits the best precision achievable for optical interferometers to $\sqrt{N_p}$, where N_p is the number of photon used for the experiment.

An atom interferometer presents the exact same behavior, meaning that the best precision is limited by the Poissonian noise of the atomic distribution that has a width $\sqrt{N_{\text{at}}}$ after the first beamsplitter. This noise found at the output of the interferometer is linked to the dispersion of \hat{J}_z that has been discussed in section 5.1.3. This idea is depicted in figure 5.4 where a clock interferometer (Ramsey) is presented. In a usual interferometric sequence, a first $\pi/2$ pulse (5.4 (b)) creates a superposition states. A following free evolution gives rise to the phase $\phi = \delta T$ in the equatorial plane, where T is the free evolution time and δ the detuning between the microwave driving field and the clock transition. In figure 5.4, the free evolution phase has been chosen to $\pi/2$ which brings the interferometer in half fringe where it has the highest phase sensitivity. After the last $\pi/2$ pulse 5.4(f), the atomic state is read and presents shot-to-shot fluctuations related to the atomic shot noise: $\Delta\hat{J}_z = \sqrt{N_{\text{at}}}/2$.

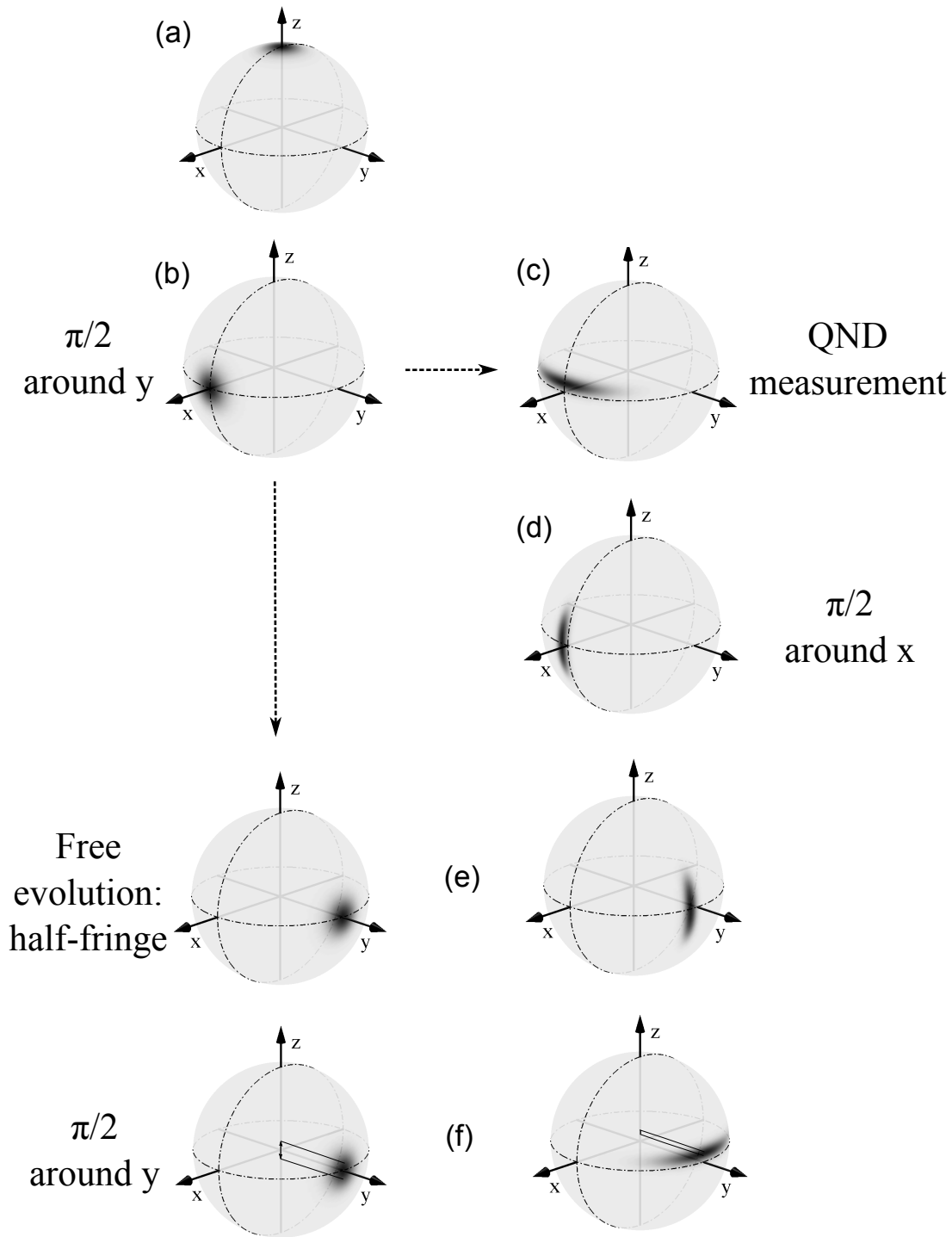


Figure 5.4: *Shot-noise and squeezed limited interferometric sequence*

On the left a typical atomic clock sequence limited by the atomic shot-noise. The atoms start all in the same state (a) and a coherent superposition is created by $\pi/2$ pulse around y (b). After a free evolution (e) the interferometer is closed by a $\pi/2$ pulse around y (f). On the right, a sequence that uses a squeezed state to improve the SNR: the coherent superposition is squeezed along z (c), a $\pi/2$ pulse around x transfer this gain on the phase quadrature (d), the interferometer is closed (e,f) and exhibits a noise reduction.

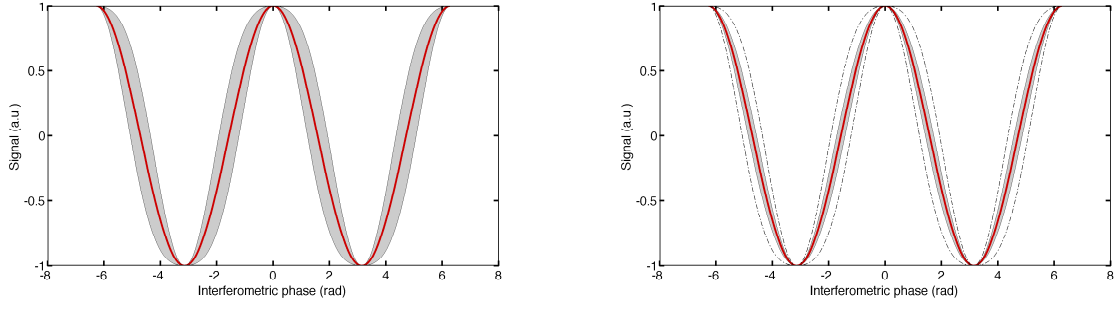


Figure 5.5: *Illustrating fringes of the shot-noise and squeezed limited interferometric sequence* On the left, a fringe that is blurred by the atomic shot noise. On the right, the improvement that can be achieved after the correlation of the QND result and the interferometric result.

Using squeezed states, the atomic shot noise influence can be lowered [Wineland 92]. After the first $\pi/2$ pulse, a QND measurement is applied on the state to reduce the variance $\Delta \hat{J}_z^2$. A $\pi/2$ pulse rotation induced by \hat{J}_x is then applied to transfer the gain obtained in the number difference quadrature on the phase quadrature. After the " $\pi/2$ " free evolution, the last $\pi/2$ pulse rotation induced by \hat{J}_y closes the interferometer, and the atomic noise clearly appears to be lowered.

Here, it is very important to notice that if directly drawn, the fringes in the squeezed case will exhibit exactly the same noise as the non-squeezed case. This is due to the fact that the position of the squeezing is non deterministic and may occur anywhere in the initial density distribution. This stochastic offset induces a noise at the output that is a priori indistinguishable from the atomic shot noise. It is only by correlating the result of the QND measurement, that gives the offset of the squeezed state with the result of the interferometer, that a substantial sensitivity improvement can be achieved.

The fringes obtained from the two sequences are presented in figure 5.5 which illustrates the improvement that brings a non-classical state on the clock sensitivity for an equal number of particles considered.

The improvement of the interferometer performance has been in the last decade one of the main reasons to investigate squeezed state of light or matter. To prepare squeezed states, the system must experience a non-linear evolution:

- A non-linear interaction in the form for example of a twisting Hamiltonian [Kitagawa 93]
- Transferring the squeezing from an optical state to an atomic state [Kuzmich 97]
- The strong non-linearity of an ideal projective measurement that collapses the state on one of the observable eigenstates, *i.e.* a Quantum Non-Demolition measurement [Kuzmich 98, Caves 80b, Thorne 78].

This last point is the one chosen in our experiment. The following part of this chapter describe the partial projection in an indirect Quantum Non-Demolition (QND) measurement.

5.2 Quantum Non-Demolition measurement

It is well known in quantum mechanics that a measurement modifies the state of the measured sample. In certain conditions, correlations between the particles can be created. At first, we will give a hand-wavy physical argument to justify the creation of correlations in the sample. The formalism of Quantum Non-Demolition measurement is then introduced before we describe the specific case of a dispersive measurement of the population difference.

5.2.1 Global measurement

To simplify our point, we consider the specific case of the collective observable \hat{J}_z which measures the atom number difference. Because it is a collective observable, it gives information on the ensemble but not on the state of a specific atom.

To illustrate the correlation, we consider for example an ideal projective measurement realized on the coherent state. As previously mentioned, in this state the atoms are independent, *i.e.* the state is separable. After the measurement, the atomic state is projected on an eigenstate $|n\rangle$ of \hat{J}_z .

In this Dicke state, we have no information on individual atoms, but it is an entangled state for the atoms. Indeed, if we were to measure one of the atoms of the ensemble, then the wavefunction of the others would be projected in accordance with the measurement result.

The acquisition of a collective information has entangled the atoms.

5.2.2 Element of theory

Before we present the specific case of the off-resonance interaction between an optical probe and a measured sample, we give the general formalism of QND measurement that is also summarized in [Grangier 98]. A pedagogical review of the indirect QND measurement is presented in [Heidmann 07].

5.2.2.1 Indirect measurement

In experimental situations, most of the apparatus that are encountered not only measure a system, but usually also destroy it. This is clearly the case for example with photodetectors where the photon is absorbed by the material or with micro-channel plates. To overcome this difficulty, the *signal* that is the system under study is measured *via* the effect it generates on a probe called *meter*.

In experimental situations, the *signal* can be either an atomic [Louchet-Chauvet 10] or a photonic system [Roch 97], whereas the *meter* is usually optical. Actually, to my knowledge, only one experiment uses an atomic *meter* to measure an optical *signal* [Guerlin 07, Gleyzes 07].

We consider a *signal* operator \hat{Q} and its conjugate \hat{P} . And a *meter* operator \hat{Y} that has conjugate \hat{X} . The commutation relations are:

$$[\hat{P}, \hat{Q}] = i, \quad [\hat{X}, \hat{Y}] = i. \quad (5.35)$$

Because the measurement is quantum non-destructive, the *signal* operator \hat{Q} has to stay unchanged during the interaction. It should then commute with the interaction Hamiltonian.

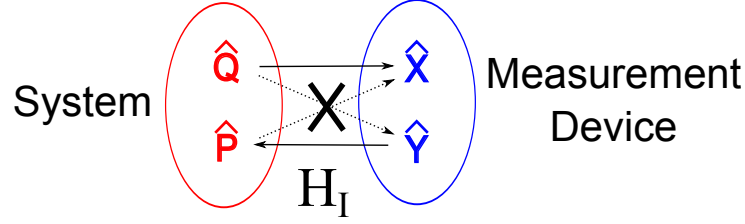


Figure 5.6: Schematic of the interaction between the system and the measurement device.

This condition will be fulfilled for example for an Hamiltonian of the form:

$$\mathcal{H}_I = \hbar g \hat{Q} \hat{Y} \quad (5.36)$$

, and for all interaction time τ , we have:

$$\hat{Y}^{\text{out}}(\tau) = \hat{Y}^{\text{in}}, \quad (5.37)$$

$$\hat{Q}^{\text{out}}(\tau) = \hat{Q}^{\text{in}} \quad (5.38)$$

The operators \hat{P} and \hat{X} are modified during the interaction, and their evolution is given by the Heisenberg equation of motion:

$$\frac{d\hat{X}}{dt} = \frac{-i}{\hbar} [\hat{X}, \mathcal{H}_I] = g\hat{Q} \quad \frac{d\hat{P}}{dt} = \frac{-i}{\hbar} [\hat{P}, \mathcal{H}_I] = g\hat{Y} \quad (5.39)$$

Hence, after an interaction time τ that leaves the operator \hat{Q} and \hat{Y} unperturbed, we have the in-out relations:

$$\hat{X}^{\text{out}} = \hat{X}^{\text{in}} + g\tau\hat{Q}^{\text{in}}, \quad \hat{Y}^{\text{out}} = \hat{Y}^{\text{in}}, \quad (5.40)$$

$$\hat{P}^{\text{out}} = \hat{P}^{\text{in}} + g\tau\hat{Y}^{\text{in}}, \quad \hat{Q}^{\text{out}} = \hat{Q}^{\text{in}}. \quad (5.41)$$

The information contained in the signal \hat{Q} is transferred onto the operator \hat{X} . In this interaction, the signal operator \hat{Q} is not changed. This interaction transfer the noise of \hat{Q} (resp. \hat{Y}) on \hat{X} (resp. \hat{P}). This noise transfer is the backaction of the measurement (see figure 5.6).

$$\Delta\hat{X}^{\text{out}2} = \Delta\hat{X}^{\text{in}2} + g^2\tau^2\Delta\hat{Q}^{\text{in}2}, \quad (5.42)$$

$$\Delta\hat{P}^{\text{out}2} = \Delta\hat{P}^{\text{in}2} + g^2\tau^2\Delta\hat{Y}^{\text{in}2}. \quad (5.43)$$

The resulting output fluctuations of \hat{X} is the result of the convolution of the initial fluctuations $\Delta\hat{X}^{\text{in}}$ with the fluctuations of the signal $\Delta\hat{Q}^{\text{in}}$.

Projection postulate

In the process described above, the *signal* variable is unchanged. From this description, it is not possible to show that the variance of the *signal* is actually lowered. The squeezing only happens because the operator \hat{X} is measured, and thus projected.

After the interaction, the *signal* and the *meter* are entangled. The measurement of the *meter* projects the state of the *signal*. This is the projection postulate that cannot be avoided to express that further measurement of the system (*signal*) will exhibit lower fluctuations.

The study presented in section 5.3 and followings, precisely addresses the problem of the collapse of the measured state, and shows that the initial coherent state stays minimal with respect to the Heisenberg inequality. If this conserved minimality is accepted, the variance of the meter can be easily calculated by:

$$\Delta \hat{Q}^{\text{out}^2} = \frac{1}{\Delta \hat{P}^{\text{out}^2}} = \frac{1}{\Delta \hat{P}^{\text{in}^2} + g^2 \tau^2 \Delta \hat{Y}^{\text{in}^2}} \quad (5.44)$$

$$= \Delta \hat{Q}^{\text{in}^2} \frac{1}{1 + \kappa^2}, \quad (5.45)$$

where

$$\kappa^2 = g^2 \tau^2 \frac{\Delta \hat{Q}^{\text{in}^2}}{\Delta \hat{X}^{\text{in}^2}}. \quad (5.46)$$

The variance of the *signal* is then always reduced with respect to the parameter κ . This parameter is the signal-to-noise of the measurement defined as the *signal* width over the *meter* width. The parameter g is the strength of the transfer of information: the higher is g , the lower the variance. In addition, the prefactor $g\tau$ converts from one variable units to the other one. For example, in the case of the dispersive measurement, this factor converts the atom number noise in light phase noise.

Decoherence

In the description of the QND measurement that we gave above, we have considered a hermitian Hamiltonian that fulfill the Heisenberg equation of motion. This equation is actually not complete and should be corrected by Lindblad operators L_ν [Lindblad 76] that describe the coupling to the environment *via* for example spontaneous emission processes.

$$\dot{\rho} = -\frac{i}{\hbar} [H, \rho] + \sum_{\nu} (2L_{\nu}\rho L_{\nu}^{\dagger} - \{L_{\nu}^{\dagger}L_{\nu}, \rho\}), \quad (5.47)$$

where $\{.,.\}$ is the anticommutator. In the case where the signal is an atomic variable, the Lindblad operator is $L_{\nu} = \sqrt{\gamma}\sigma_{-}$, where σ_{-} is the atomic lowering operator.

This coupling to the environment perturbs the free evolution described the hermitian Hamiltonian H and the non demolition character breaks down.

If we consider the case of a two level atomic system coupled to the environment, spontaneous emission processes will make all superposition states, and particularly all squeezed states decohere towards mixed states. The problem of the effect of the decoherence is a complex problem that is, yet, not completely solved. For the system previously mentioned, one of the main difficulties is that for each spontaneous emission event, the basis of eigenstate has to be extended. In the case of spin-squeezing for example, spontaneous emission makes the system exits the $(|J = N_{\text{at}}/2, n\rangle)_n$ basis which should be decomposed in the complete $(|J, n\rangle)_{-J \leq n \leq J}^{0 \leq J \leq N_{\text{at}}/2}$ basis [Chase 08]. This simple description illustrates the complexity of the problem of spontaneous emission that becomes even less intuitive when the number of atoms is not conserved or when the state loses the symmetry by particles exchange.

A qualitative shape of the influence of spontaneous processes on the variance of the final state is given in [Echaniz 05].

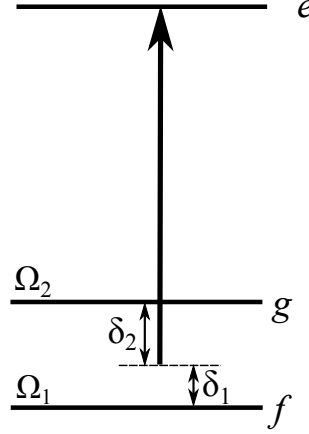


Figure 5.7: Three level system considered for the QND Hamiltonian.

5.2.2.2 Dispersive effective Hamiltonian

We focus now on the collective observable \hat{J}_z measured in the context of a dispersive measurement [Kuzmich 98]. In this section we will show that the dispersive interaction has an Hamiltonian of the form (5.36).

The system studied is a three level atom with two hyperfine ground states (f and g , figure 5.7) which are initially equally populated and one excited state (e). The transition $f \rightarrow e$ is noted 1 and $g \rightarrow e$ is noted 2. The Pauli matrices $\sigma_+^{(i)}$, $\sigma_-^{(i)}$, $\sigma_z^{(i)}$ are used to describe the transition i .

The system of one optical field interacting with this three level system can be described by a fully quantized Jaynes Cummings Hamiltonian of the form:

$$\mathcal{H}_{JC} = \hbar\delta_1\hat{\sigma}_z^{(1)} + \hbar\Omega_1 \left(\hat{\sigma}_+^{(1)}\hat{a} + \hat{\sigma}_-^{(1)}\hat{a}^\dagger \right) + \hbar\delta_2\hat{\sigma}_z^{(2)} + \hbar\Omega_2 \left(\hat{\sigma}_+^{(2)}\hat{a} + \hat{\sigma}_-^{(2)}\hat{a}^\dagger \right). \quad (5.48)$$

To derive an effective hamiltonian, we consider the evolution of the operator $\hat{\sigma}_+^{(i)}$ and $\hat{\sigma}_-^{(i)}$ that are given by:

$$\frac{d}{dt}\hat{\sigma}_\pm^{(i)} = \frac{-i}{\hbar}[\hat{\sigma}_\pm^{(i)}, \mathcal{H}_{JC}]. \quad (5.49)$$

From the commutation relations $[\hat{\sigma}_\pm^{(i)}, \hat{\sigma}_z^{(i)}] = \mp\hat{\sigma}_\pm^{(i)}$ and $[\hat{\sigma}_-^{(i)}, \hat{\sigma}_+^{(i)}] = -\hat{\sigma}_z^{(i)}/2$, we obtain:

$$\frac{d}{dt}\hat{\sigma}_+^{(i)} = i \left(\delta_i\hat{\sigma}_+^{(i)} - \frac{\Omega_i}{2}\hat{\sigma}_z^{(i)}\hat{a}^\dagger \right), \quad \frac{d}{dt}\hat{\sigma}_-^{(i)} = -i \left(\delta_i\hat{\sigma}_-^{(i)} - \frac{\Omega_i}{2}\hat{\sigma}_z^{(i)}\hat{a} \right). \quad (5.50)$$

Using the adiabatic elimination of the excited state and considering then the steady state of the evolution, $\frac{d}{dt}\hat{\sigma}_+^{(i)} = \frac{d}{dt}\hat{\sigma}_-^{(i)} = 0$, it follows:

$$\mathcal{H}_{JC} = \hbar\delta_1\hat{\sigma}_z^{(1)} + \hbar\delta_2\hat{\sigma}_z^{(2)} + \hbar \left(\frac{\Omega_1^2}{\delta_1}\hat{\sigma}_z^{(1)} + \frac{\Omega_2^2}{\delta_2}\hat{\sigma}_z^{(2)} \right) \hat{a}^\dagger\hat{a} + \frac{1}{2} \left(\frac{\Omega_1^2}{\delta_1}\hat{\sigma}_z^{(1)} + \frac{\Omega_2^2}{\delta_2}\hat{\sigma}_z^{(2)} \right). \quad (5.51)$$

Except for the off resonance two photons process that has been neglected, the hamiltonian 5.51 corresponds to the effective hamiltonian of the system [Cohen-Tannoudji 96].

In the case of a far-off resonant light, the atoms stay in the two ground states and we have $\sigma_z^{(1)} = \sigma_f = \hat{N}/2 + \hat{J}_z$ and $\sigma_z^{(2)} = \sigma_g = \hat{N}/2 - \hat{J}_z$. It comes:

$$\mathcal{H}_{\text{JC}} = K_1 \hat{\sigma}_z^{(1)} + K_2 \hat{\sigma}_z^{(2)} + \hbar \left(\frac{\Omega_1^2}{\delta_1} + \frac{\Omega_2^2}{\delta_1} \right) \hat{N} + 2\hbar \left(\frac{\Omega_1^2}{\delta_1} - \frac{\Omega_2^2}{\delta_1} \right) \hat{J}_z \hat{a}^\dagger \hat{a}, \quad (5.52)$$

where

$$K_i = \hbar \delta_i + \frac{\Omega_i^2}{2\delta_i}. \quad (5.53)$$

If, in addition, we consider detunings such that :

$$\frac{\Omega_1^2}{\delta_1} = -\frac{\Omega_2^2}{\delta_2} = \frac{\Omega^2}{\delta}, \quad (5.54)$$

the Hamiltonian of the system becomes:

$$\mathcal{H}_{\text{JC}} = K_1 \hat{\sigma}_z^{(1)} + K_2 \hat{\sigma}_z^{(2)} + 2\hbar \left(\frac{\Omega^2}{\delta} \hat{J}_z \hat{a}^\dagger \hat{a} \right). \quad (5.55)$$

The last term in equation 5.55 can either be seen as the atomic state that is energy shifted by the optical field (light-shift) or the field that is frequency shifted by the atoms (refractive index).

To measure an optical phase shift it is necessary to hold the initial phase information, *i.e.* to be able to compare the mode to a reference. This idea, which consists to compare two modes, is very general, and can be applied to any two level system such as two orthogonal polarizations, two modes of a Mach-Zehnder or two frequency components of the optical field.

We consider a reference mode a_0 of the optical field, and we assume that it does not interact with the atomic state. Using these two modes a and a_0 , we construct the Stokes operators for the light:

$$\hat{S}_0 = \frac{1}{2}(a^\dagger a + a_0^\dagger a_0), \quad (5.56)$$

$$\hat{S}_x = \frac{i}{2}(a^\dagger a_0 + a_0^\dagger a), \quad (5.57)$$

$$\hat{S}_y = \frac{i}{2}(a^\dagger a_0 - a_0^\dagger a), \quad (5.58)$$

$$\hat{S}_z = \frac{1}{2}(a^\dagger a - a_0^\dagger a_0). \quad (5.59)$$

These operators are very common in optics where they are used, for example, to describe the polarization of the light on the Poincaré sphere.

The Stokes operators are very similar to the collective-spin \hat{J} operators, and follow the same commutation relations:

$$[\hat{S}_x, \hat{S}_y] = i\hat{S}_z, \quad [\hat{S}_y, \hat{S}_z] = i\hat{S}_x, \quad [\hat{S}_z, \hat{S}_x] = i\hat{S}_y, \quad [\hat{S}_i, \hat{S}_0] = 0. \quad (5.60)$$

Clearly we have $a^\dagger a = \hat{S}_0 + \hat{S}_z$, and the Hamiltonian of the system can be described as the interaction between two fictitious spins:

$$\mathcal{H}_{\text{JC}} = K_1 \hat{\sigma}_z^{(1)} + K_2 \hat{\sigma}_z^{(2)} + 2\hbar \left(\frac{\Omega^2}{\delta} \hat{J}_z \hat{S}_0 \right) + 2\hbar \left(\frac{\Omega^2}{\delta} \hat{J}_z \hat{S}_z \right). \quad (5.61)$$

As an interferometer (Mach-Zehnder, polarimetry...) measures the \hat{S}_z component of the pseudo-spin, only this part needs to be conserved. Nevertheless, in principle, a measurement of \hat{J}_z through its interaction with \hat{S}_0 could be also implemented.

Equation 5.61 demonstrates the QND (equation 5.36) character of the off-resonance dispersive detection, where the interaction Hamiltonian is:

$$\mathcal{H}_{\text{JC,int}} = 2\hbar \left(\frac{\Omega^2}{\delta} \hat{J}_z \hat{S}_z \right). \quad (5.62)$$

Specific In - Out relations

Actually, the Hamiltonian in equation (5.62), is not exactly an Hamiltonian of the form 5.36. The difference comes from the operators \hat{J}_z and \hat{S}_z which do not have exact conjugate variables:

$$[\hat{S}_y, \hat{S}_z] = i\hat{S}_x, \quad [\hat{J}_y, \hat{J}_z] = i\hat{J}_x. \quad (5.63)$$

Nevertheless for states polarized along x , the commutation relations are almost the one of conjugate variables, and the in-out relation of the interaction are:

$$\hat{S}_y^{\text{out}} = \hat{S}_y^{\text{in}} + \frac{\Omega^2 \tau}{\delta} \langle \hat{S}_x \rangle \hat{J}_z^{\text{in}}, \quad \hat{S}_z^{\text{out}} = \hat{S}_z^{\text{in}}, \quad (5.64)$$

$$\hat{J}_y^{\text{out}} = \hat{J}_y^{\text{in}} + \frac{\Omega^2 \tau}{\delta} \langle \hat{J}_x \rangle \hat{S}_y^{\text{in}}, \quad \hat{J}_z^{\text{out}} = \hat{J}_z^{\text{in}}. \quad (5.65)$$

From here we see a limitation for the measurement, since during the collapse of the atomic state, the strength of the backaction decreases as $\langle \hat{J}_x \rangle$ decreases.

5.2.3 Optical phase detection

5.2.3.1 A classical point of view

As it was first shown in [Kuzmich 98] and reviewed in section 5.2.2, the atom light interaction can be described by the effective Hamiltonian:

$$H = \hbar \Omega \hat{S}_z \hat{J}_z. \quad (5.66)$$

Similarly as in [Brune 92], but reversing the roles played by photons and atoms, the effect of this Hamiltonian can be seen as a change of the light rotating frequency for the interaction time t_i . This results in an accumulated optical phase shift, described by an operator $\hat{\Phi} = \Omega t_i \hat{J}_z$ that applies on the optical field.

The fully quantized description presented in section. 5.2.2 is actually not necessary to understand the squeezing dynamics. The atomic sample can be treated as a dispersive sample, with a refractive index that depends on the atomic state population difference.

Considering the three level atom as described in figure 5.7, the probing light will acquire a phase shift when it passes through the sample. This phase is the sum of two opposite contributions which are weighted by the number of atoms in each state. It results in an optical phase that depends on the atomic population difference between the hyperfine states.

In practice, the optical shift is obtained by evaluating the refractive index n and its dependence with the frequency detuning δ of the electric field frequency with respect to the atomic transition. The refractive index describes the sum of the non perturbed and scattered fields:

$$\mathbf{D} = \epsilon_0 n^2 \mathbf{E} = \epsilon_0 (\mathbf{E} + \chi \mathbf{E}). \quad (5.67)$$

The perturbation is described by the susceptibility χ that is linked to the atomic polarizability α .

The refractive index is given by:

$$n = 1 + \chi = 1 + \frac{N_f \alpha_f}{2\epsilon_0} + \frac{N_g \alpha_g}{2\epsilon_0}. \quad (5.68)$$

where N_f and N_g are the linear density of atoms in state f and g , and α_f and α_g are the corresponding atomic polarizabilities.

The precise calculation of the polarizability has been introduced in section D.2 of the appendix and relies on the calculation of all the dipole elements $\langle F', m' | \hat{\mathbf{D}} | F, m \rangle$ which are also given in the appendix D.1.

The expression that is relevant for our experimental situation is given in section 6.20. We choose the detuning such that $\alpha_f = -\alpha_g = \alpha_0$. Hence, the refractive index seen by the light is:

$$n - 1 = \alpha_0 (N_f - N_g). \quad (5.69)$$

The refractive index is thus proportional to the atom number difference between the two states. The optical phase shift relation with the refractive is given through:

$$\Phi = \text{Re}((n - 1)kL_{at}) = \frac{2\pi}{\lambda} \Delta N \frac{\text{Re}(\alpha_0)}{2\epsilon_0} \quad (5.70)$$

$$= \phi \Delta N, \quad (5.71)$$

where $k = 2\pi/\lambda$ is the light wavevector, L_{at} is the atomic sample length, ΔN is the atom number difference in the probed volume, and ϕ is the phase shift for an atom number difference of one.

As a consequence, the measurement of the optical phase shift is a measurement of the population difference observable \hat{J}_z .

Another approach to study the evolution of the atomic state consists to analyze the Hamiltonian via the tensor polarizability. In that case it can be shown, that the Hamiltonian does not only lead to squeezed state [Geremia 06], but can also be engineered for quantum cloning [de Echaniz 08].

5.2.3.2 Phase shift measurement

In order to measure the optical phase shift induced by the atoms, the probe phase has to be referenced to a local oscillator. The local oscillator can be either a copy of the optical field, in which case an homodyne detection is realized (Mach-Zehnder interferometer), or an optical mode with a different frequency, namely an heterodyne detection.

In section 5.3, we will consider by turn these two techniques and study the evolution of the atomic wave function during the measurement.

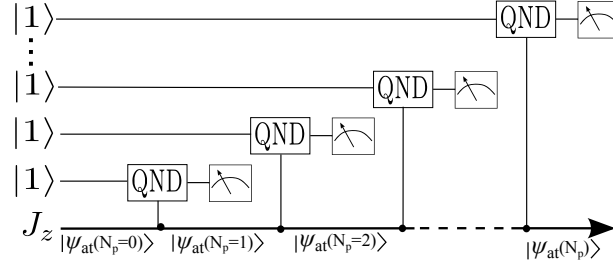


Figure 5.8: *Sequential description of the non demolition measurement*

The measurement of N_p independent photons modifies the atomic state that is partially projected from $|\psi_{\text{at}}(N_p)\rangle$ to $|\psi_{\text{at}}(N_p + 1)\rangle$.

5.3 Quantum trajectories in a wavefunction analysis of the squeezing process

To understand the physics that leads a sample from N_{at} independent atoms to a correlated sample, we developed a wavefunction description of the measurement process. This method is inspired from [Dalibard 92] where the authors reinterpret spontaneous emission effect in a wavefunction formalism. Different approaches such as stochastic master equation [Stockton 04] give similar results than the one that will be presented in the following, but these approaches are usually heavy to handle and does not intuitively present the physical arguments. In the following, we consider the wavefunction collapse of an atomic coherent state $|\Psi\rangle$ by a partial projection process that is described photon after photon. This method allows to follow the time evolution of the atomic state and to understand the effect of a single photon. In section 5.3.1, we present the general idea of the method which is then applied to the specific case of a Mach-Zehnder interferometer and to the heterodyne measurement.

For details on the partial measurement projection, one can refer to the lectures at College de France of Serge Haroche, and particularly the courses 3 and 6 of 2007-2008. In addition, our analysis follows the work [Brune 90, Brune 92, Bouchoule 02] where a description of the measurement process and the partial projection is led.

5.3.1 Background formalism

5.3.1.1 The measurement process

The method which was first introduced in [Bouchoule 02], considers the sequential process:

1. An initial atomic state $|\psi_{\text{at}}(N_p)\rangle = \sum c_n(N_p)|n\rangle$ is given, where N_p is the number of photon detected in this sequential approach.
2. A photon arrives, and interacts with the sample. An entangled state is created between the atoms and the photon.
3. The photon is measured and the atomic wavefunction gets partially projected. This new wavefunction $|\psi_{\text{at}}(N_p + 1)\rangle$ is the one that interacts with the next photon and so on.

This scheme is synthesized in figure 5.8 where the notations are introduced. A comment is given in section 5.3.7 to justify the sequential approach for pulses of photon that may all interact with the atoms before any has been measured.

5.3.1.2 The atom-photon interaction

As described in section 5.2.3, the atom number difference \hat{J}_z is measured by the phase shift it induces on a probe. A simple description of the phenomena consists to consider the single atom phase shift ϕ introduced in section 5.2.3. The electric field that probes the sample will accumulate a phase that depends on the population difference in the form:

$$\hat{\Phi} = \phi \hat{J}_z. \quad (5.72)$$

A unique photon in the mode a arrives on a beam splitter B and ends up in a superposition of the two modes α and β :

$$\begin{pmatrix} \alpha \\ \beta \end{pmatrix} = B \begin{pmatrix} a \\ b \end{pmatrix}. \quad (5.73)$$

These modes can be spatially separated as in a Mach-Zehnder, or frequency separated as for the heterodyne detection. Only one of these modes a'_0 is interacting with the atoms. The other one a'_1 serves as a phase reference. The QND interaction matrix $U_{\text{QND}}(\hat{J}_z)$ depends on \hat{J}_z and can then be written as :

$$U_{\text{QND}}(\hat{J}_z) = \begin{pmatrix} e^{i\phi\hat{J}_z} & 0 \\ 0 & 1 \end{pmatrix}. \quad (5.74)$$

Formally, the operator obtained after the non demolition interaction can be calculated by:

$$\begin{pmatrix} \alpha' \\ \beta' \end{pmatrix} = U_{\text{QND}}(\hat{J}_z) B \begin{pmatrix} a \\ b \end{pmatrix}. \quad (5.75)$$

This description corresponds to the *Heisenberg representation* that will be conserved in the following of this chapter.

5.3.1.3 The photon measurement and the partial projection

Before the measurement of the photon, the total system {Atoms + photon} is in an entangled state. The measurement of the photon partially project the atomic wavefunction. Hence the annihilation operator $u(\hat{J}_z)$ projects the state $|1_0, 0_1\rangle \otimes |\psi_{\text{at}}(N_p)\rangle$ onto $|0_0, 0_1\rangle \otimes |\psi_{\text{at}}(N_p + 1)\rangle$.

The partial projection operation satisfies:

$$|\psi_{\text{at}}(N_p + 1)\rangle \propto \langle 0_0, 0_1 | u(\hat{J}_z) \left(|1_0, 0_1\rangle \otimes |\psi_{\text{at}}(N_p)\rangle \right) \quad (5.76)$$

The proper annihilation operator u to apply depends on the exact measurement procedure and will be explicitly given in the following for each measurement device considered.

5.3.2 The Mach-Zehnder interferometer

We apply now the method previously described to study the dynamics of the squeezing process using a Mach-Zehnder interferometer as described in figure 5.9. The atoms are inserted in one arm of a Mach-Zehnder interferometer. A $\pi/2$ phase is applied in the other arm so that the interferometer operates in a balanced configuration of the two outputs.

5.3.2.1 The projection of the atomic state

At the end of the Mach-Zehnder interferometer, a photon can be detected either in u or in v , but not on both detectors. Decomposing the initial state on the basis that represent the two possible outcome, we have:

$$|1_a, 0_b\rangle \otimes |\psi_{\text{at}}(N_p)\rangle \propto |1_u, 0_v\rangle \otimes |\psi_{\text{at}}^u(N_p)\rangle + |0_u, 1_v\rangle \otimes |\psi_{\text{at}}^v(N_p)\rangle, \quad (5.77)$$

where $|1_u, 0_v\rangle$ is obtained by applying the creation operator $u^\dagger(\hat{J}_z)$ onto the vacuum state $|0_a, 0_b\rangle$. The previous decomposition of the input state shows the entanglement between the photonic and the atomic state. Detecting a photon on u consists in projecting the entangled wavefunction on $|1_u, 0_v\rangle = u^\dagger(\hat{J}_z)|0_a, 0_b\rangle$ which can be written as:

$$|\psi_{\text{at}}(N_p + 1)\rangle = \langle 1_u, 0_v | \left(|1_a, 0_b\rangle \otimes |\psi_{\text{at}}(N_p)\rangle \right) \quad (5.78)$$

$$= \langle 0_a, 0_b | u(\hat{J}_z) \left(|1_a, 0_b\rangle \otimes |\psi_{\text{at}}(N_p)\rangle \right) = |\psi_{\text{at}}^u(N_p)\rangle. \quad (5.79)$$

In conclusion, two possibilities can happen when a photon arrives in a Mach Zehnder:

- A click on u has been detected and the atomic state becomes:

$$|\psi_{\text{at}}(N_p + 1)\rangle = \langle 0_a, 0_b | u(\hat{J}_z) \left(|1_a, 0_b\rangle \otimes |\psi_{\text{at}}(N_p)\rangle \right). \quad (5.80)$$

- A click on v has been detected and the atomic state becomes:

$$|\psi_{\text{at}}(N_p + 1)\rangle = \langle 0_a, 0_b | v(\hat{J}_z) \left(|1_a, 0_b\rangle \otimes |\psi_{\text{at}}(N_p)\rangle \right). \quad (5.81)$$

5.3.2.2 The Mach-Zehnder scattering matrix: Expression of $u(\hat{J}_z)$ and $v(\hat{J}_z)$

The two beam splitters are identical and have reflexion r , and transmission t such that $r^2 + t^2 = 1$. The beam splitter matrix B and the interaction matrix as described in figure 5.9 can be expressed as:

$$B = \begin{pmatrix} t & r \\ -r & t \end{pmatrix}, \quad U_{\text{QND}}(\hat{J}_z) = \begin{pmatrix} e^{i\phi\hat{J}_z} & 0 \\ 0 & e^{i\pi/2} \end{pmatrix}. \quad (5.82)$$

The overall transfer matrix $T = BU_{\text{QND}}(\hat{J}_z)B$ gives:

$$\begin{pmatrix} u \\ v \end{pmatrix} = T \begin{pmatrix} a \\ b \end{pmatrix} = \begin{pmatrix} t^2 e^{i\phi\hat{J}_z} - ir^2 & rt(i + e^{i\phi\hat{J}_z}) \\ -rt(i + e^{i\phi\hat{J}_z}) & -r^2 e^{i\phi\hat{J}_z} + it^2 \end{pmatrix} \begin{pmatrix} a \\ b \end{pmatrix}. \quad (5.83)$$

From the transfer matrix, follows the expression for u applied on $|1_a, 0_b\rangle$:

$$u|1_a, 0_b\rangle = e^{i(\frac{\phi\hat{J}_z}{2} + \frac{\pi}{4})} \left((t^2 - r^2) \cos\left(\frac{\phi\hat{J}_z}{2} - \frac{\pi}{4}\right) + i \sin\left(\frac{\phi\hat{J}_z}{2} - \frac{\pi}{4}\right) \right) |0_a, 0_b\rangle, \quad (5.84)$$

$$(5.85)$$

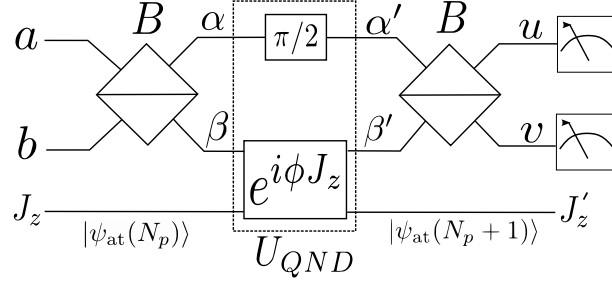


Figure 5.9: Scheme of the Mach-Zehnder interferometer considered.

The two paths are separated by a beam splitter B and latter recombined on another beam splitter. A phase of $\pi/2$ in one arm ensure that the output of Mach-Zehnder interferometer are balanced, but the beam splitter themselves can be unbalanced ($r \neq t$).

Similarly, for v applied on $|1_a, 0_b\rangle$, we have:

$$v |1_a, 0_b\rangle = 2rte^{i(\phi\hat{J}_z/2+\pi/4)} \cos\left(\frac{\phi\hat{J}_z}{2} - \frac{\pi}{4}\right) |0_a, 0_b\rangle \quad (5.86)$$

In the specific case of balanced beam splitter $r^2 = t^2 = 1/2$, the expression 5.84 and 5.86 simplify to:

$$u |1_a, 0_b\rangle = ie^{i(\frac{\phi\hat{J}_z}{2}+\frac{\pi}{4})} \sin\left(\frac{\phi\hat{J}_z}{2} - \frac{\pi}{4}\right) |0_a, 0_b\rangle, \quad (5.87)$$

$$v |1_a, 0_b\rangle = e^{i(\phi\hat{J}_z/2+\pi/4)} \cos\left(\frac{\phi\hat{J}_z}{2} - \frac{\pi}{4}\right) |0_a, 0_b\rangle. \quad (5.88)$$

5.3.2.3 The atomic state collapse

After a click on u , the atomic state is modified and becomes:

$$|\psi_{\text{at}}(N_p + 1)\rangle \propto e^{i(\frac{\phi\hat{J}_z}{2}+\frac{\pi}{4})} \left((t^2 - r^2) \cos\left(\frac{\phi\hat{J}_z}{2} - \frac{\pi}{4}\right) + i \sin\left(\frac{\phi\hat{J}_z}{2} - \frac{\pi}{4}\right) \right) |\psi_{\text{at}}(N_p)\rangle, \quad (5.89)$$

while a click on v gives:

$$|\psi_{\text{at}}(N_p + 1)\rangle \propto -2rte^{i(\frac{\phi\hat{J}_z}{2}+\frac{\pi}{4})} \cos\left(\frac{\phi\hat{J}_z}{2} - \frac{\pi}{4}\right) |\psi_{\text{at}}(N_p)\rangle. \quad (5.90)$$

For the sake of clarity, in the following, the normalization factor of $|\psi_{\text{at}}(N_p)\rangle$ will be intentionally removed.

After $N_p = N_u + N_v$ measurements with N_u clicks on u and N_v clicks on v , the atomic state distribution is obtained from the initial distribution through:

$$|\psi_{\text{at}}(N_p + 1)\rangle = \hat{\mathcal{F}}_{N_u, N_v} |\psi_{\text{at}}(0)\rangle, \quad (5.91)$$

where the distribution $\hat{\mathcal{F}}_{N_u, N_v}$ is called the squeezing function and is given by:

$$\begin{aligned} \hat{\mathcal{F}}_{N_u, N_v} = & e^{iN_p(\frac{\phi\hat{J}_z}{2} + \frac{\pi}{4})} \left((t^2 - r^2) \cos\left(\frac{\phi\hat{J}_z}{2} - \frac{\pi}{4}\right) + i \sin\left(\frac{\phi\hat{J}_z}{2} - \frac{\pi}{4}\right) \right)^{N_u} \\ & \times \left(-2rt \cos\left(\frac{\phi\hat{J}_z}{2} - \frac{\pi}{4}\right) \right)^{N_v}. \end{aligned} \quad (5.92)$$

The shape of the squeezing function describes how the initial atomic distribution is affected by the measurement.

We notice that the coefficient $c_n(N_p)$ of the decomposition of the state $|\psi_{\text{at}}(N_p)\rangle$ are amplitude of probabilities and can be complex. But the measurable quantities are real:

$$\langle \hat{J}_z \rangle = \langle \psi_{\text{at}}(N_p + 1) | \hat{J}_z | \psi_{\text{at}}(N_p + 1) \rangle \quad (5.93)$$

$$\propto \sum_{n=-N_{\text{at}}/2}^{N_{\text{at}}/2} n |\mathcal{F}_{N_u, N_v}(n)|^2 |c_n(0)|^2, \quad (5.94)$$

$$\Delta \hat{J}_z^2 = \langle \hat{J}_z^2 \rangle - \langle \hat{J}_z \rangle^2, \quad (5.95)$$

where $\mathcal{F}_{N_u, N_v}(n)$ is such that:

$$\hat{\mathcal{F}}_{N_u, N_v} |n\rangle = \mathcal{F}_{N_u, N_v}(n) |n\rangle. \quad (5.96)$$

Practically, the expression of $\mathcal{F}_{N_u, N_v}(n)$ is obtained by replacing \hat{J}_z by n in the equation 5.92.

Gaussian approximation

In figure 5.10, is presented the squeezing function $|\mathcal{F}_{N_u, N_v}(n)|^2$ with its Gaussian approximation. The analytical expression of the Gaussian approximation is derived in appendix E.1. From figure 5.10, it appears that the gaussian approximation matches well with the exact squeezing function. We have already seen in section 5.1.3 that the initial distribution $c_n(0)$ was approximated by a Gaussian. By Deriving the analytical expression of the gaussian approximation of $|\mathcal{F}_{N_u, N_v}(n)|^2$, we will obtain analytical expression for $\langle \hat{J}_z \rangle$ and $\Delta \hat{J}_z$ that will naturally arise as the first and second momenta of the distribution.

The Gaussian approximation of $|\mathcal{F}_{N_u, N_v}(n)|^2$ is:

$$|\mathcal{F}_{N_u, N_v}(n)|^2 = |\mathcal{F}_{N_u, N_v}(n_0)|^2 e^{\frac{-(n-n_0)^2}{2\sigma^2}} \quad (5.97)$$

To derive the expression of n_0 and σ , we proceed to the Taylor expansion of the Gaussian distribution that is given in appendix E.1:

$$|\mathcal{F}_{N_u, N_v}(n)|^2 \approx |\mathcal{F}_{N_u, N_v}(n_0)|^2 \left(1 - \frac{(n - n_0)^2}{2\sigma^2} \right) \quad (5.98)$$

$$\begin{aligned} & \approx |\mathcal{F}_{N_u, N_v}(n_0)|^2 + \frac{d}{dn} |\mathcal{F}_{N_u, N_v}(n)|^2 \Big|_{n_0} (n - n_0) \\ & \quad + \frac{1}{2} \frac{d^2}{dn^2} |\mathcal{F}_{N_u, N_v}(n)|^2 \Big|_{n_0} (n - n_0)^2 \end{aligned} \quad (5.99)$$

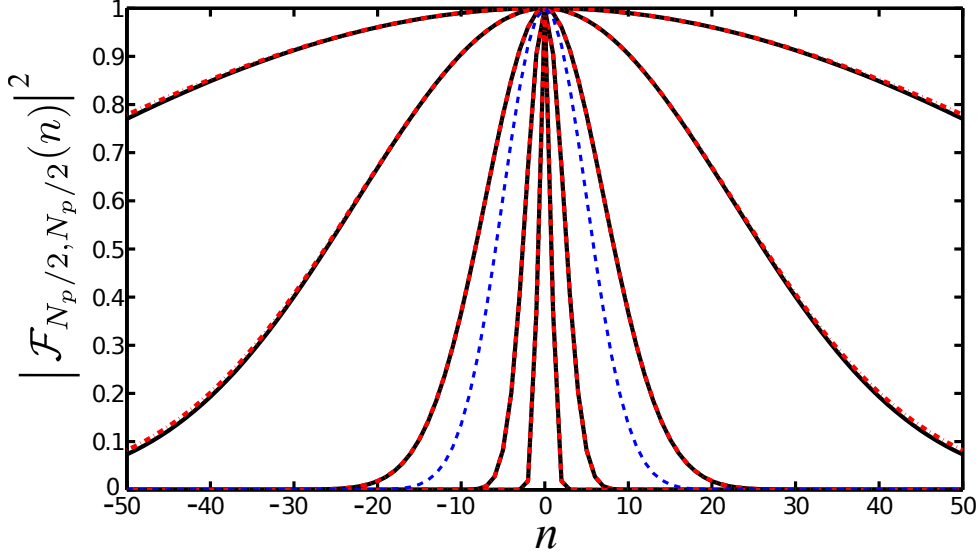


Figure 5.10: Squeezing function

The squeezing function $|\mathcal{F}_{N_p/2, N_p/2}(n)|^2$ is plotted in black for $N_{\text{at}} = 100$, $\phi = 10^{-2}$ and $N_p = 1, 10, 100, 1000, 10000$. In red dashed dotted line is given the gaussian approximation of equation 5.102. In blue dashed line is given, for reference, the initial atomic distribution $|c_n(0)|^2$.

After the stochastic measurement of N_u photons on u and N_v photons on v , the squeezing function is centered on:

$$n_0 = \frac{2}{\phi} \left[\arctan \left(-\sqrt{\frac{(N_v + 2N_u)\mathcal{C} - N_v}{N_v(1 + \mathcal{C})}} \right) + \frac{\pi}{4} \right], \quad (5.100)$$

where \mathcal{C} is the contrast of the unbalanced ($r \neq t$) interferometer:

$$\mathcal{C} = \frac{2t^2r^2}{r^4 + t^4}. \quad (5.101)$$

The variance of $|\mathcal{F}_{N_u, N_v}(n)|^2$ is given by:

$$\sigma^2 = \frac{1}{\phi^2 N_p \mathcal{C}}. \quad (5.102)$$

In equation 5.100, the negative root has been chosen so that n_0 is centered around 0 for a contrast $\mathcal{C} \sim 1$. An identical choice could have been done by taking a phase of $-\pi/2$, instead of $\pi/2$, in the second arm of the interferometer in figure 5.9. The result obtained in equation 5.102, is only valid for a contrast $\mathcal{C} \sim 1$, for which the squeezing function is centered around 0.

In equation 5.32 we have seen that the initial atomic distribution $c_n(0)$ of the coherent superposition was well approximated by a Gaussian distribution:

$$c_n(0) \approx \left(\frac{2}{\pi N_{\text{at}}} \right)^{1/4} e^{-\frac{n^2}{N_{\text{at}}}}. \quad (5.103)$$

The distribution of the Dicke state probability after N_p detection is obtained by applying the squeezing function induced by the measurement onto the initial atomic state:

$$|c_n(N_p)|^2 = |\mathcal{F}_{N_u, N_v}(n)c_n(0)|^2 \propto \sqrt{\frac{2}{\pi N_{\text{at}}}} |\mathcal{F}_{N_u, N_v}(n_0)|^2 e^{-\frac{(n-n_1)^2}{2\sigma'^2}}, \quad (5.104)$$

with

$$\sigma'^2 = \frac{N/4}{1 + \frac{\phi^2 N_{\text{at}} N_p \mathcal{C}}{4}}, \quad (5.105)$$

$$n_1 = n_0 \sigma'^2 \phi^2 N_p \mathcal{C}. \quad (5.106)$$

In conclusion, the measurement of N_u photons on u and N_v photons on v has modified the atomic state wavefunction such that:

$$\langle \hat{J}_z \rangle = n_1 = n_0 \sigma'^2 \phi^2 N_p \mathcal{C} \quad (5.107)$$

$$\Delta \hat{J}_z^2 = \xi_z^2 \Delta \hat{J}_z^2(0) = \frac{\Delta \hat{J}_z^2(0)}{1 + \kappa^2} = \frac{\Delta \hat{J}_z^2(0)}{1 + \frac{\phi^2 N_{\text{at}} N_p \mathcal{C}}{4}} \quad (5.108)$$

In consequence, while the process is purely stochastic as indicated by the random mean value $\langle \hat{J}_z \rangle$, the variance of the atomic distribution follows a deterministic compression. In addition, the stronger is the interaction ϕ , the more information is collected by each photon, and the more the variance will be lowered for a given number of photons. In the following, we parametrize the strength of the measurement by the parameter $M^2 = \mathcal{C}\phi^2/4$ such that $\kappa^2 = M^2 N_{\text{at}} N_p$. In equation 5.108, we defined the squeezing parameter ξ_z^2 , which describes the reduction of the variance. As the mean length of the Bloch representation has been reduced, the real gain for an interferometric sequence is $\xi_{\text{W}}^2 = \xi_z^2 J / \langle \hat{J}_x \rangle$ [Wineland 92].

5.3.2.4 Simulation of the collapse in a Mach-Zehnder

The formalism previously described is very well adapted to simulate the collapse of the atomic state, *via* a Monte Carlo simulation:

1. An initial atomic state with a Gaussian distribution is given: $|\psi_{\text{at}}(0)\rangle$.
2. A photon arrives at the input of the interferometer and is randomly detected on u or v with probability:

$$P_v = \left| \langle 0_u, 1_v | \left(|1_a, 0_b\rangle \otimes |\psi_{\text{at}}(N_p)\rangle \right) \right|^2 = 4r^2 t^2 \sum_{n=-N_{\text{at}}/2}^{N_{\text{at}}/2} \cos^2 \Phi(n) c_n^2(N_p) \quad (5.109)$$

3. After it has been determined whether the photon arrived on u or v , the new atomic wavefunction $|\psi_{\text{at}}(1)\rangle$ is computed using equation 5.89 and 5.90.
4. A new photon arrives and the process restarts at step 2.

The mean value and the variance of \hat{J}_z are evaluated using:

$$\langle \hat{J}_z \rangle = \sum_{n=-N_{\text{at}}/2}^{N_{\text{at}}/2} n |c_n(N_p)|^2 \quad (5.110)$$

$$\Delta \hat{J}_z^2 = \sum_{n=-N_{\text{at}}/2}^{N_{\text{at}}/2} n^2 |c_n(N_p)|^2 - \langle \hat{J}_z \rangle^2 \quad (5.111)$$

The stochastic behavior of the mean value of \hat{J}_z can be seen in figure 5.11a where each trajectory leads to the collapse of the state on a different Dicke state. In figure 5.11b, the shape of the deterministic behavior of the reduction of the variance shows that the analytical expression found by the Gaussian approximation is in very good agreement with the simulation. The long time behavior which becomes stochastic is discussed in section 5.3.3. The density of probability of this partial projection process is presented in figure 5.11c.

In figure 5.11c the Gaussian envelope describes the initial state distribution c_n^2 and shows that this photon by photon description reproduces the Born probability rule: $P_n = |\langle n | \psi_{\text{at}}(0) \rangle|^2$. This was a priori non trivial even if highly expected since the Born rule was assumed for the photonic projection.

5.3.3 Long term behavior

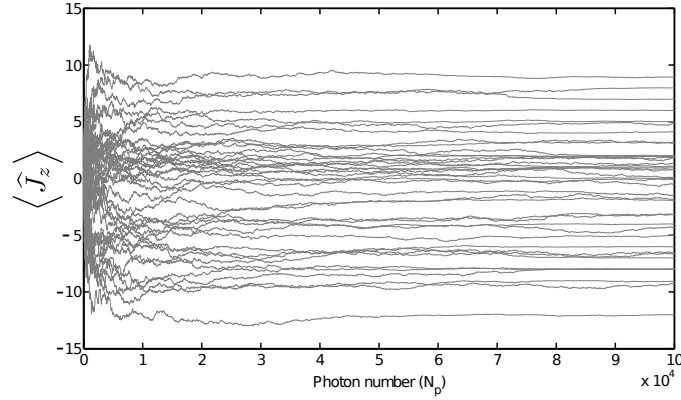
We analyze now the long term behavior of the variance that starts deterministic and ends stochastic in figures 5.11b and 5.19c. The determinist behavior that was shown for example with the Gaussian approximation method relies on the fact that the atomic distribution can be well approximated by a continuous Gaussian distribution, *i.e.* that many Dicke State contribute to form the Gaussian. This approximation is no more verified for highly squeezed states where the weights of the atomic distribution are essentially spread over only one or two Dicke states. In that case the variance strongly depends on the position of the distribution compared to the closest eigenvalue of \hat{J}_z and two extreme cases arise:

- The squeezing function is centered exactly in between two Dicke states. In that case, the variance is the one of 2 equally weighted points and separated by 1 (figure 5.12 (a)):

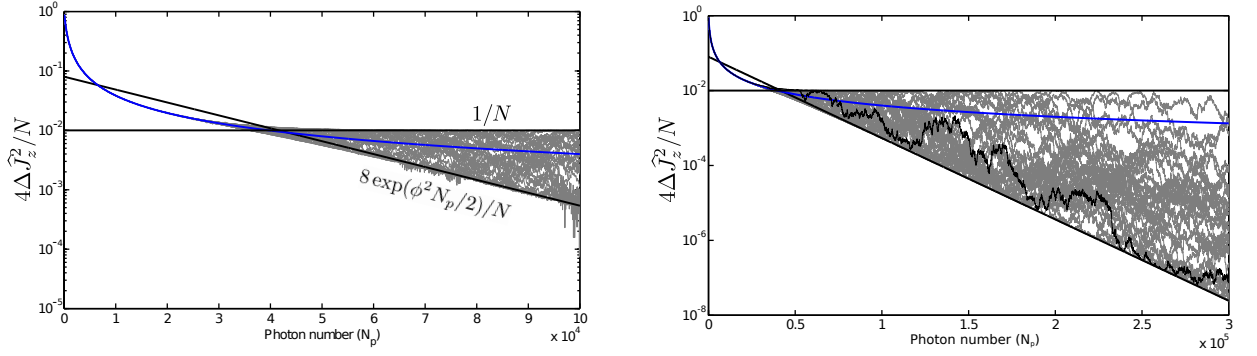
$$\Delta \hat{J}_z^2 = 1/4. \quad (5.112)$$

- The squeezing function is centered on a given Dicke state $|n_0\rangle$. In that case, three states contribute to the variance: $|n_0\rangle$ with weight ~ 1 and $|n_0 \pm 1\rangle$ with weight $\exp(-2M^2 N_p)$ (figure 5.12 (b)). In that case we have:

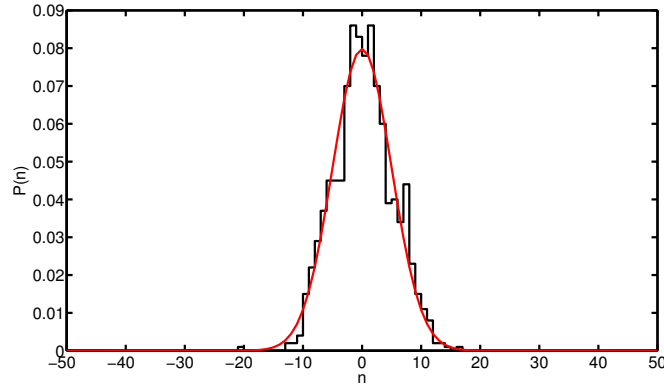
$$\Delta \hat{J}_z^2 = 2 \exp(-2M^2 N_p) \quad (5.113)$$



(a) Mean value of the atomic wavefunction for a few "experimental" realization



(b) Variance of the atomic wavefunction. Short (left) and long (right) time behavior.



(c) Mean value arrival probability traced over 1000 trajectories

Figure 5.11: Simulation of the atomic wavefunction collapse in a Mach-Zehnder measurement for $N_{\text{at}} = 100$ and $\phi = 10^{-2}$.

While the mean value has a stochastic behavior, the variance of the atomic state gets squeezed by a deterministic amount. A stochastic behavior reappears for $\Delta\hat{J}_z^2 = 1/4$ (discussed in section 5.3.3). In the long time behavior (b), it clearly appears that the steady state that corresponds to $\Delta\hat{J}_z^2 = 1/4$ is unstable and that all the trajectories converge towards a Dicke state. The partial measurement projection finally finishes with mean values that satisfies the Born probability rule $P_n = |\langle n | \psi_{\text{at}}(0) \rangle|^2$.

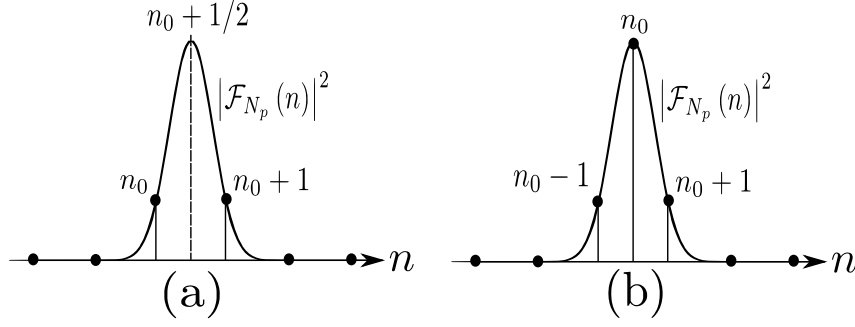


Figure 5.12: Long time behavior, the continuity breaks down

For long interrogation time, when the squeezing function approaches the single Dicke state, the precise position of the squeezing function $\mathcal{F}_{N_p}(n)$ plays a role in the determination of the variance since it matters then if the squeezing function is centered on an eigen value or in between two eigen values (see text, section 5.3.3). Thus the stochastic behavior of the mean value is transferred on the value of the variance.

These two limits are very clear on the simulations of figure 5.11b and 5.19c. These limits are reached when the atom number is known to within one atom. If the initial sample contains a tenth of atoms, a small amount of squeezing would be sufficient to enter these regime. Some experiments [Guerlin 07] should actually already see these non-determinist behaviors if they exist. Nevertheless, they are transient behavior since only the case of figure 5.12 (b) is stable since in the case 5.12 (a) any new measured photon will unbalance the equilibrium and make it converge towards a Dicke State. Every state should collapse on a Dicke state, but it can take more or less time. This is coherent with the fact that the Dicke state are the eigen vector of the measured observable.

We emphasize that in the previous wavefunction description, the spontaneous emission processes and the decoherence they induces were not taken into account [Chase 08]. These effects are among the main limiting factors to reach these highly squeezed states.

5.3.4 The Mach-Zehnder including losses and in an optical cavity

Now that we have described the collapse of the atomic wave function with the measurement, we include two more phenomena in the analysis:

- the losses of photons and thus of information.
- the coupling enhancement of a cavity.

5.3.4.1 Losses in the Mach-Zehnder interferometer

To model the losses, we consider the extra coupling of one mode to the vacuum mode through an additional beam splitter in the Mach Zehnder interferometer. It is formally presented in figure 5.13. Three modes are now entering the set-up (a, b, p) and three exiting (u, v, p'). They are linked by:

$$\begin{pmatrix} u \\ v \\ p' \end{pmatrix} = BU_{\text{loss}}U_{\text{QND}}(\hat{J}_z)B \begin{pmatrix} a \\ b \\ p \end{pmatrix}, \quad (5.114)$$

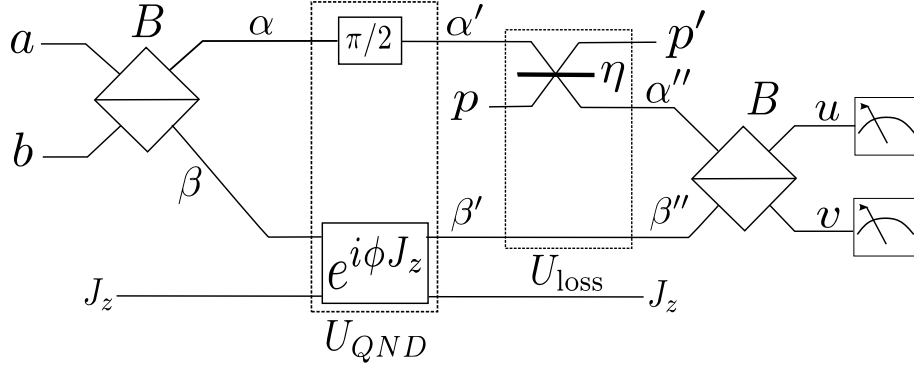


Figure 5.13: Scheme of the lossy Mach-Zehnder

The losses are modeled by the coupling of one arm to the vacuum through an additional beam splitter which reflects η in intensity (losses).

with

$$B = \begin{pmatrix} t & r & 0 \\ -r & t & 0 \\ 0 & 0 & 1 \end{pmatrix}, \quad U_{\text{QND}}(\hat{J}_z) = \begin{pmatrix} e^{i\phi\hat{J}_z} & 0 & 0 \\ 0 & e^{i\pi/2} & 0 \\ 0 & 0 & 1 \end{pmatrix}, \quad U_{\text{loss}} = \begin{pmatrix} 1 & 0 & 0 \\ 0 & \sqrt{1-\eta} & \sqrt{\eta} \\ 0 & -\sqrt{\eta} & \sqrt{1-\eta} \end{pmatrix}. \quad (5.115)$$

In the case of a balanced Mach-Zehnder interferometer ($t^2 = r^2 = 1/2$), the resulting transfer matrix is:

$$T = BU_{\text{loss}}U_{\text{QND}}(\hat{J}_z)B = \begin{pmatrix} \sinh(i\Phi' - \frac{1}{4}\ln(1-\eta)) & \cosh(i\Phi' - \frac{1}{4}\ln(1-\eta)) & \frac{1}{\sqrt{2}}\sqrt{\eta} \\ -\cosh(i\Phi' - \frac{1}{4}\ln(1-\eta)) & -\sinh(i\Phi' - \frac{1}{4}\ln(1-\eta)) & \frac{1}{\sqrt{2}}\sqrt{\eta} \\ \frac{1}{\sqrt{2}}\sqrt{\eta}i & -\frac{1}{\sqrt{2}}\sqrt{\eta}i & \sqrt{1-\eta} \end{pmatrix} \quad (5.116)$$

where $\Phi' = \phi\hat{J}_z/2 - \pi/4$.

Similarly to the method presented previously, detecting a photon on u consists to project $|1_a, 0_b, 0_p\rangle \otimes |\psi_{\text{at}}(N_p)\rangle$ on $|1_u, 0_v, 0_{p'}\rangle = u^\dagger(\hat{J}_z)|0_a, 0_b, 0_p\rangle$ and it results:

$$|\psi_{\text{at}}(N_p + 1)\rangle = \langle 0_a, 0_b, 0_p | u(\hat{J}_z) (|1_a, 0_b, 0_p\rangle \otimes |\psi_{\text{at}}(N_p)\rangle) \quad (5.117)$$

$$= e^{i(\frac{\phi\hat{J}_z}{2} + \frac{\pi}{4})} \sinh(i\Phi' - \frac{1}{4}\ln(1-\eta)) |\psi_{\text{at}}(N_p)\rangle. \quad (5.118)$$

For a click on v , we have:

$$|\psi_{\text{at}}(N_p + 1)\rangle = -e^{i(\frac{\phi\hat{J}_z}{2} + \frac{\pi}{4})} \cosh(i\Phi' - \frac{1}{4}\ln(1-\eta)) |\psi_{\text{at}}(N_p)\rangle. \quad (5.119)$$

The mean value and variance of \hat{J}_z are still described by the square modulus of the squeezing function $\mathcal{F}_{N_u, N_v}(n)$ which is now:

$$|\mathcal{F}_{N_u, N_v}(n)|^2 = \left| \sinh(i\Phi' - \frac{1}{4}\ln(1-\eta)) \right|^{2N_u} \left| \cosh(i\Phi' - \frac{1}{4}\ln(1-\eta)) \right|^{2N_v} \quad (5.120)$$

$$\propto (1 + \mathcal{C} \sin(\phi n))^{N_u} (1 - \mathcal{C} \sin(\phi n))^{N_v}, \quad (5.121)$$

where \mathcal{C} is the contrast of the interferometer:

$$\mathcal{C} = \frac{2t^2r^2\sqrt{1-\eta}}{(1-\eta)r^4+t^4} \stackrel{r^2=t^2=1/2}{=} \frac{2\sqrt{1-\eta}}{2-\eta}. \quad (5.122)$$

The Gaussian approximation of $|\mathcal{F}_{N_u, N_v}(n)|^2$ leads to:

$$|\mathcal{F}_{N_u, N_v}(n)|^2 \propto e^{-\frac{(n-n_0)^2}{2\sigma^2}}, \quad (5.123)$$

with

$$n_0 = \frac{1}{\phi} \arcsin \left(\frac{\Delta N}{\mathcal{C}(N_u + N_v)} \right), \quad (5.124)$$

$$\frac{1}{\sigma^2} = \mathcal{C}^2 \phi^2 N_p \left(1 + \left(\frac{\Delta N}{N_p \mathcal{C}} \right)^2 \right). \quad (5.125)$$

The variance reduction of $|\mathcal{F}_{N_u, N_v}(n)|^2$ is then again determinist up to the second order in the output probability.

In conclusion, photon losses in the Mach-Zehnder reduces the squeezing effect by an amount proportional to the square of the contrast reduction \mathcal{C} , *i.e.*

$$\Delta \hat{J}_z^2 = \frac{\Delta \hat{J}_z^2(0)}{1 + \kappa^2} = \frac{\Delta \hat{J}_z^2(0)}{1 + \frac{\phi^2 N_{\text{at}} N_p \mathcal{C}^2}{4}}. \quad (5.126)$$

As in equation 5.108, we can define the strength of the measurement that is now $M^2 = \phi^2 \mathcal{C}^2 / 4$ which scales quadratically with the contrast. The loss of information due to photon losses is identical to the one due to beamsplitters imbalance, and the relevant parameter to describe the loss of information is the contrast of the interferometer.

5.3.4.2 The cavity

We concentrate now on the case of a Mach-Zehnder in which the atoms are placed at the center of a Fabry-Perot cavity as presented in figure 5.14. We assume that the cavity is on resonance with the light if the atoms cause no phase shift ($n\phi = 0$), and we consider small atomic phase shifts such that the transmission of the cavity can be considered as constant.

A priori argumentation Classically, if the atoms induces in single pass a phase ϕ_{at} , a photon that makes N_c turns in the cavity accumulates a phase $2N_c\phi_{\text{at}}$. The finesse \mathcal{F} being the average number of turns of a photon, the previous argument suggests that the cavity enhancement in the reduction of $\Delta \hat{J}_z^2$ will scale as $\phi^2 \mathcal{F}^2$. Nevertheless, this scaling law can be doubted since the photons make a stochastic number of turns which may blur the accumulated information. The following demonstration intends to show that this scaling law actually applies.

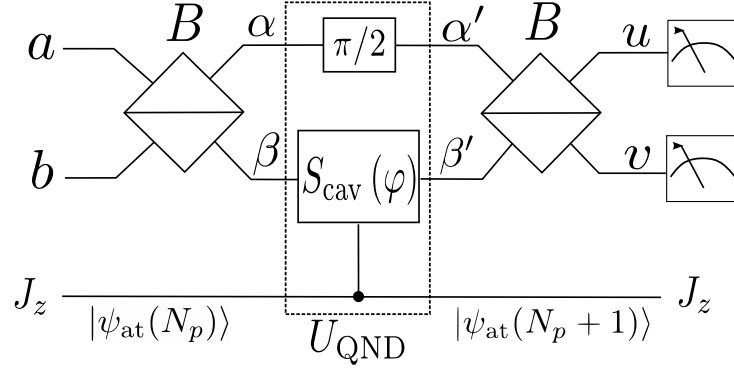


Figure 5.14: *Scheme of the Mach-Zehnder with a sensitivity increased by the cavity.*
The atoms are inserted in a Fabry-Perot cavity that modify the atom-light scattering matrix S_{cav}

Demonstration We consider the simplified case of a balanced Mach-Zender interferometer: $r^2 = t^2 = 1/2$. The cavity has mirror reflectivity R in intensity. If the k^{th} photon has made $\tilde{N}_c^{(k)}$ turn in the cavity, it has accumulated a phase shift per atom number difference that is: $2\tilde{N}_c^{(k)}\phi$.

The squeezing function as introduced previously is given by:

$$\mathcal{F}_{N_u, N_v}^{(C)}(n) = \prod_{k=1}^{N_u} \cos\left(\frac{\phi n}{2} 2\tilde{N}_c^{(k)} - \frac{\pi}{4}\right) \prod_{k=N_u+1}^{N_p} \sin\left(\frac{\phi n}{2} 2\tilde{N}_c^{(k)} - \frac{\pi}{4}\right) \quad (5.127)$$

where $\tilde{N}_c^{(k)}$ is the stochastic number of turn of the k^{th} photon. In the following we neglect the atomic absorption as well as the variation of transmission of the cavity due to the atomic phase shift. Under these conditions, the number of turns follows a stationary process, and the probability for a photon to make m turns is given by $P(m) = TR^m$.

The product of equation 5.127 can be rearranged to regroup the photons that made the same number of turns.

$$\mathcal{F}_{N_u, N_v}^{(C)}(n) = \prod_{m=0}^{\infty} \cos^{P(m)N_u}\left(\phi nm - \frac{\pi}{4}\right) \sin^{P(m)N_v}\left(\phi nm - \frac{\pi}{4}\right) \quad (5.128)$$

$$= \prod_{m=0}^{\infty} \mathcal{F}_{N_u, N_v}^{(SP)}(nm)^{P(m)} \quad (5.129)$$

where $\mathcal{F}_{N_u, N_v}^{(SP)}(nm)$ is the single pass squeezing function defined in 5.92.

Using the Gaussian approximation for $\left|\mathcal{F}_{N_u, N_v}^{(SP)}(nm)\right|^2$, it follows immediately:

$$\left|\mathcal{F}_{N_u, N_v}^{(C)}(n)\right|^2 \propto e^{-T \sum_{m=0}^{\infty} R^m (\phi^2 N_p (nm - \tilde{n}_0)^2)} \quad (5.130)$$

$$\propto e^{-T \sum_{m=0}^{\infty} R^m \phi^2 N_p n^2 m^2} e^{T \sum_{m=0}^{\infty} R^m 2nm\tilde{n}_0} \quad (5.131)$$

The variance σ^2 of $\left|\mathcal{F}_{N_u, N_v}^{(C)}(n)\right|^2$ is given by:

$$\frac{1}{\sigma^2} = 2T \sum_{m=0}^{\infty} R^m \phi^2 N_p m^2 \approx 4 \frac{\phi^2}{(1-R)^2} N_p \quad (5.132)$$

This leads to the desired result:

$$\sigma^2 \approx \frac{\pi^2}{4(\mathcal{F}\phi)^2 N_p} \quad (5.133)$$

and proves that the variance of the states decreases deterministically even if the number of turns is a stochastic parameter. In addition, it shows that the proper quantity to take into account for the enhancement of the squeezing is the finesse of the cavity \mathcal{F} .

Similarly to equation 5.108, in this enhanced measurement, the variance of \hat{J}_z evolves as:

$$\Delta \hat{J}_z^2 = \frac{\Delta \hat{J}_z^2(0)}{1 + \kappa_c^2} = \frac{\Delta \hat{J}_z^2(0)}{1 + \phi^2 \frac{\mathcal{F}^2}{\pi^2} N_{\text{at}} N_p} \quad (5.134)$$

For a cavity enhanced measurement, the measurement strength is $M^2 = \phi^2 \frac{\mathcal{F}^2}{\pi^2}$

This results suggests that the signal-to-noise κ of the measurement increases as \mathcal{F}/π . This statement can be confusing regarding [Lye 03] where the signal-to-noise is shown to scale as $\sqrt{\mathcal{F}/\pi}$. In fact, in our description, we have ignored the spontaneous emission destructivity that increases with the finesse. To understand the enhancement that brings the cavity, it is important to compare situations which are inducing the same number of spontaneous emission events. As a photon interacts \mathcal{F}/π times with the atoms, the destructivity in a cavity scales as $\mathcal{F}N_p/\pi$ whereas it scales as N_p in single pass. Hence for N_p photons used in single pass, $\pi N_p/\mathcal{F}$ should be used in the cavity, and the signal-to-noise κ_c is then truly enhanced by $\sqrt{\mathcal{F}/\pi}$ (see equation 5.134).

5.3.5 The heterodyne measurement

This section aims at the description of the partial collapse in an heterodyne measurement. The heterodyne scheme has been chosen in the experiment because of the technical advantages it exhibits in terms of common noise suppression as well as in the benefit it takes from the strong local oscillator. These technical properties will be further discussed in section 6.1.3. We concentrate here on the description of the quantum partial projection and on the squeezing dynamics of the heterodyne detection. We first describe the concept of a phase modulator for a single photon. The partial projection that each photon realizes is then discussed, and the collapse of the wavefunction is evaluated.

5.3.5.1 A frequency splitter for single photons

In appendix E.3, we derived the matrix expression of a single sideband frequency modulator. The result shows that such a frequency modulator is the frequency analog of a beam splitter, and that the splitting matrix takes the form:

$$\begin{pmatrix} a'_0 \\ a'_1 e^{i\Omega t} \end{pmatrix} = \begin{pmatrix} \sqrt{T} & \sqrt{R} e^{-i\Omega t} \\ -\sqrt{R} e^{i\Omega t} & \sqrt{T} \end{pmatrix} \begin{pmatrix} a_0 \\ a_1 e^{i\Omega t} \end{pmatrix}, \quad (5.135)$$

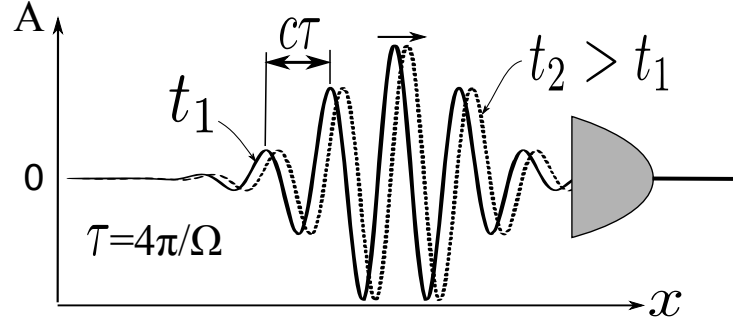


Figure 5.15: Schematic of the detection of a photon in a superposition of two modes. Here is represented the amplitude of probability A of arrival of 1 photon. The envelope describes the coherence length of the photon. The amplitude A is defined such that $P(t) = |A(t)|^2$.

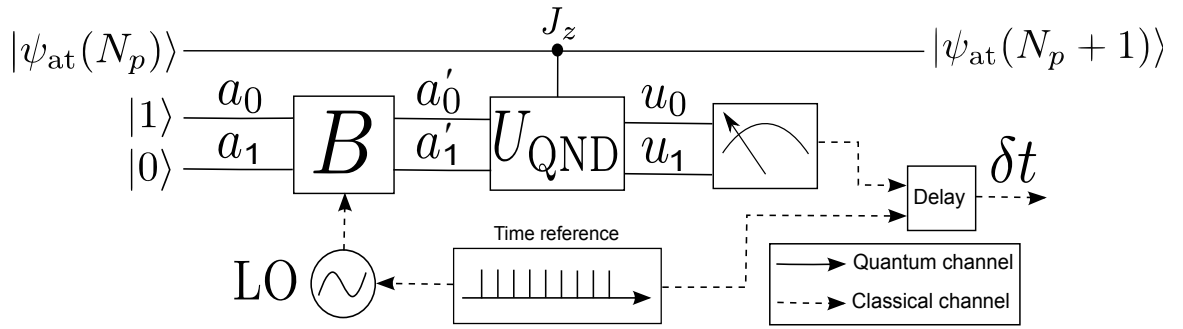


Figure 5.16: Schematic of the detection of a photon in a superposition of two modes. Single-photons are sent through a spectral beamsplitter B and interact non-destructively with the atomic ensemble (UQND). When a photon in the superposition of the mode u_0 and u_1 arrive on the detector, a click is measured. The detection time of each photon is measured by comparison with a time reference signal.

where a_0 and a_1 are two input modes of the field and Ω is the modulation frequency that corresponds to the frequency splitting between the two modes.

The effect of such a modulator on the photonic wavefunction of a single photon is illustrated in figure 5.15 where we see the modulation of the wavefunction, that is latter detected on the photodiode.

5.3.5.2 The interaction, the detection and the collapse of the atomic state

To use one of the two modes as a phase reference, one of the two modes has to be non-interacting with the atoms. Experimentally, one mode is adjusted close to the atomic resonance while the other one is far detuned. The scattering matrix $U_{\text{QND}}(\hat{J}_z)$ and the transfer matrix $S = U_{\text{QND}}(\hat{J}_z)B$ are then :

$$U_{\text{QND}}(\hat{J}_z) = \begin{pmatrix} 1 & 0 \\ 0 & e^{i\phi\hat{J}_z} \end{pmatrix}, \quad (5.136)$$

and,

$$\begin{pmatrix} u_0 \\ u_1 e^{i\Omega t} \end{pmatrix} = S(\hat{J}_z) \begin{pmatrix} a_0 \\ a_1 e^{i\Omega t} \end{pmatrix} = \begin{pmatrix} \sqrt{T} & \sqrt{R} e^{-i\Omega t} \\ -\sqrt{R} e^{i(\Omega t + \phi\hat{J}_z)} & \sqrt{T} e^{i\phi\hat{J}_z} \end{pmatrix} \begin{pmatrix} a_0 \\ a_1 e^{i\Omega t} \end{pmatrix} \quad (5.137)$$

In the Mach-Zehnder interferometer, we were projecting the atomic wavefunction differently if the photon was arriving on u or on v . Here we have only one photodetector and cannot distinguish photons that arrive from one or the other mode. In an heterodyne detection, the information is encoded in the time arrival of photons with respects to the clicks of the local oscillator. Indeed, an atomic phase shift delays or accelerates the photon, and the detected beatnote is phase shifted with respect to the local oscillator. As a consequence, there are not only two states where the photonic wavefunction can be projected but a continuum, that can be formally written as:

$$|1_{t=\tilde{t}}, 0_{t \neq \tilde{t}}\rangle = |1_{t=\tilde{t}}\rangle \quad (5.138)$$

This basis describes a photon that arrives at a time $t = \tilde{t}$ and not at any other time.

Because the local oscillator is periodic, we can reference the time of detection \tilde{t} to the closest click of the oscillator t_n , and parametrize the detection by the time delay $\tilde{\delta}t = \tilde{t} - t_n$ which is a stochastic variable that is different for each photon. With such a definition, we have:

$$|1_{t=\tilde{t}}\rangle = |1_{t=\tilde{\delta}t}\rangle \quad (5.139)$$

The state $\langle 1_{t=\tilde{\delta}t}|$ is obtained by applying the time dependent annihilation operator of the photodetection $(u_0(\hat{J}_z) + u_1(\hat{J}_z)e^{i\Omega\tilde{\delta}t})$ on the vacuum state ($\langle 0|$). Hence, we have :

$$\langle 1_{t=\tilde{\delta}t}| = \langle 0| \left[u_0(\hat{J}_z) + u_1(\hat{J}_z)e^{i\Omega\tilde{\delta}t} \right] \quad (5.140)$$

Thus, when the $N_p + 1$ photon is detected with a time delay $\tilde{\delta}t$, the atomic wave function is projected as:

$$|\psi_{\text{at}}(N_p + 1)\rangle \propto \langle 0| u_0(\hat{J}_z) + u_1(\hat{J}_z)e^{i\Omega\tilde{\delta}t} \left(|1_0, 0_1\rangle \otimes |\psi_{\text{at}}(N_p)\rangle \right) \quad (5.141)$$

$$\propto \left[(\sqrt{T} - \sqrt{R}) \cos\left(\frac{\Omega\tilde{\delta}t}{2} + \frac{\phi\hat{J}_z}{2}\right) - i(\sqrt{R} + \sqrt{T}) \sin\left(\frac{\Omega\tilde{\delta}t}{2} + \frac{\phi\hat{J}_z}{2}\right) \right] |\psi_{\text{at}}(N_p)\rangle. \quad (5.142)$$

A time delay $\tilde{\delta}t_k$ of the k^{th} photon corresponds to a phase

$$\tilde{\varphi}_k = \Omega\tilde{\delta}t_k - \pi, \quad (5.143)$$

at the detection. To obtain the expression 5.142, a phase of π has been introduced in the demodulation so that the photons arrival times coincide with a tooth of the comb of temporal pulses (time reference).

The squeezing function $\mathcal{F}_{N_p}(n)$ that was introduced in equation 5.92 becomes:

$$|\mathcal{F}_{N_p}(n)|^2 \propto \prod_{k=1}^{N_p} (1 + \mathcal{C} \cos(\tilde{\varphi}_k + \phi n)) \quad (5.144)$$

where $\mathcal{C} = 2\sqrt{RT}$ is the contrast of the beatnote.

To further continue, we derive the Gaussian approximation of $|\mathcal{F}_{N_p}(n)|^2$:

$$|\mathcal{F}_{N_p}(n)|^2 \propto \exp \left[-2M^2 N_p (n^2 + 2\overline{\delta\tilde{\varphi}}n/\phi) \right] \quad (5.145)$$

where

$$\overline{\delta\tilde{\varphi}} = \frac{1}{N_p} \sum_{j=1}^{N_p/N_t} N_t \delta\tilde{\varphi}_j \quad (5.146)$$

is the average mean phase shift over the followed trajectory. For the sake of clarity, these analytical expressions are derived in paragraph 5.3.5.3 which is rather technical. In the analysis, we consider subset of N_t successive photons for which the process is considered stationary. $\delta\tilde{\varphi}_j = -\phi \left\langle \hat{J}_z \right\rangle_i$ is the mean phase shift induced by the atoms. The hypothesis of stationarity over the subset i consists to assume that $\left\langle \hat{J}_z \right\rangle_i$ is constant over the subset, and that every photons of the subset follow the same probability distribution $P(\varphi)$ for the detected phase (φ) (see equation 5.149). $\overline{\delta\tilde{\varphi}}$ describes the mean value of the mean phase shift of each subset.

In equation 5.145, we introduced the measurement strength of the heterodyne detection:

$$M^2 = \frac{\phi^2}{4} \left(1 - \sqrt{1 - \mathcal{C}^2} \right), \quad (5.147)$$

As for the case of the Mach Zehnder (section ??), M^2 depends on the light-atom coupling ϕ and on the contrast of the interferometer \mathcal{C} .

As consequence, the heterodyne measurement is expected to collapse the atomic state with a variance that follows:

$$\Delta \hat{J}_z^2 = \frac{\Delta \hat{J}_z^2(0)}{1 + M^2 N_{\text{at}} N_p} \quad (5.148)$$

The factor $(1 - \sqrt{1 - \mathcal{C}^2})$ in the expression of M^2 is interesting because it exactly represents the fraction of photons of the less populated mode. This property matches the fact that the signal to noise of an heterodyne detection is limited by the smaller of the two beating fields.

5.3.5.3 The Gaussian approximation

To derive the Gaussian approximation for the squeezing function, we decompose the effect of the N_p photons into stationary sub-processes of N_t photons. The idea of this decomposition is to consider that the atomic state does not evolve much for the few photons of a subset. For one sub-process, the atomic state is considered fixed and modify the interferometer output in a fixed way. This decomposition into stationary sub-processes is important to extract an analytical formula for the evolution of

More precisely, we consider that the output density of probability $P(\varphi)$ does not change for the N_t consecutive photons. A sufficient condition is to use a low enough number of photons such that the signal-to-noise $\kappa^2 = \phi^2 N_{\text{at}} N_t$ is small compare to 1. The formal definition of a phase operator $\hat{\varphi}$ and of the subsequent density of probability is in general not trivial. The

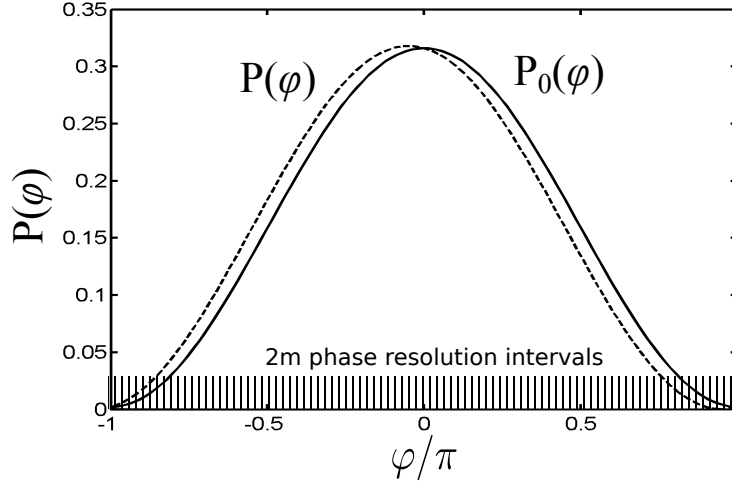


Figure 5.17: *Detection probability of a phase φ*
 $P_0(\varphi)$ is the density of probability if there is no atomic contribution, whereas $P(\varphi)$ describe the distribution when the beatnote has been shifted by a nonzero mean difference of population.

introduction of the phase by the means of the time of arrival of photons in equation 5.143 is quite intuitive but should be regarded with care for further expansion of the formalism.

The density of probability to detect a phase φ for the $(N_p + 1)^{th}$ photon knowing the state $|\psi_{at}\rangle = \sum_{n=-N/2}^{N/2} c_n(N_p) |n\rangle$ is :

$$P(\varphi) = \frac{1}{2\pi} \sum_{n=-N/2}^{N/2} |c_n(N_p)|^2 (1 + \mathcal{C} \cos(\phi n + \varphi)). \quad (5.149)$$

In the weak coupling limit, $\phi N_{at} \ll 1$, we can limit the expansion of $P(\varphi)$ to the first order in ϕn :

$$P(\varphi) = \frac{1}{2\pi} \left(\sum_{n=-N/2}^{N/2} |c_n(N_p)|^2 \left((1 + \mathcal{C} \cos \varphi) - \mathcal{C} \phi n \sin \varphi \right) \right) \quad (5.150)$$

$$= P_0(\varphi) - \frac{1}{2\pi} \mathcal{C} \phi \langle \hat{J}_z \rangle \sin(\varphi), \quad (5.151)$$

where

$$P_0(\varphi) = (1 + \mathcal{C} \cos(\varphi)) \quad (5.152)$$

is the initial density of probability to detect a phase φ . $P_0(\varphi)$ applies in particular for the first detected photon. At first order, $P(\varphi)$ is shifted by $\delta\tilde{\varphi} = -\phi \langle \hat{J}_z \rangle$ which is the mean phase shift induced by the atomic sample.

Similarly to an experiment that would have a resolution for the time arrival of the photons, we define a phase resolution π/m where m is an integer ($m \gg 1$). The squeezing function

$|\mathcal{F}_{N_p}(n)|^2$ can be further reordered following the sub-processes and regrouping the photons that arrived in the same phase interval l . The l^{th} phase interval is defined as $\varphi \in [l\pi/m(l+1)\pi/m]$

$$|\mathcal{F}_{N_p}(n)|^2 = \prod_{j=1}^{N_p/N_t} \prod_{l=-m}^{m-1} |f_{N_p}^{(j,l)}(n)|^2, \quad (5.153)$$

where

$$|f_{N_p}^{(j,l)}(n)|^2 = (1 + \mathcal{C} \cos(\phi n + \pi l/m))^{N_{j,l}}, \quad (5.154)$$

and $N_{j,l} = \frac{\pi}{m} P_j(\pi l/m) N_t$ is the number of photons of the j^{th} subprocess that arrived in the l^{th} interval. This division into all the resolution interval is valid if every interval holds a large number of photon. In particular, this should be verified for the extremal interval:

$$N_t \int_{\pi-\pi/m}^{\pi} P_0(\varphi) d\varphi \sim N_t \left[\frac{1-\mathcal{C}}{2m} + \frac{\pi^2 \mathcal{C}}{12m^3} \right] \gg 1. \quad (5.155)$$

A strong constraint of $N_t \gg m^3$ is given for $\mathcal{C} = 1$. Any other value of \mathcal{C} highly reduce this limit to $N_t \gg m$.

The Gaussian approximation of $|f_{N_p}^{(j,l)}(n)|^2$ around $n = 0$ gives

$$|f_{N_p}^{(j,l)}(n)|^2 \propto \exp \left[-2M_l^{(2)} N_{j,l} (n - n_l)^2 \right], \quad (5.156)$$

with

$$M_l^{(2)} = \frac{\mathcal{C}\phi^2}{4} \frac{\mathcal{C} + \cos(\frac{\pi l}{m})}{(1 + \mathcal{C} \cos(\frac{\pi l}{m}))^2}, \quad (5.157)$$

$$n_l = -\frac{\sin(\frac{\pi l}{m})}{\phi} \frac{1 + \mathcal{C} \cos(\frac{\pi l}{m})}{(\mathcal{C} + \cos(\frac{\pi l}{m}))}. \quad (5.158)$$

The expression of the measurement strength is easily obtained by:

$$M^2 N_p = \sum_{j=1}^{N_p/N_t} \sum_{l=-m}^m M_l^{(2)} N_{j,l}. \quad (5.159)$$

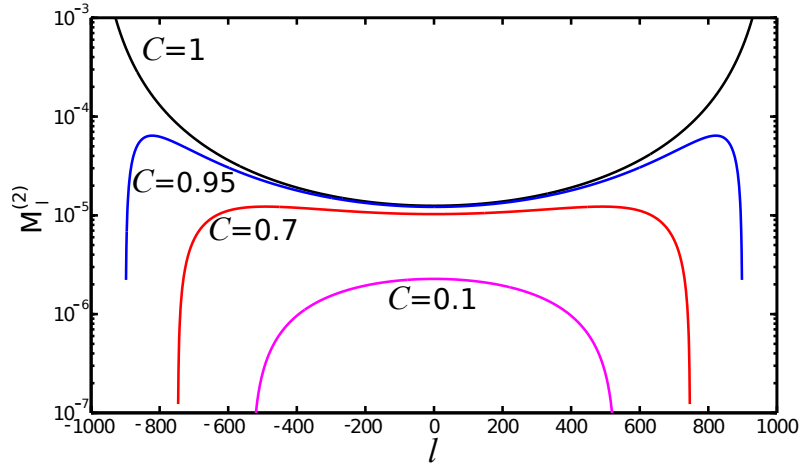
The sum over the interval can be transformed in an integral that has an analytical solution which gives:

$$M^2 = \frac{\mathcal{C}\phi^2}{8\pi} \int_{-\pi}^{\pi} \frac{\mathcal{C} + \cos(\varphi)}{1 + \mathcal{C} \cos(\varphi)} d\varphi \quad (5.160)$$

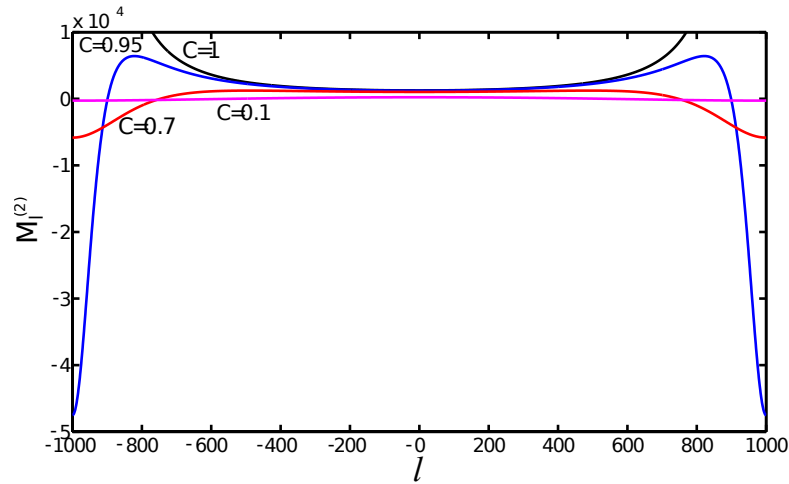
$$= \left(1 - \sqrt{1 - \mathcal{C}^2} \right) \frac{\phi^2}{4}. \quad (5.161)$$

Thus, we obtain the Gaussian approximation of $|\mathcal{F}_{N_p}(n)|^2$:

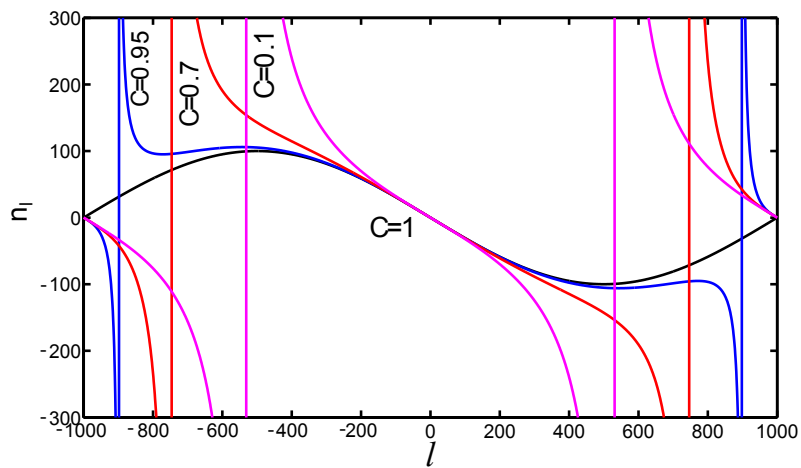
$$|\mathcal{F}_{N_p}(n)|^2 \propto \exp \left[-2M^2 N_p n^2 + T \right]. \quad (5.162)$$



(a) Measurement strength $M_l^{(2)}$ as a function of the interval l in logarithmic scale.



(b) Measurement strength $M_l^{(2)}$ as a function of the interval l in linear scale.



(c) Center n_l of the squeezing function of the l^{th} interval.

Figure 5.18: Measurement strength $M_l^{(2)}$ and center n_l of the squeezing function $\left|f_{N_p}^{(j,l)}(n)\right|^2$. The parameters are given for contrast: $C = 1$ (black), $C = 0.95$ (blue), $C = 0.7$ (red), $C = 0.1$ (magenta).

The offset of n_0 of the squeezing function is given by T :

$$T = 4nN_p \bar{\delta} \bar{\varphi} C^2 \phi \frac{1}{2\pi} \int_{-\pi}^{\pi} \frac{\sin(\varphi)^2}{1 + C \cos(\varphi)} d\varphi \quad (5.163)$$

$$= 4nN_p \phi \left(1 - \sqrt{1 - C^2}\right) \bar{\delta} \bar{\varphi}. \quad (5.164)$$

Remark:

Figure 5.18a represents the measurement strength $M_l^{(2)}$ as a function of the interval number l . It shows that for a contrast $C = 1$, the photons that bring the highest information are the one the closest from the dark port ($l = -1000$ or $l = 1000$). A trivial way to understand this increased strength of the projection, is to remark that without atoms, these borders have almost a zero probability to arise for a contrast $C = 1$. Therefore, if a click is detected in this region, it is because of the presence of the atoms [Laloë 10]. These rare photons are then giving a strong information on the sample.

This behavior breaks down when the contrast is lower than 1 ($C < 1$) since the borders are no more forbidden in the absence of the atoms. From figure 5.18b, photons that arrive on the border are even counterproductive for the squeezing of the state: they enlarge the variance of the atomic distribution.

The fact that for a contrast of one, the border photons are very efficient in terms of squeezing efficiency can be linked to [Feizpour 11, Simon 10] where the authors present a post processing of the measurement of a Mach-Zehnder. The proposal relies on the outcome from a second Mach-Zehnder interferometer tuned close to the dark fringe.

5.3.5.4 Simulations

In order to verify the previous analytical results, a Monte Carlo simulation was performed for the heterodyne measurement scheme. The algorithm that simulates the process is:

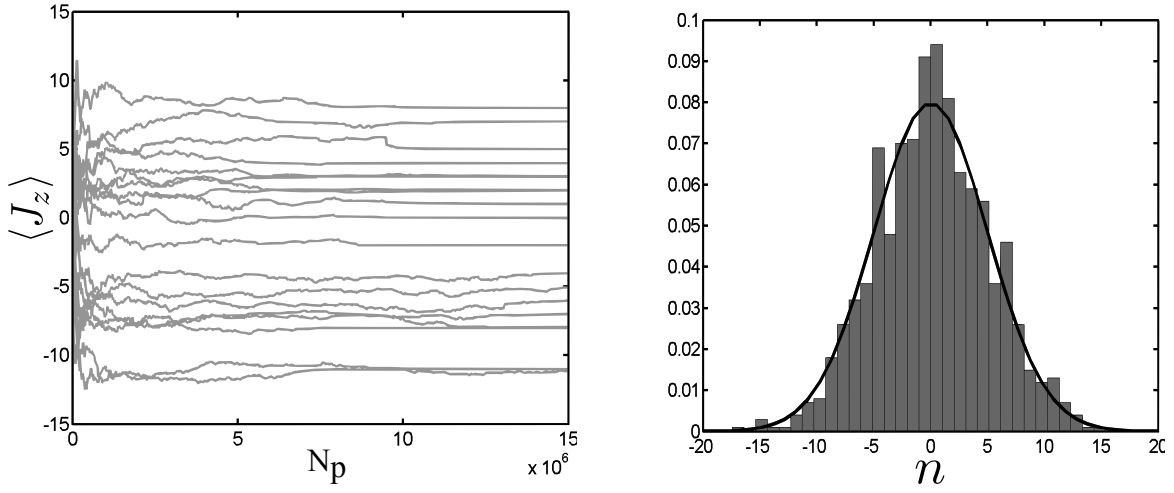
1. An initial atomic state $|\psi_{\text{at}}(0)\rangle$ is given .
2. A photon arrives at the input of the interferometer and is randomly detected with a phase φ given by the density of probability:

$$P_{N_p}(\varphi) = \frac{1}{2\pi} \sum_{n=-N/2}^{N/2} |c_n(N_p)|^2 (1 + C \cos(\phi n + \varphi)) \quad (5.165)$$

For the simulation, the density of probability is numerically integrated to obtain the cumulated density of probability:

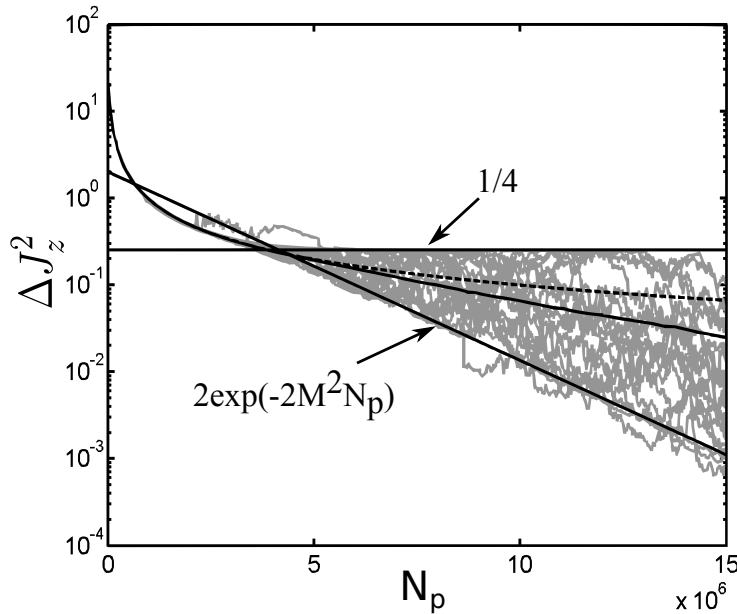
$$F_{N_p}(\varphi_0) = \int_{\varphi=-\pi}^{\varphi_0} P_{N_p}(\varphi) d\varphi \quad (5.166)$$

By generating a random number with an uniform distribution over $[0, 1]$ and numerically inverting F_{N_p+1} , we get the phase detected for the $(N_p + 1)$ -th photon.



(a) Mean value of the atomic wavefunction for a few "experimental" realizations

(b) Mean value arrival probability traced over 1000 trajectories



(c) Variance of the atomic wavefunction.

Figure 5.19: Simulation of the atomic wavefunction collapse under an heterodyne measurement for $N_{\text{at}} = 100$ and $\phi = 10^{-2}$.

Whereas the mean value has an erratic behavior, the variance of the atomic state gets squeezed by a deterministic amount. A stochastic behavior appears for $\Delta \hat{J}_z^2 = 1/4$ (discussed in section 5.3.3). The partial measurement projection finally finishes with a mean value that satisfies the

Born probability rule $P_n = |\langle n | \psi_{\text{at}}(0) \rangle|^2$. The dashed line represent the analytical expression(5.145) and the black curved line is the average variance realized over 1000 trajectories.

3. The new atomic wavefunction $|\psi_{\text{at}}(N_p)\rangle$ is computed using equation 5.142.
4. A new photon arrive and the process restarts at step 2.

The mean value and the variance of \hat{J}_z are evaluated using equation 5.110 and 5.111.

The result are shown in figure 5.11b. As expected, we obtain a similar behavior as in the case of the Mach-Zehnder measurement, *i.e.*:

- The mean value evolves as a stochastic parameter during the collapse. Nevertheless, the states converge to Dicke states with a probability that follows the Born probability rule.
- The variance of the squeezing function decreases in a deterministic way that follows the analytical result given by the Gaussian approximation

5.3.6 Comparison between the Mach-Zehnder interferometer and the heterodyne measurement

We can now underline the physical difference between the Mach-Zehnder interferometer and the heterodyne scheme. For each photon, the Mach-Zehnder interferometer gives a binary information. The photon went on u or on v . This is a strong constraint which give all photons the same weight in the projection of the atomic function. At the same time, it obliges the photon to make a choice: one way or the other.

In the heterodyne scheme, the result is continuous and photons are not forced to this binary operation. Photons can arrive at any time (weighted by the probability $P(\varphi)$). Most photons arrive in phase with the local oscillator and give a small (but nonzero) information on the atomic state. As it can be seen in figure 5.18a, the photons that are the more useful are the ones which arrive close to the other quadrature where no photons should arrive if there were no atoms.

The strength of the measurement is given in figure 5.20 as a function of the contrast for both the lossy Mach-Zehnder interferometer (section 5.3.4.1) and the heterodyne scheme (section 5.3.5). From this plot, it is clear that the forced path choice of the Mach-Zehnder interferometer is quite favorable to the measurement. For low contrast, the strength of the heterodyne scheme scales as $\mathcal{C}/\sqrt{2}$.

This result is actually quite surprising. An heterodyne measurement as presented for example on figure 5.15 can be reinterpreted as a homodyne detection of the RF field. With such an equivalence, that is presented in figure 5.21, one would expect a similar behavior for the two detection schemes. Actually, the RF equivalent Mach-Zehnder interferometer of the heterodyne scheme is an unbalanced interferometer. It has a balanced output mirror (the mixer) and an unbalanced input mirror (frequency modulator with amplitude coefficients: \sqrt{R}, \sqrt{T}). The contrast of such an unbalanced Mach-Zehnder interferometer is $\mathcal{C} = 2\sqrt{RT}$ which is the contrast found for the heterodyne detection.

5.3.7 Comment on the photon by photon versus single pulse measurement

The study previously presented was done in an interferometer operating in the single-photon regime and modifying the atomic state step by step. Experiments are not necessarily realized in these conditions. Often it is a pulse of photons that are sent on the atoms and later detected. Typical numbers consider 10^6 photons in a 1 μs pulse. This makes an average of 1 photon every

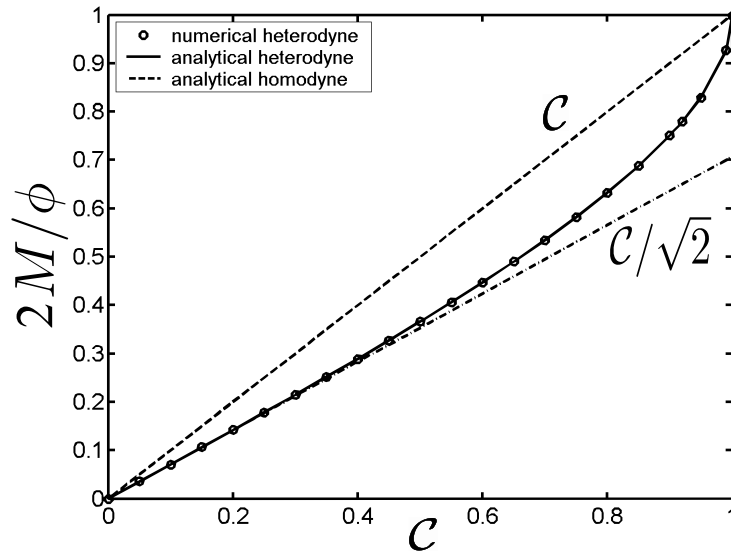


Figure 5.20: Comparison of the Mach Zehnder interferometer and the heterodyne detection. Measurement strength as a function of contrast C for the lossy Mach-Zehnder interferometer and for the heterodyne measurement.

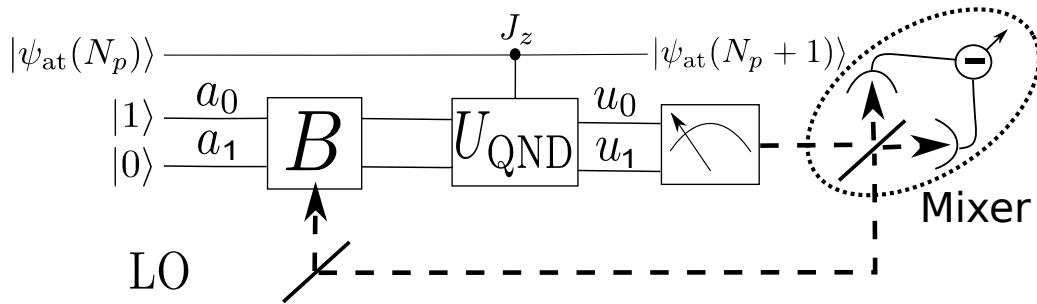


Figure 5.21: An heterodyne detection seen as an homodyne detection of the RF field. The RF field is splitted in two. One part goes directly to the mixer while the other interacts with the atoms while being transported on an optical carrier. The mixer is seen as a balanced homodyne detection

1 ps, which means that the photons are separated by 100 μm . The first photon has then not been detected before the second interacts, which looks critical in our description.

Actually it is not, since when a photon interacts and before its detection, it is in an entangled state with the atomic sample. The second photon does not interact with the atomic wave function alone but with the full entangled state. The measurement of the first photon, not only project the atomic state, but also all the photons that came afterwards. It is then effectively as if the photons were interacting and measured in a sequential way.

A second counter-argument can be raised considering that the photon number is a very well defined variable in our photon by photon description while for a coherent pulse it would present quantum fluctuations. Actually, a balanced detection in a Mach-Zehnder interferometer or an heterodyne detection scheme are experimentally only sensitive to the noise of the phase quadrature, and this noise is accounted in our model by the randomness of the detection process.

Obviously, if one uses squeezed light at the input of the interferometer, the photons could not be considered as independent and a treatment photon by photon as previously described would fall down. Nevertheless, a model could probably be developed by taking into account for the probability of the outcome of each photons, not only the atomic state with which it interacts but also the influence of all the previously detected photons.

5.3.8 Perspectives

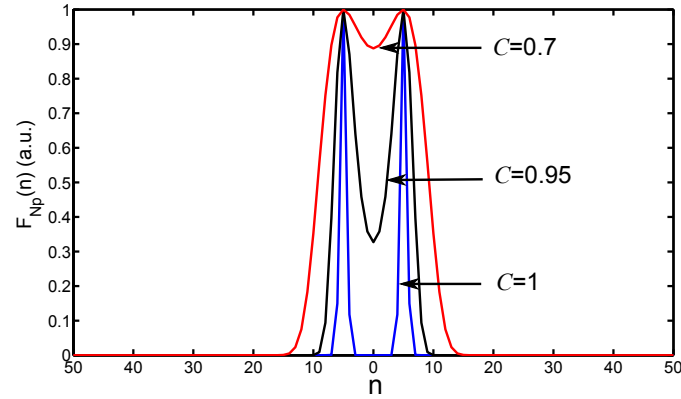
This theoretical study and the introduction of the squeezing function are powerful tools that helps to understand the process of the partial collapse of the atomic state. It also gives some formalism for the study of similar situation. Of particular interest is the creation of Schrödinger cats [Mekhov 09], the entanglement of separated clouds [Mullin 10], and the analysis of Zeno effect for collective states.

5.3.8.1 Schrödinger cats

To generalize the idea of the squeezing function, in the following we call it the backaction function. The squeezing function presented in figure 5.10, was a particular case of a backaction function. It was a Gaussian centered around 0. This choice was realized by choosing the observable (quadrature) measured, by changing the phase of the reference arm in the Mach-Zehnder interferometer or by changing the local oscillator demodulation phase in the heterodyne scheme. Choosing the opposite quadrature, the backaction function has a minima in 0 and two maxima on the side (figure 5.22a). This separation in two parts of the backaction function can be used to create Schrödinger cats. In figure 5.22a, the backaction function is presented for different contrast and in 5.22b the atomic state distribution at the output of the interferometer.

In other terms, because we have chosen the other quadrature, we are sitting at an extremum of the output fringe. Thus, for a given output, it is not possible to distinguish between the atomic phase shift ϕn_0 and $-\phi n_0$. The measurement make us converge towards non-classical states of the form $|n_0\rangle + |-n_0\rangle$ which is the superposition of two Dicke state. This state has a zero average phase shift but an important and stochastic dispersion.

Unstable preparation?



(a) Squeezing function for three different contrast.

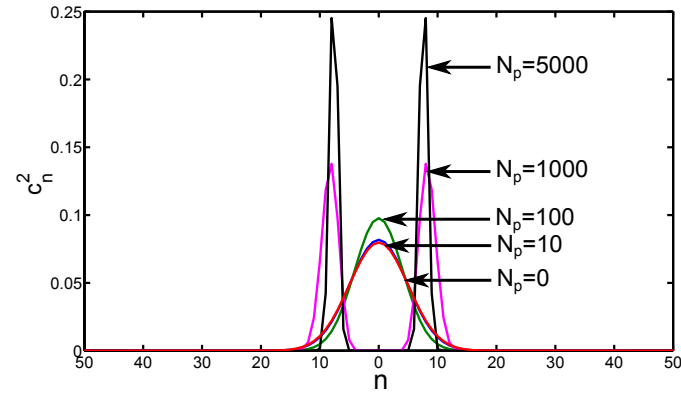
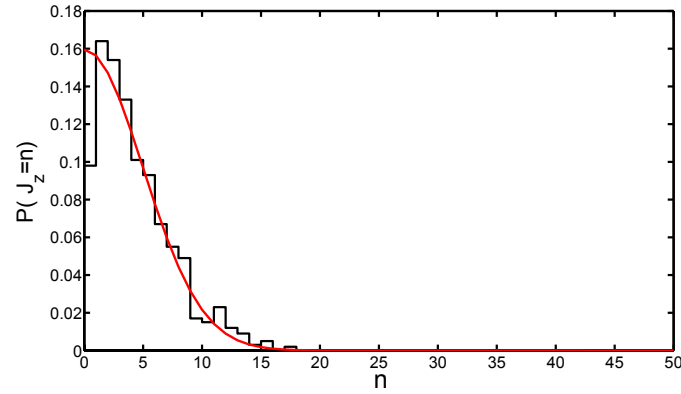

 (b) Evolution of a state on a single trajectory for $C = 1$.

 (c) Density distribution of the final state $|n_0\rangle + |-n_0\rangle$ for $C = 1$

Figure 5.22: Simulation of the atomic wavefunction collapse into Schrödinger cats for a Mach-Zehnder interferometer.

(a) The squeezing function presented for three different contrast, $C=1, 0.95, 0.7$. The dip for $n = 0$ is a numerical issue and is not physical. (b) The state distribution evolve with the number of photon N_p measured, (c) The state converge stochastically towards Schrödinger cats with a probability that satisfies the Born probability rule.

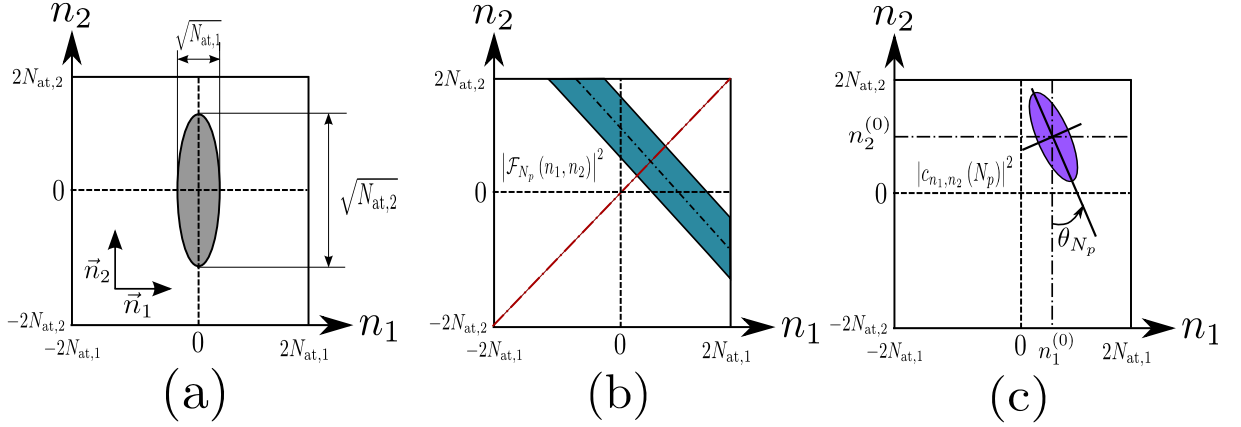


Figure 5.23: Description in the plane (n_1, n_2) of the entanglement of two clouds.

(a) The initial atomic state, (b) the squeezing function and (c) the resulting atomic state.

Unfortunately, this process suffers from two weaknesses: The first is linked to the measurement process itself: it does not create a Cat state in a deterministic way. This is a stochastic process. Nevertheless, the information on which state has been created is contained in the output probability of the interferometer. The higher is n_0 for the cat state $|n_0\rangle + |-n_0\rangle$, the higher the probability of the dark port. As the information is given to the experimentalist, it could be in principle possible to engineer quantum feedback to prepare deterministically the output state.

Secondly, this scheme relies on a well centered squeezing function. Experimentally, this means that the demodulation phase has to be controlled to better than the phase induced by the atomic dispersion ($\delta\phi_{\text{dem}} \ll \phi\sqrt{N_{at}}$). If not, the measurement loses its symmetry and the production of Cat states becomes impossible.

5.3.8.2 Multi-cloud entanglement

Previously, we have seen that the measurement was unable to distinguish between the particle. Thus, the collected information on the sample is entangling the particles. In the same way, two clouds on the path of a single beam would as well be entangled, since it is not possible to distinguish between a phase shift induced by one or the other.

The initial state is a coherent state for both clouds which have $N_{at,1}$ and $N_{at,2}$ atoms respectively. The state can be written as the product of two gaussian distributions:

$$|\psi_{at}\rangle = \sum_{n_1=-N_{at,1}/2}^{N_{at,1}/2} \sum_{n_2=-N_{at,2}/2}^{N_{at,2}/2} \exp(-n_1^2/N_{at,1} - n_2^2/N_{at,2}) |n_1, n_2\rangle. \quad (5.167)$$

This state is depicted in figure 5.23 (a) where it is plotted in the 2D plane (n_1, n_2) .

The squeezing function $\mathcal{F}_{N_p}(n)$ that acts on this state, only depends on $n = n_1 + n_2$. It is centered in n_0 and has a standard deviation that decreases with N_p . It is represented in figure 5.23 (b) by the green zone. After the measurement, the resulting state is the product of the initial states with the squeezing function. It is a tilted and compressed state in the total number difference n . The angle of the state θ_{N_p} in figure 5.23 (c) contains the entanglement information. The atomic state cannot be expressed anymore as the product of two independent distributions that would correspond to the two independent clouds. Instead, we have an entangled state.

These entanglement of two clouds is of interest for the improvement of atom interferometry and could be used as the two input state of a Ramsey-Bordé interferometer. It was shown in

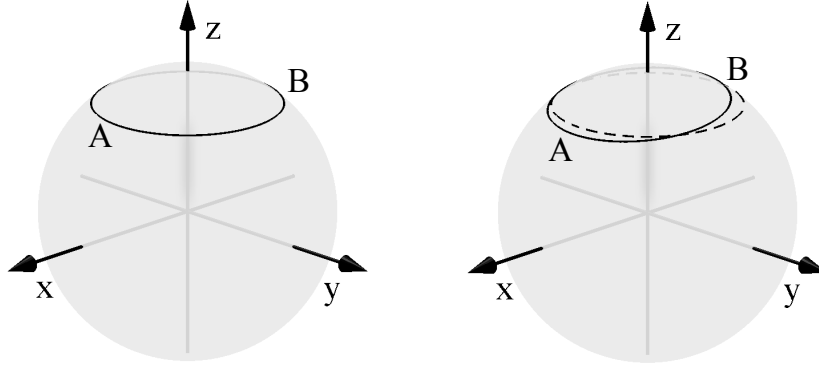


Figure 5.24: *Representation of the Dicke state rotation*

The effect of the rotation induced by the microwave is reduced by the absence of coherence of the Dicke state.

[Bouyer 97, Caves 81, Pezzé 06] that it could enhance the interferometer performance down to the Heisenberg limit.

5.3.8.3 Zeno effect induced squeezing

In the following, the prospect is to try to revisit the Zeno effect with the language of measurement induced squeezed atomic ensembles. The Zeno effect arises when a repeated [Morton 05] or continuous [Streed 06] measurement is applied on an evolving system. The information obtained by each measurement projects the system in an eigenstate and stops its evolution. The Zeno effect was observed on the photon number of a cavity mode [Bernu 08] and on single qubits, but what would happen for a collective measurement?

The argument is fairly simple. We consider an initial sample with all atoms in the $|F = 1, m_F = 0\rangle$ hyperfine ground state. At $t = 0$, a linear microwave field is shined on the sample and drives a Rabi oscillation towards $|F = 2, m_F = 0\rangle$ with Rabi frequency Ω_R . With a high repetition rate $1/\delta t$ compare to Ω_R , the sample is measured by an ideal quantum nondemolition measurement, *i.e.* the atomic state $|\psi_{\text{at}}\rangle$ is projected on a Dicke state $|n\rangle$ with probability $P = |\langle n | \psi_{\text{at}} \rangle|^2$. In between two measurements, the projected state evolves because of the microwave excitation.

On the Bloch sphere representation of the process, in figure 5.24, the Zeno effect arise from the total loss of coherence of \hat{J}_x and \hat{J}_y during the ideal QND measurement. Indeed, the Dicke state, that is obtained after each measurement, is fully spread over the sphere and the influence of the microwave is reduced since it acts in reverse for two opposite points on the sphere. In figure 5.24, we see for example that a part of the state goes up (point B) when the other side goes down (point A). Nevertheless, because the rotation is around the y-axis that is off centered compare to the Dicke state mean value, the average effect is non zero. As shown on figure 5.25, this effect has an exponential behavior:

$$\langle \hat{J}_z \rangle = \frac{1}{2} \left(1 + \exp(\Omega_R^2 \frac{\delta t}{2} T) \right) \quad (5.168)$$

which has an initial slope $\Omega_R^2 \delta t / 4$ which is identical to the slope obtained for the Zeno effect of a single particle [Streed 06]. Nevertheless, in this collective state approach, and contrarily to the case of a Zeno effect for single particles, the state does not evolve towards all the atoms in

$|F = 2\rangle$ but towards the Dicke state $|n = 0\rangle$, which is a pointer state of the evolution.

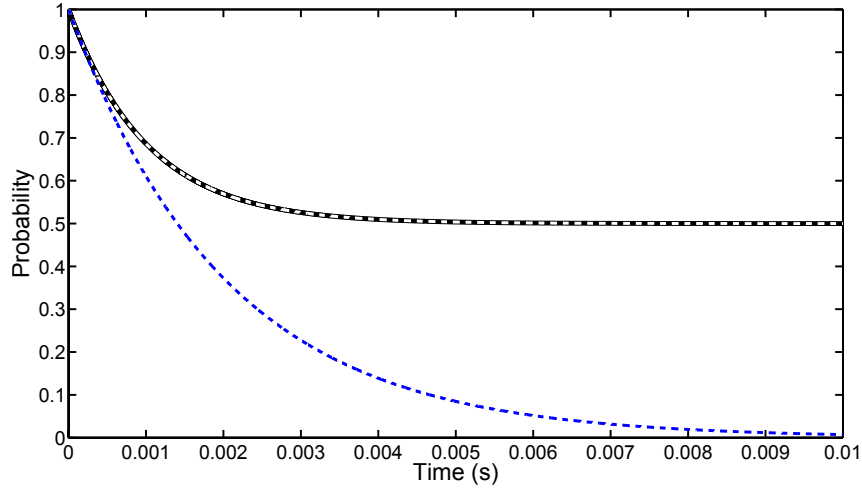


Figure 5.25: Mean value of $\langle \hat{J}_z \rangle$ for a collective Zeno effect.

The probability follows an exponential decay. In Black the simulation of a rotated Dicke state and in white the analytical expression $\langle \hat{J}_z \rangle = 1/2(1 + \exp(\Omega_R^2 \delta t / 2T))$. In blue (below) the expected Zeno effect for the single atom case: $\exp(\Omega_R^2 \delta t / 4)$. The simulation and analytical expression are given for $\Omega_R = 2\pi 10^3$ Hz and $\delta t = 0.1$ μ s which are experimentally achieved parameters.

In the simulation presented in figure 5.25 and realized for $\Omega_R = 2\pi 10^3$ Hz and $\delta t = 0.1$ μ s, one can observe a characteristic time of the state evolution of about 1 ms while the free evolution would lead to a π pulse in only 50 μ s. The convergence towards a state of equal population difference can also be seen in figure 5.25.

Obviously, one would think to use this driven evolution to deterministically generate the Dicke state $|n = 0\rangle$. Actually, the closer the state is from the equator, the slower is the convergence towards $|n = 0\rangle$. This Dicke state $|n = 0\rangle$ is only an asymptotic limit. It would take an infinite amount of time to reach the Dicke state, except if one was to start with only a few particles.

We clearly see here an effect of the correlations that are induced by the measurement. As it would not have been expected for independent particles, the Dicke state $|n = 0\rangle$ is invariant under the total evolution: "Microwave + measurement". In order to experimentally realize such a Zeno effect, it is actually crucial that the nondemolition measurement probes **both** states. For example, in the demonstration of the Zeno effect in [Streed 06], one state is measured and is fully depleted at each pulse. This does not create correlations in the sample, and the remaining atoms are kept in a separable state. In such a system, we expect the sample to fully deplete and not to converge to an equal population in both states. The equal population convergence is specific to collective ensembles.

5.4 Summary

In this chapter, we detailed the formalism background to treat the problem of multi-particles coherent and squeezed states. For that purpose, we introduced the collective spin operators \hat{J}

and gave their evolution through the interaction Hamiltonian.

We also presented the potential enhancement of atomic interferometer sensitivity with the used of spin-squeezed state. The experiment intended to reach squeezed states through the measurement process, we reminded some basics of the theory of QND measurement. We have shown that in the specific case of an off-resonance dispersive measurement has indeed a QND character.

In the last part, we developed a wave function formalism introduced in [Bouchoule 02] that allows to understand the dynamics of the squeezing evolution. This description allowed us to emphasize on the critical parameters to reach highly squeezed state and to quantify the influence of each term. This description was applied to both the Mach-Zehnder interferometer and the heterodyne detection. Even if these apparatus look quite different, it was shown that, in principle, they should have similar performances.

At last, we detailed three possible applications of the method that seems adapted to the description of Schrödinger cats preparation, multi-cloud entanglement and Zeno effect on spin-squeezed system.

Non-demolition measurement: experiment

Contents

6.1	Heterodyne detection and detector performance	152
6.1.1	General Argumentation	152
6.1.2	Considered case	154
6.1.3	A low sensitivity to common mode noise	156
6.1.4	Optical set-up	158
6.1.5	The optical detector	159
6.1.6	Atomic phase and spontaneous emission	161
6.2	Non demolition measurement of the atomic sample	164
6.2.1	Dispersive spectroscopic measurement	164
6.2.2	Probe induced destructivity	164
6.2.3	Non-demolition measurement of Rabi oscillations.	166
6.2.4	Interferometric phase in a spin-echo sequence	171
6.2.5	First study of the atomic noise	173
6.3	Perspectives: High SNR cavity measurement	177
6.4	Summary	179

The implementation of an efficient Quantum Non-Demolition measurement as described in the previous chapter is experimentally challenging. Indeed, in the previous description, it has been emphasized that spontaneous emission processes were blurring the squeezing effect. Even if some particular cases of atoms in lattice have proven that the decoherence could be suppressed [Meiser 08], the optimal detection to generate spin-squeezed states should still be able to use as few photons as possible to collect as much information as possible. In other word, one should reach a shot noise limited detection for low optical powers. In this chapter, we present the experimental progress that have been achieved in this direction.

At first, we detail the frequency modulated spectroscopy that has been set-up and focus on its noise sensitivity. In the second part, we show a characterization of the effect of the probe on the atomic sample itself. In particular, we will detail the spontaneous rate induced by the probe as well as the inhomogeneous light-shift it induces on a sample that undergoes Rabi oscillations. Finally, we give the perspective for the atomic noise measurement and the cavity enhanced measurement.

6.1 Heterodyne detection and detector performance

6.1.1 General Argumentation

As discussed in section 5.2.2.2, the dispersive measurement of an atomic sample can realize a quantum nondemolition measurement of the atomic population difference in the two ground states [Kuzmich 98]. Two main constraints are actually limiting such a dispersive measurement. The first is the effect of spontaneous emission, that makes the measurement partially destructive (see section 6.1.6). The second constraint is the ability of the experimentalist to realize such a measurement in optimal conditions, that are to be fully limited by quantum noises.

The argumentation of section 5.2.2.2 has shown that the implementation of a phase detection relies on the comparison of the phase induced on a mode of the optical field to the phase of a reference mode. Several techniques can then be implemented to measure this phase shift, including Mach-Zehnder interferometry [Louchet-Chauvet 10], mapping phase fluctuations into intensity fluctuations using a cavity tuned on the side of its resonance [Schleier-Smith 10b], or comparing the probe dephasing to a far from resonance local oscillator [Teper 08, Vanderbruggen 11].

Mach-Zehnder interferometry

In the case of the Mach-Zehnder, the two modes that are compared are the two spatially separated arms. This system has been extensively studied in the group of E. Polzik [Oblak 05]. This technique presents the strong advantage that the local oscillator which is in one arm does not couple to the atoms which are in the other arm. As a consequence it induces no spontaneous emission. The main drawback is that the sensitivity of the interferometer to length fluctuations (δL) scales only as $\delta L/\lambda$ where $\lambda \approx 1 \mu\text{m}$ is the optical wavelength. This high sensitivity to noise can be reduced using a multi-color probing [Saffman 09] that rejects common mode noise. This scheme has already proved that it can enhance the sensitivity of an atomic clock [Louchet-Chauvet 10]. Another experimental difficulty of this set-up lies in the measurement that is realized in *DC* and which is then affected by $1/f$ low frequency classical noise. A special very low noise detector had then to be developed [Hansen 01].

Cavity intensity fluctuations

The second implementation that has already been experimentally realized in the group of V. Vuletić, consists in using the cavity as a tunable attenuator [Schleier-Smith 10b]. A laser tuned on the side of the cavity resonance converts the atomic population fluctuations into frequency shifts of the cavity mode, resulting in a modification of the transmission of the cavity. Again, in this method, the measurement is realized in *DC*, and is sensitive to $1/f$ noise. In addition, as the measurement is realized with a cavity, path length fluctuations have to be well controlled.

In the latter stage of this experiment, it has been shown that a non-linear coupling between the light and the atoms could be mediated by the cavity [Leroux 10, Schleier-Smith 10a]. This method proved quite efficient to generate up to 5.6 dB of metrological squeezing [Wineland 92].

Polarization birefringence and magnetometry

Another method takes advantage of the polarization dependence of atomic states and measures this birefringence with precise polarimeters [Chaudhury 06, Smith 04]. Again, this is a *DC* measurement which makes it difficult to be limited by the optical shot noise. Nevertheless, impressive results have been obtained, among which is the estimation of a quantum state with

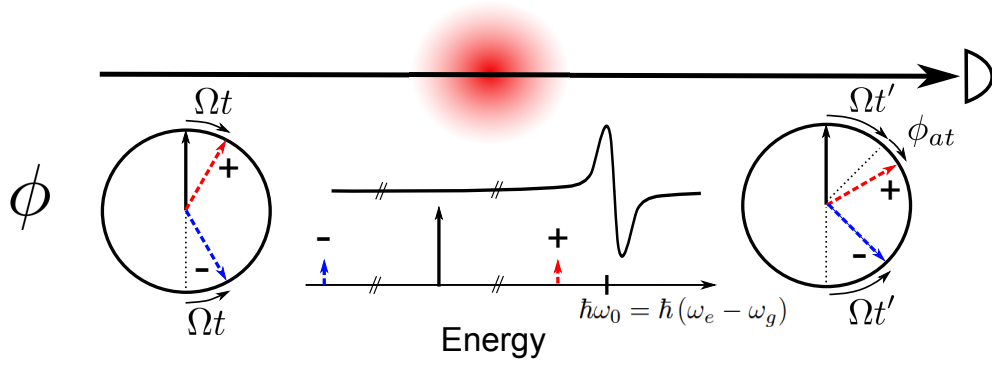


Figure 6.1: *Schematic view of a population sensitive heterodyne measurement.*

The circles are instantaneous phase representation of the optical frequency components in the frame rotating at the carrier frequency. The positive sideband (+) starts in phase with carrier and turns with angular frequency Ω while the negative sideband (-) starts opposite phase and turns with angular frequency $-\Omega$. The (+) sideband (blue) is close to the atomic transition (ω_0), it accumulates an additional phase (ϕ_{at}) that is extracted after demodulation.

a fidelity higher than 0.90% [Smith 06], and the generation of spin-squeezed states of ^{171}Yb [Takano 09].

Heterodyne measurement

Last but not least, is the heterodyne detection. In particular, we focus on the frequency modulation spectroscopy technique [Drever 83b, Black 01, Bjorklund 83]. A laser beam is phase modulated to produce frequency sidebands one sideband is placed close to an atomic transition and experiences a phase shift ϕ_{at} passing through the atomic sample, the second side-band is far from resonance and experiences essentially no phase shift. The detection of the beatnote at the modulation frequency gives an estimation of the atomic population of the probed state. This situation is represented in the rotating frame in figure 6.1.

Actually, the real strength of the heterodyne scheme lies in the full transfer of a phase shift in the optical range onto a phase shift in the microwave range. This point is illustrated in figure 6.2. If the two beating field are in phase at time 0, the beatnote is constructive (figure 6.2a) while if the two fields start in opposite phase, their interference is destructive (figure 6.2b). As a consequence, the difference of phase between the two fields is mapped onto the phase of the microwave, that is detected after comparison (mixing) with a reference that is the microwave local oscillator.

In addition, this scheme highly benefits from the almost noninteracting carrier used as a local oscillator. For a laser, limited by its quantum fluctuations (see section 6.1.3.2 and 6.1.5), the signal-to-noise ratio (SNR) of the detection is

$$\text{SNR} \propto \frac{\sqrt{N_s N_c}}{\sqrt{(\sqrt{N_s})^2 + (\sqrt{N_c})^2 + (\sqrt{N_e})^2}} \sin \phi_{at}, \quad (6.1)$$

where N_s represents the total number of photon detected in the sideband and N_c the number of photons in the carrier. The contribution of technical noises in units of photon number is N_e . We underline that in a heterodyne measurement, the two first terms of the denominator in equation

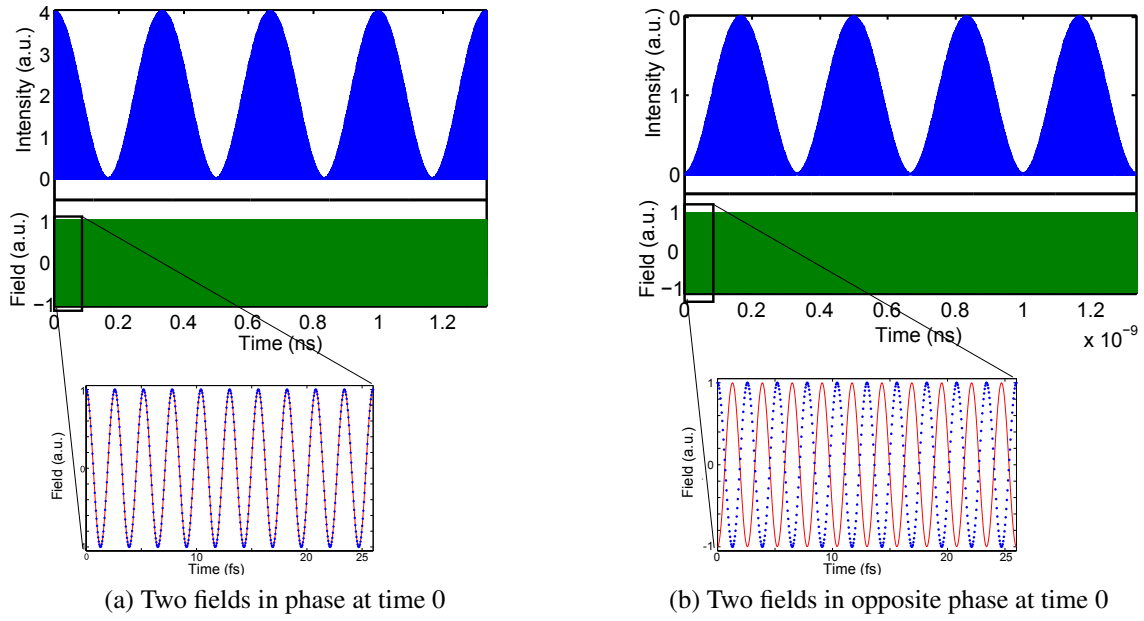


Figure 6.2: Phase transfer from the optical range to the microwave range.

(a) up is the beatnote detected by the photodetector at the modulation frequency, a zoom of the two beating field that are in phase is shown (b) Beat-note of two fields that are in opposite phase (zoom).

6.1 are the quantum phase noise of the laser expressed in terms of photon number [Aspect 06]. In the case of a frequency modulation these terms represent the amplitude noise (see section 6.1.3.2).

For a high power in the local oscillator, the shot noise overcomes the detection noise $N_e \gg N_s$, and equation 6.1 simplifies to $\text{SNR} \approx \sqrt{N_s} \sin \phi_{\text{at}}$, which corresponds to a sideband shot noise limited detection, independently of the sideband power. This property is of primary importance for a shot noise limited detection of very low signals.

In the following, we study the sensitivity to the fluctuations of the optical path length that have not been considered in equation (6.1). In section 6.1.3.2 we also discuss the influence of the noise of the laser.

6.1.2 Considered case

In order to clarify the experimental situation that will be encountered, we give in figure 6.3 the relative frequency component position with respect to the atomic transition. In figure 6.3a, 6.3b and 6.3c, we present the experimental configurations that allows to probe respectively the $|F = 1\rangle$ population, $|F = 2\rangle$ population and the population difference between the two hyperfine states.

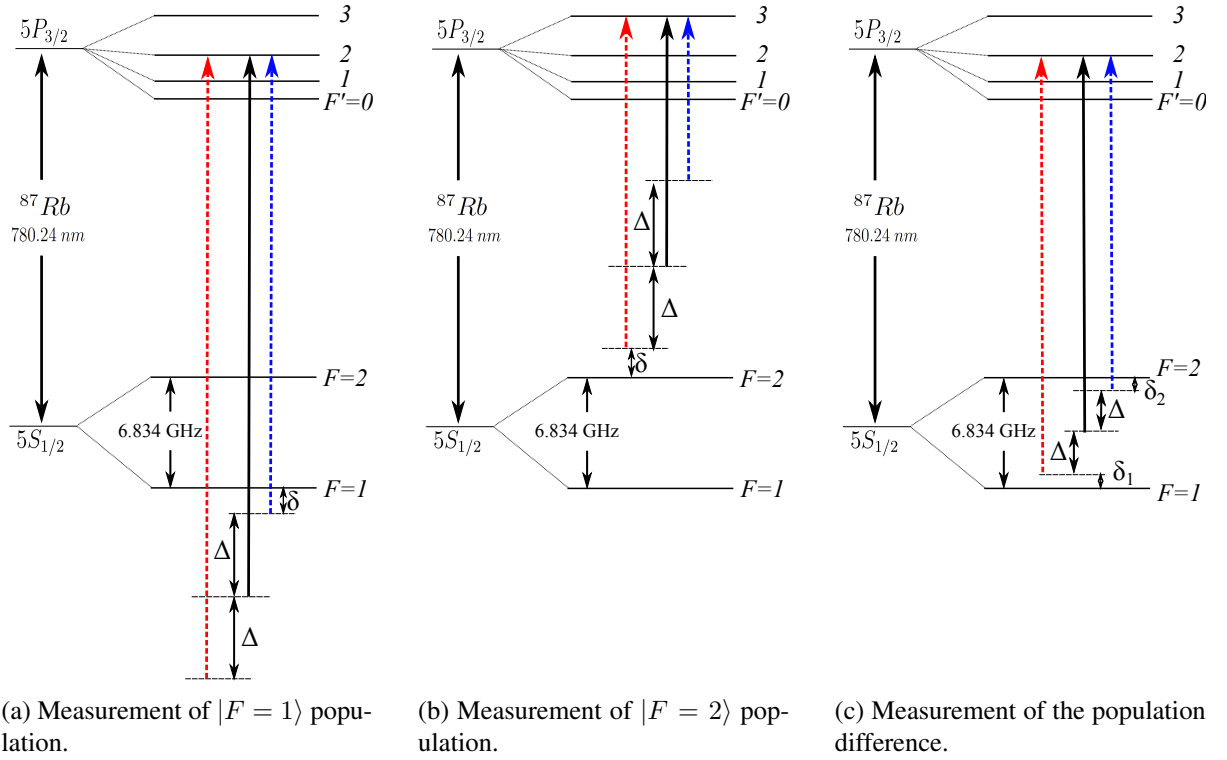


Figure 6.3: *Presentation of the laser frequency configurations considered to probe of the atomic population.*

In black is represented the carrier of the phase modulated optical probe and in red and blue are presented the positive and negative sideband. To switch from one configuration to the other, both the absolute frequency ($\delta + \Delta$) of the carrier and the modulation frequency ($\Omega = \Delta$) have to be changed.

6.1.3 A low sensitivity to common mode noise

6.1.3.1 Path length fluctuations

In homodyne detections, such as the Mach-Zehnder interferometry, the sensitivity to path length fluctuations is determined by the optical wavelength λ . In a heterodyne detection scheme for which frequency components are spatially overlapped, the relevant length is the modulation wavelength $\lambda_{\text{mod}} = \Omega/(2\pi c)$. For a modulation in the microwave range, λ_{mod} is of the order of a few centimeters, whereas λ is of the order of the micrometer. As a consequence, the sensitivity to length fluctuations is greatly reduced.

In the following, we focus on the sensitivity of a phase modulated detection with respect to length fluctuations, and consider the effect of residual amplitude modulation (RAM) [Gehrtz 85, Johnson 00]. An optical field E , phase modulated at Ω , can be written as:

$$E = E_0 \sum_{n=-\infty}^{\infty} J_n(\beta) \cos(\omega_c t + n\Omega t), \quad (6.2)$$

where J_n are Bessel functions of the first kind and β is the modulation depth.

For a small modulation depth ($\beta \ll 1$) the expansion can be limited to the first orders ($J_0(\beta)$, $J_1(\beta)$, $J_{-1}(\beta)$) $\approx (1, \beta, -\beta)$. Let ϕ_0 , ϕ_1 , and ϕ_{-1} be the different atomic phase shift experienced by each frequency component of the optical field. The photocurrent i_{det} at the output of the photodetector is

$$i_{\text{det}} = \eta P_{\text{opt}} \left(1 + \beta \cos\left(\Omega t - \frac{\Omega L}{c}\right) \Delta\Phi_+ + \beta \sin\left(\Omega t - \frac{\Omega L}{c}\right) \Delta\Phi_- \right), \quad (6.3)$$

where L is the distance from the modulator to the detector, P_{opt} the optical power in the local oscillator, η is the detection sensitivity of the photodiode, and

$$\Delta\Phi_+ = \cos(\phi_1 - \phi_0) - \cos(\phi_0 - \phi_{-1}), \quad (6.4)$$

$$\Delta\Phi_- = \sin(\phi_1 - \phi_0) - \sin(\phi_0 - \phi_{-1}). \quad (6.5)$$

After the demodulation of i_{det} by $\sin(\Omega t + \Phi_{\text{dem}})$ with $\Phi_{\text{dem}} = \Omega L/c$, and for length noise fluctuations δL of the optical path integrated in the detection bandwidth Δf , the dispersive signal obtained is $S = S_0 + \delta S_L$ where:

$$S_0 = \eta \beta P_{\text{opt}} \Delta\Phi_-, \quad (6.6)$$

$$\delta S_L = 2\pi \eta \beta P_{\text{opt}} \frac{\delta L}{\lambda_{\text{mod}}} \Delta\Phi_+, \quad (6.7)$$

where δS_L is the contribution of the optical path length fluctuations to the noise.

Since the atomic contributions to phase shift are small ϕ_{-1} , ϕ_0 , $\phi_1 \ll 1$, we have at second order:

$$\Delta\Phi_+ = \frac{1}{2} (\phi_1 - \phi_{-1}) (2\phi_0 - \phi_1 - \phi_{-1}), \quad (6.8)$$

$$\Delta\Phi_- = \phi_1 + \phi_{-1} - 2\phi_0. \quad (6.9)$$

Considering the cases (a), (b) and (c) depicted in figure 6.3, we have: In table 6.1, $\phi_{\text{at}}^{\text{res}}$ repre-

	Population in $ F = 1\rangle$	Population in $ F = 1\rangle$	Population difference
ϕ_0	0	0	0
ϕ_1	0	ϕ_{at}	$-\phi_{\text{at}}$
ϕ_{-1}	$-\phi_{\text{at}}$	0	ϕ_{at}
$\Delta\Phi_+$	$\phi_{\text{at}}^2/2$	$-\phi_{\text{at}}^2/2$	0
$\Delta\Phi_-$	ϕ_{at}	ϕ_{at}	$\phi_{\text{at}}\phi_{\text{at}}^{\text{res}}$

Table 6.1: Signal and noise contribution in the different configuration

sents the nonzero phase contribution of the carrier.

From equations (6.7), (6.8) and (6.9), the detection noise in the three configuration is:

$$\delta S_L = \eta\beta P_{\text{opt}}\phi_{\text{at}}^2 \frac{\delta L}{2\lambda_{\text{mod}}}, \quad \delta S_L = \eta\beta P_{\text{opt}}\phi_{\text{at}}^2 \frac{\delta L}{2\lambda_{\text{mod}}}, \quad \delta S_L = \eta\beta P_{\text{opt}}\phi_{\text{at}}\phi_{\text{at}}^{\text{res}} \frac{\delta L}{\lambda_{\text{mod}}} \quad (6.10)$$

Hence, for a pure phase modulation, a small atomic phase shift ϕ_{at} makes the signal even less sensitive to length fluctuations than $\delta L/\lambda_{\text{mod}}$. In the case of the population difference measurement, the rejection is even higher.

A major noise source in this heterodyne scheme arises from the residual amplitude modulation due to phase modulation imperfections. The residual amplitude modulation unbalances the field amplitude in the sidebands and the optical electric field can be written as $E = E_0 e^{i\omega_c t} [1 + \beta(1 + \epsilon)e^{i\Omega t} - \beta(1 - \epsilon)e^{-i\Omega t}]$. The signal after demodulation is:

$$S = \eta\beta P_{\text{opt}} \left[(\Delta\Phi_- + \epsilon\Delta\Phi_{-, \text{AM}}) + 2\pi \frac{\delta L}{\lambda_{\text{mod}}} (\Delta\Phi_+ + \epsilon\Delta\Phi_{+, \text{AM}}) \right] \quad (6.11)$$

where $\Delta\Phi_{+, \text{AM}}$ and $\Delta\Phi_{-, \text{AM}}$ are the atomic phase contribution for a pure amplitude modulation:

$$\Delta\Phi_{+, \text{AM}} = 2 + \frac{1}{2} [(\phi_1 - \phi_0)^2 + (\phi_{-1} - \phi_0)^2], \quad (6.12)$$

$$\Delta\Phi_{-, \text{AM}} = \phi_1 - \phi_{-1}. \quad (6.13)$$

The contribution for the cases (a), (b) and (c) depicted in figure 6.3, are presented in table 6.2.

	Population in $ F = 1\rangle$	Population in $ F = 1\rangle$	Population difference
$\Delta\Phi_{+, \text{AM}}$	2	2	2
$\Delta\Phi_{-, \text{AM}}$	$-\phi_{\text{at}}$	ϕ_{at}	0

Table 6.2: Signal and noise contribution in the different configuration

In the cases 6.3(a) and 6.3(b), the overall noise contribution of length fluctuations is:

$$\delta S_L = \eta\beta P_{\text{opt}}(\phi_{\text{at}}^2 + \epsilon) \frac{\delta L}{\lambda_{\text{mod}}}. \quad (6.14)$$

and for the case (c) we have:

$$\delta S_L = \eta \beta P_{\text{opt}} (\phi_{\text{at}} \phi_{\text{at}}^{\text{res}} + \epsilon) \frac{\delta L}{\lambda_{\text{mod}}}. \quad (6.15)$$

It clearly appears that the cases (a) and (b) are the most sensitive to optical path length fluctuations. For comparison, the optical shot noise is given by $\delta S_{\text{shot}} = \sqrt{2e\eta P_{\text{opt}} \Delta f}$. As a consequence, in a phase modulated detection, the length fluctuations are at least rejected by a factor $(\phi_{\text{at}}^2 + \epsilon)\lambda/\lambda_{\text{mod}}$ with respect to a Mach-Zehnder interferometer (equation (6.14)). For our experimental parameters, $\epsilon = 10^{-2}$, $\lambda_{\text{mod}} = 10$ cm, $\lambda = 1$ μm , and for $\phi_{\text{at}} < 100$ mrad, it represents 7 orders of magnitude of rejection on δS_L . In addition, since $\delta S_L/\delta S_{\text{shot}}$ scales as $\sqrt{P_{\text{opt}}}$, if the photodetector is shot noise limited for a low optical power in the local oscillator (section 6.1.5) there is no need of a dynamical control of the optical path length¹.

6.1.3.2 Laser noise

In the previous section, we have shown that the influence of the path length fluctuations was essentially rejected, but what about the classical noise of the laser? Actually, as the phase modulator exactly copies the phase noise of the carrier on the sideband, and thanks to the mode comparison (equation 6.5) the phase noise is rejected.

On the other hand, in equation 6.6 the signal is proportional to the optical power. Hence, if the optical power fluctuates, it will be imprinted in the signal. Nevertheless, as $\Delta\Phi_- \neq 0$, this enters as a second order effect. The frequency modulation technique is very similar to a self locked Mach-Zehnder interferometer with zero path length difference. The spectral coherence of the source has no importance.

6.1.4 Optical set-up

The optical setup is presented in Fig. 6.4. The detection beam is generated by an extended cavity diode laser (ECDL) frequency locked to a reference laser. The reference laser is the repump laser that is locked on the $|F = 1\rangle \rightarrow |F' = 1, 2\rangle$ crossover transition using standard frequency modulation spectroscopy technique (see section 2.1.4.1). The beatnote between the detection and the reference laser is detected on a fast photodetector (Hamamatsu, mod. G4176 - 10 GHz bandwidth on 50 Ω). This beatnote is frequency referenced [Appel 09a] to a 40 ± 10 MHz tunable oscillator through a high-frequency Phase Locked Loop (PLL: Analog devices, mod. ADF4108). The tunability of this oscillator allows to shift both the carrier, and the sidebands, relatively to the atomic transition.

The detection beam is sent through an acousto-optic modulator (AOM) used as a switch to generate probe pulses with 300 ns rise time. The beam is injected in a polarization maintaining fibered electro-optic modulator (EOM) (NIR-MPX800-LN-05-P-P-FA-FA from Photline Technologies), before passing through the atomic cloud. The beatnote is detected on a fast photodiode (see section. 6.1.5) and demodulated with the local oscillator. The demodulated signal is acquired with a digital oscilloscope.

¹Looking back to the case of the population difference measurement (figure 6.3c), we also remark that the presence of an amplitude modulation does not produce any offset in the signal (see table 6.2).

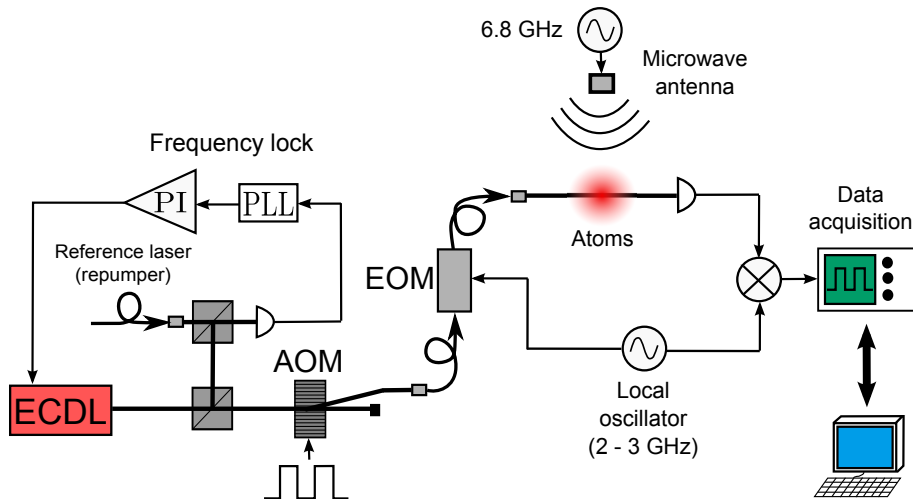


Figure 6.4: *Set-up of the single-pass non-destructive measurement.*

The probing light is generated by an extended cavity diode laser and offset locked to the atomic transition via a phase locked loop and a proportional integrator feedback loop. The absolute frequency of the light is controlled by changing the reference frequency of the Phase Locked Loop. The atoms are probed with the optical pulses generated by the AOM. The sidebands for the heterodyne detection are inserted by a phase modulator.

The internal atomic state is manipulated with a microwave signal at about 6.834 GHz generated by the home-made frequency chain that was mentioned in section 2.1.4.3. After amplification, about 27 dBm of microwave power arrive on the linear dipolar antenna which is placed at about 20 cm from the sample. The multiple reflections on the metallic chamber walls establish stationary waves. In addition, due to this reflections in the chamber, the direction of the linear polarization is not conserved on the atoms.

6.1.5 The optical detector

The beatnote signal is detected on a fast GaAs PIN photodiode with integrated transimpedance amplifier designed for high-speed optical communications at 850 nm (Finisar, model. HFD3180-203). The electronic scheme for the photodiode and the amplifier is presented in figure 6.5. The integration of the photodiode and amplifier in the same package greatly reduces parasitic capacitances and allows a high detection bandwidth of a few GHz together with a high transimpedance gain of the order of one $k\Omega$. The detector is mounted on a home-made high frequency printed circuit board. The output of the transimpedance amplifier is differential, but only one output is used. Except for the rejection of the noise of the electronic ground this does not affect the signal-to-noise. The outputs of the integrated differential amplifier is connected to a 50 Ω matched coplanar waveguide and AC-coupled to a SMA connector. To avoid microwave reflections, the output that is not used is 50 Ω terminated.

The noise at the output of the photodiode has been measured with a spectrum analyzer. The output of the transimpedance amplifier was amplified by 36 dB to overcome the noise level of the spectrum analyzer. The noise power spectral density of the illuminated detector was measured at 1 GHz and 2 GHz, as reported in figure 6.6.

The measurement shows a very good linearity of the noise power spectral density versus

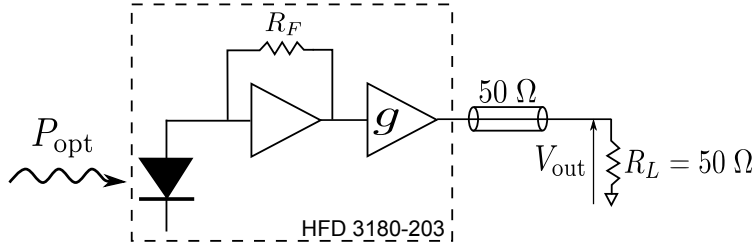


Figure 6.5: Scheme of the optical detector.

It is composed of a fast photodiode followed by a transimpedance amplifier of gain R_F and a buffer with gain g .

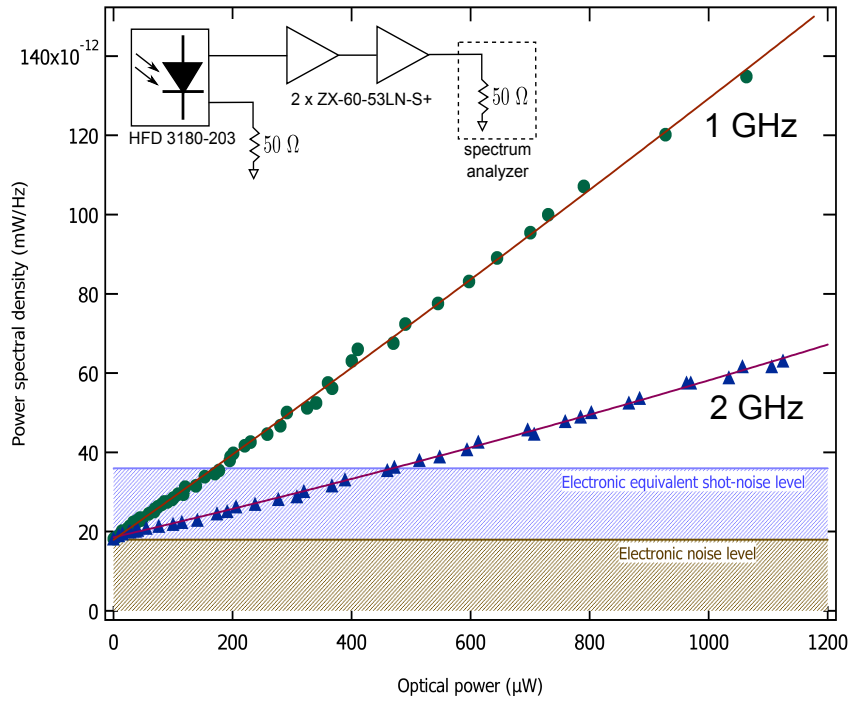


Figure 6.6: Noise power spectral density of the detector.

Noise power spectral density versus the incident optical power for two different detection frequencies, 1 GHz (circles) and 2 GHz (triangles). The inset presents the set-up used for the noise measurement.

the incident power, which means that the laser is shot-noise limited at the adopted frequencies. Actually, it also suggests that at low optical power involved (few 100 μW), the detector noise is limited to the optical shot-noise. The figure of merit κ considered is the electronic noise equivalent light shot-noise, that is, the optical power required to generate the same noise as the detection electronics [Windpassinger 09]. We measured $\kappa = 165 \mu\text{W}$ at 1 GHz, and $\kappa = 469 \mu\text{W}$ at 2 GHz.

Moreover, the slope provides a direct measurement of the photodiode gain $G_{\text{PD}} = V_{\text{out}}/P_{\text{opt}} = gR_F\eta$ where $\eta \sim 0.5 \text{ A/W}$ is the sensitivity of the photodiode (see figure 6.5 for notations). At the output of the transimpedance amplifier, voltage fluctuations induced by the light shot noise are $v_n = gR_F\sqrt{2e\eta P_{\text{opt}}\Delta f}$, where e is the charge of the electron and Δf the detection band-

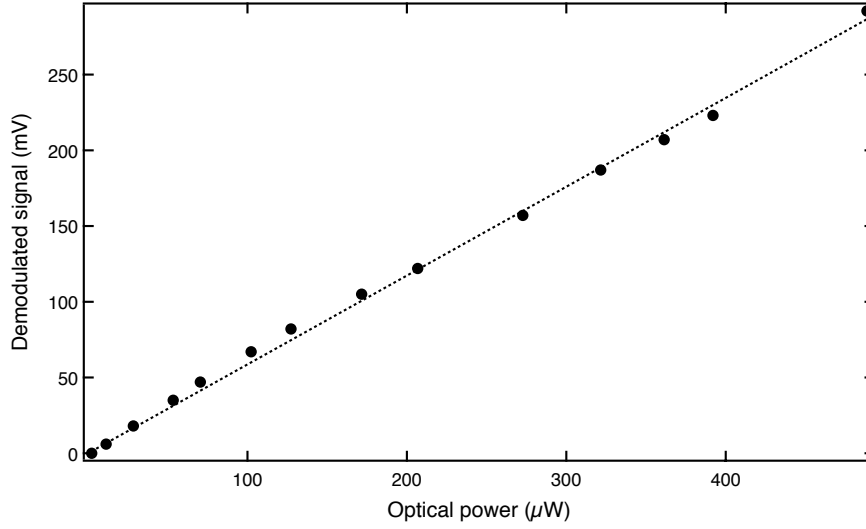


Figure 6.7: *Linearity after demodulation of the signal on the fast photodetector.*
The optical power on the detector is varied and the corresponding demodulated output is measured.

width. Hence the noise power spectral density on a resistance load R_L of 50Ω is:

$$\text{PSD}_n = \frac{v_n^2}{R_L \Delta f} = 2e \frac{G_{\text{PD}}^2}{R_L \eta} P_{\text{opt}}. \quad (6.16)$$

From the slopes of figure 6.6, one gets $G_{\text{PD}} = 1466 \text{ V/W}$ at 1 GHz and $G_{\text{PD}} = 880 \text{ V/W}$ at 2 GHz , values in good agreement with the nominal value of 1250 V/W .

In addition, we have checked the linearity of the output signal after demodulation with respect to the input power P_{opt} . In order to obtain a beatnote on the photodetector, the atoms were introduced in the path to dephase one of the side-band. The result is presented in figure 6.7. The slope of this curve gives the atomic phase shift through:

$$V_{\text{dem}} = G_{\text{PD}} \beta P_{\text{opt}} \sin(\phi_{\text{at}}). \quad (6.17)$$

In practice, for optical powers above $100 \mu\text{W}$, the photodiode presents an unexpected and unexplained dead time of $50 \mu\text{s}$. This makes impossible to pulse the light in a detection configuration that would be shot noise limited ($P_{\text{opt}} > 200 \mu\text{W}$). For this reason, and because we wanted pulsed measurement to induce a low destructivity, in the following, the power in the carrier is kept below $100 \mu\text{W}$ even if the detection is then not fully optimal. As the QND measurement will be ultimately realized with the cavity (see section 6.3), this dead time will be avoided with a carrier continuously on.

6.1.6 Atomic phase and spontaneous emission

In section 6.1.3.1, we have seen the dependance of the detected signal on the phase induced by the atoms. In this section, we will express this phase shift as a function of the experimental parameters: the frequency detuning, and the size of the atomic and optical profile.

In appendix D we derive the complete expression of the polarizability. We consider here an excitation at 780 nm , the counter-rotating term can be neglected. Hence, in equation D.20, we

have:

$$\frac{\Delta\omega_{F,F'}}{\Delta\omega_{F,F'}^2 - \omega^2 + i\Gamma\frac{\omega^3}{\omega_0^2}} \approx \frac{1}{2} \frac{\Delta_{F,F'} + i\gamma}{\Delta_{F,F'}^2 + \gamma^2}, \quad (6.18)$$

where $\gamma = \Gamma/2$ and $\Delta_{F,F'} = \Delta\omega_{F,F'} - \omega$.

For atoms in the $|F, m_F\rangle$ state, and for a light polarized along the normalized vector $\mathbf{u} = \epsilon_{-1}\mathbf{e}_{-1} + \epsilon_0\mathbf{e}_0 + \epsilon_1\mathbf{e}_1$, the polarizability α_{F,m_F} on this specific polarization is:

$$\alpha_{F,m_F} = \frac{1}{\hbar} \sum_{J',F',m'_F,q} \left| \left\langle J', F', m'_F | \hat{d}_q | J, F, m_F \right\rangle \right|^2 \epsilon_q^2 \frac{\Delta_{F,F'} + i\gamma}{\Delta_{F,F'}^2 + \gamma^2}, \quad (6.19)$$

where $\hat{d}_q = e\hat{r}_q$ is the dipole operator.

From there, we intend to derive the expression of the atomic phase shift and the spontaneous emission rate when the hyperfine splitting cannot be neglected.

The atomic transition probed is the D_2 line at 780 nm ($5^2S_{1/2} \rightarrow 5^2P_{3/2}$). In the experimental configuration considered, all the light components are at maximum a few GHz away from the atomic transition. The closest atomic transition is the D_1 line at 795 nm that is 7250 GHz away from the optical excitation, and that contribute to the signal for less than 1‰. Hence, only the D_2 line needs to be considered and the sum on J' is unnecessary.

For an atomic distribution $\rho^{F,m_F}(x, y, z)$ in the hyperfine ground states, the optical refractive index $n(x, y, z)$ experienced by the light is:

$$n(x, y, z) = 1 + \frac{1}{2\hbar\epsilon_0} \sum_{F,m_F} \rho^{F,m_F}(x, y, z) \sum_{F',m'_F,q} \left| \left\langle F', m'_F | \hat{d}_q | F, m_F \right\rangle \right|^2 \epsilon_q^2 \frac{\Delta_{F,F'} + i\gamma}{\Delta_{F,F'}^2 + \gamma^2}. \quad (6.20)$$

Phase

The phase accumulated by one frequency component at ω along the propagation in the sample is:

$$\Phi(x, y) = \int_z (k - k_0) dz = \int_z \frac{2\pi}{\lambda} \text{Re}(n(x, y, z) - 1) dz. \quad (6.21)$$

For a Gaussian distribution of the atomic density $\rho(x, y, z) = \rho_0 e^{-\frac{2(x^2+y^2+z^2)}{w_{\text{at}}}}$, one finds:

$$\Phi(x, y) = \frac{\sqrt{2}\pi^{3/2}}{\lambda} w_{\text{at}} \text{Re} [n(x, y, 0) - 1]. \quad (6.22)$$

When the probe is measured, the phase detected Φ_{det} is the integral of $\Phi(x, y)$ weighted by the density of photon that passed in (x, y) , *i.e.* the optical intensity $I(x, y) = I_0 e^{-\frac{2(x^2+y^2)}{w_{\text{ph}}}}$:

$$\Phi_{\text{det}} = \frac{\int_{x,y} \Phi(x, y) I(x, y) dx dy}{\int_{x,y} I(x, y) dx dy}. \quad (6.23)$$

For the Gaussian distributions considered previously, the equation 6.23 has the following analytical solution:

$$\Phi_{\text{det}} = \frac{\sqrt{2}\pi^{3/2}}{\lambda} \frac{w_{\text{at}}}{2\hbar\epsilon_0} \frac{w_{\text{eff}}^2}{w_{\text{ph}}^2} \sum_{F,m_F} \rho_0^{F,m_F} \sum_{F',m'_F,q} \left| \langle F', m'_F | \hat{d}_q | F, m_F \rangle \right|^2 \epsilon_q^2 \frac{\Delta_{F,F'}}{\Delta_{F,F'}^2 + \gamma^2}, \quad (6.24)$$

$$= \frac{\omega_0}{\hbar\epsilon_0 c} \frac{1}{w_{\text{at}}^2 + w_{\text{ph}}^2} \sum_{F,m_F} N_{F,m_F} \sum_{F',m'_F,q} \left| \langle F', m'_F | \hat{d}_q | F, m_F \rangle \right|^2 \epsilon_q^2 \frac{\Delta_{F,F'}}{\Delta_{F,F'}^2 + \gamma^2}, \quad (6.25)$$

where we have introduced the effective waist w_{eff} and the total atom number N_{F,m_F} in the state $|F, m_f\rangle$:

$$w_{\text{eff}} = \left(\frac{1}{w_{\text{ph}}^2} + \frac{1}{w_{\text{at}}^2} \right)^{-1/2}, \quad (6.26)$$

$$N_{F,m_F} = \left(\frac{\pi}{2} \right)^{3/2} \rho_0^{F,m_F} w_{\text{at}}^3. \quad (6.27)$$

Equation 6.25 shows that if the atoms are well within the probe volume ($w_{\text{at}} \ll w_{\text{ph}}$), the detected phase only depends on the total atom number and not on the column density.

Spontaneous emission

The scattering rate Γ_{sc} of an atom situated in (x, y) is given by:

$$\Gamma_{\text{sc}}(x, y) = \frac{I(x, y)}{\hbar\epsilon_0 c} \text{Im}(\alpha). \quad (6.28)$$

Hence, the average scattering per atom is:

$$\Gamma_{\text{sc,tot}} = \frac{1}{N_{\text{at}}} \iiint \rho(x, y, z) \Gamma_{\text{sc}}(x, y) dx dy dz = N_{\text{ph}} \frac{w_{\text{eff}}^2}{w_{\text{at}}^2 w_{\text{ph}}^2} \frac{\text{Im}(\alpha)}{\hbar\epsilon_0 c}. \quad (6.29)$$

The optimal configuration

We consider now the optimal optical waist that should be used to probe a given atomic distribution w_{at} . The effective number of atoms $N_{\text{at}}^{\text{eff}}$ seen by the probe is:

$$N_{\text{at}}^{\text{eff}} = \frac{1}{I_0} \iiint \rho(x, y, z) I(x, y) dx dy dz = N_{\text{at}} \frac{w_{\text{eff}}^2}{w_{\text{at}}^2}. \quad (6.30)$$

Hence, the atomic shot noise measured by the probe scales as $\sqrt{N_{\text{at}} w_{\text{eff}}}/w_{\text{at}}$ in atom number, and each atom contributes to the detected phase proportionally to $w_{\text{eff}}^2/(w_{\text{at}}^2 w_{\text{ph}}^2)$ (see equation 6.25).

We define the signal-to-quantum-noise κ as the phase contribution of the atomic noise over the optical phase noise, that is $1/\sqrt{N_{\text{ph}}}$:

$$\kappa \propto \frac{w_{\text{eff}}^3}{w_{\text{at}}^3 w_{\text{ph}}^2} \sqrt{N_{\text{at}} N_{\text{ph}}}. \quad (6.31)$$

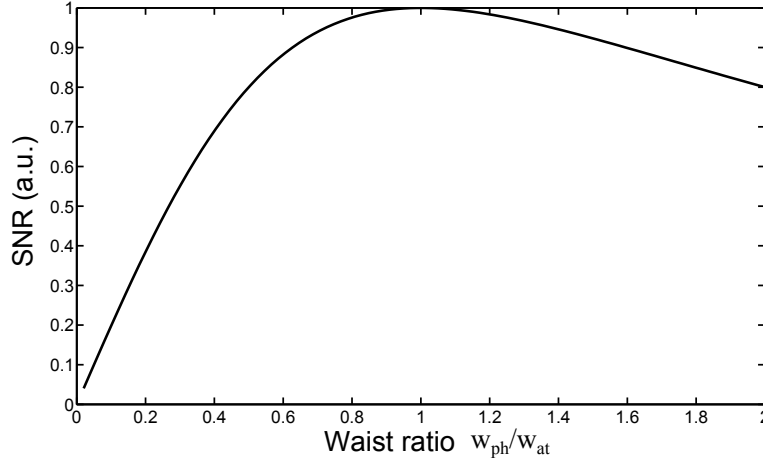


Figure 6.8: *Signal-to-noise as a function of the ratio $w_{\text{ph}}/w_{\text{at}}$.*

If we compare situations that are inducing the same average scattering per atom, that is for $\Gamma_{\text{sc,tot}}$ constant, we have:

$$\kappa \propto \frac{w_{\text{eff}}^2}{w_{\text{at}}^2 w_{\text{ph}}} \sqrt{N_{\text{at}}} = \frac{w_{\text{ph}}}{w_{\text{at}}^2 + w_{\text{ph}}^2} \sqrt{N_{\text{at}}}. \quad (6.32)$$

This equation is plotted in figure 6.8 as a function of $w_{\text{ph}}/w_{\text{at}}$. It presents a maximum for $w_{\text{ph}} = w_{\text{at}}$ that is the optimal situation. In addition, equation 6.32 indicates that the signal-to-noise increases as the optical density. We underline that an optical cavity effectively increases the optical density of the sample, and will then increase the signal-to-noise of the measurement.

The optimal situation is then to have a sample as dense as possible and to adjust the optical waist on the atomic waist.

6.2 Non demolition measurement of the atomic sample

6.2.1 Dispersive spectroscopic measurement

Because of the low power/destructivity of the probe, we are able to realize on-resonance dispersive measurement on the MOT. For the signal presented in figure 6.9, the probe is frequency swept over 20 MHz in 2 ms around the atomic resonance. The measurement is realized. The fitting procedure on the data gives a linewidth $\Gamma = 2\pi \times 9.65 \pm 0.1 \cdot 10^6 \text{ rad.s}^{-1}$, larger than the natural linewidth of $2\pi \times 6 \cdot 10^6 \text{ rad.s}^{-1}$. As the measurement is realized directly on the MOT, we believe that this enlargement is essentially due to the magnetic gradient that splits the Zeeman sublevels.

6.2.2 Probe induced destructivity

In measurement induced squeezing experiments, the probe induced spontaneous emission is among the limiting factor to reach highly entangled states [Echaniz 05]. In order to quantify the destructivity in our detection set-up, a careful study has been devoted to measure the spontaneous emission rate induced by the probe. Our goal in this study is to check that the spontaneous emission rate of the different frequency components of the light is as expected.

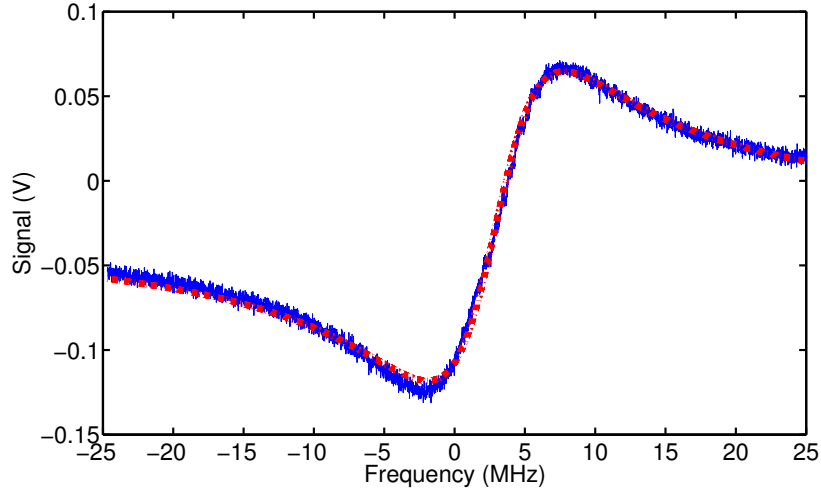


Figure 6.9: Spectroscopy on the MOT

The probe is scanned through the resonance. This spectroscopy is realized on the transition $|F = 1\rangle \rightarrow |F' = 2\rangle$. The absolute value of the frequency is not calibrated.

The measurement uses the probe both to induce and to measure the spontaneous emission rate. In that purpose, the atoms are prepared in the $|F = 1\rangle$ hyperfine ground state in the dipole trap. The dipole trap is used here to create a dense and well delimited atomic cloud within the probe waist. To avoid the differential light-shift induced by the 1560 nm radiation (see section 3.2.5.2), the atoms are released from the trap. Thus, the sample is in free fall during the measurement.

The cloud contains 4.7(3) million atoms in an initial rms size $\sigma_{\text{at}} = 41 \mu\text{m}$ and expands due to a nonzero temperature of 55(5) μK . The positions adopted for the optical frequencies with respect to the atomic transitions are presented in figure 6.3a. The modulation frequency is fixed to 2.808 GHz, the detuning (δ) of the probing sideband with respect to the atomic transition is changed by moving the absolute frequency of the carrier. As a consequence, the demodulation stays on the same quadrature, independently from the detuning δ . The probe passes on the atoms only once and has a linear polarization.

Spontaneous emissions induced by the probe transfer the atoms to $|F = 2\rangle$ where they become transparent for the probe. The measured exponential decay time τ of the signal (inset of figure 6.10) expressed as a decay rate $\gamma = 1/(\pi\tau)$ in figure 6.10 is then closely linked to the spontaneous emission rate of the probe.

The predicted decay rate γ shown in figure 6.10 (gray zone) is calculated from the beam waist (245 μm), the carrier power (120 μW), and the power in each sideband (76 nW) of the linearly polarized probe, and is expressed as:

$$\gamma = \gamma_p + \gamma_{\text{CA}} + \gamma_{\text{exp}} = b_2 \frac{\Gamma I_p / (2I_{\text{sat},2})}{1 + 4 \left(\frac{\delta}{\Gamma}\right)^2 + I_p / I_{\text{sat},2}} + \sum_{i=0}^2 b_i \frac{\Gamma I_c / (2I_{\text{sat},i})}{1 + 4 \left(\frac{\Delta_i}{\Gamma}\right)^2 + I_c / I_{\text{sat},i}} + \gamma_{\text{exp}}, \quad (6.33)$$

where $I_{\text{sat},i}$ is the saturation intensity for the π transition from $|F = 1\rangle$ to $|F' = i\rangle$ and the Zeeman sub-levels are considered equally populated. We have $I_{\text{sat},0} = 16.67 \text{ W/m}^2$, $I_{\text{sat},1} = 26.7 \text{ W/m}^2$ and $I_{\text{sat},2} = 61.23 \text{ W/m}^2$. The branching probabilities b_i to spontaneously scatter from $|F' = i\rangle$ to $|F = 2\rangle$ are $b_0 = 0$, $b_1 = 1/5$ and $b_2 = 1/2$. $I_p = 2P_p/(\pi w^2)$ is the sideband

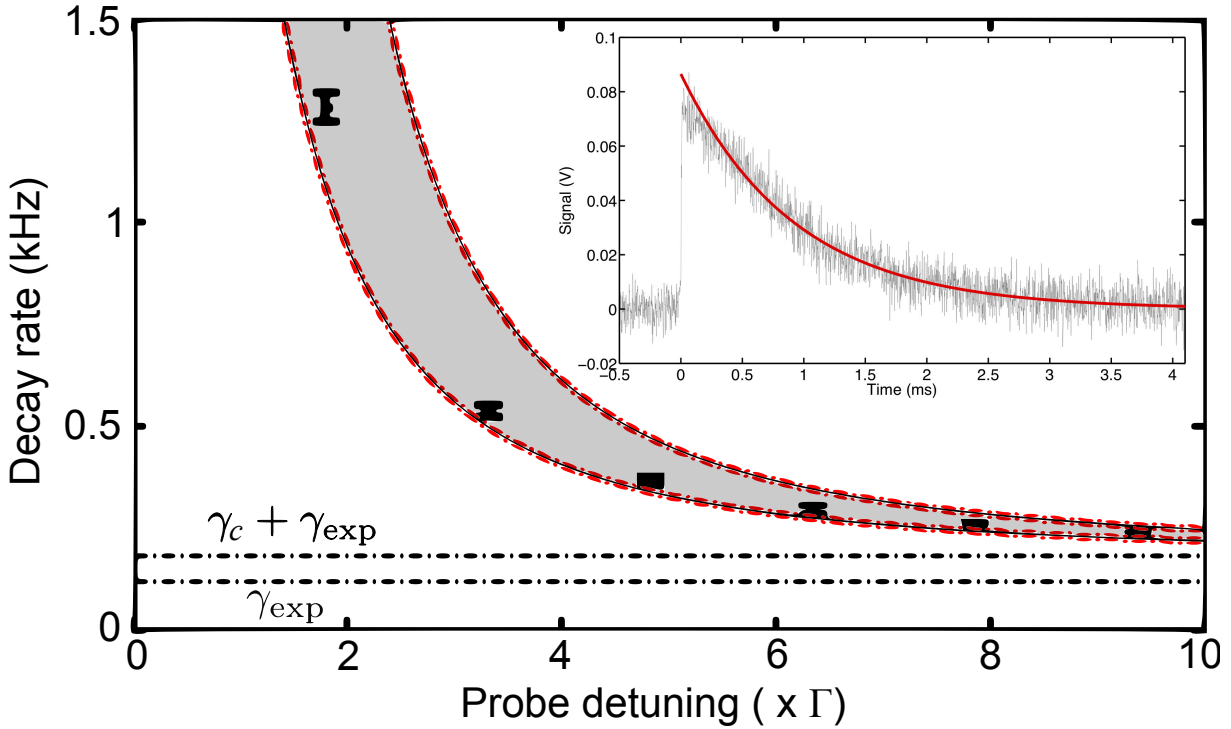


Figure 6.10: *Destructivity as a function of probe detuning.*

Probe induced scattering rate. The red dashed line represents the theoretical decay rate. The only adjustable parameter is the expansion rate of the cloud ($\gamma_{\text{expansion}}$). In the inset the continuous measurement of the decay and its exponential fit at $\delta = 4.81\Gamma$ is shown.

intensity while I_c is the carrier intensity, $\Delta_i = 2.808 + \Delta_{2i}$ GHz is the carrier detuning from the transition and Δ_{2i} is the angular frequency difference between $|F' = 2\rangle$ and $|F' = i\rangle$. $\gamma_{\text{exp}} = 120$ Hz is a constant to take into account the signal loss due to the combination of fall and expansion of the cloud. It is the only adjusted parameter in figure 6.10. A simulation of the loss of signal with the expansion gives a decay rate of 159 Hz, showing good qualitative agreement with the value found for γ_{exp} .

The gray zone in figure 6.10 accounts for uncertainties in the experimental parameters evaluation, and shows that the model used well describes the spontaneous emission. Figure 6.10 shows that, whereas the probe is very weak compared to the carrier, it induces more spontaneous emission for $\delta < 5\Gamma$ in this specific experimental realization.

6.2.3 Non-demolition measurement of Rabi oscillations.

Microwave driven Rabi oscillation is a well understood physical phenomenon and one of the main examples of coherent manipulation. It is therefore very convenient to precisely characterize how a non-destructive probe affects the oscillating system [Windpassinger 08a, Windpassinger 08b, Chaudhury 06] .

6.2.3.1 Non-demolition measurement of the oscillations

The atomic system is prepared in the hyperfine ground state $|F = 1, m_F = 0\rangle$. At $t = 0$, the atoms are released from the MOT and a microwave driven Rabi oscillation starts between $|F = 1, m_F = 0\rangle$ and $|F = 2, m_F = 0\rangle$. A magnetic bias field of 0.5 G is applied along the vertical axis so that other Zeeman transitions are off-resonance. The cloud with an initial rms size of $\sigma_{\text{at}} = 150 \mu\text{m}$ contains $\sim 10^7$ atoms and expands with a temperature of 80 μK . The probe used in this experiment has a waist of $w_{\text{ph}} = 800 \mu\text{m}$ and delivers pulses of 1.25 μs every 10 μs or 20 μs with a carrier power of 70 μW and a sideband power of 90 nW. As described in figure 6.11a, one sideband is detuned by δ from the $|F = 2\rangle \rightarrow |F' = 3\rangle$ transition whereas the carrier is 2.5 GHz away from the resonance. Hence, the configuration is probing the population in the $|F = 2\rangle$ state. In this experiment, the probe is retroreflected and the polarization is rotated by a $\lambda/4$ placed close to the retroreflecting mirror, realizing a lin perp lin probing. In addition, the quantization axis was defined at 45° from both linear polarization. Hence, the polarization on the sample is essentially a balanced superposition of all angular momentum ($\sigma \pm, \pi$).

Figure 6.11 shows two examples of these real time measurements of the atomic evolution obtained in a single shot. Figure 6.11b was taken with a probe detuning of 7.9Γ and shows a trace of Rabi oscillations undergoing decoherence. Figure 6.11c, which was taken for a detuning of 0.8Γ , presents an up-lift of the average oscillation. This effect is qualitatively explained by taking into account the probe induced spontaneous emission which transfers atoms from $|F = 2, m_F = 0\rangle$ to $|F = 2, m_F \neq 0\rangle$. There, the atoms still contribute to the detected signal while being off resonance from the microwave excitation.

Figure 6.12a presents the Rabi frequency difference ($\delta\Omega_R = \Omega_{R,10\mu\text{s}} - \Omega_{R,20\mu\text{s}}$) of two different pulses repetition times of 10 μs and 20 μs as a function of detuning. The Rabi frequency is obtained by fitting the first 800 μs of the oscillation where the expansion has little effect. It clearly shows that the probe light modifies the Rabi frequency ($\Omega_R \sim 6.6 \text{ kHz}$). For the experimental parameters cited above, the carrier induces a light-shift of $\Delta E_C/h \sim 2 \text{ kHz}$ for a 10 μs pulse repetition time while the sideband light-shift is below 380 Hz for the smallest detuning considered. The difference in Rabi frequency calculated from the carrier light-shift is $\delta\Omega_R = 227 \text{ Hz}$, in reasonable agreement with the 197 Hz average of figure 6.12a. In addition, from the fitting procedure, we extract a detection SNR=1 for a destructivity of $2.6 \cdot 10^{-6}$ scattering event per atom.

The damping rate β presented in figure 6.12b describes an exponential damping of the Rabi oscillations and is the sum of three independent terms:

$$\beta = \beta_{\text{spont}} + \beta_{\text{shift}} + \beta_{\text{else}}, \quad (6.34)$$

where β_{spont} represents the damping of the oscillation by the spontaneous emission process of both the carrier and the sideband, β_{shift} stand for the light-shift inhomogeneity of the light Gaussian profile which is essentially limited to the carrier effect and β_{else} are the probe independent decoherence effects such as the microwave inhomogeneity or the expansion of the cloud.

Inhomogeneous light-shift.

The carrier light-shift inhomogeneity β_{shift} contributes to the damping rate of the oscillations by the Rabi frequency dispersion $\Delta\Omega_R = \sqrt{\langle\Omega_R^2\rangle - \langle\Omega_R\rangle^2}$ it causes on the size of the sample.

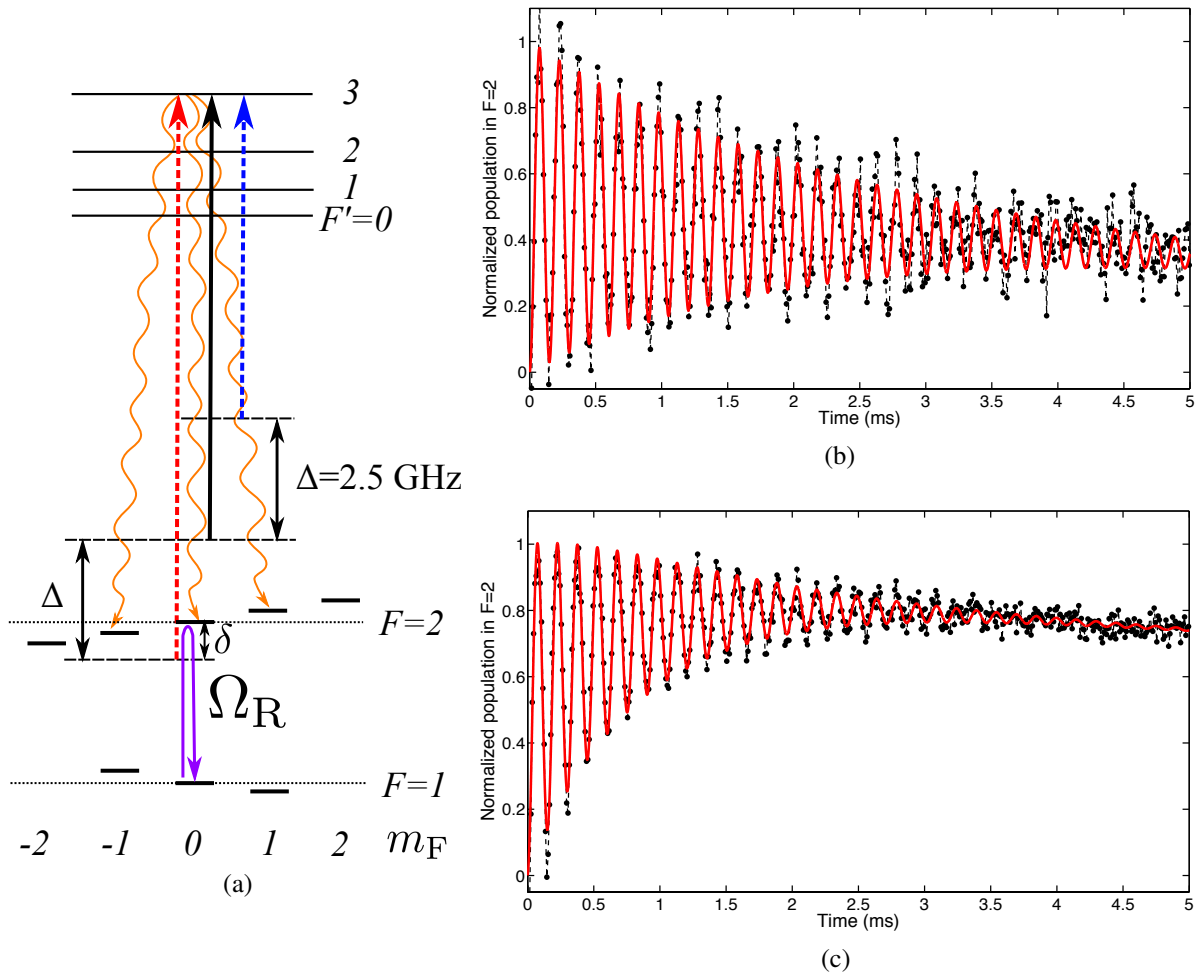


Figure 6.11: Non-demolition measurement of the atomic population in $|F = 2\rangle$ when Rabi oscillations are driven in the atomic sample.

The probing sequence is realized with a $1.25 \mu\text{s}$ long pulse repeated every $10 \mu\text{s}$. Each graph is realized in a single experimental cycle. The detuning of the probe to the transition is set to 7.9Γ (b) and 0.8Γ (c). The dashed black line helps as a guide for the eyes.

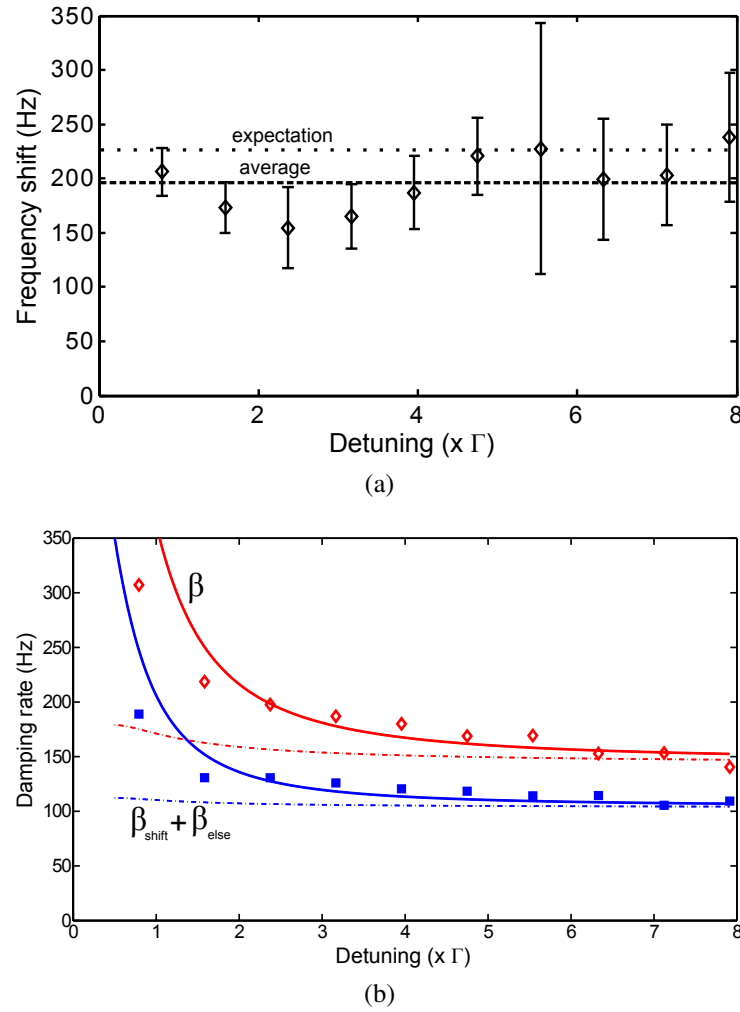


Figure 6.12: *Dependence of the Rabi oscillation parameters from the probe detuning.*

(a) Rabi frequency difference of the two set of pulse repetition time of 10 μ s (20 μ s). (b) Damping rate of the coherence. In red open diamond (blue plain square) data with a repetition time of 10 μ s (20 μ s) are presented. The solid lines are the expected decay rate taking into account spontaneous emission, inhomogeneous light-shift and the expansion. The dashed lines are the same without the spontaneous emission.

For the following calculation, we consider a Gaussian optical and atomic profile with respective waist w_{ph} and $w_{\text{at}} = 2\sigma_{\text{at}}$. An atom placed at a position x, y in the Gaussian optical profile will oscillate with a Rabi frequency:

$$\Omega_{\text{eff}}(x, y) = \sqrt{\Omega_R^2 + \frac{\Delta E_C^2}{\hbar^2} e^{-\frac{4(x^2+y^2)}{w_{\text{ph}}^2}}}, \quad (6.35)$$

and the mean value of the Rabi frequency is obtained by:

$$\langle \Omega_R \rangle = \frac{1}{N_{\text{at}}} \iiint_{x,y,z=-\infty}^{\infty} \Omega_{\text{eff}}(x, y) \rho_0 e^{-\frac{2(x^2+y^2+z^2)}{w_{\text{at}}^2}} dx dy dz \quad (6.36)$$

As the inhomogeneity is measured by the probe itself, it is not the full inhomogeneity that is measured, but only its value weighted by the optical profile:

$$\langle \Omega_R^{\text{mes}} \rangle = \frac{2^{3/2}}{\pi^{3/2} \rho_0 I_0 w_{\text{at}} w_{\text{eff}}^{(0)2}} \iiint_{x,y,z=-\infty}^{\infty} I(x, y) \Omega_{\text{eff}}(x, y) \rho_0 e^{-\frac{2(x^2+y^2+z^2)}{w_{\text{at}}^2}} dx dy dz \quad (6.37)$$

and in the limit $\Delta E_C / (\hbar \Omega_R) \ll 1$, we have:

$$\frac{\langle \Omega_R^{\text{mes}} \rangle^2}{\Omega_R^2} = 1 + \left(\frac{\Delta E_C}{\hbar \Omega_R} \right)^2 \left(\frac{w_{\text{eff}}^{(1)}}{w_{\text{eff}}^{(0)}} \right)^2 - \frac{1}{4} \left(\frac{\Delta E_C}{\hbar \Omega_R} \right)^4 \left(\left(\frac{w_{\text{eff}}^{(2)}}{w_{\text{eff}}^{(0)}} \right)^2 - \left(\frac{w_{\text{eff}}^{(1)}}{w_{\text{eff}}^{(0)}} \right)^4 \right) \quad (6.38)$$

where the effective waists are given by:

$$w_{\text{eff}}^{(0)} = \left(\frac{1}{w_{\text{ph}}^2} + \frac{1}{w_{\text{at}}^2} \right)^{-1/2}, \quad (6.39)$$

$$w_{\text{eff}}^{(1)} = \left(\frac{3}{w_{\text{ph}}^2} + \frac{1}{w_{\text{at}}^2} \right)^{-1/2}, \quad (6.40)$$

$$w_{\text{eff}}^{(2)} = \left(\frac{5}{w_{\text{ph}}^2} + \frac{1}{w_{\text{at}}^2} \right)^{-1/2}. \quad (6.41)$$

From there, it comes the dispersion of the Rabi frequency:

$$\Delta \Omega_R^{\text{mes}} = \frac{\Delta E_C^2}{2\hbar^2 \Omega_R} \sqrt{\left(\frac{w_{\text{eff}}^{(2)}}{w_{\text{eff}}^{(0)}} \right)^2 - \left(\frac{w_{\text{eff}}^{(1)}}{w_{\text{eff}}^{(0)}} \right)^4} = \frac{\alpha \Delta E_C^2}{2\hbar^2 \Omega_R}. \quad (6.42)$$

Using the experimental parameters given above, we find $\alpha = 0.162$ which is used for the theoretical curves plotted in figure 6.12b. The offset is adjusted on the data and gives $\beta_{\text{else}} = 90$ Hz.

Spontaneous emission rate

The spontaneous emission rate β_{spont} for atoms in $|F = 2\rangle$ is calculated similarly as in equation 6.33:

$$\beta_{\text{spont}} = \frac{\Gamma I_p / (4I_{\text{sat},2})}{1 + 4 \left(\frac{\delta}{\Gamma}\right)^2 + I_p / I_{\text{sat},2}} + \sum_{i=0}^2 \frac{\Gamma I_c / (4I_{\text{sat},i})}{1 + 4 \left(\frac{\Delta_i}{\Gamma}\right)^2 + I_c / I_{\text{sat},i}} + \gamma_{\text{exp}}. \quad (6.43)$$

Here, there is no need to consider the branching ratios since each spontaneous event makes the system decohere. Since the atoms oscillate during the measurement between the two states $|F = 1\rangle$ and $|F = 2\rangle$, a factor 1/2 has been applied in equation 6.43 to take into account for the effective time the atoms spend in $|F = 2\rangle$.

The sum of the three damping coefficients reproduces well the observed behavior. Close to resonance, the damping of the oscillation is dominated by spontaneous emission events from the sideband. This study shows that whereas the spontaneous scattering events can be dominated by the sideband contribution, the carrier in a heterodyne detection still plays a role by the inhomogeneous light-shift it induces on the sample. A complementary study of the probe induced light-shift can be found in [Windpassinger 08a] where a two colors Mach-Zehnder interferometer was used to realize the measurement.

6.2.4 Interferometric phase in a spin-echo sequence

The following experiment aims at the nondemolition measurement of the atomic state during an interferometric sequence. We are particularly interested in the evolution in the equatorial plane, *i.e.* the evolution of the interferometric phase. It is usually stated that the superposition state of an interferometer cannot be measured without blurring the fringes. Indeed, for example in Young's slits experiment, if we know by which slit the particle passed, no interference will be observed on the screen. This is only true for an infinite signal-to-noise where we know with probability 1 that the particle passed in one or the other slit. In the general case, a weak measurement can be realized on the system and give some information on the interferometric state without a complete destruction of the coherence.

In the following experiment, the atoms are initially prepared in the $|F = 1, m_F = 0\rangle$ state and probed in the configuration described in figure 6.3b. The interferometer is a $\frac{\pi}{2} - \pi - \frac{\pi}{2}$ spin-echo sequence. Because the atoms are released, the sequence was run in less than 500 μs to avoid loss of signal due to the expansion. The π pulse has a duration of 74.5 μs . The intermediate π pulse allows us to map the inter-state phase on the measured observable $\hat{J}_z + \hat{N}/2$ (z-axis in the Bloch sphere - figure 6.13c). To modify the inter-state atomic phase, the frequency of the microwave driving field is scanned with respect to the ground state hyperfine transition. Figure 6.13a shows the traces of the interferometer acquired in real time for different microwave detunings.

To quantitatively understand the observed behavior, we use the Bloch sphere representation introduced in section 5.1.1. In the present case, the interaction is sequentially governed by two different Hamiltonians:

- $\mathcal{H} = \hbar\delta\hat{J}_z + \hbar\Omega_R\hat{J}_y$, when the microwave is shined on the atomic sample (noted (1) in the figures). This evolution generates a rotation of the Bloch vector around the axis $(0, \Omega_R, \delta)$ with angular frequency $\sqrt{\Omega_R^2 + \delta^2}$,

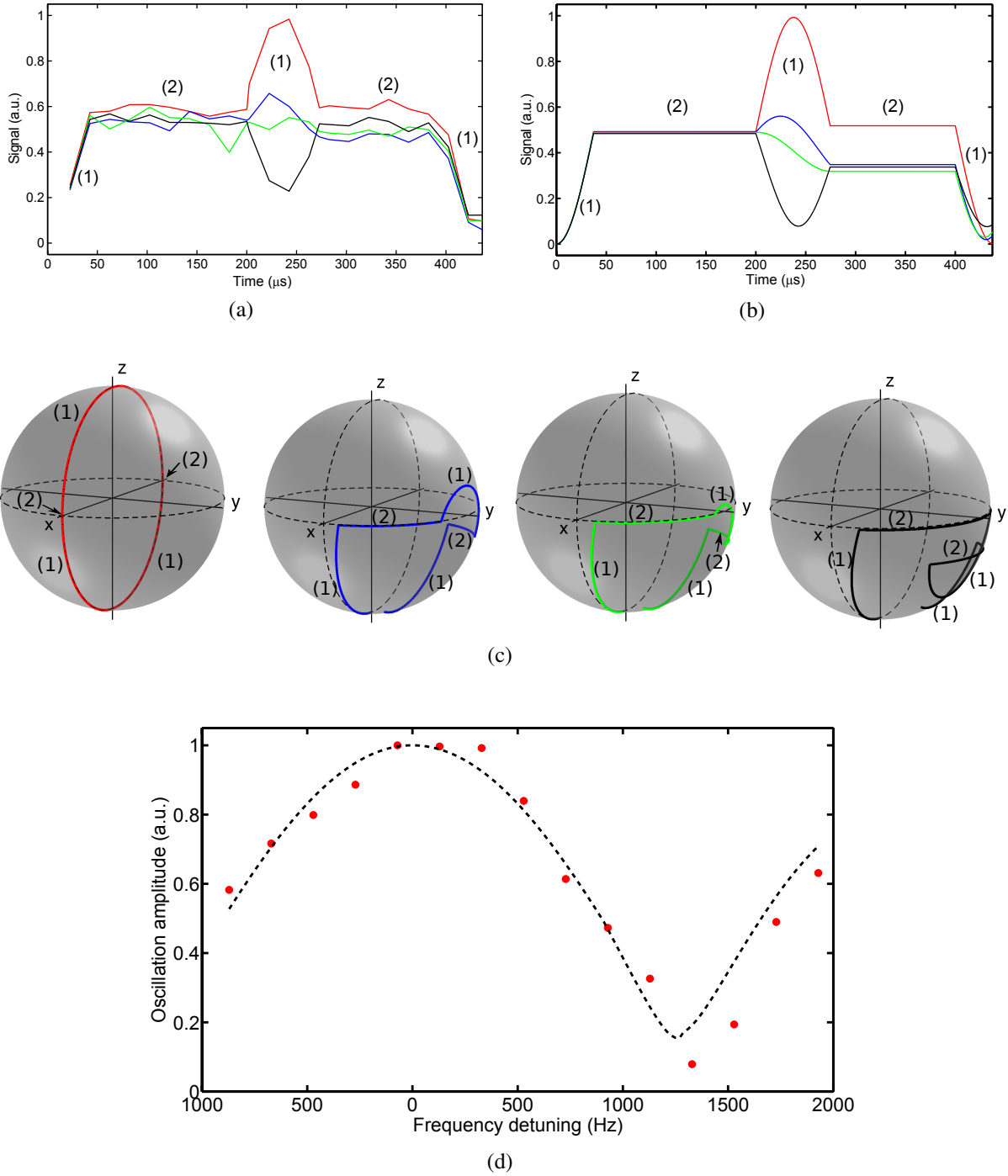


Figure 6.13: *Spin-echo sequence.*

(a) Non-demolition measurement during the interferometric sequence. Each curve is the average of three repetitions. The measurement uses $1.25 \mu\text{s}$ detection pulses repeated every $10 \mu\text{s}$. The different curves are obtained by changing the microwave frequency. The microwave detuning from the atomic transition is 0 Hz (red curve), 1 kHz (blue curve), 1.2 kHz (green curve) and 1.8 kHz (black curve). The colors in (b) and (c) refer to the same microwave detuning. (b) Simulation of the interferometric state. (c) Trajectories of the atomic state on the Bloch sphere. (d) Absolute value of the amplitude of the intermediate π pulse. The red dots are extracted from the fitted data whereas the black dashed line is the expected amplitude.

- $\mathcal{H} = \hbar\delta\hat{J}_z$, which is the free evolution when the microwave is turned off. (noted (2) in the figures). On the Bloch sphere, the state precesses around the z axis with angular frequency δ .

The simulation of these rotations reproduces very well the observed behavior (figure 6.13b-6.13c).

The amplitudes of the intermediate π oscillations were extracted from the traces and compare well with the predicted ones (figure 6.13d). This study shows that the superposition state of an interferometer can be measured without necessarily blurring the fringes. The weak measurement that was presented here does not strongly projects the interferometric state.

Moreover, in a usual interferometric sequence, the atoms are lost after the destructive measurement. With such a nondemolition measurement at the end of the sequence, the atoms can be reused so as to increase the duty cycle of atomic interferometers [Lodewyck 09].

6.2.5 First study of the atomic noise

In the previous sections, we described the ability of the set-up to probe atomic states in the weak coupling regime. Meaning that we are able to extract a signal without creating much decoherence in the sample. This allows us to repeat measurements on the same sample [Andrews 96, Savalli 99]. This is a necessary condition to generate spin-squeezed atomic states, but it is not sufficient. Indeed, it should also be shown that if the number of photon per pulse is increased, *i.e.* that the optical shot noise is lowered, one measures the atomic shot noise distribution.

6.2.5.1 Atomic noise contribution

The atomic noise of the population difference after a $\pi/2$ pulse is the exact equivalent of the photonic noise that is found at the output of a beam splitter in optics. It arises from the independence of the particles that choose in between the two output modes without being affected by the other particles. Hence, for the atomic noise, it is expected to measure Poissonian fluctuations with a standard deviation:

$$\sigma_{at} = \sqrt{N_{at}}. \quad (6.44)$$

To measure such a noise of the population difference, the scheme proposed is described in figure 6.3c.

The atomic state considered is a coherent superposition of $|F = 1, m_F = 0\rangle$ and $|F = 2, m_F = 0\rangle$ with atomic population $N_1 = N_{F=1, m_F=0} = \frac{N_{at}}{2}(1 + \epsilon)$ and $N_2 = N_{F=2, m_F=0} = \frac{N_{at}}{2}(1 - \epsilon)$.

Considering the case where the carrier accumulates no phase shift and where each sideband is only sensitive to the closest hyperfine ground state, the atomic phase shift contribution are given by equation 6.25:

$$\phi_0 = 0 \quad (6.45)$$

$$\phi_1 = \frac{1}{\hbar\epsilon_0} \frac{1}{w_{at}^2 + w_{ph}^2} N_1 \sum_{F', m'_F} \left| \langle F', m'_F | \hat{d}_q | 1, 0 \rangle \right|^2 \epsilon_q^2 \frac{\Delta_{1, F'}}{\Delta_{1, F'}^2 + \gamma^2}, \quad (6.46)$$

$$\phi_{-1} = \frac{1}{\hbar\epsilon_0} \frac{1}{w_{at}^2 + w_{ph}^2} N_2 \sum_{F', m'_F} \left| \langle F', m'_F | \hat{d}_q | 2, 0 \rangle \right|^2 \epsilon_q^2 \frac{\Delta_{2, F'}}{\Delta_{2, F'}^2 + \gamma^2}. \quad (6.47)$$

Because the detunings $\Delta_{F=1,F'}$ and $\Delta_{F=2,F'}$ are of opposite sign, it is possible to choose the position of the carrier and the modulation such that :

$$\begin{aligned} \sum_{F',m'_F} \left| \left\langle F', m'_F | \hat{d}_q | 1, 0 \right\rangle \right|^2 \epsilon_q^2 \frac{\Delta_{1,F'}}{\Delta_{1,F'}^2 + \gamma^2} &= - \sum_{F',m'_F} \left| \left\langle F', m'_F | \hat{d}_q | 2, 0 \right\rangle \right|^2 \epsilon_q^2 \frac{\Delta_{2,F'}}{\Delta_{2,F'}^2 + \gamma^2} \\ &= D^2. \end{aligned} \quad (6.48)$$

From equation 6.6 and 6.9, the signal detected is:

$$S = \eta \beta P_{\text{opt}} \Delta N \frac{D^2}{\hbar \epsilon_0 (w_{\text{at}}^2 + w_{\text{ph}}^2)}, \quad (6.49)$$

where $\Delta N = N_{F=2,m_F=0} - N_{F=1,m_F=0}$ is the population difference between the two ground states. The detected signal is then sensitive to the atomic population difference and its standard deviation should be proportional to $\sqrt{N_{\text{at}}}$.

6.2.5.2 Classical noise

In section 6.1.3, we have emphasized that the sensitivity of our detection scheme to optical classical noise such as length fluctuations was very much suppressed. But what happens with the atomic classical noise ?

First of all, in experiments, there are shot-to-shot fluctuations in the atom number N_{at} . In the best case, these fluctuations are Poissonian fluctuations in $\sqrt{N_{\text{at}}}$. In the case where the population difference is probed, the detection is insensitive to the initial atom number fluctuations at first order.

Nevertheless, some classical noise can be mediated by the atomic sample. We consider for example frequency noise on the carrier. In section 6.1.3.2 we argued that this noise should be rejected, but it was without counting on the frequency dependence of the light-atoms coupling. Hence, if we consider a change of the carrier frequency by $\delta\omega$, then the side-band detuning $\Delta_{i,F'}$ with respect to the atomic transition are modified in equation 6.48 by:

$$\Delta_{1,F'} \rightarrow \Delta_{1,F'} + \delta\omega, \quad \Delta_{2,F'} \rightarrow \Delta_{2,F'} - \delta\omega. \quad (6.50)$$

For far detuned sidebands $\Delta_{i,F'} \gg \gamma$, it results in a change of the coupling D_i^2 of each side-band (*i*) to the atomic state:

$$D_1^2 = \sum_{F',m'_F} \left| \left\langle F', m'_F | \hat{d}_q | 1, 0 \right\rangle \right|^2 \epsilon_q^2 \frac{\Delta_{1,F'}}{\Delta_{1,F'}^2 + \gamma^2} \quad (6.51)$$

$$\approx D^2 - \delta\omega \sum_{F',m'_F} \left| \left\langle F', m'_F | \hat{d}_q | 1, 0 \right\rangle \right|^2 \epsilon_q^2 \frac{1}{\Delta_{1,F'}^2} \quad (6.52)$$

$$= D^2 - \delta\omega K_1, \quad (6.53)$$

and,

$$D_2^2 = \sum_{F', m'_F} \left| \langle F', m'_F | \hat{d}_q | 2, 0 \rangle \right|^2 \epsilon_q^2 \frac{\Delta_{2, F'}}{\Delta_{2, F'}^2 + \gamma^2} \quad (6.54)$$

$$\approx D^2 + \delta\omega \sum_{F', m'_F} \left| \langle F', m'_F | \hat{d}_q | 2, 0 \rangle \right|^2 \epsilon_q^2 \frac{1}{\Delta_{2, F'}^2} \quad (6.55)$$

$$= D^2 + \delta\omega K_2. \quad (6.56)$$

The detected signal has now a contribution that is directly proportional to the total number of atoms:

$$S = \eta\beta P_{\text{opt}} \frac{1}{\hbar\epsilon_0(w_{\text{at}}^2 + w_{\text{ph}}^2)} (\Delta N D^2 - N_{\text{at}}\delta\omega(K_1 + K_2)). \quad (6.57)$$

In conclusion, in the detection of the atomic population, we expect three kinds of noise behavior:

- The detection is limited by the optical shot noise $\delta S_{\text{opt shot}}$ and no dependance on the atomic number is expected.
- The detection is limited by the atomic shot noise $\delta S_{\text{at shot}}$ and the standard deviation of the signal scales as $\sqrt{N_{\text{at}}}$.
- The detection is limited by classical noise δS_{cl} and the standard deviation scales as N_{at} .

In general the variance of the noise δS^2 is the sum of these three contributions::

$$\delta S^2 = \delta S_{\text{opt shot}}^2 + \delta S_{\text{at shot}}^2 + \delta S_{\text{cl}}^2. \quad (6.58)$$

6.2.5.3 First measurement

To evaluate the contributions of the different noise sources, a first series of measurements was led on atoms released from the MOT. A cloud containing 7×10^7 atoms in the $|F = 1, m_F = 0\rangle$ state is continuously probed with the frequency configuration described in figure 6.3a. As it has been seen in section 6.2.2, the probe transfers the atoms in the $|F = 2\rangle$ states and is no more affected by their presence. In the data presented in figure 6.14, the carrier power was continuously shined with 500 μW (shot noise limited detection) and the sideband was turned on at time $t = 0$ with a power of ~ 500 nW and detuned by 21.4 MHz from the transition $|F = 1\rangle \rightarrow |F = 2\rangle$.

The transfer of atoms leads to an exponential decay of the atomic population in $|F = 1\rangle$ presented in inset of figure 6.14. Looking to the variance δS^2 of the signal as a function of the height in the exponential over 100 repetitions of the sequence, directly measures the standard deviation δS as a function of the atom number. For that purpose, the exponential decay traces are subdivided in steps of 215 μs . The mean value of the signal of the k -th step of the i -th repetition (one shot) is noted $S_k^{(i)}$ (see figure 6.14). Figure 6.14 shows the variance calculated over the repetitions $\delta V(k)^2 = \text{Var}(S_k^{(i)})^2$ as a function of the mean value of the exponential for the k -th step $V(k) = \langle S_k^{(i)} \rangle_i$.

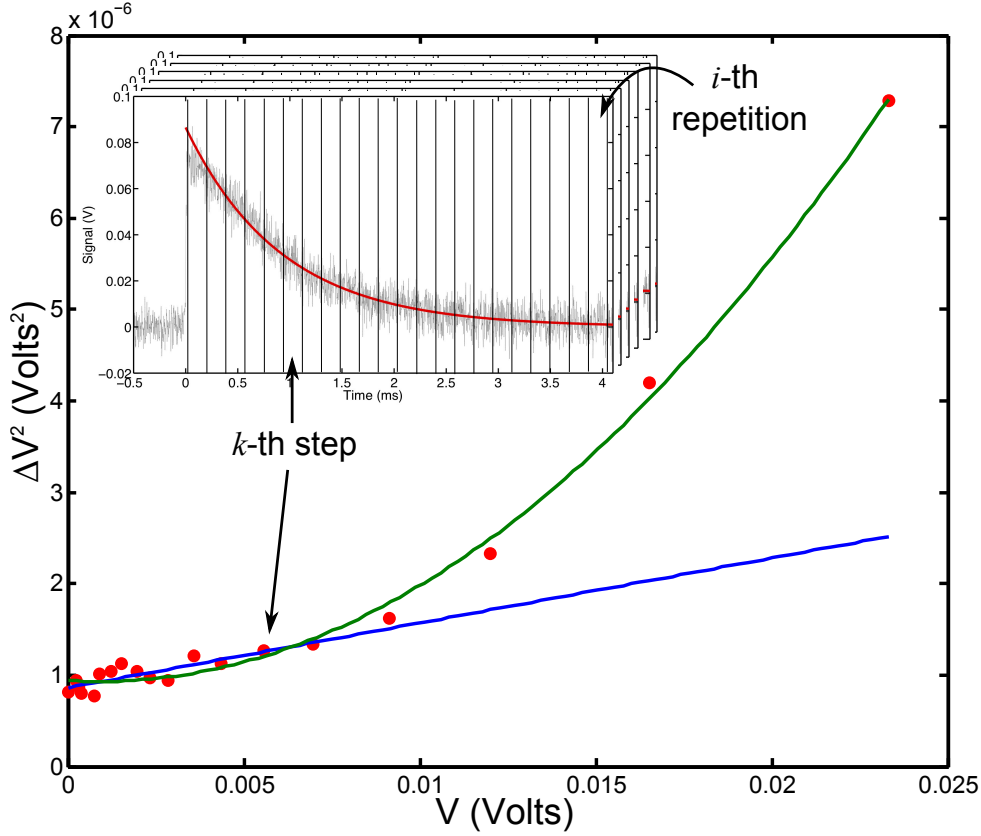


Figure 6.14: Variance of the signal $\delta V^2 = \delta S^2$ as a function of its mean value $\langle V \rangle = \langle S \rangle \propto N$.

The probe is 21.4 MHz away from the resonance. The data presented are given for slices of $\tau_p = 215 \mu\text{s}$. The blue line is a linear fit on the first 10 points and the green curve is a quadratic fit on the whole set. In the inset a typical exponential decay curve is presented with the step decomposition for the data analysis.

Model We note $\delta V(0)^2 = \text{Var}(S_0^{(i)})^2$ the initial variance on the preparation of the sample, which can be either due to atomic shot noise or to classical atomic noise. If we assume a deterministic exponential decay with time: $V(t) = V_0 e^{-t/\tau}$, the variance becomes $\delta V^2 = \delta V(0)^2 e^{-2t/\tau} = \delta V(0)^2 / V_0^2 \times V(t)^2$ and scales quadratically with V .

For low values of the signal V , the deterministic character of the decay is blurred by the Poissonian noise induced by the spontaneous emission process. Indeed, an atom excited to $|F_p = 2\rangle$ as a probability $1/2$ to fall back in $|F = 1\rangle$. Hence, for low values of V the variance δV^2 should scale linearly with V , indicating for the Poissonian nature of the distribution.

The data and the fit that are presented in figure 6.14 suggest that we have indeed a quadratic behavior for the high values of V . The low values seem to present a linear behavior that would be the signature of a Poissonian noise, but the quality of the data does not allow us to be sure about it.

To confirm this result, similar measurements are planned to be done on the dipole trap where the atomic density is much higher. In addition, it is planned to measure the population number difference that is insensitive to the fluctuations of the initial preparation. In these conditions, it is expected to see a linear behavior of the variance of the signal with the number of atoms, which is the signature of the atomic shot noise.

6.3 Perspectives: High SNR cavity measurement

As shown in equation 5.108, [Oblak 05] the optimal level of squeezing $\xi^2 = 1/(1 + \kappa^2)$ is related to the signal to noise ratio (κ) of the measurement [Vanderbruggen 11]:

$$\kappa^2 = \frac{\phi^2 N_{\text{at}} N_p}{2} = \mu \rho_0 \eta \quad (6.59)$$

where ϕ is the single atom induced phase shift, μ is the detuning dependence of the SNR, ρ_0 is the resonant optical density and η is the single atom spontaneous emission probability for a pulse of N_p photons. The expression of μ and η in the configuration depicted in figure 6.3 are given by [Vanderbruggen 11]:

$$\mu = \frac{S^2}{\mathcal{L}}, \quad \text{and} \quad \eta = \frac{\rho_0}{N_{\text{at}}} \frac{\mathcal{C}^2 N_p}{2} \mathcal{L}, \quad (6.60)$$

where

$$S \approx S_1 = \sum_{F'} \frac{\gamma \Delta_{1F'}}{\Delta_{1F'}^2 + \gamma^2} S_{FF'} = - \sum_{F'} \frac{\gamma \Delta_{2F'}}{\Delta_{2F'}^2 + \gamma^2} S_{FF'} = -S_2, \quad (6.61)$$

$$\mathcal{L} = \sum_{FF'} \frac{\gamma^2}{\Delta_{FF'}^2 + \gamma^2} S_{FF'}. \quad (6.62)$$

$S_{FF'}$ is the oscillator strength of the transition $F \rightarrow F'$ and $\Delta_{FF'}$ is the detuning of the optical frequency with respect to the $F \rightarrow F'$ transition. S_i describe the dispersive coupling strength of each sideband to the closest transition i which scales as $1/\Delta$ and \mathcal{L} is the normalized spontaneous rate that scales as $1/\Delta^2$.

Hence, the detuning dependence μ is bound to 1 and there is no need or interest to work at very large detuning since $\mu \xrightarrow{\Gamma/\delta \rightarrow 0} 1$. In addition, the coherence loss due to spontaneous emission cannot be avoided since η enters directly in the equation of κ . Nevertheless, using a cavity to strengthen the atom-light interaction increases the coupling ϕ by the cavity finesse \mathcal{F} . This results in a SNR enhancement proportional to $\sqrt{\mathcal{F}}$ [Lye 03] for an overall given spontaneous emission rate ($\eta \propto N_s$).

To prevent for the light-shift effect of the carrier, the measurement can be realized in reflection [Teper 08]. In the scheme presented in figures 6.15 and 6.16, the detection realized with the two sidebands, that measures the population difference is shot noise limited because of the strong local oscillator. In addition, the effective interaction between atoms and photons can take advantage of the trapping and probing that exploit the same cavity mode.

In this scheme, the carrier does not enter the cavity. All the frequency components are then no more overlapped during the propagation, and the fluctuations of the cavity length will directly enter as noise in the detected signal. These fluctuations are even increased by the finesse of the cavity and could be very critical.

The solution foreseen to avoid these fluctuations is to lock the carrier in between two resonances. For that purpose, we exploit the specificity of our design that uses 1560 nm light that is the half of the probing frequency at 780 nm. As presented in figure 6.16, the 1560 nm radiation is locked on the cavity. A part of the signal is frequency doubled in a PPLN crystal. The doubled 1560 nm is used both to reference the cavity lines to Rubidium through a comparison with the repump laser and to lock the 780 nm QND probe. To reference the cavity resonance

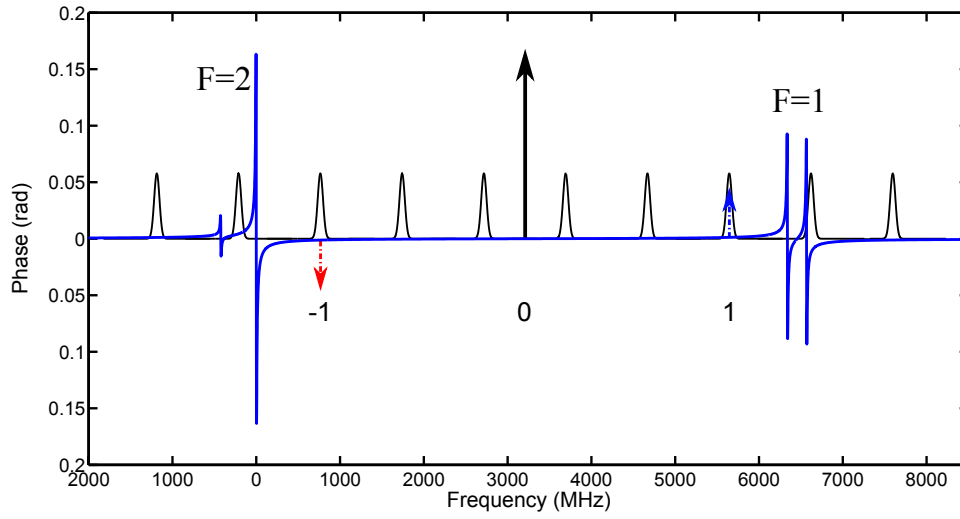


Figure 6.15: *Scheme of the Pound-Drever-Hall like measurement method.*
The carrier is locked at the center of two cavity resonances to suppress cavity noise. Each sideband probes one of the hyperfine states.

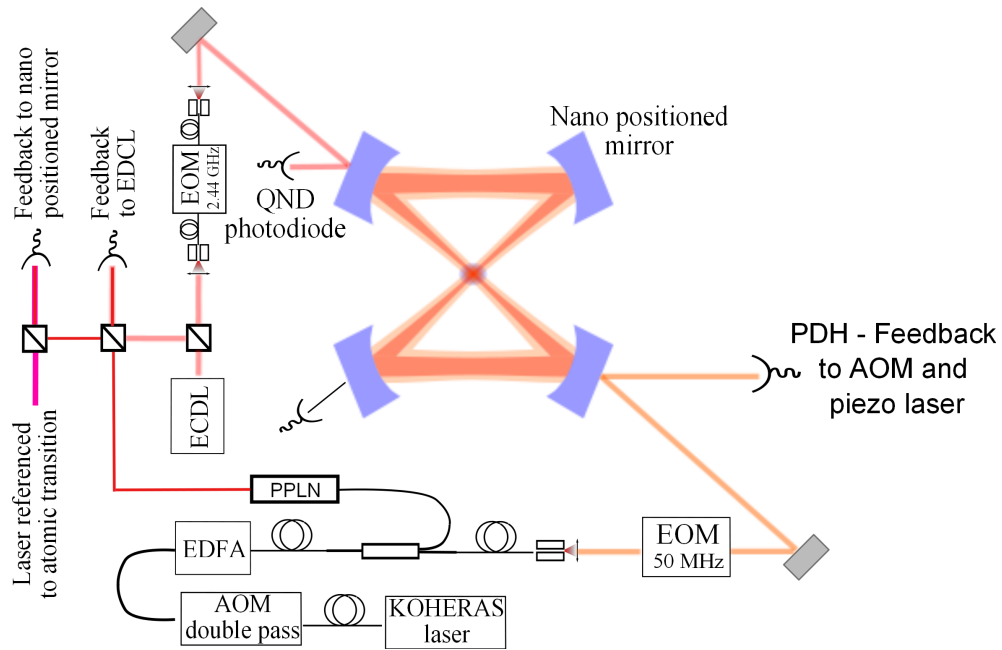


Figure 6.16: *Complete locking scheme foreseen for the QND measurement.*
The trapping light at 1560 nm is locked to the cavity and doubled in a PPLN crystal to serve as a reference for the 780 nm probing light (QND). The cavity resonance are fixed with respect to the atomic transition by comparing the doubled light to the repumper laser.

to the atomic structure, a slow feedback below 20 Hz is applied on the piezo of the cavity. To reference the QND laser to the cavity resonance, a fast feedback loop locks the QND probe to the doubled 1560. Indeed, because the 1560 nm radiation is locked on the cavity, its doubled components also follows the cavity lines at 780 nm. Hence, by locking the QND probe to this doubled light, the detection becomes insensitive at first order to the fluctuations of the cavity.

Nevertheless, even for a carrier that stays perfectly in between two resonances, a fluctuation of the cavity length L by δL modifies the free spectral range (FSR) by $c\delta L/L^2$. Hence the transitions that are 2.5 FSR away from the carrier are frequency shifted by $2.5c\delta L/L^2$. Actually, for a *frequency/phase modulation*, the probed cavity resonances move in opposite direction with respect to the carrier, *i.e.* both goes away from the carrier or both comes closer. Hence the two side-bands accumulate an opposite phase shift which cancels in equation 6.9. Unfortunately, the residual amplitude modulation does not benefit from such a suppression (see equation 6.13) and will be fully sensitive to the cavity length fluctuations.

6.4 Summary

We have presented in this chapter the apparatus that has been developed for the production of spin-squeezed cold atomic samples in a dual-frequency high-finesse cavity. The high rejection of optical path length fluctuations as well as the rejection of the laser noise were pointed out. We have seen that the apparatus developed is limited by the optical shot noise of the sideband for modulations up to a few GHz, and this for any power in the sideband.

In addition, we demonstrated the method in single pass by performing nondestructive measurements of the coherent evolution of internal atomic states. From the nondestructive measurement of Rabi oscillations, we have shown that the decoherence induced by the probe can be limited by the inhomogeneous light-shift from the carrier and not by the spontaneous emission induced by the sideband. We also presented a real-time measurement of the atomic state evolution in a Ramsey interferometer with low decoherence, where we were able to look at the evolution of the interferometric phase.

Some first measurements of the noise have shown a contribution of the atomic noise. Nevertheless, the test was not fully conclusive on the shot-noise nature of this noise, and further measurements on a denser sample are planned. As a perspective, we emphasized on the potential gain of a cavity enhanced measurement and gave the set-up foreseen for a practical implementation insensitive to the cavity noise.

Raman laser

Contents

7.1	Experimental set-up	181
7.1.1	Vacuum chamber integrated cavity	182
7.1.2	The linear cavity	182
7.1.3	The laser system	183
7.2	Raman laser	185
7.2.1	Principle	185
7.2.2	Laser characteristics	186
7.3	Summary	190

In this chapter, we present the realization of a narrow linewidth Raman laser [Hilico 92, Guerin 08] that uses cold atoms as the gain medium. The experiment was realized in the group of Pr Kasevich in Stanford.

The achievement of ultra-narrow lasers is of primary importance for ultra-high spectroscopy and metrology applications. Recent works [Meiser 09] have shown that using cold atoms in high-finesse cavity, would allow to generate very narrow linewidth laser that would improve the sensitivity of optical clock by two orders of magnitude. Thanks to the high-finesse cavity, the Raman laser that is presented in the following presents such a narrow Schawlow-Townes linewidth limit in the 100 mHz range [Grynberg 10, Schawlow 58]. Such narrow linewidths are usually attributed to actively stabilized diode lasers [Schoof 01, Fox 03]. In addition, Raman lasers present a narrow gain bandwidth and an easily tunable absolute frequency which has been extensively used for the characterization of the process. The tunability of Raman gain could be used to generate anomalous dispersion in optical cavities, and hence increase the signal-bandwidth of gravitational wave detectors [Pati 07].

In this chapter we will shortly present the experimental apparatus and emphasize on the relevant experimental parameter for the Raman laser. In a second part, we present the Raman laser realized and its characterization in terms of laser threshold, laser linewidth, and at last an interesting atomic population dependance of the laser absolute frequency.

7.1 Experimental set-up

The experimental vacuum system is composed of two chambers. One is used to generate a 2D MOT. The jet of atoms created loads the 3D MOT centered on the linear high-finesse cavity in the second chamber. In this section, we will present the specificities of the experimental apparatus, namely the stable vacuum system, the high-finesse linear cavity and the narrow linewidth laser system.

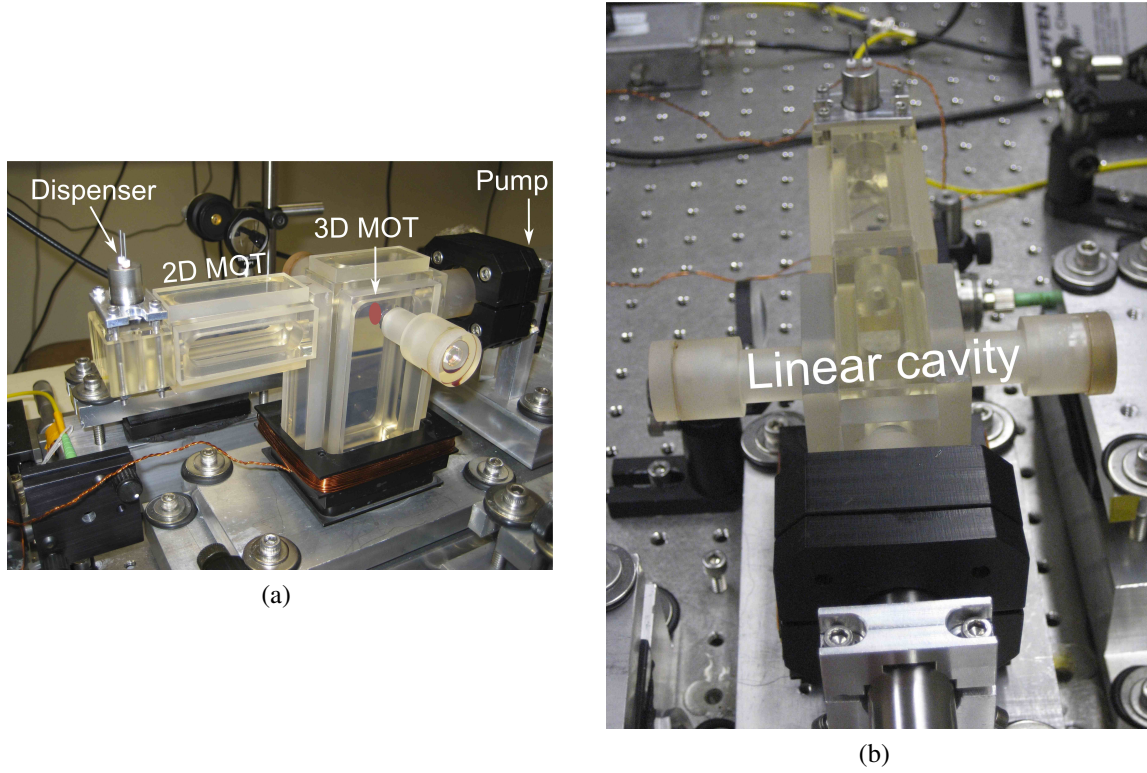


Figure 7.1: The Zerodur vacuum system with the integrated linear cavity.

7.1.1 Vacuum chamber integrated cavity

The entire vacuum system is realized in Zerodur, which is a ceramic with a near-to-zero thermal expansion coefficient ($2 \times 10^{-8} \text{ K}^{-1}$). It is completely a-magnetic and then very suitable for atom interferometry applications. The different components of the chamber are glued together. The compactness of the design results in a very short distance between the 2D MOT and the 3D MOT trapping region which optimizes the loading rate. The source of atoms of the 2D MOT comes from a dispenser that is situated on the opposite side with respect to the 3D MOT. No push beam is used in the 2D MOT set-up.

The high-finesse linear cavity has been directly integrated in the 3D MOT chamber. The whole vacuum is pumped by a single ion pump on the 3D MOT side where the vacuum is below 10^{-9} mbar. The compact opto-mechanical design is contained in the black box presented in figure 7.2. All the beams used on the atoms arrive fibered on the structure, and all the optics are tightly fixed to this aluminum (black) structure that surrounds the cavity. This structure gives long term stability to the design, and reduces the optical path such that steering effects of the beams are minimized.

7.1.2 The linear cavity

The linear cavity is made of two 10 cm radius-of-curvature mirrors that are separated by $L = 10.7$ cm. The cavity is then close to the confocal configuration (Fabry-Perot, see figure 3.14 in chapter 2) where transverse modes are almost degenerate. At 780 nm the beam waist is $110 \mu\text{m}$ at the center of the cavity where the atoms are situated. The mirrors are highly reflective at both 780 nm and 1560 nm, resulting in a measured finesse of $\mathcal{F}_{780} = 175,000$ and $\mathcal{F}_{1560} = 117,000$ and linewidths $\kappa_{780} = 2\pi \times 4 \cdot 10^3 \text{ rad.s}^{-1}$ and $\kappa_{1560} = 2\pi \times 6 \cdot 10^3 \text{ rad.s}^{-1}$.

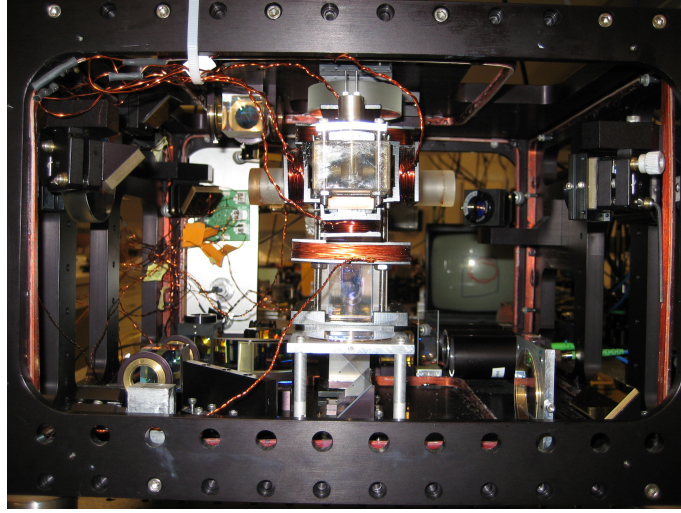


Figure 7.2: *Compact opto-mechanical design.*

The MOT and cavity beams reach the opto-mechanical set-up through optical fibers connected to collimators tightly fixed to the vacuum chamber.

The longitudinal mode spacing is given by the free spectral range $\Delta\nu_{FSR} = c/2L = 1.396$ GHz, and the transverse mode spacing is $\Delta\nu_{tms} = \Delta\nu_{FSR}/2 + 37.5$ MHz. This results in a spacing of $2\Delta\nu_{tms} - \Delta\nu_{FSR} = 75$ MHz between nearest transverse modes. This splitting quantifies the difference with the exact-confocal geometry. Due to a small imperfection in the cavity mirrors, the cavity is slightly astigmatic. Hence, the transverse modes TEM_{mn} that have the same order ($n + m = \text{Cte}$) are non-degenerate and their profile is given by the Hermite-Gauss functions. For example, the TEM_{01} and TEM_{10} modes are separated by 515 kHz. The spectral properties of the cavity are measured using the spectroscopic method described in section 3.2.6. This method relies on the injection and frequency control of the sidebands that are generated by frequency modulating the light that probes the cavity.

Since the vacuum chamber is entirely realized in Zerodur, the cavity length is very stable and is tuned by controlling the temperature of the chamber. This allows to precisely set the absolute frequency of the cavity modes.

7.1.3 The laser system

The laser system used to generate the frequencies at 780 nm for the cooling and trapping stays all within the surface of an A4 paper. It is composed of two Littrow extended diode lasers, spectroscopically locked to rubidium. One is on the $|F = 1\rangle \rightarrow |F_p = 2\rangle$ transition and is used as a repump, the other one is locked on the $|F = 2\rangle \rightarrow |F_p = 2, 3\rangle$ crossover, and frequency shifted by a double pass acousto optic modulator. To increase the power of the cooling laser, a slave laser is optically injected and about 60 mW are available directly on the atoms for the operation of both the 2D MOT and 3D MOT.

The 1560 nm laser

As it will be described in section 7.2, the cavity length is tracked using a laser at 1560 nm locked on the cavity (see figure 7.3). The source of the radiation is a 1560 nm Vortex

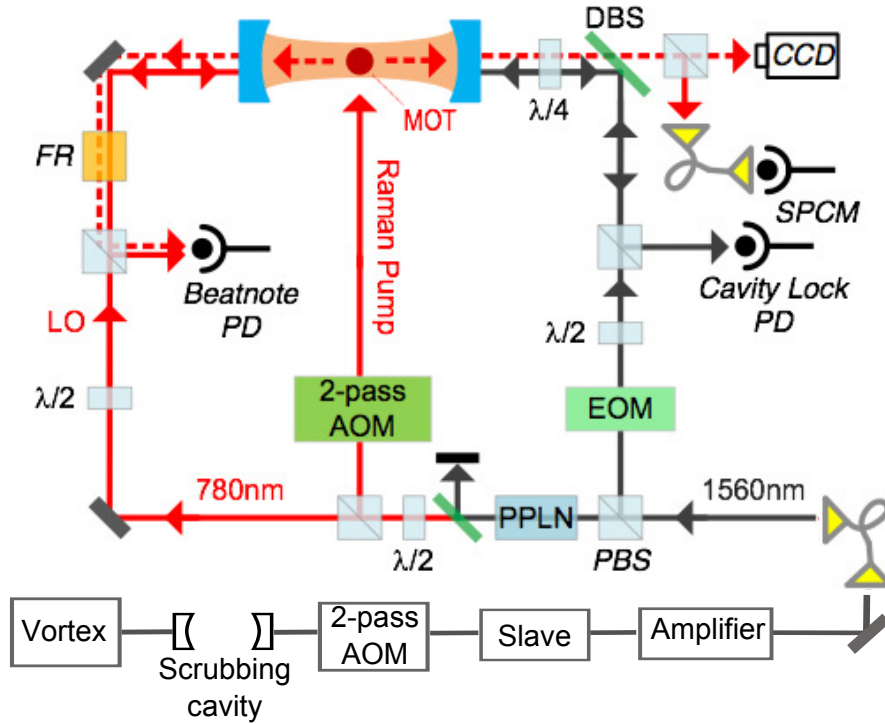


Figure 7.3: Optical system of the Raman laser experiment.

A vortex at 1560 nm is phase locked to a scrubbing cavity. The transmitted light is amplified and is used both to reference the cavity length through a PDH lock and doubled in a non-linear crystal to serve as an optical pump for the Raman process.

with a linewidth of a few hundred kHz. The light of this laser is phase locked on a scrubbing cavity that has characteristics similar to the science cavity. The transmitted light has a few kHz linewidth, and injects a slave diode that injects a 1 W Erbium doped amplifier. The amplified light is frequency locked to the cavity using the Pound Drever Hall (PDH) method [Drever 83b]. Instead of the usual scheme that locks the carrier to the cavity, the sideband is here injected. This presents two advantages:

- The power coupled into the cavity can be easily changed by modifying the power in the sideband, and the PDH beatnote always benefits from a strong local oscillator (carrier).
- The exact frequency of the carrier can be chosen independently from the cavity lines, by modifying the modulation frequency of the PDH.

The lock on the science chamber has a slow feedback applied on the piezo that controls the length of the scrubbing cavity and a fast correction is realized by a double pass acousto-optic. A part of the carrier light that is not injected in the science cavity is frequency doubled in a periodically poled lithium niobate (PPLN) waveguide crystal to generate 780 nm light. As only a few hundred μW are obtained after doubling, the doubled 1560 nm light is injected in a slave diode that gives ~ 7 mW of light. This light at 780 nm has a linewidth below $2\pi \cdot 6 \cdot 10^3 \text{ rad.s}^{-1}$ and is referenced to the cavity length. If the cavity length changes, the modes of the cavity at 780 nm and the doubled 1560 nm are shifted by the same amount.

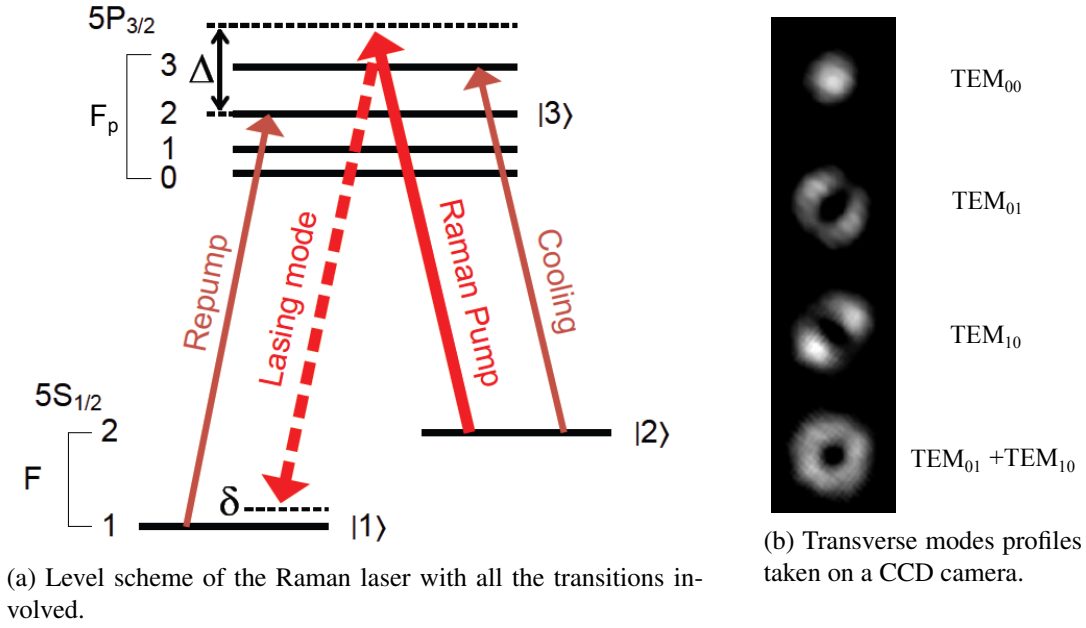


Figure 7.4: Frequency scheme and spatial modes of the Raman laser.

The Raman pump drives a two photons process that is completed down to $|F = 1\rangle$ by a cavity mode.

7.2 Raman laser

The possibility to engineer the laser gain medium is an interesting feature of Raman lasers that can emit at any frequency. In addition, the large experimental control of the parameters in cold atomic physics is advantageous to precisely characterize the gain mechanism and the laser limitations.

7.2.1 Principle

The system under study is a magneto-optical trap operated at the center of the high finesse linear cavity, and an off-resonant laser called Raman pump is shined on the atoms of the MOT.

The atoms undergo a two-photon Raman transition driven by this frequency tunable pump laser which excites the atoms from the $|F = 2\rangle$ hyperfine ground state to an intermediate virtual state. The two photon transition is completed by the emission of a photon in an allowed cavity resonance which has a frequency that matches the transition between the virtual level and the $|F = 1\rangle$ hyperfine ground state. The atoms are driven back to $|F = 2\rangle$ by the repump light associated with the 3D-MOT. Hence, the repumper ensures the inversion of population and the continuous operation of the laser. The relevant atomic energy levels and laser frequencies are shown in figure 7.4a.

In practice, an interesting feature is given by the Raman pump that is frequency referenced to the cavity length. If the cavity changes its length, because for example of thermal drifts, the Raman pump follows the frequency drift of the cavity mode that completes the two-photon process. Hence, when a given resonant condition of the two-photons process is found, changing

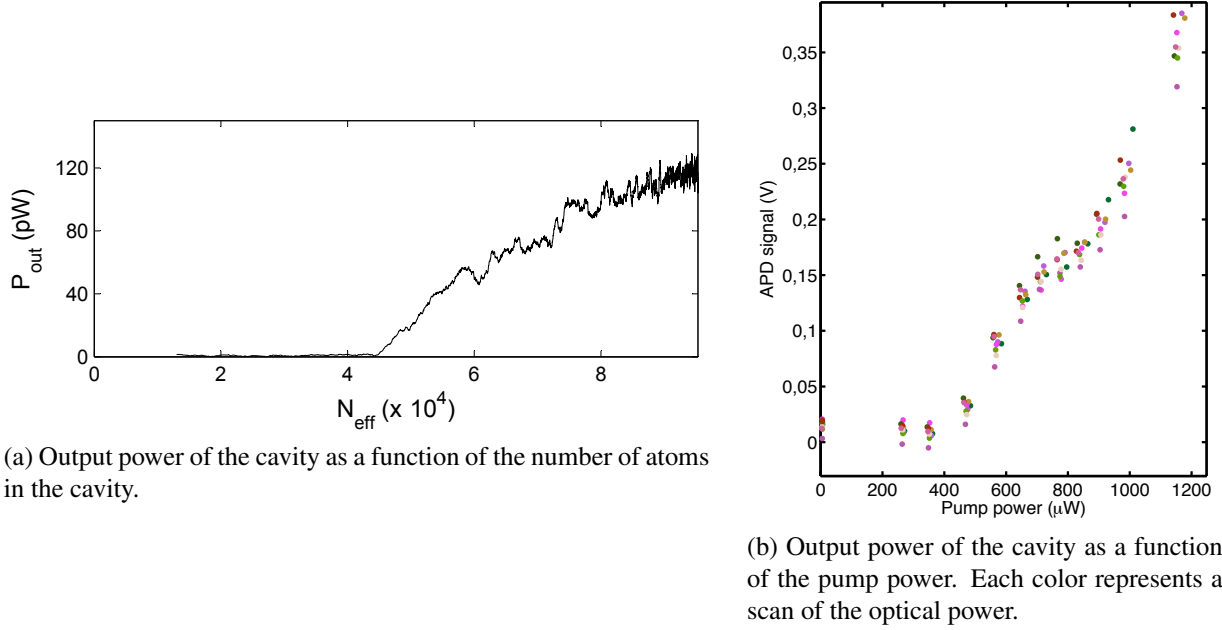


Figure 7.5: *Threshold of the laser*

the cavity length preserves the resonance condition and allows us to scan the detuning Δ of the virtual state with respect to the $|F = 2\rangle \rightarrow |F_p = 2\rangle$ transition.

To reach a resonant condition, the frequency of the Raman pump is arranged so that its separation from the cavity mode is exactly the hyperfine ground state splitting. In that purpose, both the 1560 nm carrier tunability from the cavity resonance (see section 7.1.3) and an acousto-optic modulator in double pass are used.

The cavity mode that completes the process can be either a fundamental mode or a higher transverse mode. In figure 7.4b four transverse profiles of the output laser are shown including the TEM_{00} , TEM_{01} , TEM_{10} , and both the TEM_{01} and TEM_{10} that emit at the same time.

7.2.2 Laser characteristics

7.2.2.1 Laser threshold

In order to prove that this laser is indeed a Raman laser and not just a Raman two-photon transition that would emit in the cavity mode, we measured the output power of the cavity as a function of the atom number (figure 7.5a) and of the pump power (figure 7.5b). The two signals present clear thresholds, which correspond to the point where the losses of the mirrors are overcome by the gain of the medium. These thresholds prove that we are in the presence of a lasing behavior.

7.2.2.2 Raman gain profile

Usually Raman two-photon transitions, are driven by two coherent laser fields. As a consequence, one could expect the laser to show a very narrow transition gain profile, of the order of the cavity linewidth ($\sim 2\pi \times 4 \times 10^3 \text{ rad.s}^{-1}$). In figure 7.6 is presented the output power of the cavity when the Raman pump is scanned through the resonance condition. The three structures are three identical sweeps across the resonance. In this particular case, we were addressing

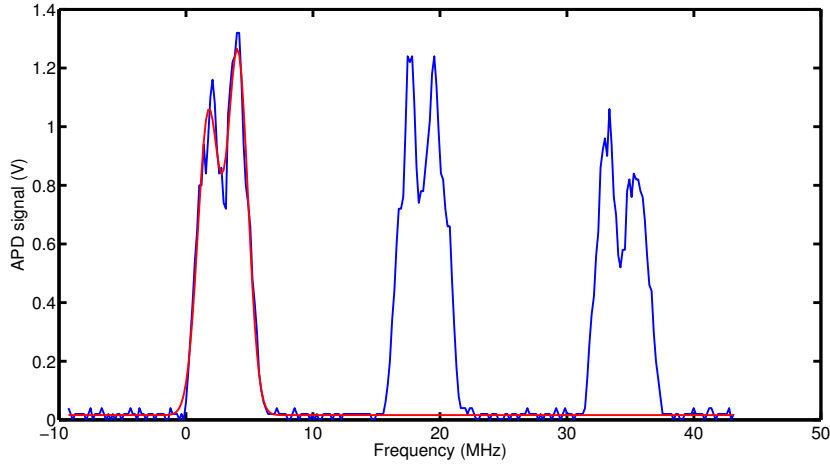


Figure 7.6: Output power of the cavity when the Raman pump laser is scanned across the resonance condition.

the first transverse modes (TEM_{10} and TEM_{01}) separated by 515 kHz. This explains the sub-structure in the profile. Each bump is due to one of the two modes. When the gain is tuned in between the modes, we have mode competition and both modes can emit together (see figure 7.4b). The Gaussian rms size of the individual bump is 1.1 ± 0.1 MHz, which indicates a much broader gain profile than the expected kHz. This can be explained by the fact that the atoms are subjected to the MOT light. They are then continuously cycling in a saturated transition. In that case, the ground state $|F = 2\rangle$ can be described as a state with an effective linewidth that is of the order of the excited state linewidth (\sim MHz).

In addition, to check on the gain profile, we artificially enlarged the Raman pump using the double pass acousto-optic modulator (figure 7.3) and saw that the laser output power was independent of the Raman pump linewidth. This is in agreement with the large gain profile observed.

7.2.2.3 Laser linewidth

Another very interesting feature is given by the Schawlow-Townes linewidth limit of the laser [Grynberg 10, Schawlow 58]. This limit gives the smallest linewidth achievable:

$$\Delta\nu_{ST} = \frac{2\pi\hbar\nu\kappa^2}{P_{\text{out}}} \approx 100 \text{ mHz} \quad (7.1)$$

Thanks to the high-finesse of the cavity, this linewidth is particularly small. The measurement of such a low linewidth is an experimentally challenging problem. The usual method consists to compare two identical lasers. Obviously this was not possible for us since we would have needed a second identical vacuum chamber. Instead, we looked to the beatnote of two transverse modes that were emitting simultaneously, namely the TEM_{10} and TEM_{01} . We underline that this is not a measurement of the laser linewidth since common noise is rejected in such a procedure.

Since the transverse modes are spatially orthogonal, both modes were partially injected in the same single mode fiber and the beatnote was recorded on an Single Photon Counting Module avalanche photodiode. The recorded beatnote linewidth is presented in figure 7.7. The result is a 117 Hz Lorentzian linewidth for one mode. This "high" value for the linewidth is attributed

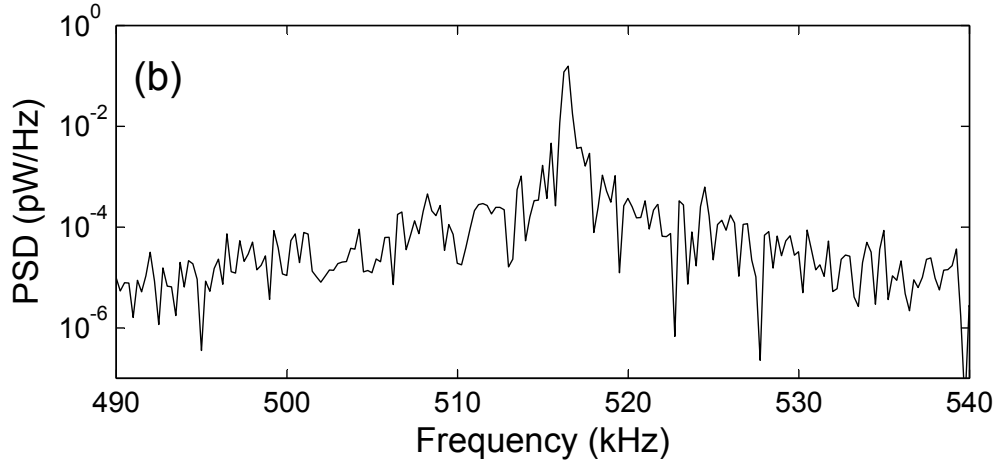


Figure 7.7: Beatnote of the TEM_{10} and TEM_{01} modes.

The beatnote of the two modes has a Lorentzian linewidth of 234 Hz, leading to 117Hz linewidth for one laser.

to the transverse modes spatially addressing different parts of the atomic cloud. Hence, spatial fluctuations of the atom number which shift the cavity resonant frequency of each modes, are not common mode noise and can then enlarge the beatnote.

The problem of spatial fluctuations is typical of a MOT operation where the particles are in motion. Using localized trapped ions as a gain media could in principle solve this problem.

7.2.2.4 Frequency shift of the laser

The Rabi frequency of a two-photon process scales as :

$$\Omega = \frac{\Omega_1 \Omega_2}{2\Delta} \quad (7.2)$$

where Δ is detuning of the driving field from the atomic transition, and $\Omega_{1/2}$ are the one photon on-resonance Rabi frequencies induced by the Raman pump and the cavity field. Hence, to keep an efficient process, Δ should be relatively small. As a consequence, the cavity mode that completes the two photons process is close to the atomic transition and can be frequency shifted by the atomic population that acts as a refractive medium. In addition, this frequency shift is emphasized by the finesse of the cavity, or in other words by the single photon Rabi frequency g [Miller 05]. Using the notations of strongly coupled cavities, the cavity mode frequency shift is $\Delta f = N_{\text{at}} g^2 / \Delta$ and in our configuration we have $g = 116$ kHz.

This is exactly what is shown in figure 7.8 where the absolute frequency of the mode is shifted as the atom number increases. Experimentally, the absolute frequency of the laser is obtained by beating the output field of the cavity with the doubled 1560 nm used as a local oscillator. The beatnote at 6.834 GHz is observed on a high frequency photodiode. We underline again the high sensitivity of heterodyne detections since in this laser the output power of the cavity is ~ 1 nW.

As we compare the doubled 1560 nm that is referenced to the length of the cavity and the cavity mode at 780 nm, a drift of the beatnote is a signature of a frequency dependent shift.

Figure 7.8 shows that for two opposite detunings, the cavity mode is shifted in opposite directions. This indicates that the shift is related to the population in $|F = 1\rangle$.

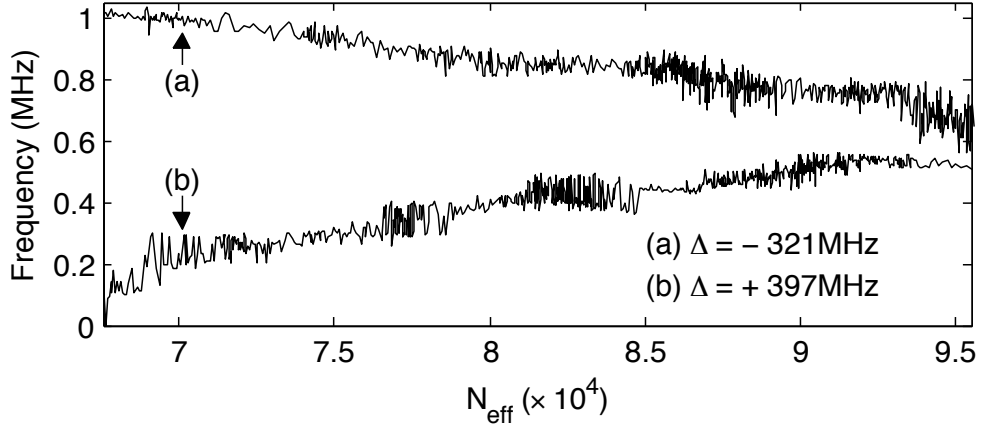


Figure 7.8: Absolute frequency drift as a function of the effective atom number for (a) red and (b) blue detuned light.

The opposite slopes are due to the positive and negative susceptibilities associated with the red and blue detuned configurations respectively. The relative position of the two curves is arbitrary.

Concerning the curve (a) in figure 7.8, the detuning $\Delta = -321$ MHz indicates that the cavity mode is on the red of all the atomic transition. In equation 6.20, we find a refractive index above 1 ($\Delta = -\Delta_{F,F'}$). Hence, the effective length at 780 nm will increase with the number of atoms in $|F = 1\rangle$, and the absolute frequency of the mode will then decrease as seen in figure 7.8. The same reasoning can be realized for the opposite detuning (curve (b)).

In figure 7.8, we observe that the slope has a higher absolute value for (b) than for (a). Regarding the excited state hyperfine splitting in figure 7.4a, we expect the coupling of the cavity mode to the atomic state to be higher in (a) than in (b) since $|F = 1\rangle$ is only coupled to $|F_p = 0, 1, 2\rangle$. This contradiction actually indicates that the atoms in $|F = 2\rangle$ play a role in this frequency shift. Indeed, for the case (b), the cavity mode is blue detuned both for the atoms in $|F = 1\rangle$ and for the atoms in $|F = 2\rangle$. On the contrary, for (a) the cavity mode is red detuned with respect to atoms in $|F = 1\rangle$ and blue detuned for the atoms in $|F = 2\rangle$, resulting in opposite shifts, in agreement with the reduced slope of figure 7.8(a).

This also brings to light the solution to suppress such a shift: one should tune Δ in a position where both shifts cancel, *i.e.* find the 0 of refractive index.

We consider now the threshold scan presented in figure 7.9. Each curve is a measurement of the threshold of the TEM_{01} and TEM_{10} modes as a function of the Raman Pump. These thresholds are parametrically plotted against the detuning Δ at which they were taken. Interestingly, we see a dependance of the shape of the threshold with Δ . This dependance can be qualitatively understood by the single photon spontaneous emission rate. For a small detuning Δ , the Raman pump depumps the atoms from $|F = 2\rangle$ to $|F = 1\rangle$. Hence it increases the population in $|F = 1\rangle$ which frequency shifts the cavity mode as previously explained.

Three cases can be distinguished:

- The Raman pump is far from the $|F = 2\rangle \rightarrow |F_p = 2\rangle$ transition (labelled "3" in figure 7.9) and induces very little spontaneous emission. A classical threshold is expected.

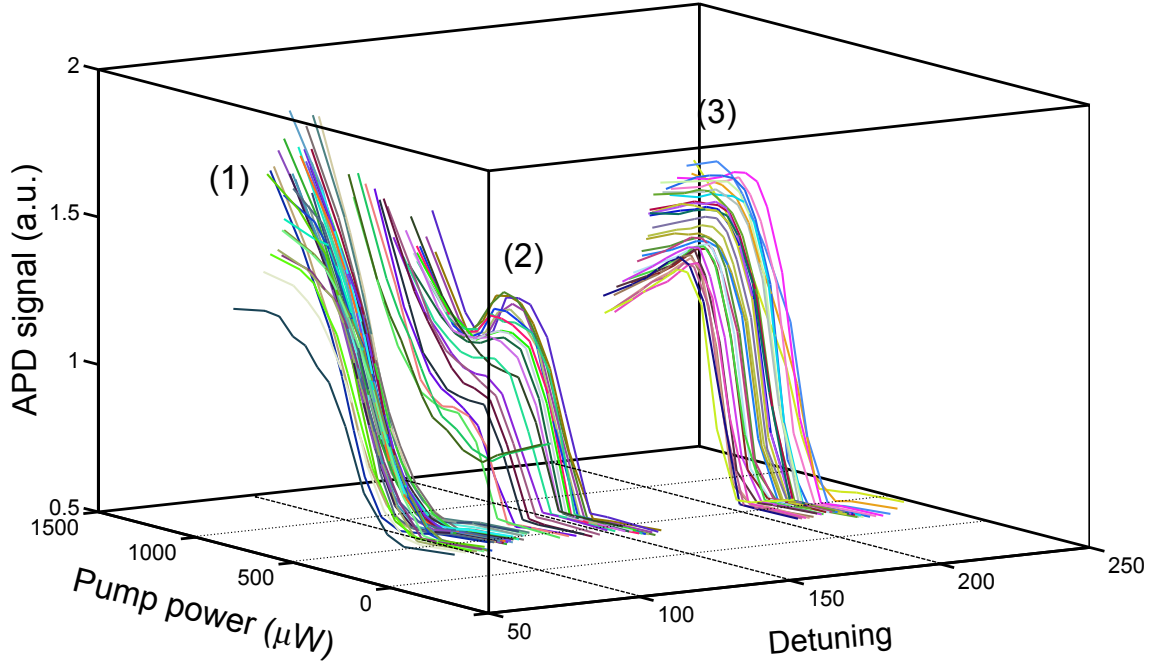


Figure 7.9: Laser threshold shape as a function of the detuning Δ .

The shape of the threshold is affected by the single photon and two photon depumping rates which are linked with the relative detuning Δ of the Raman pump with respect to the atomic transition.

- The Raman pump is closer to resonance (labelled "2"). The Raman pump threshold is reached while the cavity mode is still on the lower frequency mode (e.g. TEM_{01}). By increasing the pump, more atoms are transferred to $|F = 1\rangle$ and the cavity mode shifts to higher frequency. It first experiences the intermediate dip in the gain (figure 7.6) before it switches to the other transverse mode (TEM_{10}).
- For smaller Δ , the Raman pump is increased and the threshold is reached when the cavity mode has already been shifted to the next transverse mode. No deep is present in the threshold curve (labelled "1").

7.3 Summary

In this chapter, we have presented the experimental apparatus developed in the group of Pr. Kasevich in Stanford. The apparatus is the fruit of many years of technical research that led to a very compact and stable set-up.

We presented the principle of the Raman laser that we operated in the ultra-high finesse cavity. This laser is based on a two photons Raman transition between a Raman pump and a cavity mode.

With this laser, we demonstrated a common mode narrow linewidth of 117 Hz that could be further engineered to reach the Schawlow-Townes limit that is below the Hz level. In the actual set-up, it is believed that the main source of frequency noise comes from spatial atom number fluctuations.

At last we have shown a dependance of the cavity absolute frequency on the atom number, and qualitatively described it by arguing on the refractive index induced by the atoms.

Conclusion

In this thesis, we have presented the work realized towards the creation of non-classical states of matter with high particle numbers. This work was carried out with both the intention to improve the sensitivity of atom interferometers below the atomic shot-noise, but also to study the fundamental properties of such non-classical states.

As a first PhD student on the experiment, my first task has been to design and assemble the experimental apparatus. A system of 2D and 3D magneto-optical traps has been set-up and allowed to load an optical dipole trap at 1560 nm. The mode that is generated by the optical dipole trap is one of the specificities of our design: it is the mode of a crossed optical cavity. Because of the crossed geometry, the trapping frequencies are high in all directions of space and the cooling by an evaporation procedure can be considered. Concerning the creation of a degenerate gas, we obtained some recent breakthrough such as the ability to load high numbers of particles and to lower all the heating sources below the residual background collisions, but up to now no condensed fraction has been observed. Nevertheless, the ability to trap large numbers of particles in the dipole trap allows us to reach dense samples which can be further exploited for the creation of highly squeezed states.

As presented in chapter four, the generation of non-classical states requires the effect of a non-linear evolution of the atomic state. Interestingly, the measurement in quantum mechanics and more precisely the Quantum Non-Demolition measurement offers such a non-linearity. For the improvement of atom interferometry, the relevant observable is the population difference between the hyperfine ground states of the system. It was shown that a dispersive measurement that precisely evaluates the population difference realizes a QND measurement. To intuitively understand the dynamics that leads an ensemble of independent particles to a correlated sample, a wavefunction analysis was developed. The application of this formalism relies on a precise description of the experimental apparatus, and has the advantage to obtain the key experimental parameters. Using this description we studied two experimental apparatus that are the Mach-Zehnder interferometer and the heterodyne detection. On these well known test apparatus, we have shown that during the measurement, the variance of the atomic state decreases in a deterministic way that essentially depends on the coupling strength and the contrast. In addition, the model reproduces well the randomness of the measurement result that follows the Born probability rule.

To practically realize the dispersive measurement, we have studied and implemented a frequency modulation method that has a very low sensitivity to classical noise. The key experimental difficulty of this method relies on the photodetector that needs both to be shot noise limited for a low power ($< 500 \mu\text{W}$) and to operate with a high bandwidth (2 GHz). These two properties, that are usually not conciliable, were achieved by taking advantage of the advances of the telecommunication technology. Applying this heterodyne detection in single pass, we

were able to non-destructively follow an atomic sample undergoing Rabi oscillations. On this test-bench that are the Rabi oscillations, we proved that even if the spontaneous emission induced by the carrier of the frequency modulation can be neglected, the inhomogeneous light shift generated by the carrier is our main source of decoherence for far off-resonance probing. In addition, the detection scheme was applied to follow an interferometric sequence where it showed its non-destructive character. For the creation of squeezed states, the measurement needs to be pushed forward to exhibit a sensitivity to the atomic shot-noise. The first series of measurements of the atomic noise realized on a MOT have essentially shown an influence of the classical atomic noise. The use of a denser sample and of the coupling enhancement due to the cavity will increase the signal-to-noise ratio and should make the measurement below the atomic shot noise possible.

Cold atoms and a high-finesse cavity are two well known systems that raise a rich physics when coupled to each other. Going to Stanford gave me the possibility to work on an experimental apparatus complementary to the one developed in our experiment. There we studied a Raman laser that uses cold atoms as the gain medium. The atomic sample being surrounded by a high finesse ($\sim 10^5$) cavity, the expected linewidth of the laser is in the 100 mHz range. The beatnote of two transverse modes of this laser was measured to 171 Hz, without any dynamical stabilization. The discrepancy with the theoretical limit is attributed to atom number fluctuations. As the lasing cavity mode is close to the atomic transitions, population fluctuations modify the refractive index seen by the cavity mode and induce a shift of the lasing frequency.

Perspectives

This experiment that we constructed has a potential for many applications.

Obviously I hope that soon the QND measurement of large atomic sample will be realized and that the potential of highly squeezed states will really prove valuable for the improvement of atom interferometry. The demonstrations that have been shown all around the world were necessary steps but an implementation on large sample will prove that the use of non-classical states can bring a real advantage. In this perspective, our experiment already proved its ability to trap large number of particles. In addition, the first successful tests of nondemolition measurement in single pass suggest a great potential for the implementation of the measurement in the cavity.

Our wavefunction description that was applied to study the squeezing dynamics was able to describe the generation of Schrödinger Cat states. The experimental implementation that it suggests is no more complex than the generation of squeezed states, and only the observed quadrature should be changed. These Schrödinger Cat states of large particle numbers are very sensitive to decoherence and could give new perspectives to our understanding of the coupling to the environment.

The creation of a condensate in the fundamental mode of the cavity would represent an interesting experimental achievement and would strongly reduce the constraint on the optical power necessary for its obtention. This gain that is usually of no interest in a laboratory may prove determinant for the application of atom interferometry and more generally of cold atomic physics in space. In addition, the ability to split and recombine the condensate at will using the transverse modes may give the possibility to carry a wide range of experiments on the phase coherence of the sample.

Similarly to the experiment performed in Stanford, our experimental apparatus in France has also shown some lasing properties. The lasing process has not been identified yet, but our design that does not involve standing waves can lead to interesting processes such as the collective atomic recoil lasing [Zimmermann 04].

List of publications

R. Kohlhaas, T. Vanderbruggen, S. Bernon, A. Bertoldi, A. Landragin, and P. Bouyer
Robust laser frequency stabilization by serrodyne modulation
 Submitted to Optics Letters

G. Vrijsen, O. Hosten, J. Lee, S. Bernon, and M. A. Kasevich
Raman lasing with a cold atom gain medium in a narrow linewidth optical cavity
 Physical Review Letters, Vol. **107**, pp. 063904 (2011)

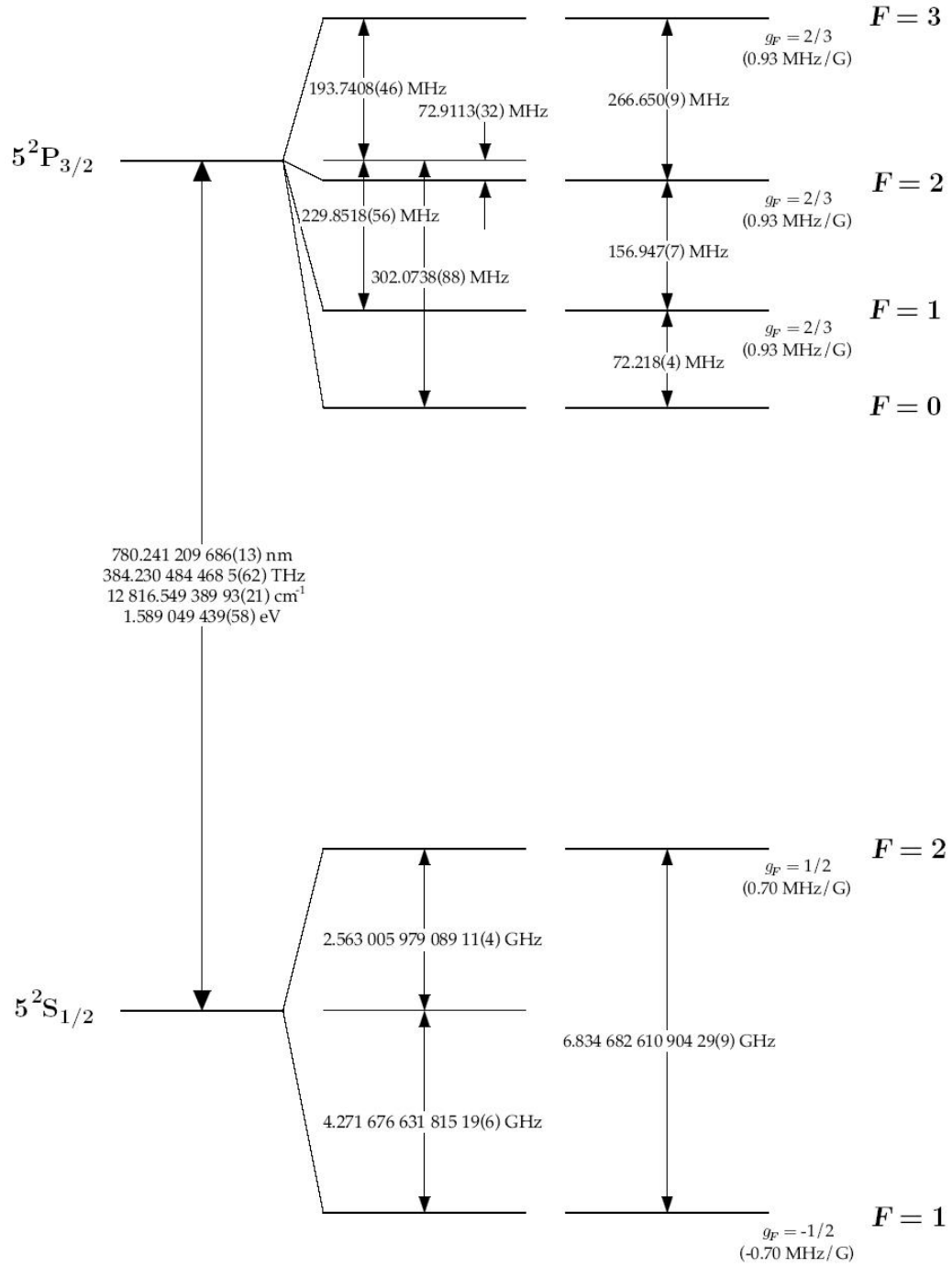
S. Bernon, T. Vanderbruggen, R. Kohlhaas, A. Bertoldi, A. Landragin and P. Bouyer.
Heterodyne nondemolition measurements on cold atomic samples: towards the preparation of non-classical states for atom interferometry
 New Journal of Physics, Vol. **13**, pp. 065021 (2011)

T. Vanderbruggen, S. Bernon, A. Bertoldi, A. Landragin, and P. Bouyer
Spin-squeezing and Dicke-state preparation by heterodyne measurement
 Physical Review A, Vol. **83**, pp. 013821 (2011)

A. Bertoldi, S. Bernon, T. Vanderbruggen, A. Landragin and P. Bouyer
In situ characterization of an optical cavity using atomic light shift
 Optics Letters, Vol. **35** Issue 22, pp. 3769 (2010)

APPENDIX A

Rubidium D_2 transition



Phase and frequency modulation

In experimental physics, modulation techniques are very often used for precision measurement. They present the advantage to transfer the measurement in AC where they become insensitive to low frequency noise. When it comes to optical frequency, one uses acousto optics modulator (AOM) or electro-optics modulator (EOM) to generate the modulation. The first shift the frequency by diffracting the light on a refractive index grating which was creating by an acoustic wave. The second modulate the refractive index on the optical path and then the phase of the optical beam. The EOM or Pockels cell are then very well adapted to create phase modulation. The light electric field E after modulation at Ω writes:

$$E = E_0 \cos(\omega_0 t + \Phi(t)) \quad (\text{B.1})$$

$$= E_0 \cos(\omega_0 t + \beta \cos \Omega t). \quad (\text{B.2})$$

The equation B.10 can be rewritten as a serie including a Bessel decomposition:

$$E = E_0 \sum_{n=-\infty}^{\infty} J_n(\beta) \cos(\omega_0 t + n\Omega t), \quad (\text{B.3})$$

where J_n are the first kind Bessel functions

$$J_n(x) = \left(\frac{x}{2}\right)^n \sum_{p=0}^{\infty} \frac{(-1)^p}{2^{2p} p! (p+n)!} x^{2p}. \quad (\text{B.4})$$

The expression B.3 can be demonstrated by a careful decomposition in series of $e^{i\omega_0 t + i\beta \sin(\Omega t)}$.

With an EOM, β is the modulation depth and is proportional to the applied electric field and to the relevant element of the electro-optical tensor of the material [Jonathan 05].

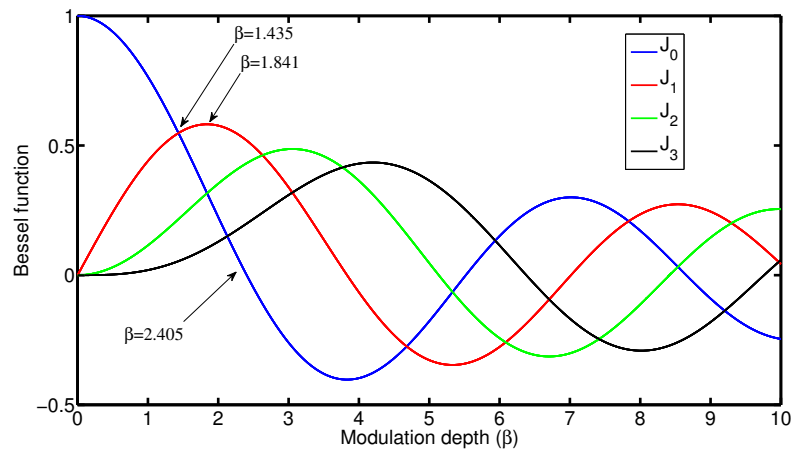
For small modulation depth $\beta \ll 1$, one has:

$$J_0(\beta) = 1 \quad J_1(\beta) = \beta \quad J_{-1}(\beta) = -\beta, \quad (\text{B.5})$$

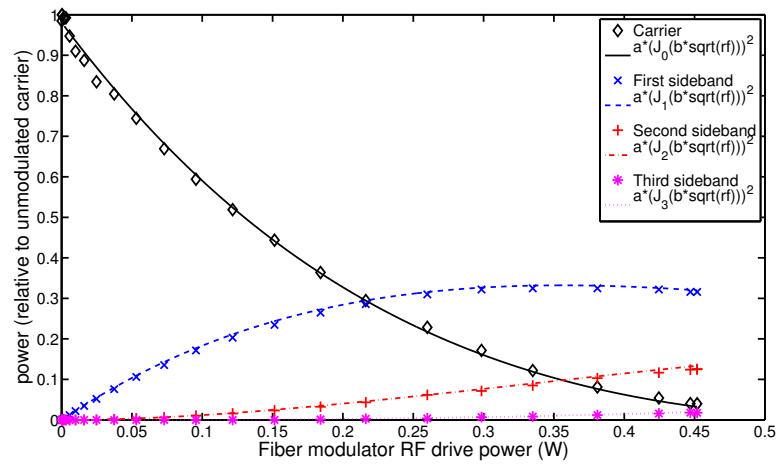
and the expression B.3 becomes:

$$E \approx E_0 (J_0(\beta) \cos(\omega_0 t) + J_1(\beta) \cos((\omega_0 + \Omega)t) + J_{-1}(\beta) \cos((\omega_0 - \Omega)t)) \quad (\text{B.6})$$

$$\approx \frac{E_0}{2} e^{i\omega_0 t} (J_0(\beta) + J_1(\beta) e^{i\Omega t} + J_{-1}(\beta) e^{-i\Omega t}) + c.c. \quad (\text{B.7})$$



(a) First kind Bessel function.



(b) Phase modulation.

Figure B.1: Bessel function of a phase modulation.

FM modulation

Frequency modulation is a particular case of phase modulation. It can be directly obtained by modulating for example the input of a VCO. In that case one has:

$$E = E_0 \cos(\Phi(t)) \quad (\text{B.8})$$

$$= E_0 \cos\left(\int_0^t (\omega_0 + \omega_\Delta \cos \Omega\tau) d\tau\right) \quad (\text{B.9})$$

$$= E_0 \cos\left(\omega_0 t + \frac{\omega_\Delta}{\Omega} \sin(\Omega t)\right) \quad (\text{B.10})$$

where $\omega_i = \omega_0 + \omega_\Delta \cos \Omega\tau$ is the instantaneous angular frequency. Hence, the frequency modulation is a phase modulation with modulation depth $\beta = \omega_\Delta/\Omega$.

Interlude on alignment locks

Because the cavity is under vacuum, a great care has been given to the understand the critical parameters of its injection. A lock of the geometrical injection has been foreseen, but it has not yet been implemented. In this section we give a description of the general method which was first presented in [Anderson 84]. The method takes advantage of the transverse mode of the cavity and their partial coupling when the alignment is not well realized. It would be very suitable in our astigmatic cavity were transverse direction are non degenerate and can be distinguished from each other. In the following, one consider only one transverse direction x and only the fundamental $U_0(x)$ and first transverse $U_1(x)$ modes.

It is possible to show [Anderson 84], that an injection beam $\Psi(x)$ translated by t_x compared to the optical axis can be decomposed on the eigenmodes of the cavity. At first order, one obtains:

$$\Psi(x) \approx A \left[U_0(x) + \frac{t_x}{w_0} U_1(x) \right], \quad (\text{C.1})$$

where w_0 is the waist of the cavity modes. Similarly, for a rotation θ_x , one can show:

$$\Psi(x) \approx A \left[U_0(x) + \pi i \frac{\theta_x w_0}{\lambda} U_1(x) \right]. \quad (\text{C.2})$$

If the injection beam is gaussian, a criterium to know if the injection is well realized is to minimize the injection of higher order modes while maximizing the injection of the fundamental mode. This is the standard procedure. It is actually possible to go further as will be shown in the following.

The scheme presented on figure C.1b is derivated from [Anderson 84] and allows the lock of the cavity injection. In order to create the error signal, two side bands are introduced (amplitude E_1) around the carrier frequency (amplitude E_0). These sidebands are created by a phase modulation at ν_0 , which corresponds to the frequency difference between the transverse U_0 and U_1 .

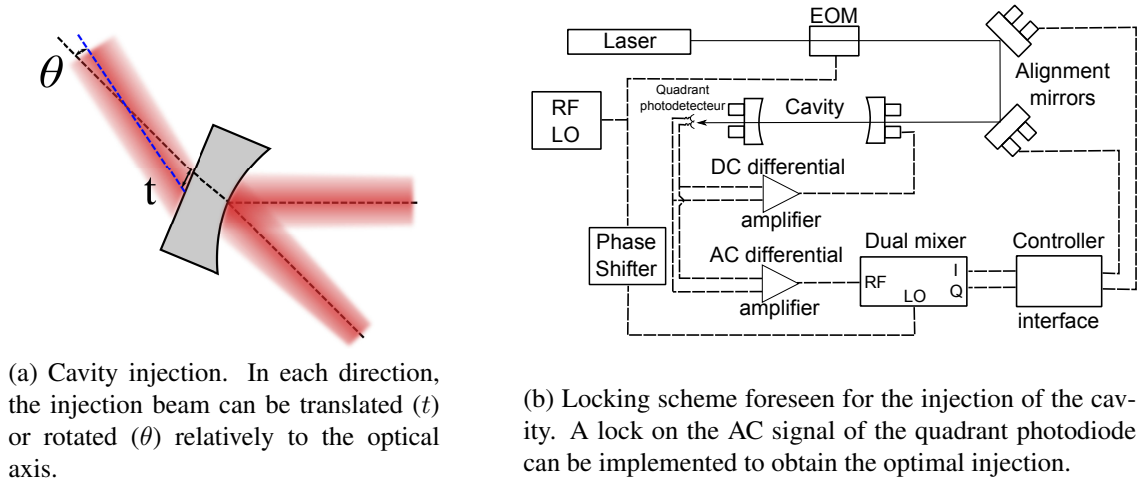
The intensity profile $I(x)$ of the beam on the quadrant detector is (??) :

$$I(x) = \|E_0 U_0(x)\|^2 + \|A_1 E_1 U_1(x)\|^2 + 2A_1 E_0 E_1 U_0(x) U_1(x) \cos(\nu_0 t + \varphi + \varphi_0), \quad (\text{C.3})$$

where

$$A_1 = \left[\left(\frac{a_x}{w_0} \right)^2 + \left(\frac{\pi \alpha_x w_0}{\lambda} \right)^2 \right]^{1/2}, \quad (\text{C.4})$$

$$\varphi = \tan^{-1} \frac{\pi \alpha_x w_0^2}{\lambda a_x}. \quad (\text{C.5})$$

Figure C.1: *Locking the alignment of the cavity.*

Alignment of the optical axis

As seen in section 3.2.3.2, displacements of cavity mirrors are changing the position of the optical axis. This could be used to overlap the optical axis with the injection beam. It is usually preferred to do the opposite, *i.e.* to align the injection on the optical axis using external mirrors. Nevertheless, it can be an advantage to move the cavity mirrors since this action can recenter the out-coupled beam on the quadrant detector and then compensate for drift of the optical axis. In that purpose, one can use the DC signal of equation C.4. Looking to the difference on the quadrants, an error signal can be obtained and used to correct the position of one mirror.

Locking the injection.

Starting from equation C.4 we want to show now that it is also possible to lock the injection direction and then obtain an optimal coupling.

To obtain such an error signal, one uses the AC part of the signal $I(x)$ (C.4). We note that U_0 and U_1 are orthogonal modes. A classical detector that would fully integrate the interference of these two fields would not measure any interference. Nevertheless, using a quadrant photodetector and subtracting the two opposites parts, one obtains a signal $V(t)$ of the form:

$$V(t) \propto A_1 E_0 E_1 \cos(\nu_0 t + \varphi + \varphi_0). \quad (\text{C.6})$$

After demodulation, the two quadratures become:

$$V_P \propto A_1 E_0 E_1 \cos(\varphi) = \frac{a_x}{w_0} E_0 E_1, \quad (\text{C.7})$$

$$V_Q \propto A_1 E_0 E_1 \sin(\varphi) = \frac{\pi \alpha_x w_0}{\lambda} E_0 E_1. \quad (\text{C.8})$$

Each quadrature shows linear dependence with the misalignment parameters. These two signals can then be employed as error signals for translation (furthest mirror) and rotation (closest mirror), for an automatic injection of the cavity.

Complete expression of the polarizability

D.1 Dipole elements

The dipolar excitation correspond to the interaction between the outer electron charge with the electric field. Under this excitation, the electron may change states and bring the atom in an excited states. Obviously this process can only happen if the initial state and the final state are overlapping through the dipolar interaction. The strength of the overlap and then of the probability of transition are given by the dipole elements [?]. To calculate these matrix elements, we use the Wigner-Eckart theorem [Igor 06, Landau 91]:

$$\langle L, I, J, F m_F | \hat{\mathbf{d}} | L', I', J', F' m'_F \rangle = \langle F m_F | e r_q | F' m'_F \rangle \quad (\text{D.1})$$

$$= \langle L, I, J, F || e r || L', I', J', F' \rangle \langle F m_F | F' 1 m'_F q \rangle \quad (\text{D.2})$$

$$= \langle L, I, J, F || e r || L', I', J', F' \rangle (-1)^{F'-1-m_F} \sqrt{2F+1} \begin{pmatrix} F' & 1 & F \\ m'_F & q & -m_F \end{pmatrix} \quad (\text{D.3})$$

$$= (-1)^{2*F'-m_F+J+I} \sqrt{(2F+1)(2F'+1)} \begin{pmatrix} F' & 1 & F \\ m'_F & q & -m_F \end{pmatrix} \left\{ \begin{matrix} J & J' & 1 \\ F' & F & I \end{matrix} \right\} (L, I, J || d || L', I', J') \quad (\text{D.4})$$

where L is the orbital angular momentum of the outer electron, I is the total nuclear angular momentum, $J = L + S$ is the total electron angular momentum with $S = 1/2$ the spin angular momentum of the electron. It result in a total atomic angular momentum $F = I + J$. Because the dipolar interaction only concern the electron that has a much lower inertia than the nucleus, the total nuclear angular momenta is conserved during the interaction, resulting in $I = I'$.

Some examples of states of ^{87}Rb used through out this manuscript are given in table ??:

State	$5S_{1/2}$	$5P_{1/2}$	$5P_{3/2}$	$4D_{3/2}$	$4D_{5/2}$
L	0	1	1	2	2
I	3/2	3/2	3/2	3/2	3/2
J	1/2	1/2	3/2	3/2	5/2
F	1,2	1,2	0,1,2,3	0,1,2,3	1,2,3,4

Table D.1: *Quantum numbers of some states*

The element $(L, I, J || d || L', I', J')$ of the Rb^{87} transition can be found in [Arora 07, Clement 08]. They are their expressed in units of ea_0 where e is the unitary charge and $a_0 = 4\pi\epsilon_0\hbar^2/(m_e e^2) = 52.910^{-12}m$ the bohr radius.

D.2 Dipolar electric interaction: complete expression of the polarizability

The atomic polarizability expresses the overall atom light interaction for an Electric-dipole hamiltonian. Once it has been properly calculated, it becomes then straight forward to calculate the atomic AC Stark shift or the optical phase shift induced on a beam. Even spontaneous emission processes can be accounted for if decoherence processes are taken into account.

A fully quantized picture can be developed to express the atomic polarizability [Stockton 05]. Nevertheless, to take into account decoherence processes in this frame, it obliges to involve master equation in the Lindblad form to describe the non-unitary evolution of the density matrix ρ . This makes the calculation and the interpretation quite complex while a semi-classical picture of an electron elastically linked to the nucleus gives similar result.

In the following, we intend to derive a complete expression for the polarizability that takes into account down to the hyperfine splitting. The result obtained in equation D.20 is used in the manuscript for two different limit:

- The excitation by a very far off resonance excitation at 1560 nm, that realize a dipole trap.
- A far but closer to resonance excitation at 780 nm that is in the context of dispersive non-demolition measurement.

Remark:

In the context of far off resonance excitation, a very elegant method to derive the polarizability consists to consider the operator V_{EE} ([Schmieder 72]):

$$V_{EE} = \sum_{F'', m''} \hat{\mathbf{d}} |F'', m''\rangle \langle F'', m''| \hat{\mathbf{d}} \quad (\text{D.5})$$

This operator describes the second order expansion of the atomic states energy under the (small) perturbation of the dipolar interaction. The calculation of the different elements $\langle F, m | V_{EE} | F', m' \rangle$ is developed in [Schmieder 72] and rely on the precise analysis of the symmetry of the spherical harmonics. From there, the authors expresses the dipolar elements as a function of the $\{3J\}$ and $\{6J\}$ coefficient.

$$\langle F, m | V_{EE} | F', m' \rangle = -\frac{1}{2}\alpha_0(\omega)\delta_{F,F'}\delta_{m,m'} - \frac{1}{2}\alpha_2(\omega)Q_{FF' mm'} \quad (\text{D.6})$$

where α_0 and α_2 are the scalar and the tensorial polarizabilities given in [Safronova 06, Arora 07]. The tensorial element $Q_{FF' mm'}$ is given by:

$$Q_{FF' mm'} = \sqrt{\frac{15}{2}} \sqrt{\frac{(J+1)(2J+1)(2J+3)}{J(2J-1)}} \sum_{q, \eta_\mu, \eta_{\mu'}} \begin{pmatrix} 1 & 2 & 1 \\ \mu & -q & -\mu' \end{pmatrix} (-1)^{I+J+F+F'-m'} \sqrt{(2F+1)(2F'+1)} \begin{pmatrix} F & 2 & F' \\ m & q & -m' \end{pmatrix} \left\{ \begin{matrix} F & 2 & F' \\ J & I & J \end{matrix} \right\} \quad (\text{D.7})$$

Unfortunately, this method relies on the calculation of the scalar and tensorial polarizabilities which are usually expressed without taking into account the hyperfine splitting. Therefore, in the case of close to resonance excitation (\sim GHz) where the hyperfine splitting cannot be neglected, this is not applicable.

As a consequence, the polarizability is derived in the following by summing over all the possible hyperfine transition. Before we express the semi-classical expression of the polarizability, we show at first the frequency dependance of the interaction.

Classical expression of the forced oscillation of an electron

In order to express the polarizability from the dipole elements, let's consider first the simple model of an electron (mass m and charge e) elastically linked to the nucleus [Aspect 06].

We consider an electric field $\mathbf{E} = \mathcal{E}_0 \cos(\omega t) \mathbf{e}$, where \mathcal{E}_0 is the amplitude of the oscillation and \mathbf{e} is the polarization of the field. In the basis of the angular momenta, the light polarisation is $\mathbf{e} = (e_1, e_0, e_{-1})$ where the angular basis is:

$$\mathbf{u}_1 = \frac{-1}{\sqrt{2}} (\mathbf{u}_x + i\mathbf{u}_y) \quad (\text{D.8})$$

$$\mathbf{u}_0 = \mathbf{u}_z \quad (\text{D.9})$$

$$\mathbf{u}_{-1} = \frac{1}{\sqrt{2}} (\mathbf{u}_x - i\mathbf{u}_y) \quad (\text{D.10})$$

The force that generates this electric field on the electron is $e\mathbf{E}$. The position r of the electron obeys the differential equation [Aspect 06]:

$$m\ddot{r} + m\omega_0^2 r - 2/3 \frac{ma_0}{c} \ddot{r} = e\mathcal{E}_0 \cos(\omega t) \quad (\text{D.11})$$

where $m\omega_0^2 r$ is the force of the spring that link the electron to the nucleus and $2/3 \frac{ma_0}{c} \ddot{r}$ is the friction force due to the energy loss issued from the radiation of the oscillating electron. This last terms describe a loss of mechanical energy that exactly matches the radiated energy. Thus preserving the conservation of energy. $a_0 = e^2/(4\pi\epsilon_0 mc^2)$ is the classical radius of the electron.

Looking for a solution, of the movement of the electron in the form:

$$r = s_0 \exp(-\Gamma_{cl}t/2) * \cos(\omega_0 t), \quad (\text{D.12})$$

one can show that the complex amplitude s_0 must satisfy:

$$s_0 = \frac{qE_0}{m} \frac{1}{\omega_0^2 - \omega^2 + i\frac{\Gamma_{cl}\omega^3}{\omega_0^2}}. \quad (\text{D.13})$$

The classical polarizability α_{cl} is defined by its relation to the electric dipole p :

$$\mathbf{p} = e\mathbf{r} = \alpha_{cl}\mathbf{E} \quad (\text{D.14})$$

The previous calculation leads to:

$$\alpha = \frac{e^2}{m} \frac{1}{\omega_0^2 - \omega^2 + i\frac{\Gamma_{cl}\omega^3}{\omega_0^2}}. \quad (\text{D.15})$$

The frequency dependance of the polarizability scales then as:

$$\frac{1}{\omega_0^2 - \omega^2 + i\frac{\Gamma_{cl}\omega^3}{\omega_0^2}} \underset{\omega \sim \omega_0}{\approx} \frac{1}{2\omega_0} \frac{\Delta + i\gamma}{\Delta^2 + \gamma^2}. \quad (\text{D.16})$$

where $\Delta E = \hbar\omega_0$ is the energy splitting of the transition considered.

Semi-classical expression of the polarizability

For a sinusoidal perturbation such as the one created by an electro-magnetic field, the perturbation theory leads us to an energy shift of the state k :

$$\Delta E_k = \frac{1}{2} \alpha_k \mathcal{E}_{\text{eff}}^2 = \frac{1}{4} \alpha_k \mathcal{E}_0^2 \quad (\text{D.17})$$

where the atomic polarizability is given by [Grimm 00]:

$$\alpha_k = \frac{2}{\hbar} \sum_{\nu} \frac{\left| \langle \nu | \hat{\mathbf{d}} \cdot \mathbf{e} | k \rangle \right|^2 (\omega_k - \omega_{\nu})}{(\omega_k - \omega_{\nu})^2 - \omega^2} \quad (\text{D.18})$$

The summation is performed over ν which scan all the atomic state that have an overlap with k through the dipolar operator.

The expression D.19 of α_k does only account for coherent processes. In the previous section, we have introduced energy loss of the atoms through the radiation of the atoms. This can be taken into account by a dissipative term in the polarizability (complex term) in the form:

$$\alpha_k = \frac{2}{\hbar} \sum_{\nu} \frac{\left| \langle \nu | \hat{\mathbf{d}} \cdot \mathbf{e} | k \rangle \right|^2 (\omega_k - \omega_{\nu})}{(\omega_k - \omega_{\nu})^2 - \omega^2 + i\Gamma \frac{\omega^3}{\omega_0^2}} \quad (\text{D.19})$$

In the precise case of the hyperfine state, $|L, I, J, F, m_F\rangle$, the atomic polarizability is:

$$\alpha_{L,I,J,F,m_F} = \frac{2}{\hbar} \sum_{L',I',J',F',m'_F,q} \frac{\left| \langle L', I', J', F', m'_F | \hat{d}_q \cdot \mathbf{e}_q | L, I, J, F, m_F \rangle \right|^2 \Delta\omega_{F,F'}}{\Delta\omega_{F,F'}^2 - \omega^2 + i\Gamma \frac{\omega^3}{\omega_0^2}} \quad (\text{D.20})$$

The calculation of the dipole elements $\langle L', I', J', F', m'_F | \hat{d}_q \cdot \mathbf{e}_q | L, I, J, F, m_F \rangle$ has been given in annexe D.1.

Theory calculation

In this appendix, we detail some of the calculation that were eluded in chapter 5. The first concerns the derivation of the Gaussian approximation in equation 5.102. The second gives two useful identities to treat the problem of losses (equation 5.121) and the last describes the quantum description of the single photon frequency splitter (section 5.3.5.1).

E.1 The Gaussian approximation of the Mach Zehnder interferometer

To derive the Gaussian approximation of the squeezing function $|\mathcal{F}_{N_u, N_v}(n)|^2$, we proceed to the Taylor expansion as described in equations 5.98 and 5.98. The first momenta (mean value) is obtained after first differentiation of $|\mathcal{F}_{N_u, N_v}(n)|^2$:

$$\frac{d}{dn} |\mathcal{F}_{N_u, N_v}(n)|^2 = 0 \quad (\text{E.1})$$

$$\begin{aligned} & \propto \sin \Phi(n) \cos \Phi(n) [(1 - \mathcal{C}) \cos^2 \Phi(n) + (1 + \mathcal{C}) \sin^2 \Phi(n)]^{N_u-1} \\ & \times [\mathcal{C} \cos^2 \Phi(n)]^{N_v-1} \mathcal{C} [(N_v + 2N_u)\mathcal{C} - N_v] \cos^2 \Phi(n) - N_v(1 + \mathcal{C}) \sin^2 \Phi(n) \end{aligned} \quad (\text{E.2})$$

where $\Phi(n) = \phi n/2 - \pi/4$.

The distribution is then centered in n_0 which verifies:

$$\tan^2 \Phi(n_0) = \frac{(N_v + 2N_u)\mathcal{C} - N_v}{N_v(1 + \mathcal{C})} \quad (\text{E.3})$$

To obtain the second momenta (variance) of the distribution, one needs to evaluate the second derivative of $|\mathcal{F}_{N_u, N_v}(n)|^2$ in n_0 :

$$\left| \frac{d^2}{dn^2} |\mathcal{F}_{N_u, N_v}(n)|^2 \right|_{n_0} = -4 |\mathcal{F}_{N_u-1, N_v-1}(n_0)|^2 \sin^2 \Phi(n_0) \cos^2 \Phi(n_0) \phi^2 N_p \mathcal{C}^2 \quad (\text{E.4})$$

$$\approx -|\mathcal{F}_{N_u, N_v}(n_0)|^2 \phi^2 N_p \mathcal{C}^2 \quad (\text{E.5})$$

E.2 Losses

For the calculation of equation 5.121, on the consequence of losses in the Mach Zehnder, we have used the following identities of the hyperbolic function:

$$\left| \sinh(i\Phi' - \frac{1}{4} \ln(1 - \eta)) \right|^2 = \frac{1}{2} \left(\frac{1}{2} (\sqrt{1 - \eta} + \frac{1}{\sqrt{1 - \eta}}) - \cos(\Phi n - \frac{\pi}{2}) \right) \quad (\text{E.6})$$

$$= \frac{1}{2} \left(\frac{2 - \eta}{2\sqrt{1 - \eta}} + \sin(\Phi n) \right) \quad (\text{E.7})$$

$$\left| \cosh(i\Phi' - \frac{1}{4} \ln(1 - \eta)) \right|^2 = \frac{1}{2} \left(\frac{2 - \eta}{2\sqrt{1 - \eta}} - \sin(\phi n) \right) \quad (\text{E.8})$$

E.3 Frequency splitter

To describe the heterodyne measurement of single photons, a clear understanding of the effect of a phase or frequency modulation on a single photon wavefunction is needed. We consider in the following the case of a single sideband modulator, that mixes the mode a_0 and a_1 . The hamiltonian which describe the transfer of photons from one mode to the other is:

$$\mathcal{H} = i\hbar g (a_m^\dagger a_0^\dagger a_1 - a_m a_0 a_1^\dagger) \quad (\text{E.9})$$

The energy difference between the two modes is transferred to the RF field.

Such a Hamiltonian clearly couples the mode a_0 and a_1 . As on a beam splitter, the - sign in the hamiltonian guarantees the conservation of energy.

The evolution of the state $|\Psi_{\text{in}}\rangle$ is given by:

$$|\Psi_{\text{out}}\rangle = e^{i\frac{\mathcal{H}t'}{\hbar}} |\Psi_{\text{in}}\rangle \quad (\text{E.10})$$

where t' is the interaction time.

We consider a coherent states on the RF field and a single photon that can be either in a_0 or a_1 . Using the identities given at the end of the section, we have for an input state $|\Psi_{\text{in}}\rangle = |\alpha_m\rangle \otimes |1_0, 0_1\rangle$:

$$\begin{aligned} |\Psi_{\text{out}}\rangle &= \sum_{k=0}^{\infty} \frac{(gt')^{2k}}{(2k)!} (a_m^\dagger a_0^\dagger a_1 - a_m a_0 a_1^\dagger)^{2k} (|\alpha_m\rangle \otimes |1_0, 0_1\rangle) \\ &\quad + \sum_{k=0}^{\infty} -\frac{(gt')^{2k+1}}{(2k+1)!} (a_m^\dagger a_0^\dagger a_1 - a_m a_0 a_1^\dagger)^{2k+1} (|\alpha_m\rangle \otimes |1_0, 0_1\rangle) \end{aligned} \quad (\text{E.11})$$

$$\begin{aligned} &= \sum_{k=0}^{\infty} \frac{(-1)^k (gt' \alpha_m)^{2k}}{(2k)!} (|\alpha_m\rangle \otimes |1_0, 0_1\rangle) \\ &\quad + \sum_{k=0}^{\infty} \frac{(-1)^k (gt' \alpha_m)^{2k+1}}{(2k+1)!} (|\alpha_m\rangle \otimes |0_0, 1_1\rangle) \end{aligned} \quad (\text{E.12})$$

$$|\Psi_{\text{out}}\rangle = \cos(\alpha_m gt') (|\alpha_m\rangle \otimes |1_0, 0_1\rangle) + \sin(\alpha_m gt') (|\alpha_m\rangle \otimes |0_0, 1_1\rangle) \quad (\text{E.13})$$

For $|\Psi_{\text{in}}\rangle = |\alpha_m\rangle \otimes |1_0, 0_1\rangle$, the same calculation leads to:

$$|\Psi_{\text{out}}\rangle = \cos(\alpha_m gt') (|\alpha_m\rangle \otimes |0_0, 1_1\rangle) - \sin(\alpha_m gt') (|\alpha_m\rangle \otimes |1_0, 0_1\rangle) \quad (\text{E.14})$$

The phase modulator is then exactly a frequency splitter which follows the splitting matrix B :

$$B = \begin{pmatrix} \cos(\alpha_m g t') & \sin(\alpha_m g t') \\ -\sin(\alpha_m g t') & \cos(\alpha_m g t') \end{pmatrix} \quad (\text{E.15})$$

This matrix takes only into account for the amplitude of coupling between the two modes but forget about their frequency shift. Thus, the full frequency beam splitter matrix can be rewritten as:

$$\begin{pmatrix} a'_0 \\ a'_1 e^{i\Omega t} \end{pmatrix} = \begin{pmatrix} \cos(\alpha_m g t') & \sin(\alpha_m g t') e^{-i\Omega t} \\ -\sin(\alpha_m g t') e^{i\Omega t} & \cos(\alpha_m g t') \end{pmatrix} \begin{pmatrix} a_0 \\ a_1 e^{i\Omega t} \end{pmatrix} \quad (\text{E.16})$$

In the following, we will use simplified notation for the beam splitter matrix using $\sqrt{T} = \cos(\alpha_m g t')$ and $\sqrt{R} = \sin(\alpha_m g t')$, which gives:

$$\begin{pmatrix} a'_0 \\ a'_1 e^{i\Omega t} \end{pmatrix} = \begin{pmatrix} \sqrt{T} & \sqrt{R} e^{-i\Omega t} \\ -\sqrt{R} e^{i\Omega t} & \sqrt{T} \end{pmatrix} \begin{pmatrix} a_0 \\ a_1 e^{i\Omega t} \end{pmatrix} \quad (\text{E.17})$$

In conclusion, the beam splitter creates a superposition of the two modes which beat together on the photodetector as depicted in figure 5.15.

Useful identities For the calculation, in equations E.11 and E.13, we have used the following identities for $|1_0, 0_1\rangle$:

$$\begin{aligned} (a_m^\dagger a_0^\dagger a_1 - a_m a_0 a_1^\dagger)^{2k} (|\alpha_m\rangle \otimes |1_0, 0_1\rangle) &= (-1)^k |\alpha_m|^{2k} a_0^\dagger a_1 a_0 a_1^\dagger (|\alpha_m\rangle \otimes |1_0, 0_1\rangle) \\ &= (-1)^k |\alpha_m|^{2k} (|\alpha_m\rangle \otimes |1_0, 0_1\rangle) \end{aligned} \quad (\text{E.18})$$

$$\begin{aligned} (a_m^\dagger a_0^\dagger a_1 - a_m a_0 a_1^\dagger)^{2k+1} (|\alpha_m\rangle \otimes |1_0, 0_1\rangle) &= (-1)^{k+1} |\alpha_m|^{2k+1} a_0 a_1^\dagger (|\alpha_m\rangle \otimes |1_0, 0_1\rangle) \\ &= (-1)^{k+1} |\alpha_m|^{2k+1} (|\alpha_m\rangle \otimes |0_0, 1_1\rangle) \end{aligned} \quad (\text{E.19})$$

and for $|0_0, 1_1\rangle$:

$$(a_m^\dagger a_0^\dagger a_1 - a_m a_0 a_1^\dagger)^{2k} (|\alpha_m\rangle \otimes |0_0, 1_1\rangle) = (-1)^k |\alpha_m|^{2k} (|\alpha_m\rangle \otimes |0_0, 1_1\rangle) \quad (\text{E.20})$$

$$(a_m^\dagger a_0^\dagger a_1 - a_m a_0 a_1^\dagger)^{2k+1} (|\alpha_m\rangle \otimes |0_0, 1_1\rangle) = (-1)^k |\alpha_m|^{2k+1} (|\alpha_m\rangle \otimes |1_0, 0_1\rangle) \quad (\text{E.21})$$

CQED and classical definitions

In this appendix, our goal is to show the equivalence between the Cavity Quantum Electrodynamics (CQED) definition of the cavity frequency shift and the shift that arise from our definition of the effective single pass phase introduced in section 6.1.6.

In Cavity Quantum Electro-Dynamics (CQED) experiment, the strength of the coupling between the atom and the cavity field of a Fabry-Perot resonator is described by the single photon Rabi frequency of an atom placed at a maximum of the electric field:

$$g = \sqrt{\frac{\omega}{2\hbar V_{\text{mode}} \epsilon_0}} \langle e | \hat{\mathbf{d}} \cdot \mathbf{e} | g \rangle, \quad (\text{F.1})$$

and the volume of the mode for a Fabry Perot cavity is given by:

$$V_{\text{mode}} = \frac{1}{|E_0|^2} \iiint |E(\mathbf{r})|^2 d^3r \approx \frac{\pi}{4} w_{\text{ph}}^2 L, \quad (\text{F.2})$$

where the electric field is:

$$\mathbf{E}(\mathbf{r}) = E_0 \cos(\mathbf{k} \cdot \mathbf{z}) \exp\left(-\frac{x^2 + y^2}{w_{\text{ph}}^2}\right) \mathbf{e} \quad (\text{F.3})$$

The frequency shift of the cavity is:

$$\Delta\omega_{\text{CQED}} = N_{\text{at}} \frac{g^2}{\Delta} = 2N_{\text{at}} \frac{\omega}{\hbar\epsilon_0 L} \left| \langle e | \hat{\mathbf{d}} \cdot \mathbf{e} | g \rangle \right|^2 \quad (\text{F.4})$$

In section 6.1.6, we have shown that the classical phase shift acquired by a Gaussian beam was:

$$\Phi_{\text{det}} = \frac{\omega}{\hbar\epsilon_0 c} \frac{1}{w_{\text{ph}}^2} N_{\text{at}} \left| \langle e | \hat{\mathbf{d}} | g \rangle \right|^2 \frac{1}{\Delta} \quad (\text{F.5})$$

where it is assumed that the atoms stand at the center of the beam.

For the Fabry-Perot resonator considered, the phase is accumulated twice per turn, and a phase of 2π corresponds to a cavity frequency shift of one FSR. Hence the classical frequency shift is:

$$\Delta\omega_{\text{Cl}} = \frac{2\Phi_{\text{det}}}{2\pi} \frac{c}{2L} = N_{\text{at}} \frac{\omega}{\hbar\epsilon_0 L} \left| \langle e | \hat{\mathbf{d}} \cdot \mathbf{e} | g \rangle \right|^2 = \frac{\Delta\omega_{\text{CQED}}}{2} \quad (\text{F.6})$$

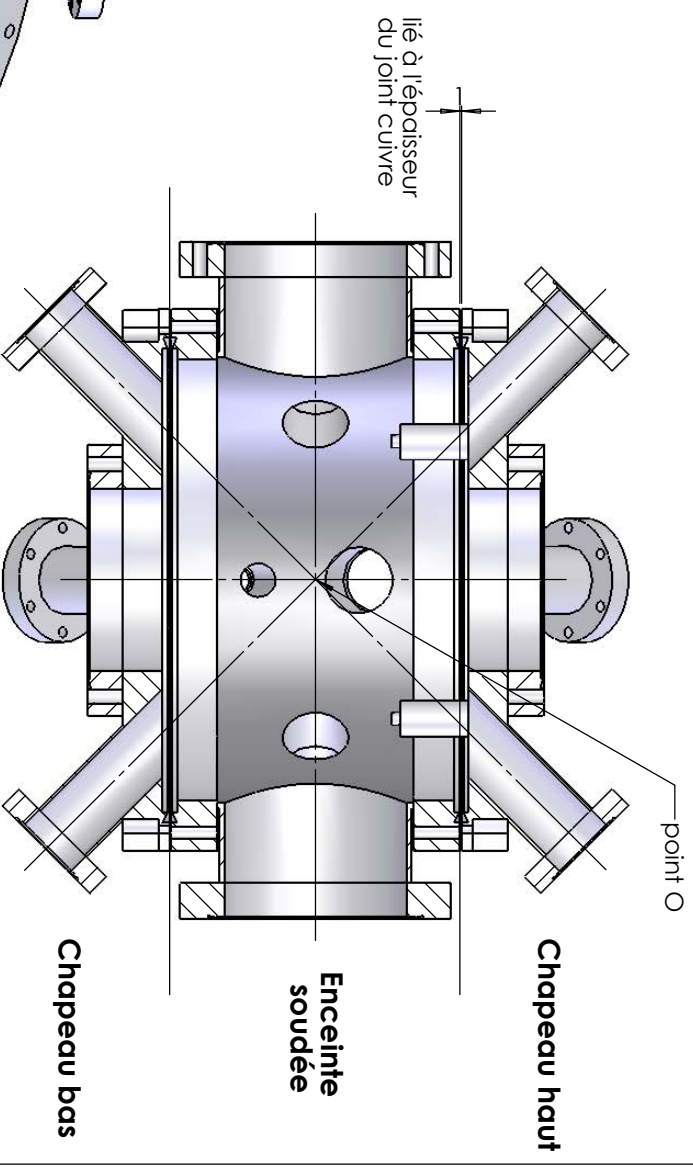
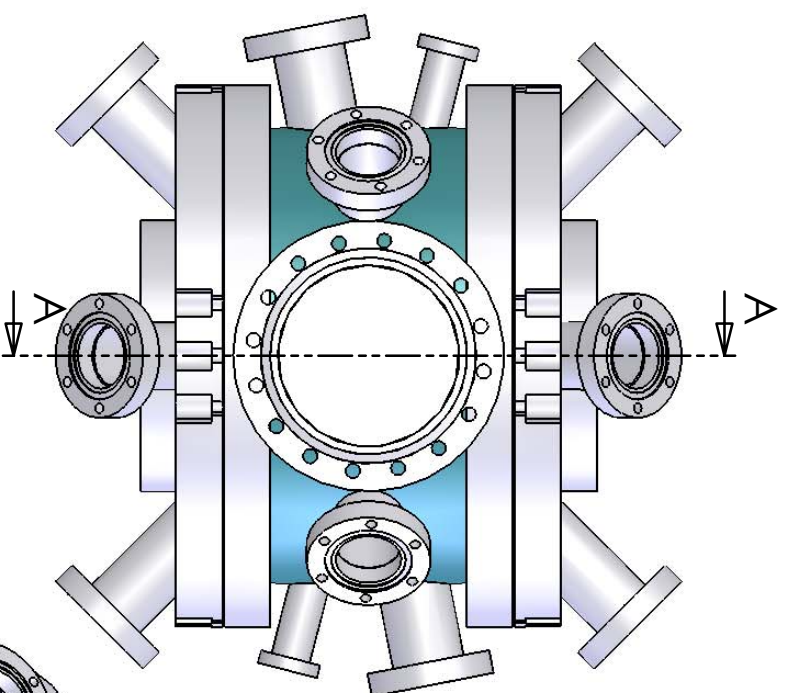
This results shows that the description of an effective phase on the beam takes well into account for the dilution of the photon into the mode. Nevertheless there is still a factor 1/2 difference between the two descriptions. This factor is the consequence of the standing wave in the cavity that is not taken into account in the classical description where the forward and the backward field are described as two independent propagating field. Indeed, in the CQED description, we placed the atoms at a node of the standing wave and the mode volume was then divided by two.

APPENDIX G

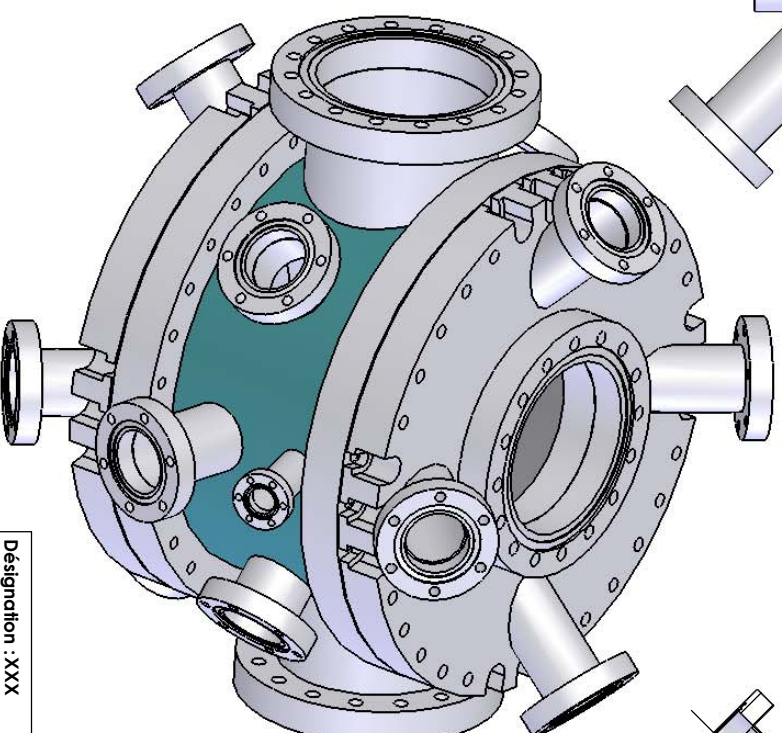
Mechanical design

In this appendix, we give the mechanical drawings of the chamber that should be helpful if latter modification of the under-vacuum set-up were to be realized. This design and the drawing were realized in close collaboration with the Syrte-Observatoire de Paris, and particularly with David Holleville who very much helped us for all the design.

Tous les axes concourant au point O



COUPE A-A
ECHELLE 1 : 3



Enceinte soudée

- 2 brides CF250
- 2 manchon CF100
- 6 manchons CF40 à bride tournante
- 2 manchons CF 16 à bride tournante

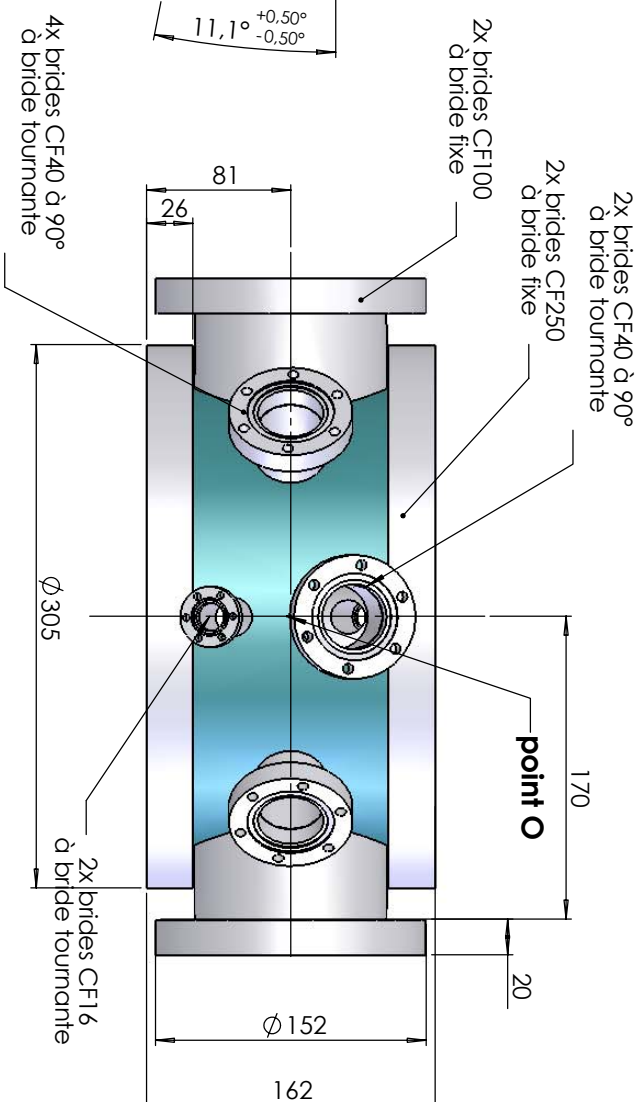
Chapeau haut





- 1 bride CF250 modifiée haut (suivant plan)
- 1 bride CF100
- 4 manchons CF40 à bride tournante
- 4 tiges soudées

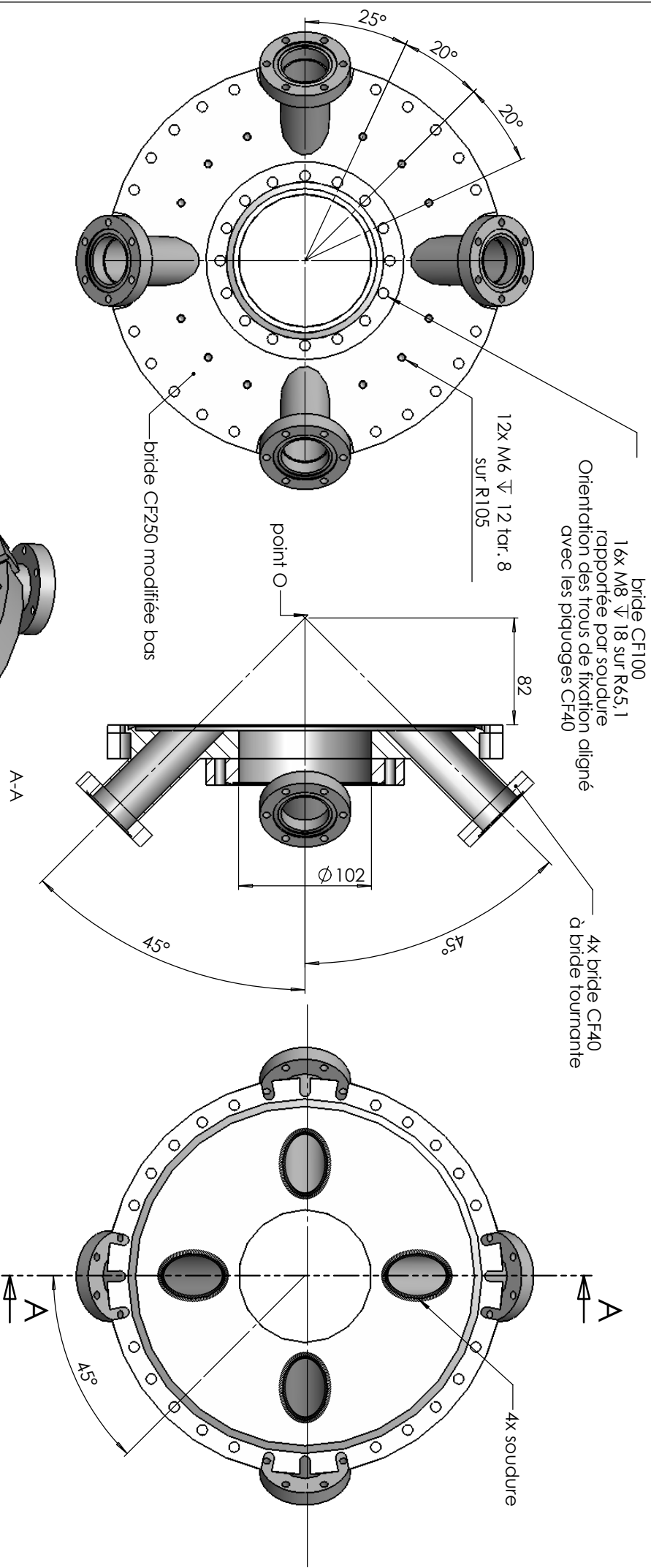
Chapeau bas

- 1 bride CF250 modifiée bas (suivant plan)
- 1 bride CF100
- 4 manchons CF40 à bride tournante

Désignation : XXX		Tol. gén. : js13js13	Qté : X
Monip : XXX	Matériau : XXX	unité : mm, degré	⊗
Référence : XXX	Date de création : 06/12/2007	Page : 1 / 1	Echelle 1:2
Nom du fichier : H:\Dovidi\boulot\Maripis\Biao\ Enceinte CF250_0\gamelle			
Dernière modif : Jeudi 6 décembre 2007 00:23:53			
David Holleville		tel : 01 40 51 23 89	
		fax : 01 43 25 55 42	
		SYRTE / CNRS UMR 8630	
		Observatoire de Paris	
		61 avenue de l'Observatoire 75014 Paris	
		mail : davidholleville@obspm.fr	

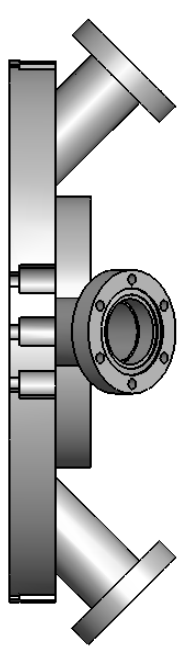
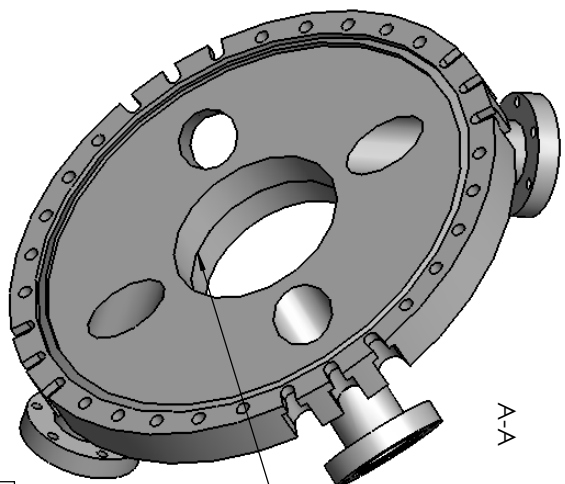
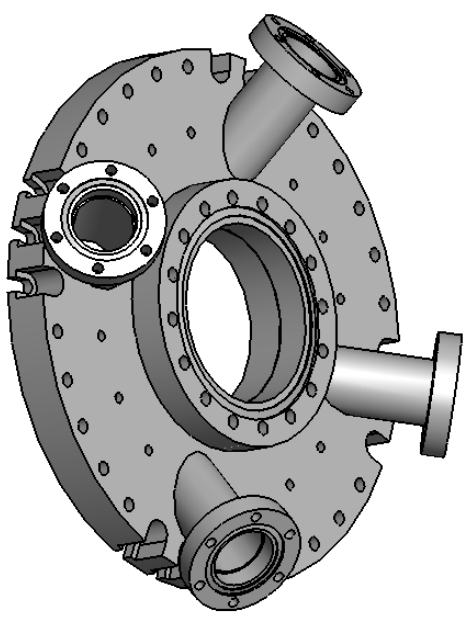


Désignation : Enciente soudée		Tol. gén. : J5 J3 J13	Qté : 1
Marque : BIA RO	Matériau : inox 316L	unité : mm, degré 	
Référence : XXX	Date de création : 06/12/2007	Page : 1 / 1	Echelle 1:3
Nom du fichier : H:\Dowell\boulot\Maripas Vigoro_Enciente CP250_0_venciente soudée Dernier modif. : jeudi 6 décembre 2007 01:05:26			
 		David Holleville tél. 01 40 51 23 88 fax 01 40 51 25 42 SYRTE / CNRS UMR 8630 Observatoire de Paris 61 avenue de l'Observatoire 75014 Paris mail : david.holleville@obspm.fr	

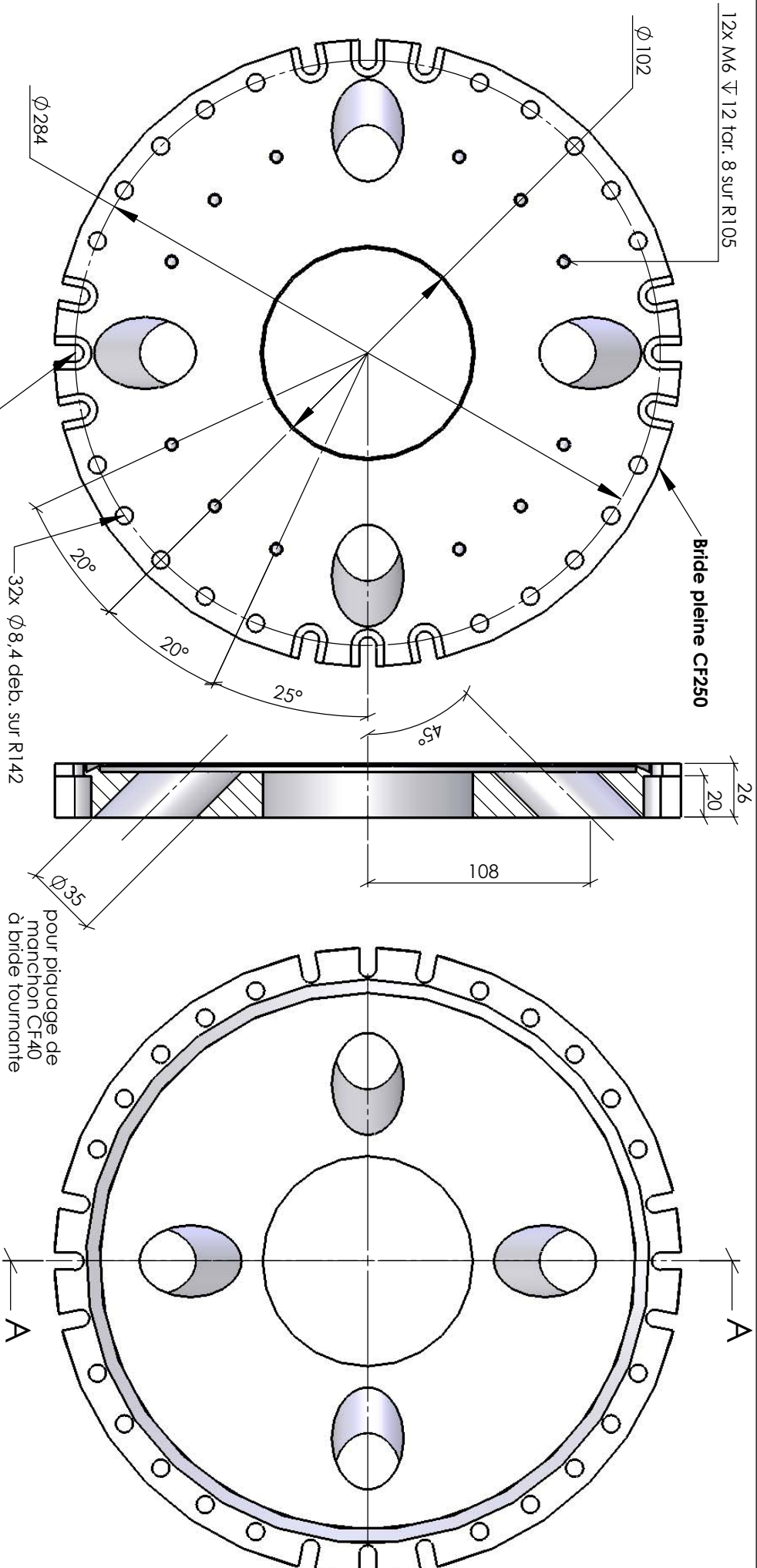



IMPORTANT :
Toutes les soudures à l'intérieur
toutes les brides avec couteau pour joint cuivre
aucune incrustation magnétique

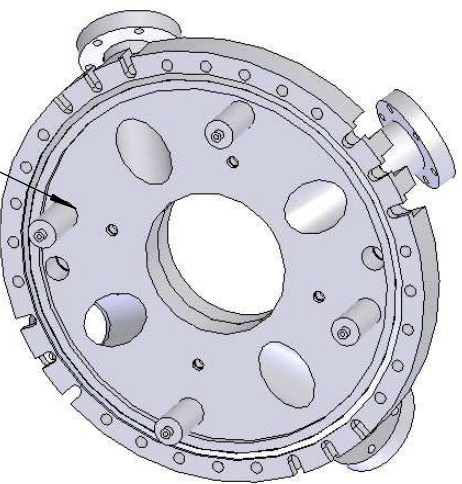
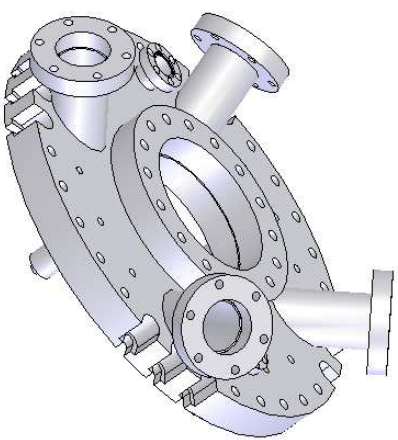
soudure



Désignation : Chapeau bas			Tol. gén. : js13js13	Qté : 2
Manip : BIARO	Matériau : Inox 316L	unité : mm, degré		
Référence : XXX	Date de création : 06/12/2007	Page : 1 / 1	Echelle 1:3	
Nom du fichier : H:\David\Boulou\Manips\Biaro\Encerinte CF250_0\bas\bride CF250 5 entree\2007\163754				
Dernière modif : jeudi 6 décembre 2007 16:37:54				
David Holleville			tel : 01 40 51 23 89	
			fax : 01 43 25 55 42	
			SYRTE / CNRS UMR 8630	
			Observatoire de Paris	
			61 avenue de l'Observatoire 75014 Paris	
			mail : davidholleville@obspm.fr	

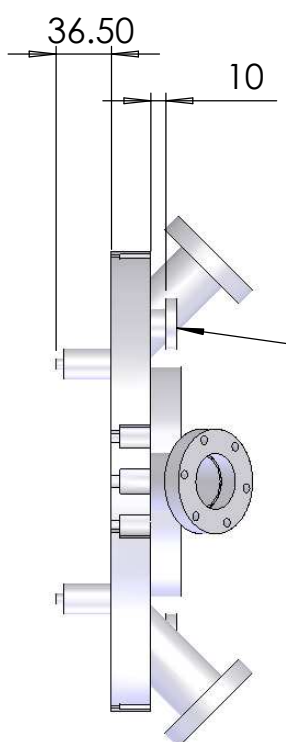


Désignation : Bride CF250 modifiée bas			
Monip : BIARO	Matériau : Inox 316L	Tol. gén. : Jst 3-jst 3	Qté : 2
Référence : XXX	Date de création : 06/12/2007	unité : mm, degré	Page : 1 / 1
Nom du fichier : H:\David\Boulon Manips\Biaro\Encerinte CF250_0\bas\CF250_top		Echelle 2:1	
Dernière modif : Jeudi 6 décembre 2007 17:30:41			
			
David Holleville tel : 01 40 51 23 89 fax : 01 43 25 55 42 SYRTE / CNRS UMR 8630 Observatoire de Paris 61 avenue de l'Observatoire 75014 Paris mail : davidholleville@obspm.fr			



4 x soudures étanches

2 x CF 16 à 180°
sur R = 115

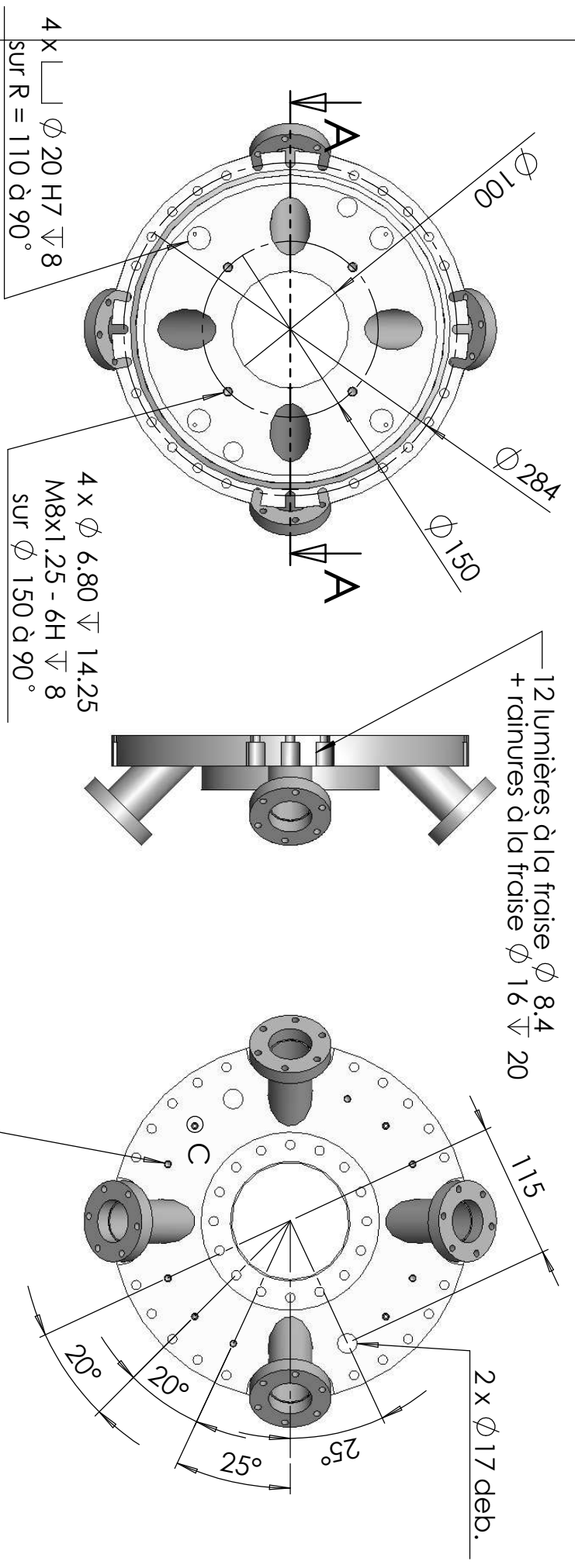


- Toutes soudures intérieures
- Soudures sans incrustation magnétique

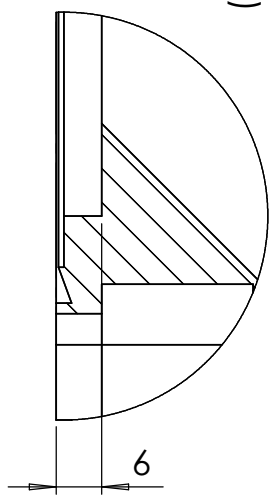
Désignation : chapeau haut	Tol. gén. : js13-j5-13	Qté : 1
Manip : BIARCO	Matériau : inox 316 L	unité : mm, degré
Référence : XXX	Dernière modif. : 2/16/2009	Page : 1 / 3
Nom du fichier : D:\Simon\ Dessin \Encointe CF250\ bride CF250 top_new	Echelle : 1:5	
Date de création : Monday, February 16, 2009 4:25:49 PM		

Bernon Simon

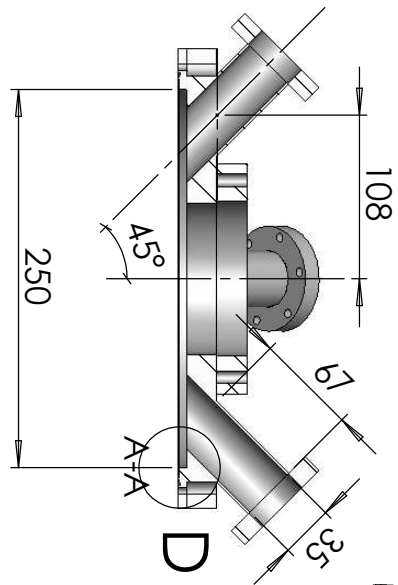
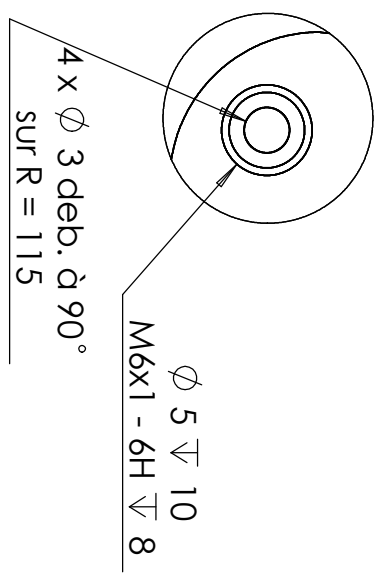
Tel : 01 64 53 33 23
Fax : 01 64 53 31 01
Institut d'optique
Laboratoire Charles Fabry
Groupe d'Optique Atomique
91 127 Palaiseau
mail : simon.bernon@institutoptique.fr



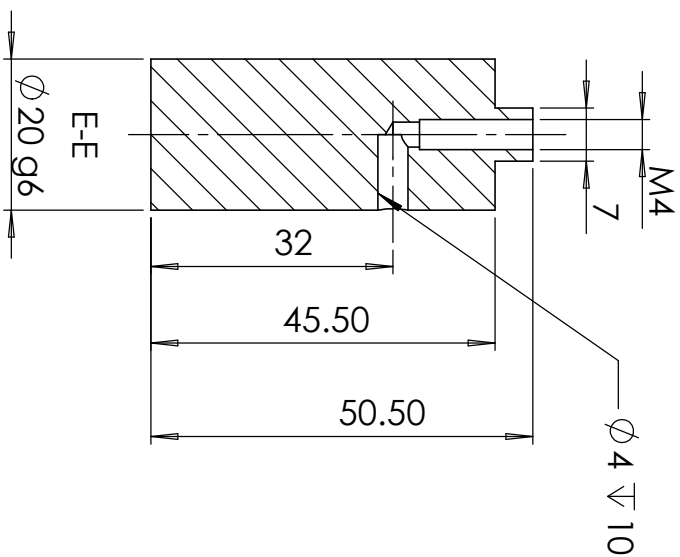
D (1 : 1)



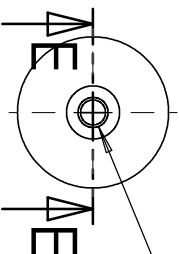
C (2 : 1)



Désignation : Chapeau haut sans CF16 et pions	Tol. gén. : Js13-j5-13	Qté : 1
Manip : BIARCO	Matériau : Inox 316L	Unité : mm, degré
Référence : XXX	Dernière modif. : 2/16/2009	Page : 2 / 3
Echelle : 1:5		
Nom du fichier : D:\Simon\ Dessin \Venceinte CF250\ bride CF250 top_new		
Date de création : Monday, February 16, 2009 4:25:49 PM		
Bernon Simon Tel : 01 64 53 33 23 Fax : 01 64 53 31 01 Institut d'optique Laboratoire Charles Fabry Groupe d'Optique Atomique 91 127 Palaiseau mail : simon.bernon@institutoptique.fr		

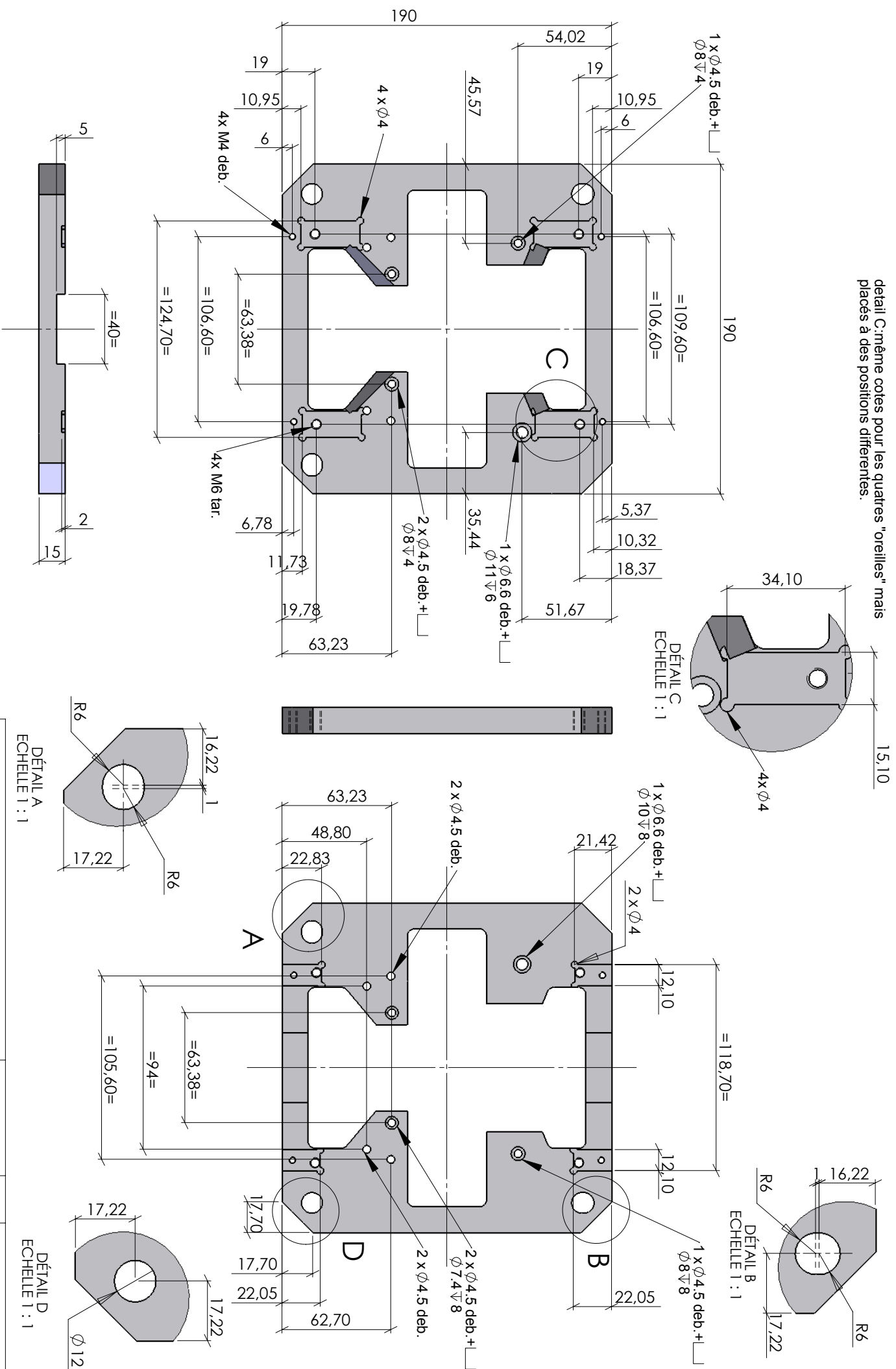


$\varnothing 3.30 \pm 18.50$
 $M4 \times 0.7 - 6H \pm 15$



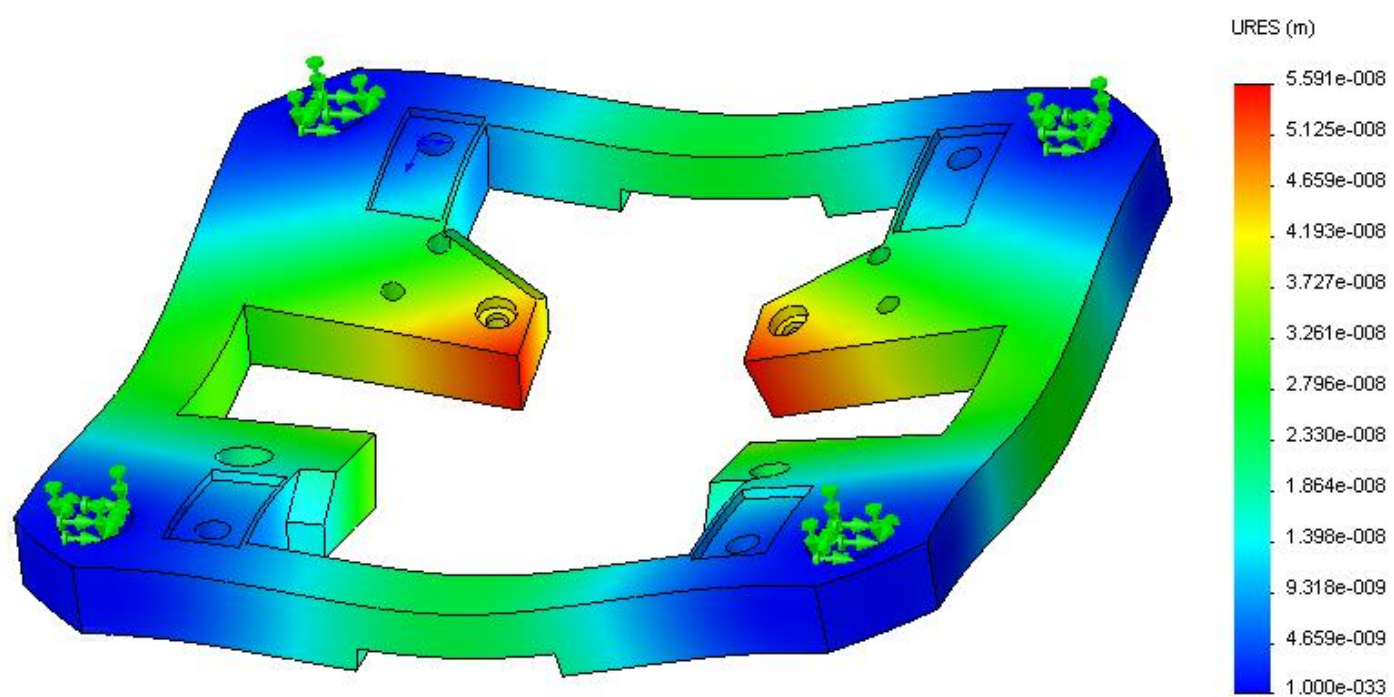
Désignation : Pion à souder	Tol. gén. : Js13-j5-13	Qté : 4
Manip : BLARCO	Matériau : Inox 316L	Unité : mm, degré
Référence : XXX	Dernière modif. : 2/16/2009	Page : 3 / 3
Nom du fichier : D:\Simon\ Dessin \Encointe CF250\ bride CF250 top_new	Echelle : 1:1	
Date de création : Monday, February 16, 2009 4:25:49 PM		
Bernon Simon Tel : 01 64 53 33 23 Fax : 01 64 53 31 01 Institut d'optique Laboratoire Charles Fabry Groupe d'Optique Atomique 91 127 Palaiseau mail : simon.bernon@institutoptique.fr		

détail C: même cotes pour les quatres "oreilles" mais placés à des positions différentes.

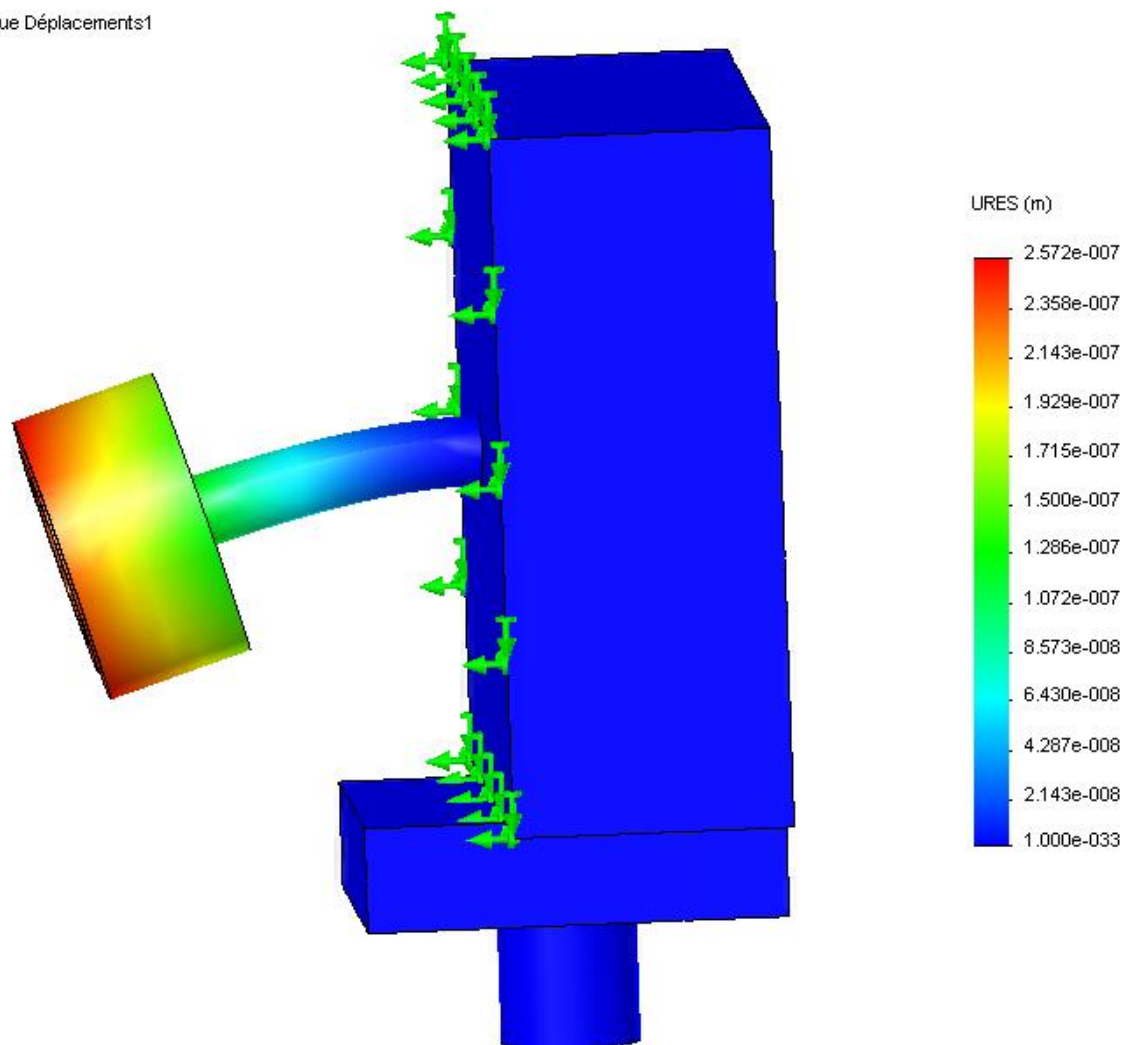


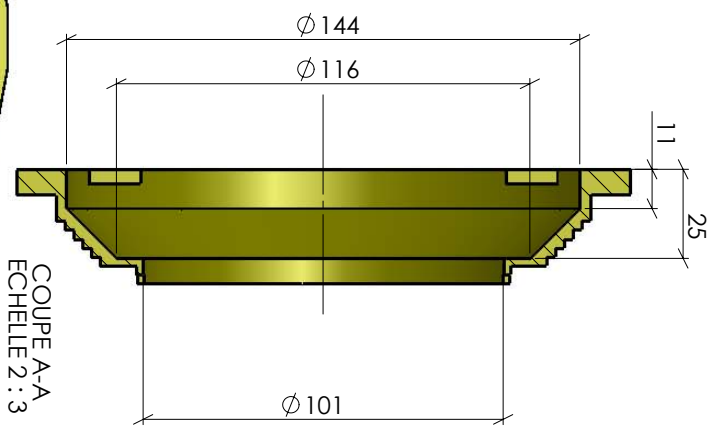
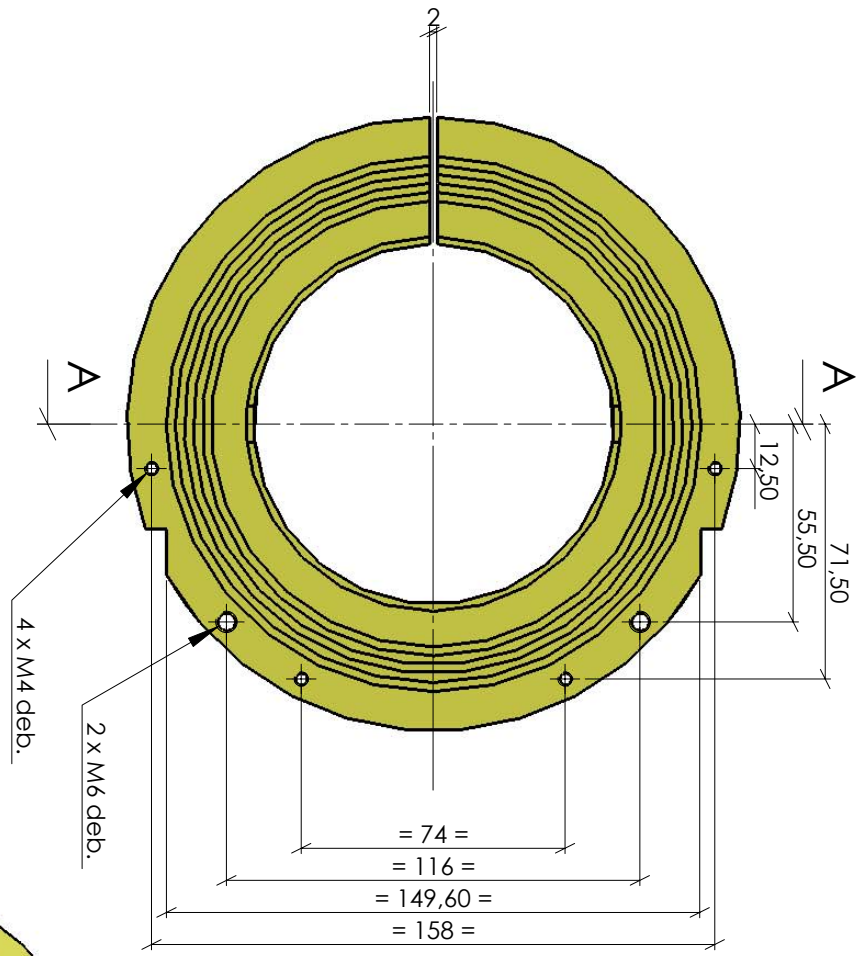
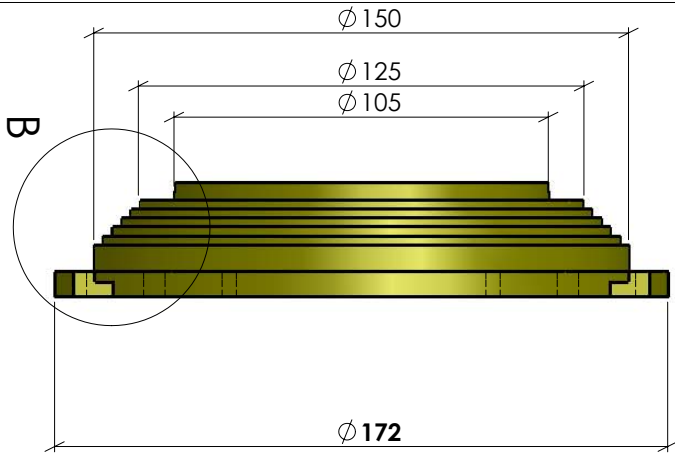
Désignation : XXX		Tol. gén. : js13js13	Qté : X
Matériau : XXX	Matériau : XXX	unité : mm, degré	Qté : X
Référence : XXX	Date de création : 09/07/2008	Page : 1 / 2	Echelle 1:2
Norm du fichier : D:\David\Boulet\Morris\Boulet\David\modif plaque - juillet 2008.plaque filr			
Dernière modif : mercredi 9 juillet 2008 13:53:02			
David Holleville		tel : 01 40 51 23 89	fax : 01 43 25 55 42
Observatoire de Paris		61 avenue de l'Observatoire 75014 Paris	mail : david.holleville@obspm.fr

Nom du modèle: plaque2
Nom de l'étude: Etude 1
Type de tracé: Déplacement statique Déplacements1
Echelle de déformation: 342816

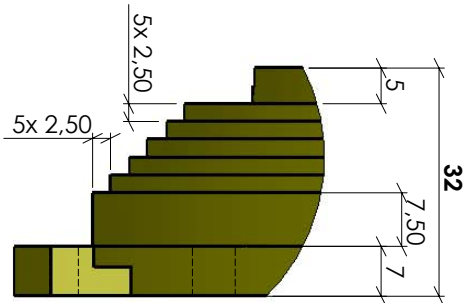


Nom du modèle: OPTOphase
Nom de l'étude: Etude 1
Type de tracé: Déplacement statique Déplacements1
Echelle de déformation: 28666.6

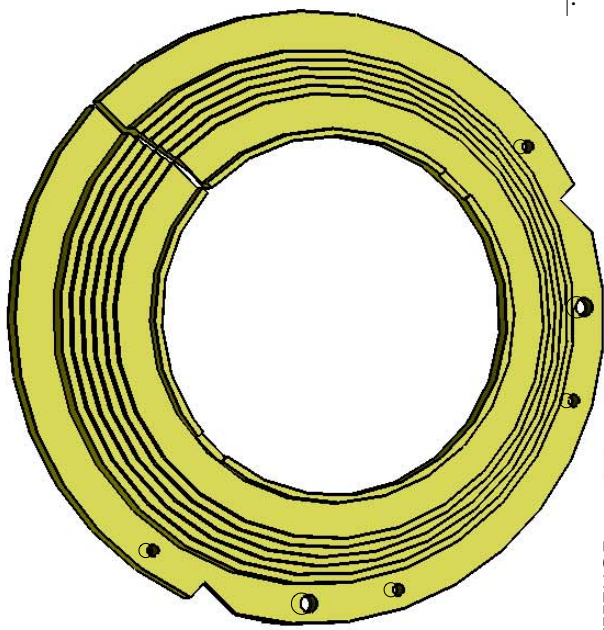
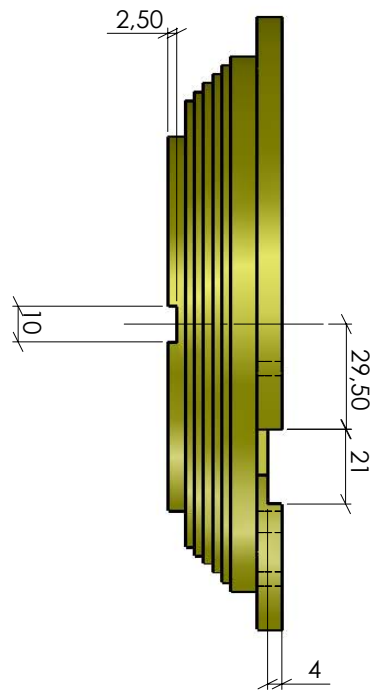




COUPE A-A
ECHELLE 2 : 3



DÉTAIL B
ECHELLE 4 : 3



Désignation : Support bobine			
Matp : BIARO	Matériau : CUC1 - OFHC	Tol. gén. : Jst3-jst3	Qté : 2
Référence : XXX	Date de création : 26/02/2008	Page : 1 / 1	Echelle 1:2
Nom du fichier : H:\David\boulet\Memija\Biaro\David support bobine			
Dernière modif : mardi 26 février 2008 00:40:49			
<div>David Holleville</div> <div> tel : 01 40 51 23 89 fax : 01 43 25 55 42 site / CNRS UMR 8630 Observatoire de Paris mail : david.holleville@obspm.fr </div>			

Bibliography

- [Adams 97] C.S. Adams & E. Riis. *LASER COOLING AND TRAPPING OF NEUTRAL ATOMS*. Prog. Quantum Electron., vol. 21, 1997.
- [Anderson 84] D Z Anderson. *Alignment of resonant optical cavities*. Appl. Opt., vol. 23, no. 17, page 2944, 1984.
- [Anderson 95] M.H. Anderson, J.R. Ensher, M.R. Matthews, C.E. Wieman & E. Cornell. *Observation of Bose-Einstein Condensation in a Dilute Atomic vapor*. Science (Washington), vol. 269, no. 5221, page 198, 1995.
- [Andrews 96] M.R. Andrews, M. Mewes, N.J. Van Druten, DS Durfee, D.M. Kurn & W. Ketterle. *Direct, nondestructive observation of a Bose condensate*. Science, vol. 273, no. 5271, page 84, 1996.
- [Antoine 03] C Antoine & C.J. Bordé. *Exact phase shifts for atom interferometry*. Phys. Lett. A, vol. 306, no. 5, page 277, 2003.
- [Appel 09a] J. Appel, A. MacRae & A. I. Lvovsky. *Versatile digital GHz phase lock for external cavity diode lasers*. Meas. Sci. Technol., vol. 20, page 055302, 2009.
- [Appel 09b] J Appel, P J Windpassinger, D Oblak, U B Hoff, N Kjaergaard & E S Polzik. *Mesoscopic atomic entanglement for precision measurements beyond the standard quantum limit*. Proceedings of the National Academy of Sciences of the United States of America, vol. 106, no. 27, page 10960, 2009.
- [Arecchi 72] F. T Arecchi, E. Courtens, R. Gilmore & H. Thomas. *Atomic Coherent States in Quantum Optics*. Phys. Rev. A, vol. 6, no. 6, page 2211, 1972.
- [Arora 07] B. Arora, M. S. Safronova & C. W. Clark. *Magic wavelengths for the np-ns transitions in alkali-metal atoms*. Phys. Rev. A, vol. 76, page 052509, 2007.
- [Aspect 82] A. Aspect, J. Dalibard & G. Roger. *Experimental Test of Bell's Inequalities Using Time-Varying Analyzers*. Phys. Rev. Lett., vol. 49, no. 25, page 1804, 1982.
- [Aspect 06] A. Aspect & P. Grangier. *Optique quantique 2: Tome 1 et 2*. Edition Ecole Polytechnique, 2006.

- [Baillard 06] X. Baillard, A. Gauguet, S. Bize, P. Lemonde, Ph. Laurent, A. Clairon & P. Rosenbusch. *Interference-filter-stabilized external-cavity diode lasers*. Opt. Commun., vol. 266, no. 2, page 609, 2006.
- [Banerjee 06] D. Banerjee. *PLL Performance, Simulation and Design Handbook (4th ed.)*. National Semiconductor, 2006.
- [Barrett 01] M. Barrett, J. Sauer & M. Chapman. *All-Optical Formation of an Atomic Bose-Einstein Condensate*. Phys. Rev. Lett., vol. 87, page 010404, 2001.
- [Bartenstein 04] M. Bartenstein, A. Altmeyer, S. Riedl, S. Jochim, C. Chin, J. Hecker Denschlag & R. Grimm. *Collective Excitations of a Degenerate Gas at the BEC-BCS Crossover*. Phys. Rev. Lett., vol. 92, no. 20, page 203201, 2004.
- [Bell 66] J.S. Bell. *On the Problem of Hidden Variables in Quantum Mechanics*. Rev. Mod. Phys., vol. 38, no. 3, page 447, 1966.
- [Bennett 62] W. R. Bennett. *Hole Burning Effects in a He-Ne Optical Maser*. Phys. Rev., vol. 126, no. 2, page 580, 1962.
- [Bernu 08] J. Bernu, S. Deléglise, C. Sayrin, S. Kuhr, I. Dotsenko, M. Brune, J. M. Raimond & S. Haroche. *Freezing Coherent Field Growth in a Cavity by the Quantum Zeno Effect*. Phys. Rev. Lett., vol. 101, page 180402, 2008.
- [Bertoldi 10] A. Bertoldi, S. Bernon, T. Vanderbruggen, A. Landragin & P. Bouyer. *In situ characterization of an optical cavity using atomic light shift*. Opt. Lett., vol. 35, page 3769, 2010.
- [Bitbol 97] M. Bitbol. *En quoi consiste la 'Révolution Quantique'*. Revue Internationale de Systémique, vol. 11, no. 6867, page 215, 1997.
- [Bitbol 99] M. Bitbol. *MECANIQUE QUANTIQUE : Une introduction philosophique*. Champs Flammarion, no. 391, 1999.
- [Bjorklund 80] Gary C Bjorklund. *Frequency-modulation spectroscopy: a new method for measuring weak absorptions and dispersions*. Opt. Lett., vol. 5, page 15, 1980.
- [Bjorklund 83] G. C. Bjorklund, M. D. Levenson, W. Lenth & C. Ortiz. *Frequency Modulation (FM) Spectroscopy*. Appl. Phys. B, vol. 32, page 145, 1983.
- [Black 01] E. D. Black. *An introduction to Pound Drever Hall laser frequency stabilization*. Am. J. Phys., vol. 69, page 79, 2001.
- [Bohm 52] D. Bohm. *A Suggested Interpretation of the Quantum Theory in Terms of "Hidden" Variables. I*. Phys. Rev, vol. 85, no. 2, page 166, 1952.

- [Bordé 89] C.J. Bordé. *Atomic interferometry with internal state labeling*. Physics letters A, vol. 140, page 10, 1989.
- [Bouchoule 02] I. Bouchoule & K. Mølmer. *Preparation of spin-squeezed atomic states by optical-phase-shift measurement*. Phys. Rev. A, vol. 66, page 043811, 2002.
- [Bourdel 04] T. Bourdel, L. Khaykovich, J. Cubizolles, J. Zhang, F. Chevy, M. Teichmann, L. Tarruell, S. Kokkelmans & C. Salomon. *Experimental Study of the BEC-BCS Crossover Region in Lithium 6*. Phys. Rev. Lett., vol. 93, page 050401, 2004.
- [Bouyer 96] P. Bouyer, T. L. Gustavson, K. G. Haritos & M. A. Kasevich. *Microwave signal generation with optical injection locking*. Opt. Lett., vol. 21, no. 18, page 1502, 1996.
- [Bouyer 97] P. Bouyer & M. A. Kasevich. *Heisenberg-limited spectroscopy with degenerate Bose-Einstein gases*. Phys. Rev. A, vol. 56, page R1083, 1997.
- [Bradley 95] C.C. Bradley, C.A. Sackett, J.J. Tollett & R.G. Hulet. *Evidence of Bose-Einstein Condensation in an Atomic Gas with Attractive Interactions*. Phys. Rev. Lett., vol. 75, no. 9, page 1687, 1995.
- [Brantut 08a] J. P. Brantut, J. F. Clément, M. Robert de Saint Vincent, G. Varoquaux, R. A. Nyman, A. Aspect, T. Bourdel & P. Bouyer. *Light-shift tomography in an optical-dipole trap for neutral atoms*. Phys. Rev. A, vol. 78, page 031401(R), 2008.
- [Brantut 08b] J.P. Brantut. *Manipulation d'atomes froids dans des potentiels lumineux*. PhD thesis, 2008.
- [Brune 90] M. Brune, S. Haroche, V. Lefevre, J. M. Raimond & N. Zagury. *Quantum nondemolition measurement of small photon numbers by Rydberg-atom phase-sensitive detection*. Phys. Rev. Lett., vol. 65, no. 8, page 976, 1990.
- [Brune 92] M. Brune, S. Haroche, J. M. Raimond, L. Davidovich & N. Zagury. *Manipulation of photons in a cavity by dispersive atom-field coupling: Quantum-nondemolition measurements and generation of "Schrödinger cat" states*. Phys. Rev. A, vol. 45, no. 7, page 5193, 1992.
- [Brune 96] M. Brune, E. Hagley, J. Dreyer, X. Maître, a. Maali, C. Wunderlich, Jm Raimond & S. Haroche. *Observing the Progressive Decoherence of the "Meter" in a Quantum Measurement*. Phys. Rev. Lett., vol. 77, no. 24, page 4887, 1996.
- [Carnal 91] O. Carnal & J. Mlynek. *Young's double-slit experiment with atoms: A simple atom interferometer*. Phys. Rev. Lett., vol. 66, no. 21, page 2689, 1991.

- [Caves 80a] C.M. Caves. *Quantum-mechanical radiation-pressure fluctuations in an interferometer*. Phys. Rev. Lett., vol. 45, no. 2, page 75, 1980.
- [Caves 80b] C.M. Caves, K.S. Thorne & R.W.P. Drever. *On the measurement of a weak classical force coupled to a quantum-mechanical oscillator. I. Issues of principle*. Rev. Mod. Phys., 1980.
- [Caves 81] C. M. Caves. *Quantum-mechanical noise in an interferometer*. Phys. Rev. D, vol. 23, no. 8, page 1693, 1981.
- [Chase 08] B. Chase & J. Geremia. *Collective processes of an ensemble of spin-1/2 particles*. Phys. Rev. A, vol. 78, page 052101, 2008.
- [Chaudhury 06] S. Chaudhury, G. Smith, K. Schulz & P.S. Jessen. *Continuous Nondemolition Measurement of the Cs Clock Transition Pseudospin*. Phys. Rev. Lett., vol. 96, page 043001, 2006.
- [Cheinet 06] P. Cheinet. *Conception et Réalisation d'un Gravimètre à Atomes Froids*. PhD thesis, Laboratoire National de Métrologie et d'Essai SYstèmes de Référence Temps-Espace, 2006.
- [Chu 85] S. Chu, L. Hollberg, JE Bjorkholm, A. Cable & A. Ashkin. *Three-dimensional viscous confinement and cooling of atoms by resonance radiation pressure*. Phys. Rev. Lett., vol. 55, no. 1, page 48, 1985.
- [Clement 08] J.F. Clement. *Réalisation d'un condensat de Bose-Einstein dans un piège dipolaire optique à 1560 nm*. PhD thesis, 2008.
- [Clément 09] J.-F. Clément, J.-P. Brantut, M. Robert de Saint-Vincent, R. A. Nyman, A. Aspect, T. Bourdel & P. Bouyer. *All-optical runaway evaporation to Bose-Einstein condensation*. Phys. Rev. A, vol. 79, page 061406(R), 2009.
- [Cohen-Tannoudji 86] Claude Cohen-Tannoudji, Bernard Diu & Franck Laloë. *Mécanique quantique*. Hermann, Editeur des sciences et des arts, 1986.
- [Cohen-Tannoudji 96] Claude Cohen-Tannoudji, Jacques Dupont-Roc & Gilbert Grynberg. *Processus d'interaction entre photons et atomes*. EDP Sciences, 1996.
- [Cohen-Tannoudji 97] C. N. Cohen-Tannoudji. *Manipulating atoms with photons*. Nobel Lecture, page 166, 1997.
- [Colella 75] R. Colella, A. W. Overhauser & S. A. Werner. *Observation of Gravitationally Induced Quantum Interference*. Phys. Rev. Lett., vol. 34, no. 23, page 1472, 1975.

- [Courtier 00] N. Courtier, B. Ducarme, J. Goodkind, J. Hinderer, Y. Imanishi, N. Seama, H. Sun, J. Merriam, B. Bengert & D. E. Smylie. *Global superconducting gravimeter observations and the search for the translational modes of the inner core*. Physics of The Earth and Planetary Interiors, vol. 117, no. 1-4, page 3, 2000.
- [Dalfovo 99] F. Dalfovo, S. Giorgini & S. Stringari. *Theory of Bose-Einstein condensation in trapped gases*. Rev. Mod. Phys., vol. 71, no. 3, page 463, 1999.
- [Dalibard 92] J. Dalibard, Y. Castin & K. Mølmer. *Wave-function approach to dissipative processes in quantum optics*. Phys. Rev. Lett., vol. 68, page 580, 1992.
- [Davis 95] K.B. Davis, M.O. Mewes, M.R. Andrews, N.J. Van Druten, D.S. Durfee, D.M. Kurn & W. Ketterle. *Bose-Einstein Condensation in a Gas of Sodium Atoms*. Phys. Rev. Lett., vol. 75, no. 22, page 3969, 1995.
- [Davisson 27] C. J. Davisson & L.H. Germer. *The Scattering of Electrons by a Single Crystal of Nickel*. Nature, no. 119, page 558, 1927.
- [de Echaniz 08] S. de Echaniz, M. Koschorreck, M. Napolitano, M. Kubasik & M. Mitchell. *Hamiltonian design in atom-light interactions with rubidium ensembles: A quantum-information toolbox*. Phys. Rev. A, vol. 77, page 032316, 2008.
- [Drever 83a] R W P Drever. *Laser Phase and Frequency Stabilization Using an Optical Resonator*. Appl. Phys. B, vol. 105, page 97, 1983.
- [Drever 83b] R. W. P. Drever, J. L. Hall, F. V. Kowalski, J. Hough, G. M. Ford, A. J. Munley & H. Ward. *Laser phase and frequency stabilization using an optical resonator*. Appl. Phys. B, vol. 31, page 97, 1983.
- [Echaniz 05] S. R. De. Echaniz, M. W. Mitchell, M. Kubasik, M. Koschorreck, H. Crepaz, J. Eschner & E. S. Polzik. *Conditions for spin squeezing in a cold ^{87}Rb ensemble*. J. Opt. B: Quantum Semiclassical Opt., vol. 7, no. 12, page S548, 2005.
- [Einstein 35] A. Einstein, B. Podolsky & N. Rosen. *Can Quantum-Mechanical Description of Physical Reality Be Considered Complete?* Phys. Rev., vol. 47, no. 10, page 777, 1935.
- [Ertmer 85] W. Ertmer, R. Blatt, J. L. Hall & M. Zhu. *Laser Manipulation of Atomic Beam Velocities: Demonstration of Stopped Atoms and Velocity Reversal*. Phys. Rev. Lett., vol. 54, no. 10, page 996, 1985.
- [Esteve 08] J. Esteve, C. Gross, A. Weller, S. Giovanazzi & M. K. Oberthaler. *Squeezing and entanglement in a Bose-Einstein condensate*. Nature, vol. 455, page 1216, 2008.

- [Faller 67] J E Faller. *Precision Measurement of the Acceleration of Gravity*. Science, vol. 158, no. 3797, page 60, 1967.
- [Fattal 04] D. Fattal, K. Inoue, J. Vučković, C. Santori, G. Solomon & Y. Yamamoto. *Entanglement Formation and Violation of Bell's Inequality with a Semiconductor Single Photon Source*. Phys. Rev. Lett., vol. 92, page 037903, 2004.
- [Feizpour 11] A. Feizpour, X. Xing & A. M. Steinberg. *Weak Measurement Amplification of Single-Photon Nonlinearity*. arXiv, no. 1101.0199v1, 2011.
- [Feng 01] S. Feng & H. G Winful. *Physical origin of the Gouy phase shift*. Opt. Lett., vol. 26, no. 8, page 485, 2001.
- [Fox 03] R. W. Fox, C. W. Oates & L. W. Hollberg. *Stabilizing diode lasers to high-finesse cavities*. Exp. Methods Phys. Sci., vol. 40, 2003.
- [Gauguet 09] A. Gauguet, B. Canuel, T. Lévêque, W. Chaibi & A. Landragin. *Characterization and limits of a cold-atom Sagnac interferometer*. Phys. Rev. A, vol. 80, page 063604, 2009.
- [Gehm 98] M. E. Gehm, T. A. Savard & J. E. Thomas. *Dynamics of noise-induced heating in atom traps*. Phys. Rev. A, vol. 58, no. 5, page 3914, 1998.
- [Gehrtz 85] M. Gehrtz, G. C. Bjorklund & E.A. Whittaker. *Quantum-limited laser frequency-modulation spectroscopy*. J. Opt. Soc. Am. B, vol. 2, page 1510, 1985.
- [Geremia 06] J. M. Geremia, J. K. Stockton & H. Mabuchi. *Tensor polarizability and dispersive quantum measurement of multilevel atoms*. Phys. Rev. A, vol. 73, page 042112, 2006.
- [Gleyzes 07] S. Gleyzes, S. Kuhr, C. Guerlin, J. Bernu, S. Deléglise, U. Busk Hoff, M. Brune, J.-M. Raimond & S. Haroche. *Quantum jumps of light recording the birth and death of a photon in a cavity*. Nature, vol. 446, pages 297–300, 2007.
- [Goda 08] K. Goda, O. Miyakawa, E. E. Mikhailov, S. Saraf, R. Adhikari, K. McKenzie, R. Ward, S. Vass, A. J. Weinstein & N. Mavalvala. *A quantum-enhanced prototype gravitational-wave detector*. Nat. Physics, vol. 4, page 472, 2008.
- [Goodkind 99] John M. Goodkind. *The superconducting gravimeter*. Review of Scientific Instruments, vol. 70, no. 11, page 4131, 1999.
- [Gouët 08] J. Le Gouët, T. Mehlstäubler, J. Kim, S. Merlet, A. Clairon, A. Landragin & F. Pereira Dos Santos. *Limits to the sensitivity of a low noise compact atomic gravimeter*. App. Phys. B, vol. 92, page 133, 2008.

- [Gouy 90a] L.G.. Gouy. *Sur la propagation anormale des ondes*. Compt. Rendue Acad. Sci. Paris, no. 111, page 33, 1890.
- [Gouy 90b] L.G.. Gouy. *Sur une propriété nouvelle des ondes lumineuses*. Acad. Sci. Paris, no. 110, page 1251, 1890.
- [Grangier 98] P. Grangier, J. A. Levenson & J.-P. Poizat. *Quantum non-demolition measurements in optics*. Nature, page 537, 1998.
- [Greiner 02] M. Greiner, O. Mandel, T. Esslinger, T.W. Hänsch & I. Bloch. *Quantum phase transition from a superfluid to a Mott insulator in a gas of ultracold atoms*. Nature, vol. 415, no. 6867, page 39, 2002.
- [Greiner 03] M. Greiner, C. a Regal & D. S Jin. *Emergence of a molecular Bose-Einstein condensate from a Fermi gas*. Nature, vol. 426, no. 6966, page 537, 2003.
- [Griffin 06] P. F. Griffin, K. J. Weatherill, S. G. MacLeod, R. M. Potvliege & C. S. Adams. *Spatially selective loading of an optical lattice by light-shift engineering using an auxiliary laser field*. New J. Phys., vol. 8, page 11, 2006.
- [Grimm 00] R. Grimm, M. Weidemüller & Y. B. Ovchinnikov. *Optical dipole traps for neutral atoms*. At. Mol. Opt. Phys., vol. 42, page 95, 2000.
- [Gross 10] C. Gross, T. Zibold, E. Nicklas, J. Estève & M. K. Oberthaler. *Nonlinear atom interferometer surpasses classical precision limit*. Nature, vol. 464, page 1165, 2010.
- [Grynberg 10] G. Grynberg, A. Aspect & C. Fabre. *Introduction to quantum optics*. Cambridge university press, 2010.
- [Guerin 08] W. Guerin, F. Michaud & R. Kaiser. *Mechanisms for Lasing with Cold Atoms as the Gain Medium*. Phys. Rev. Lett., vol. 101, page 093002, 2008.
- [Guerlin 07] C. Guerlin, J. Bernu, S. Dele, C. Sayrin, S. Kuhr, S. Gleyzes, M. Brune, J.-M. Raimond & S. Haroche. *Progressive field-state collapse and quantum non-demolition photon counting*. Nature, vol. 448, page 889, 2007.
- [Halban 36] H. V. Halban & P. Preiswerk. *Preuve expérimentale de la diffraction des neutrons*. Compte rendu à l'académie des sciences de Paris, no. 203, page 73, 1936.
- [Hansen 01] H. Hansen, T. Aichele, C. Hettich, P. Lodahl, AI Lvovsky, J. Mlynek & S. Schiller. *Ultrasensitive pulsed, balanced homodyne detector: application to time-domain quantum measurements*. Opt. Lett., vol. 26, no. 21, page 1714, 2001.

- [Haroche 08] S Haroche. *Mesures Quantiques Non Destructives*. Cours au College de France, 2007-08.
- [Heidmann 07] A. Heidmann. *Mesures à la limite quantique*. Cours à l'école pré-doctorale des Houches, 2007.
- [Hilico 92] L. Hilico, C. Fabre & E. Giacobino. *Operation of a "Cold-Atom Laser" in a Magneto-Optical Trap*. Europhys. Lett., vol. 18, no. 8, page 685, 1992.
- [Hoffnagle 88] J.A. Hoffnagle. *Proposal for continuous white-light cooling of an atomic beam*. Opt. Lett, vol. 13, page 102, 1988.
- [Hughes 09] K. J. Hughes, J. H. T. Burke & C. A. Sackett. *Suspension of Atoms Using Optical Pulses, and Application to Gravimetry*. Phys. Rev. Lett., vol. 102, page 150403, 2009.
- [Igor 06] S Igor. *Theory of Atomic Spectra*. Lavoisier, 2006.
- [Impens 06] F. Impens, P. Bouyer & C.J. Bordé. *Matter-wave cavity gravimeter*. Appl. Phys. B, vol. 84, no. 4, page 603, 2006.
- [Itano 82] Wayne M. Itano, L. L. Lewis & D. J. Wineland. *Shift of S_{122} hyperfine splittings due to blackbody radiation*. Physical Review A, vol. 25, no. 2, page 1233, 1982.
- [Jaynes 63] E.T. Jaynes & F.W. Cummings. *Comparison of quantum and semiclassical radiation theories with application to the beam maser*. Proceedings of the IEEE, vol. 51, no. 1, page 89, 1963.
- [Johnson 00] M.A. Johnson & C.H. Townes. *Quantum effects and optimization of heterodyne detection*. Opt. Commun., vol. 179, page 183, 2000.
- [Johnson 10] DMS Johnson, JM Hogan, S Chiow & MA Kasevich. *Broadband optical heterodyne frequency shifting*. Opt. Lett., vol. 35, no. 5, page 745, 2010.
- [Jonathan 05] J. M. Jonathan. *Electro-Acousto Optique*. Cours de l'Institut d'optique, Graduate School, 2005.
- [Jördens 08] R. Jördens, N. Strohmaier, K. Gunter, H. Moritz & T. Esslinger. *A Mott insulator of fermionic atoms in an optical lattice*. Nature, vol. 455, no. 7210, page 204, 2008.
- [Kasevich 91] M. Kasevich & S. Chu. *Atomic interferometry using stimulated Raman transitions*. Phys. Rev. Lett., vol. 67, no. 2, page 181, 1991.
- [Kater 18] H Kater. *An account of experiments for determining the length of the pendulum vibrating seconds in the latitude of London*. Philosophical Transactions of the Royal Society of London, page 104, 1818.

- [Keith 91] D.W. Keith, C.R. Ekstrom, Q.A. Turchette & D.E. Pritchard. *An Interferometer for Atoms*. Phys. Rev. Lett., vol. 66, no. 21, page 2693, 1991.
- [Ketterle 93] W. Ketterle, K.B. Davis, M.A. Joffe, A. Martin & D.E. Pritchard. *High densities of cold atoms in a dark spontaneous-force optical trap*. Phys. Rev. Lett., vol. 70, no. 15, page 2253, 1993.
- [Kitagawa 93] M. Kitagawa & M. Ueda. *Squeezed spin states*. Phys. Rev. A, vol. 47, page 5138, 1993.
- [Kogelnik 66] H. Kogelnik & T. Li. *Laser Beams and Resonators*. Appl. Opt., vol. 5, no. 10, page 1550, 1966.
- [Kuzmich 97] A. Kuzmich, K. Molmer & E. S. Polzik. *Spin Squeezing in an Ensemble of Atoms Illuminated with Squeezed Light*. Phys. Rev. Lett., vol. 79, no. 24, page 4782, December 1997.
- [Kuzmich 98] A. Kuzmich, N. P Bigelow & L Mandel. *Atomic quantum non-demolition measurements and squeezing*. Europhys. Lett., vol. 42, no. 5, page 481, 1998.
- [LaCoste 67] LJB LaCoste, N. Clarkson & G. Hamilton. *LACOSTE AND ROMBERG STABILIZED PLATFORM SHIPBOARD GRAVITY METER*. Geophysics, vol. 32, page 99, 1967.
- [Laloë 10] F. Laloë & WJ Mullin. *Quantum properties of a single beam splitter*. Arxiv preprint arXiv:1004.1731, 2010.
- [Landau 91] L.D. Landau & E.M. Lifshitz. *Quantum Mechanics Non-Relativistic Theory*. Butterworth-Heinemann, 1991.
- [Lawrence 99] M J Lawrence, B Willke, M E Husman, E K Gustafson & R L Byer. *Dynamic response of a Fabry-Perot interferometer*. J. Opt. Soc. Am. B, vol. 16, no. 4, page 523, 1999.
- [Leroux 10] I. D. Leroux, M. H. Schleier-Smith & V. Vuletić. *Implementation of Cavity Squeezing of a Collective Atomic Spin*. Phys. Rev. Lett., vol. 104, page 073602, 2010.
- [Lindblad 76] G. Lindblad. *On the generators of quantum dynamical semi-groups*. Commun. Math. Phys., vol. 48, no. 2, page 119, 1976.
- [Lodewyck 09] J. Lodewyck, P. G. Westergaard & P. Lemonde. *Nondestructive measurement of the transition probability in a Sr optical lattice clock*. Phys. Rev. A, vol. 79, page 061401, 2009.
- [Louchet-Chauvet 10] A. Louchet-Chauvet, J Appel, J. J. Renema, D. Oblak, N. Kjaergaard & E. S. Polzik. *Entanglement-assisted atomic clock beyond the projection noise limit*. New J. Phys., vol. 12, page 065032, 2010.

- [Lucas-Leclin. 98] G. Lucas-Leclin. *Importance des propriétés spectrales des lasers pour les performances des horloges à pompage optique*. PhD thesis, University Paris XI, 1998.
- [Luiten 96] O.J. Luiten, M. W. Reynolds & J. T. M. Walraven. *Kinetic theory of the evaporative cooling of a trapped gas*. Phys. Rev. A, vol. 53, no. 1, page 381, 1996.
- [Lye 03] J. E. Lye, J. J. Hope & J. D. Close. *Nondestructive dynamic detectors for Bose-Einstein condensates*. Phys. Rev. A, vol. 67, page 043609, 2003.
- [MacAdam 92] K. B. MacAdam, A. Steinbach & C. Wieman. *A narrow-band tunable diode laser system with grating feedback, and a saturated absorption spectrometer for Cs and Rb*. Am. J. Phys., vol. 60, no. 12, page 1098, 1992.
- [Maier-Leibnitz 62] H. Maier-Leibnitz & T. Springer. *Ein Interferometer für langsame Neutronen*. Zeitschrift für Physik A Hadrons and Nuclei, vol. 167, page 386, 1962.
- [Marson 86] I. Marson & JE Faller. *g-the acceleration of gravity: its measurement and its importance*. Journal of Physics E: Scientific Instruments, vol. 19, page 22, 1986.
- [Marton 52] L. Marton. *Electron Interferometer*. Phys. Rev., vol. 85, no. 6, page 1057, 1952.
- [Meiser 08] D. Meiser, J. Ye & M. J. Holland. *Spin squeezing in optical lattice clocks via lattice-based QND measurements*. New J. Phys., vol. 10, page 073014, 2008.
- [Meiser 09] D. Meiser, Jun Ye, D. Carlson & M. Holland. *Prospects for a Millihertz-Linewidth Laser*. Phys. Rev. Lett., vol. 102, page 163601, 2009.
- [Mekhov 09] I.B. Mekhov & H. Ritsch. *Quantum Nondemolition Measurements and State Preparation in Quantum Gases by Light Detection*. Phys. Rev. Lett., vol. 102, page 20403, 2009.
- [Metcalf 01] H. J. Metcalf & P. Van Der Straten. *Laser Cooling and Trapping*. Springer, 2001.
- [Metcalf 03] H. J. Metcalf & P. van der Straten. *Laser cooling and trapping of atoms*. J. Opt. Soc. Am. B, vol. 20, no. 5, page 887, 2003.
- [Miller 05] R. Miller, T. E. Northup, K. M. Birnbaum, A. Boca, A. D. Boozer & H. J. Kimble. *Trapped atoms in cavity QED: coupling quantized light and matter*. J. Phys. B: At., Mol. Opt. Phys., vol. 38, no. 9, page S551, 2005.

- [Morton 05] J.J.L. Morton, A.M. Tyryshkin, A. Ardavan, S.C. Benjamin, K. Porfyrakis, SA Lyon & G.A.D. Briggs. *Bang-bang control of fullerene qubits using ultrafast phase gates*. Nat. Phys., vol. 2, no. 1, page 40, 2005.
- [Müller 07] T. Müller, T. Wendrich, M. Gilowski, C. Jentsch, E. M. Rasel & W. Ertmer. *Versatile compact atomic source for high-resolution dual atom interferometry*. Phys. Rev. A, vol. 76, page 063611, 2007.
- [Mullin 10] W. J. Mullin & F. Laloë. *Creation of NOON States from Double Fock-State/Bose-Einstein Condensates*. J. Low Temp. Phys., vol. 162, page 250, 2010.
- [Nellessen 90] J Nellessen, J Werner & W Ertmer. *Magneto-optical compression of a monoenergetic sodium atomic beam*. Opt. Commun., vol. 78, page 300, 1990.
- [Nez 93] F. Nez, F. Biraben, R. Felder & Y. Millerioux. *Optical frequency determination of the hyperfine components of the $5S_{1/2}$ - $5D_{3/2}$ two-photon transitions in rubidium*. Opt. Commun., vol. 102, no. 5, page 432, 1993.
- [Nicolas 05] Nicolas. *Optique des lasers*. Cours de l'Institut d'optique, Graduate School, 2005.
- [Niebauer 95] TM Niebauer, GS Sasagawa, JE Faller, R Hilt & F Klopping. *A new generation of absolute gravimeters*. Metrologia, vol. 32, no. 3, page 159, 1995.
- [Oblak 05] D. Oblak, P. G. Petrov, C. L. Garrido Alzar, W. Tittel, A. K. Vershovski, J. K. Mikkelsen, J. L. Sørensen & E. S. Polzik. *Quantum-noise-limited interferometric measurement of atomic noise: Towards spin squeezing on the Cs clock transition*. Phys. Rev. A, vol. 71, page 043807, 2005.
- [Pati 07] G. Pati, M. Salit, K. Salit & M. Shahriar. *Demonstration of a Tunable-Bandwidth White-Light Interferometer Using Anomalous Dispersion in Atomic Vapor*. Phys. Rev. Lett., vol. 99, page 133601, 2007.
- [Petrich 94] W. Petrich, M. H. Anderson, J. R. Ensher & E. a. Cornell. *Behavior of atoms in a compressed magneto-optical trap*. J. Opt. Soc. Am. B, vol. 11, no. 8, page 1332, 1994.
- [Pezzé 06] Luca Pezzé & Augusto Smerzi. *Phase sensitivity of a Mach-Zehnder interferometer*. Phys. Rev. A, vol. 73, page 011801, 2006.

- [Phillips 85] W. D. Phillips, J. V. Prodan & H. J. Metcalft. *Laser cooling and electromagnetic trapping of neutral atoms*. J. Opt. Soc. Am. B, vol. 2, no. 11, page 1751, 1985.
- [Prothero 68] W. A. Prothero & J. M. Goodkind. *A Superconducting Gravimeter*. Review of Scientific Instruments, vol. 39, no. 9, page 1257, 1968.
- [Ramsey 50] Norman F. Ramsey. *A Molecular Beam Resonance Method with Separated Oscillating Fields*. Phys. Rev., vol. 78, no. 6, page 695, 1950.
- [Riccardi 02] U Riccardi, G Berrino & G Corrado. *Changes in instrumental sensitivity of some feedback systems used in LaCoste-Romberg gravimeters*. Metrologia, vol. 39, no. 5, page 509, 2002.
- [Riedel 10] M. F. Riedel, P. Böhi, Y. Li, T. W. Hänsch, A. Sinatra & P. Treutlein. *Atom-chip-based generation of entanglement for quantum metrology*. Nature, vol. 464, no. 7292, page 1170, 2010.
- [Riehle 91] F. Riehle, T. Kisters, A. Witte, J. Helmcke & C.J. Bordé. *Optical Ramsey spectroscopy in a rotating frame: Sagnac effect in a matter-wave interferometer*. Phys. Rev. Lett., vol. 67, no. 2, page 177, 1991.
- [Riis 90] E. Riis, D.S. Weiss, K.A. Moler & S. Chu. *Atom funnel for the production of a slow, high-density atomic beam*. Phys. Rev. Lett., vol. 64, no. 14, page 1658, 1990.
- [Robert-de Saint-Vincent 10] M. Robert-de Saint-Vincent, J.-P. Brantut, Ch. J. Bordé, a. Aspect, T. Bourdel & P. Bouyer. *A quantum trampoline for ultra-cold atoms*. Europhys. Lett., vol. 89, page 10002, 2010.
- [Roch 97] J.F. Roch, K. Vigneron, P. Grelu, A. Sinatra, J.P. Poizat & P. Grangier. *Quantum nondemolition measurements using cold trapped atoms*. Phys. Rev. Lett., vol. 78, no. 4, page 634, 1997.
- [Rohde 02] H Rohde, J Eschner & R Blatt. *Optical decay from a Fabry-Perot cavity faster than the decay time*. OSA B, vol. 19, no. 6, page 1425, 2002.
- [Rowe 01] M a Rowe, D Kielpinski, V Meyer, C A Sackett, W M Itano, C Monroe & D J Wineland. *Experimental violation of a Bell's inequality with efficient detection*. Nature, vol. 409, no. 6822, page 791, 2001.
- [Saffman 09] M. Saffman, D. Oblak, J. Appel & E. Polzik. *Spin squeezing of atomic ensembles by multicolor quantum nondemolition measurements*. Phys. Rev. A, vol. 79, page 023831, 2009.

- [Safronova 06] M. S. Safronova, B. Arora & C. W. Clark. *Frequency-dependent polarizabilities of alkali-metal atoms from ultraviolet through infrared spectral regions*. Phys. Rev. A, vol. 73, page 022505, 2006.
- [Santarelli 99] G. Santarelli, Ph. Laurent, P. Lemonde, A. Clairon, A. G. Mann, S. Chang, A. N. Luiten & C. Salomon. *Quantum projection noise in an atomic fountain: a high stability cesium frequency standard*. Phys. Rev. Lett., vol. 82, page 4619, 1999.
- [Savalli 99] V. Savalli, G.Z.K. Horvath, P.D. Featonby, L. Cognet, N. Westbrook, C.I. Westbrook & A. Aspect. *Optical detection of cold atoms without spontaneous emission*. Opt. Lett., vol. 24, no. 22, page 1552, 1999.
- [Savard 97] T. Savard, K. O. Hara & J. Thomas. *Laser-noise-induced heating in far-off resonance optical traps*. Phys. Rev. A, vol. 56, no. 2, page R1095, 1997.
- [Schawlow 58] A.L. Schawlow & C.H. Townes. *Infrared and optical masers*. Phys. Rev., vol. 112, no. 6, page 1940, 1958.
- [Schleier-Smith 10a] M. H. Schleier-Smith, I. D. Leroux & V. Vuletić. *Squeezing the collective spin of a dilute atomic ensemble by cavity feedback*. Phys. Rev. A, vol. 81, page 021804(R), 2010.
- [Schleier-Smith 10b] M. H. Schleier-Smith, I. D. Leroux & V. Vuletić. *States of an Ensemble of Two-Level Atoms with Reduced Quantum Uncertainty*. Phys. Rev. Lett., vol. 104, page 073604, 2010.
- [Schleier-Smith 10c] M. H. Schleier-Smith, I. D. Leroux & V. Vuletić. *States of an Ensemble of Two-Level Atoms with Reduced Quantum Uncertainty: Auxiliary Material*. Unpublished, 2010.
- [Schmieder 72] Robert W Schmieder. *Matrix Elements of the Quadratic Stark Effect on Atoms with Hyperfine Structure*. Am. J. Phys., vol. 40, page 297, 1972.
- [Schoof 01] A. Schoof, J. Grünert, S. Ritter & A. Hemmerich. *Reducing the linewidth of a diode laser below 30 Hz by stabilization to a reference cavity with a finesse above 10(5)*. Opt. Lett., vol. 26, no. 20, page 1562, 2001.
- [Shirley 82] J. H. Shirley. *Modulation transfer processes in optical heterodyne saturation spectroscopy*. Opt. Lett., vol. 7, no. 11, page 537, 1982.
- [Siegman 86] A. E. Siegman. Lasers. University Science Books, 1986.
- [Simon 10] C. Simon & E. S Polzik. *Fock-state view of weak-value measurements and implementation with photons and atomic ensembles*. ArXiv, no. 1010.3695V1, 2010.

- [Smith 04] G. Smith, S. Chaudhury, A. Silberfarb, I. Deutsch & P.S. Jessen. *Continuous Weak Measurement and Nonlinear Dynamics in a Cold Spin Ensemble*. Phys. Rev. Lett., vol. 93, page 163602, 2004.
- [Smith 06] G.A. Smith, A. Silberfarb, I.H. Deutsch & P.S. Jessen. *Efficient quantum-state estimation by continuous weak measurement and dynamical control*. Phys. Rev. Lett., vol. 97, page 180403, 2006.
- [Steck 10] D. A. Steck. *Rubidium 87 D Line Data*. Published on-line: <http://steck.us/alkalidata/rubidium87numbers.pdf>, 2010.
- [Steuernagel 05] O Steuernagel. *Equivalence between focused paraxial beams and the quantum harmonic oscillator*. Am. J. Phys., vol. 73, no. 7, page 625, 2005.
- [Stockton 04] J. K. Stockton, R. van Handel & H. Mabuchi. *Deterministic Dicke-state preparation with continuous measurement and control*. Phys. Rev. A, vol. 70, page 022106, 2004.
- [Stockton 05] John K Stockton. *Adiabatic elimination with a multi-level Alkali atom driven off-resonance*. Quantum, 2005.
- [Streed 06] E. Streed, J. Mun, M. Boyd, G. Campbell, P. Medley, W. Ketterle & D. Pritchard. *Continuous and Pulsed Quantum Zeno Effect*. Phys. Rev. Lett., vol. 97, page 260402, 2006.
- [Takano 09] T. Takano, M. Fuyama, R. Namiki & Y. Takahashi. *Spin Squeezing of a Cold Atomic Ensemble with the Nuclear Spin of One-Half*. Phys. Rev. Lett., vol. 102, page 033601, 2009.
- [Teper 08] I. Teper, G. Vrijsen, J. Lee & M. A. Kasevich. *Backaction noise produced via cavity-aided nondemolition measurement of an atomic clock state*. Phys. Rev. A, vol. 78, page 051813(R), 2008.
- [Thorne 78] K. S. Thorne, R. W. P. Drever & C. M. Caves. *Quantum nondemolition measurements of harmonic oscillators*. Phys. Rev. Lett., vol. 40, no. 11, 1978.
- [Vanderbruggen 11] T. Vanderbruggen, S. Bernon, A. Bertoldi, A. Landragin & P. Bouyer. *Spin-squeezing and Dicke-state preparation by heterodyne measurement*. Phys. Rev. A, vol. 83, page 013821, 2011.
- [Von Laue 15] M Von Laue. *Concerning the detection of X-ray interferences*. Nobel lecture, 1915.
- [Vuletic 00] V Vuletic & S Chu. *Laser cooling of atoms, ions, or molecules by coherent scattering*. Phys. Rev. Lett., vol. 84, no. 17, page 3787, 2000.

- [Wasilewski 10] W. Wasilewski, K. Jensen, H. Krauter, J. J. Renema, M. V. Balabas & E. S. Polzik. *Quantum Noise Limited and Entanglement-Assisted Magnetometry*. Phys. Rev. Lett., vol. 104, page 133601, 2010.
- [Weihs 98] G. Weihs, T. Jennewein, C. Simon, H. Weinfurter & A. Zeilinger. *Violation of Bell's Inequality under Strict Einstein Locality Conditions*. Phys. Rev. Lett., vol. 81, no. 23, page 5039, 1998.
- [Windpassinger 08a] P. J. Windpassinger, D. Oblak, U. Busk Hoff, J. Appel, N. Kjaergaard & E. S. Polzik. *Inhomogeneous light shift effects on atomic quantum state evolution in non-destructive measurements*. New J. Phys., vol. 10, page 053032, 2008.
- [Windpassinger 08b] P. J. Windpassinger, D. Oblak, P. G. Petrov, M. Kubasik, M. Saffman, C. L. Garrido Alzar, J. Appel, J. H. Müller, N. Kjaergaard & E. S. Polzik. *Nondestructive Probing of Rabi Oscillations on the Cesium Clock Transition near the Standard Quantum Limit*. Phys. Rev. Lett., vol. 100, page 103601, 2008.
- [Windpassinger 09] P. J. Windpassinger, M. Kubasik, M. Koschorreck, A. Boisen, E. S. Polzik N. Kjaergaard & J. H. Müller. *Ultra-low noise differential AC-coupled photodetector for sensitive pulse detection applications*. Meas. Sci. Technol., vol. 20, page 055301, 2009.
- [Wineland 92] D. J. Wineland, J. J. Bollinger, W. M. Itano, F. L. Moore & D. J. Heinzen. *Spin squeezing and reduced quantum noise in spectroscopy*. Phys. Rev. A, vol. 46, page R6797, 1992.
- [Wu 97] H. Wu, E. Arimondo & C. Foot. *Dynamics of evaporative cooling for Bose-Einstein condensation*. Phys. Rev. A, vol. 56, no. 1, page 560, 1997.
- [Zeller 10] Wolfgang Zeller, Lars Naehle, Peter Fuchs, Florian Gerschuetz, Lars Hildebrandt & Johannes Koeth. *DFB Lasers Between 760 nm and 16 μ m for Sensing Applications*. Sensors, vol. 10, no. 4, page 2492, 2010.
- [Zimmermann 04] C. Zimmermann, D. Kruse, C. Von Cube, S. Slama, B. Deh & P. Courteille. *Collective atomic recoil lasing*. J. Mod. Opt., no. 51, page 957, 2004.
- [Zurek 81] W.H. Zurek. *Pointer basis of quantum apparatus: Into what mixture does the wave packet collapse?* Phys. Rev. D, vol. 24, no. 6, page 1516, 1981.

